CAIO DE CARVALHO LUCARELLI

PERFORMANCE INVESTIGATION OF A CLIMATE-ACTIVE TOP LIGHTING CELL DEVELOPED WITH GENERATIVE PROCESSES AND DIGITAL MANUFACTURING

Thesis submitted to the Architecture and Urban Planning Graduate Program of the Universidade Federal de Viçosa in partial fulfillment of the requirements for the degree of *Doctor Scientiae*.

Adviser: Joyce Correna Carlo

VIÇOSA - MINAS GERAIS
2024

Ficha catalográfica elaborada pela Biblioteca Central da Universidade Federal de Viçosa - Campus Viçosa

T

L932p
2024

Lucarelli, Caio de Carvalho, 1994-

Performance investigation of a climate-active top-lighting cell developed with generative processes and digital manufacturing / Caio de Carvalho Lucarelli. – Viçosa, MG, 2024.

1 tese eletrônica (270 f.): il. (algumas color.).

Texto em inglês.

Inclui apêndices.

Orientador: Joyce Correna Carlo.

Tese (doutorado) - Universidade Federal de Viçosa, Departamento de Arquitetura e Urbanismo, 2024.

Inclui bibliografia.

DOI: https://doi.org/10.47328/ufvbbt.2024.284

Modo de acesso: World Wide Web.

1. Iluminação (Arquitetura e decoração). 2. Luz na arquitetura - Simulação por computador. 3. Luz na arquitetura - Projeto auxiliado por computador. 4. Inteligência artificial. I. Carlo, Joyce Correna, 1973-. II. Universidade Federal de Viçosa. Departamento de Arquitetura e Urbanismo. Programa de Pós-Graduação em Arquitetura e Urbanismo. III. Título.

CDD 22. ed. 729.28

Bibliotecário(a) responsável: Alice Regina Pinto Pires CRB-6/2523

CAIO DE CARVALHO LUCARELLI

PERFORMANCE INVESTIGATION OF A CLIMATE-ACTIVE TOP-LIGHTING CELL DEVELOPED WITH GENERATIVE PROCESSES AND DIGITAL MANUFACTURING

Thesis submitted to the Architecture and Urban Planning Graduate Program of the Universidade Federal de Viçosa in partial fulfillment of the requirements for the degree of *Doctor Scientiae*.

APPROVED: February 22, 2024.

Assent:

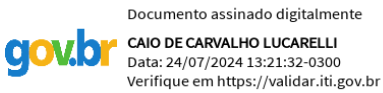

Caio de Carvalho Lucarelli
Author

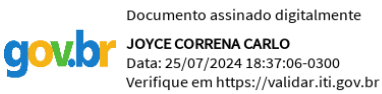

Joyce Correna Carlo
Adviser

To my family, friends, and colleagues.

To those who left and those who remain.

ACKNOWLEDGEMENTS

Above all, I thank God for accompanying me through the darkest hours and most pleasant moments.

I acknowledge Universidade Federal de Viçosa (UFV), the Department of Architecture and Urban Planning (DAU), and its postgraduate program (PPGau). I thank my advisor, Doctor Joyce Carlo, for helping me be concise and not tell tales throughout this Thesis. Sometimes, I still did. Once more, I thank you for the psychological and emotional support, or at least for trying (and, this time, it worked). I appreciate your dedication to our study, for teaching me how to snatch funding opportunities, for compelling me to pursue empirical investigations, and for the reassurance in each hardship. Thank you for believing in my competence and for nourishing me in the not-so-early stages of my academic life. I will be forever grateful and remember these years with tenderness.

I thank my family and friends, to whom I dedicate this thesis. I am grateful to my mother, Hêliandra; my aunt, Evelize; my grandpa, Helvécio; my sister, Nicole; my nephew and godson, Miguel; and my godmother, Fatinha. Mel, I will remember and love you forever. I am also forever grateful to my friends. I harbored many, but I want to recognize especially Ediones, Matheus, Elisa, João, João Victor, Luiz, Paula, Pece, and Carol, who were with me almost every day.

I thank my colleagues, advisees, and friends at our research laboratory, LATECAE, for the laughs and all the help. Thanks, and sorry for having to put up with my grumpiness and aloofness. I cherish you with all my heart: Matheus, Pece, Olga, Thaís, João, Raquel, Gustavo, Denis, Mário, and Ligi (in order of your arrival on the day I wrote this text).

I acknowledge LEC *("Laboratório de Materiais Construtivos" and "Laboratório de Testes Mecânicos"*), part of the Civil Engineering Department at the Federal University of Viçosa, for helping me with the structural and rapid aging experiments. In addition, I thank *CenTev TecnoParq ("Centro Tecnológico de Desenvolvimento Regional de Viçosa"*), especially both Maker Labs and their employees, for expediting the prototyping process.

Finally, I would like to acknowledge the *"Coordenação de Aperfeiçoamento de Pessoal de Nível Superior"* – Brazil (CAPES) – which granted my scholarship

via Finance Code 001; *“Fundação de Amparo à Pesquisa de Minas Gerais”* (FAPEMIG) that sponsored this research via the financing notice N° 001/2021 Universal Demand - under process code APQ-00266-21; and *“Conselho Nacional de Desenvolvimento Científico e Tecnológico”* (CNPQ) – financing notice N° 59/2022 – under process code 406426/2022-8.

“It does not do to dwell on dreams and forget to live”.

(J. K. Rowling)

THESIS ABSTRACT

LUCARELLI, Caio de Carvalho, D.Sc. Universidade Federal de Viçosa, March. 2024. **Performance Investigation of a Climate-Active Top Lighting Cell Developed with Generative Processes and Digital Manufacturing.** Adviser: Joyce Correna Carlo.

Building electricity demands have risen due to floor area growth, increased indoor time, overreliance on artificial systems, aging infrastructures, and distribution bottlenecks. Since 2017, energy expenses have increased up to 20%, totalizing 40% of worldwide requirements and 36% of carbon emissions in the early 2020s. In this scenario, early-stage building design and performance simulation demonstrate the highest potential and lowest cost for energy saving. Among all building subsystems, enclosures are multicriteria mediators that partake in most indoor/outdoor energy flow, naturally conditioning buildings, and promoting occupant comfort. However, as prescriptive solutions, they only operate within predetermined environmental thresholds and cannot account for environmental dynamicity or long-term climate changes. Conversely, climate-active building envelopes potentially improve occupants' comfort in real-time, responding to environmental fluctuations while maintaining acceptable levels of energy consumption. Although their ideation, design, simulation, and materialization are still complex, their various iterations can lead to more optimal solutions. Thus, there is a need to address how to design, operate, and maintain active envelopes and access their adaptation, behavior, performance parameters, and materialization. This research covered the ideation, whole-building environmental performance simulation, design, and manufacturing process of a climate-active top lighting cell. It assessed its contributions to human visual and thermal comfort and its optical and structural properties before and after desktop digital manufacturing. It followed a research-through-design and investigated a design-for-manufacturing-and-assembly workflow to help solve the oversimplification of simulations for active typologies, still employing low computational time and cost via iterative simulation and post selection instead of design optimization. As the main results, this study offered an integrative theoretical background on climate-

active skins and a preamble for future active building classifications. Further, it created a more comprehensive parametric modeling and simulation workflow for building motion and real-time simulation, defined a variance-based simplification strategy for motion constraints, and demonstrated the incapacity of current simulation approaches (that only consider solstices and equinoxes as key dates) to represent the dynamicity and performance of active systems. This research also evaluated various processes within the design-for-manufacture approach, assessing the visual and structural properties of thermoplastics as end-use materials for physical prototypes and potential experiments to complement or replace software-intensive or time-consuming applications such as luminance-based high dynamic range imaging for daylight assessment and standard material degradation. Finally, this Thesis is an extensively documented and replicable research of a simulation and experiment-based digital modeling and physical manufacturing process for a cyber-physical system that acts upon environmental sensing to potentialize human comfort within buildings.

Keywords: *Research-through-design; design-for-manufacture-and-assembly; top lighting; climate-active building envelopes.*

RESUMO DA TESE

LUCARELLI, Caio de Carvalho, D.Sc. Universidade Federal de Viçosa, março 2024. **Investigação do Desempenho de uma Célula Ativa para Controle de Iluminação Zenital materializada por Processos Generativos e Manufatura Digital.** Orientadora: Joyce Correna Carlo.

A demanda por eletricidade em edificações é advento do crescimento da área edificada, do aumento nas horas despendidas em ambientes internos, da dependência exacerbada de equipamentos de condicionamento artificial, do envelhecimento da infraestrutura do espaço construído e dos gargalos da distribuição elétrica. Esse consumo cresceu em até 20% desde 2017, somando 40% da demanda de energia global em apenas um setor que já responde por 36% das emissões de carbono mundiais desde o início da década de 2020. Dentre os subsistemas das edificações, os envelopes construtivos mediam a maior parte dos fluxos de energia entre os ambientes externo e interno, agindo no condicionamento natural e promoção do conforto para usuários. Apesar disso, soluções de projeto prescritivas só operam entre circunstâncias ambientais predeterminadas e têm baixa capacidade de resposta à dinamicidade do clima local e as mudanças ao longo dos anos. Contrário, envelopes construtivos ativos potencialmente aumentam o conforto ambiental dos usuários em tempo real, reagindo a flutuações ambientais enquanto mantêm níveis aceitáveis de consumo energético. Apesar da concepção, projeto, simulação e materialização complexas, sua natureza iterativa pode acarretar mais soluções ótimas de projeto. Assim, é necessário descobrir como conceituar, projetar, operar e manter componentes construtivos ativos, bem como avaliar seus parâmetros de adaptação, controle, estímulos e materialização. Essa pesquisa cobre a ideação, simulação computacional de desempenho ambiental, projeto e manufatura para uma célula ciberfísica de controle de iluminação natural zenital. O estudo avalia as contribuições do produto para o conforto visual e térmico de usuários, bem como as propriedades estruturais e óticas dos materiais e componentes projetados e fabricados por manufatura digital. O estudo segue a metodologia de "pesquisa por projeto" *(i.e., research-through-design)* e investiga o processo de

“projeto para manufatura e montagem” para solucionar a simplificação demasiada das simulações computacionais em pesquisas com tipologias construtivas ativas, ainda adotando baixos tempo e custo computacional com simulação iterativa em substituição à otimização. Como principais resultados, o estudo apresenta um referencial integrativo sobre o estado dos componentes construtivos ativos e oferece preâmbulo para caracterizações futuras. Além disso, ele define um processo holístico de modelagem e simulação para responsividade imediata, apresentando uma estratégia para simplificação de parâmetros de controle e movimentação mecânica por Análise de Variância e demonstrando a inaptidão dos processos estabelecidos até então (adeptos de datas chave como equinócio e solstícios) em representar a dinamicidade dos sistemas ativos. Essa pesquisa ainda avaliou etapas pertinentes ao projeto para manufatura, estudando as propriedades estruturais e óticas de termoplásticos para aplicações em produtos e como insumo para protótipos, bem como em experimentos físicos para complementar ou substituir aplicações computacionais intensivas ou extensas como análises de luminância por Grande Amplitude Dinâmica ou degradação de polímeros. Finalmente, essa Tese representa uma sistematização replicável de uma pesquisa em simulação e experimentação física e digital para avaliação e manufatura de um sistema ciberfísico de sensoriamento e resposta com objetivo de potencializar conforto humano em edificações.

Palavras-chave: *Pesquisa pelo design; projeto para manufatura e montagem; iluminação zenital; elementos construtivos ativos.*

LIST OF ILLUSTRATIONS

Pre-Textual

Chapter I

Chapter II

Chapter III

Chapter IV

Chapter V

Chapter V

LIST OF TABLES AND CHARTS

Chapter I

Chapter II

Chapter III

Chapter IV

Chapter V

SUMMARY

THESIS OVERVIEW

This Thesis concerns a Research-through-Design process that lends various stages from Design-for-Manufacture-and-Assembly to develop a climate-active top lighting cell. **Although the product is not the main scope of this Thesis, it appears as its main driver, with all methodologies culminating in its digital fabrication.** Likewise, all fabrication parameters derive from findings during the ideation. For instance, the product aims to enhance the Indoor Useful Daylight Illuminance while avoiding excessive illuminance that could lead to glare. Its final shape is a result of Building Performance Simulations and digital modeling for cyber-physical product design.

Thus, this study encompasses extensive theoretical frameworks, an integrative literature review, thermal model calibration for more realistic building computational simulation outcomes, human visual assessment, desktop manufacturing strategies' selection, material and component structural and optical analysis, and the development of a beta prototype of a **climate-active top lighting cell** based on all compiled information (Figure 1).

Figure 1: (a) Final digital model size and motion; (b) beta prototype developed in Chapter V; (c) and (d) building roof and space for simulation and physical analysis and surveying.

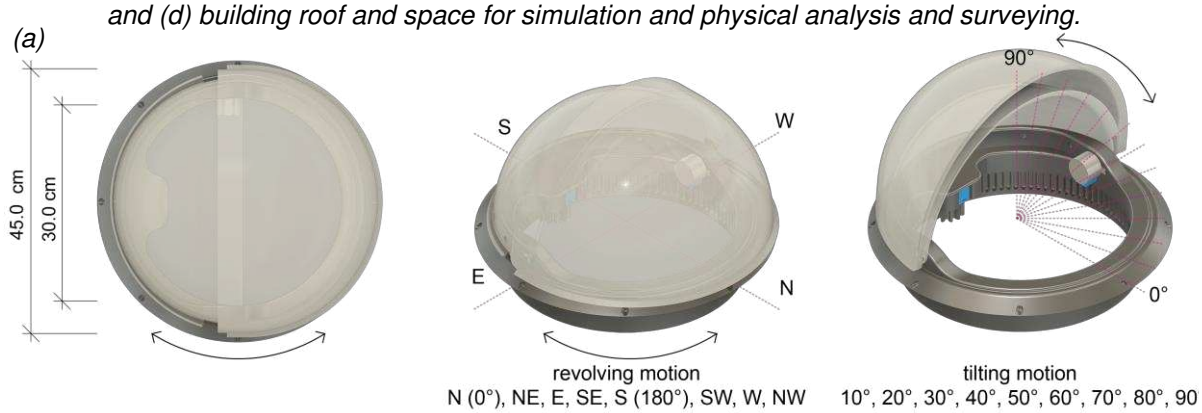

Source: The Author (2024).

Although research-assisted design processes follow an iterative methodology (Figure 2), in this Thesis, the Chapters follow a single thread or a linear process.

Figure 2: Thesis Overview and preview of product design.

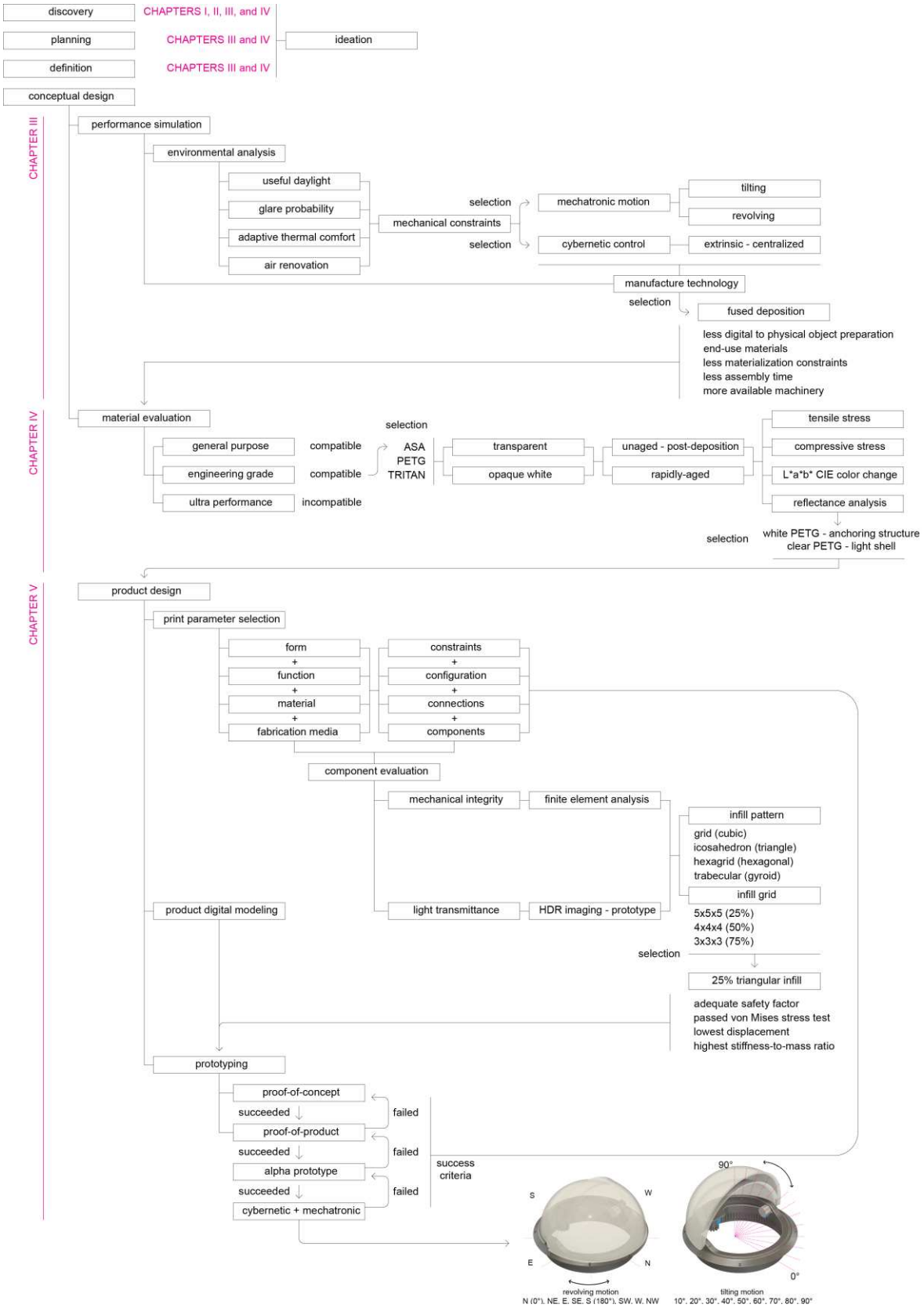

Source: The Author (2024).

Each methodology's subsequent stages depend on the findings gathered from the previous ones, and, in some cases, their execution is concomitant. Also, the author presents each Chapter, beginning with Chapter II, using a research paper template. **Figures 1 and 2a, b, c, and d show the overall workflow guiding this Thesis and a preview of the climate-active top lighting from model to prototypes;** the Thesis structure is as follows:

Pre-Textual Elements

Thesis Introduction: This section provides background information on the increase in electric energy expenditure, emphasizing building envelopes as environmental mediators and energy buffers, tracing the evolution from passive and prescriptive design solutions to climate-active building typologies. Its background and motivations section explains the rationale behind designing active components as opposed to adopting only passive strategies. Later, Chapter I revisits and deepens all topics presented in this Introduction.

The subsequent topic indicates the aims and possible contributions, outlining potential research outcomes from the author's perspective. It indicates the demand for a design workflow that treats building climate-active components as simulation problems with less simplistic resolutions, emphasizing the need to test computational models in real-world applications. Additionally, this section introduces the research **Hypotheses** and their driving **Questions**.

The author then presents the research objectives. Starting from Chapter II, each Chapter materializes one specific objective following the order presented later. Finally, the section concludes by highlighting the theme's originality, pointing out the scarcity of research and methodologies covering the entire Design-to-Manufacturing process (i.e., documenting, ideation, conception, development, and completion). The theme's originality, relevance, and justifications derive from the findings in the Theoretical Frameworks, Chapter I, and in the Integrative Review, Chapter II.

Chapter I - Building Envelopes Overview and Architecture in the Digital Age: This Chapter provides a comprehensive theoretical framework that serves as a foundation for all subsequent Chapters. As each Chapter needs to stand alone, the author acknowledges the recurrence of certain topics and discussions throughout the various theoretical frameworks. Despite this recapitulation, each framework introduces

new, in-depth, and essential information for executing the proposed methodology in their respective Chapter.

The author justifies the inclusion of one Section solely dedicated to theory to indicate research gaps further, substantiate the Thesis, and potentially uncover solutions to the addressed problems. Additionally, due to the variety of topics and methodologies connected throughout the design process for manufacturing and assembly of building components, this study requires interdisciplinary knowledge to comprehend various domains, particularly those related to climate-active architecture, design strategies for enhancing human comfort, building performance criteria and simulation metrics, and desktop manufacturing tools for transposing digital elements into physical elements. Thus, the author covers various terms and definitions, addressing discrepancies among studies and compiling the basic information required for developing the subsequent Chapters.

Overall, this Chapter has two major sections: Active Building Envelopes and Digital Methods for Design and Manufacturing. In the former, the author presents passive and active design strategies for providing human comfort, examining kinematic, intelligent, responsive, biomimetic, media, and smart typologies (within the scope of this research), tackling geometric, mechanical, and control approaches for mechatronic and cybernetic systems.

In the second part, the author explores digital and physical materialization techniques and parametric and generative design processes. They also concentrate on the most typical human comfort assessment criteria, comfort metrics, and digital simulation and experimental comfort evaluations, selecting key discussion topics based on Chapter II, an Integrative Literature Review. As implied by the Thesis title, the author perceives materialization techniques as a crucial step in the climate-active building envelope's assessment. Therefore, they dedicate a subsection for presenting the most employed desktop digital manufacturing techniques.

Chapter II - Climate-Active Building Enclosures - An Integrative Literature: While the authors presented the Chapter using the template common to all other Chapters, the corresponding paper has already been published. As the tables discussed throughout the paper are not in the publication, the author designated them as **Appendices II and III.** They are also retrievable as a Dataset in Zenodo.

Paper Doi: [https://doi.org/10.20396/parc.v14i00.8671581]

Dataset Doi: [https://doi.org/10.5281/zenodo.8316380]

This Chapter addresses **objective (a)** and presents an Integrative Literature Review, a State-of-the-Art compilation, and a bibliometric analysis for climate-active building components. It displays tabular information regarding study methodology, location, active approach, mechanical motion, and digital modeling and simulation software. The results obtained from this review aided in justifying the originality of this Thesis, selecting the fittest strategies for mechanical control and movement, choosing building modeling and simulation software, defining the simulation goals for human comfort, evaluating the strategies for prototyping, and electing the most prominent research methodologies.

Chapter III - Assessing Visual Comfort for Active Building Enclosures - A Novel Simulation Workflow for Environmentally Active Top Lighting Cells: Chapter III explored existing methodologies for simulating active building elements and proposed a new, detailed, and streamlined approach to define mechanical movement and geometric constraints for active components, answering to specific **objective (c).** This section was the first to present the product's ideation and its implementation in a building, already validated according to in situ air temperature and humidity. The building component strived to enhance natural lighting and maintain users' thermal and visual comfort levels.

The Chapter covered point-in-time and image-based simulations for representative dates, increasing the number of computational simulations compared to similar studies. It progressed to grid-based daylight simulations that demonstrated a high similarity with more compute-expensive simulations. Based on the point-in-time simulations, the author established tilting as the most contributing factor (using Analysis of Variance) for enhancing the Average Useful Daylight Illuminance inside the building. Adopting only grid-based simulations, Useful Daylight Illuminance, and Daylight Glare Probability mathematical equations, the author reduced the simulation time and created a simulation process that comprised all hours of the year with daylight availability. Instead of a multi-criteria optimization, they iterated all design solutions. They produced a matrix of outcomes representing the optimal positions for maximizing natural lighting indoors while reducing visual glare probability.

All motion criteria, initial product design, and geometrical constraints applied in this Chapter appear in the later manufacturing processes (Chapter V).

Chapter IV - Structural and Optical Behavior of Rapidly-Aged and Unaged Engineering-Grade Copolymers Produced via Fused Deposition: Following the daylight simulations for human visual comfort, the selection of motion typologies and constraints (outlined in Chapter III), and based on the literature indicating additive manufacturing as a facilitator for Design-to-Manufacturing (Chapters I, II, and V), the author evaluated the structural and optical characteristics of fused-deposition modeling feedstock as part of specific **objective (d).** They adopted three commercially available materials in two colors, white and clear, given that copolymers with higher absorptance levels would exhibit greater and faster degradation (due to higher thermal gains), and assessed structural integrity and optical properties post-deposition and after rapid aging. Therefore, Chapter IV helped choose a material with lower optical degradability and less loss of physical and mechanical integrity.

Since the building performance simulation, the product's digital modeling, and the optical and structural copolymer analysis were concurrent; the author analyzed white materials for the cell's building anchoring elements and the clear options for the lighting control wedges. Making the control shells translucent is intended to allow natural light indoors even when the cell remains closed (and even if the achieved illuminance level is below the appropriate threshold for more demanding working activities). Further, this Chapter indicated the copolymers' potential to withstand weathering when employed as the end-use material for prototypes and, later, actual building components.

Chapter V - Research-through-Design for Manufacturing and Assembly of a Cyber-physical Climate-Active Top Lighting Cell: Chapter V delved into the digital modeling process, iterative prototyping and editing, and the fitting of microcontrollers, sensors, and actuators to embody a cyber-physical system, answering specific **objective (d).** As the manufacturing and assembly process methodology is cyclical, the cell's geometric constraints derive from Chapter III, the cybernetic controlling techniques from Chapter II, and the materials align with Chapter IV's findings, granting the whole Thesis a Research-through-Design character.

Given that the manufacturing and assembly process demands control over every project stage and the designer works directly with the end-use material, this Chapter further analyzed structural and optical properties within the fabrication process rather

than material-specific evaluations as those presented in Chapter IV. With Chapter IV's defined material, the author dissected the influence of infill patterns and density on structural integrity and light transfer capacity of the component when applied to the evaluated building. In addition, the author needed to evaluate geometries closer to the final top lighting cell design and, therefore, employed a finite element analysis to understand which parts of the prototype would need reinforcement.

This Chapter also scrutinizes the fabrication process within the architecture domain, progressing through ideation, alpha prototyping, beta product, and the integration of a sensing and actuating system supported by microcontrollers with the assessed building.

Chapter VI - Conclusions: The final chapter recapitulated all research findings and provided critical insights into the adopted methodologies, establishing a reproducible workflow, which the literature identified as a research gap (Chapter V). The author highlighted the main challenges in adopting a Research-trough-Design methodology and made recommendations for future studies. Moreover, they revisited the Research Hypothesis, addressed the questions presented in the Introduction, and reaffirmed the study's objectives, offering a comprehensive perspective on the research outcomes.

Appendices: Appendix I is a paper published in conference proceedings (*Anais do XIX Encontro Nacional de Tecnologia no Ambiente Construído - ENTAC 2022 - Doi: https://doi.org/10.46421/entac.v19i1.1961*), written and executed before Chapter II of this Thesis. It answered **objective (b)** of surveying, modeling, simulating, and calibrating the building adopted throughout this study, decreasing the number of simulation uncertainties; **Appendices II** and **III** comprise the Integrative Literature Review datasets; **Appendix IV** is the sensing and actuating Arduino sketch for the cyber-physical system depicted in Chapter V;

THESIS INTRODUCTION

1. Background and Motivations

The increase in building energy consumption resulted in a shortage of energy resources and environmental deterioration (Zhou *et al.*, 2019). The demand for energy has become a primary concern of scholars since the building and construction sectors surpassed industrial and transportation (Aflaki *et al.*, 2015). Out of the final energy use, buildings are among the largest consumers, with up to 40% of the electric energy requirement and 36% of carbon emissions worldwide. Building energy expenditure increase is 0.1% of global economic output with a 2 °C rise in global mean surface temperature. Still, predicted net buildings' energy expenditures are not consistent globally (Clarke *et al.*, 2018).

Despite the growth of economies in emerging countries and fast advancements in living conditions, developed countries are still responsible for an unbalanced energy consumption per capita. Therefore, final energy consumption is contingent on population increase, floor area per capita, and energy usage per m^2 (Nguyen, 2019). The anthropogenic greenhouse gas emissions have also risen regularly since the preindustrial period, reaching the highest levels in the present, leading to an increase in atmospheric concentrations of carbon dioxide, methane, and nitrous oxide, which induce thermal accumulation that has a significant share in climate change. According to Nguyen (2019), roughly half of the anthropogenic carbon emissions in the past 270 years happened in the last 40 years. In addition, energy security has become an issue, impacting buildings' energy sources and shifting the over-reliance on fossil fuels to renewable energies.

In Brazil, buildings account for 51.2% of the total electric energy consumption, with an energy matrix composed of around 95% fossil fuels. Brazil is also the eighth largest consumer of primary energy globally (Balanço Energético Nacional, 2023), even though its electric matrix is primarily renewable. Even though heating demands are already negligible in low latitudes and predominantly tropical climates, (Lopes; Cóstola; Labaki, 2017), energy consumption percentages are more expressive due to high temperatures and humidity that force occupants to use electro-mechanical ventilation and are likely to increase considerably (Lopes; Cóstola; Labaki, 2017). Thus, these

numbers have led to a growing interest in the efficient appraising of human comfort, with earlier studies showing that passive strategies can reduce world energy requirements by 2.35% (Aflaki *et al.*, 2015) with indications of a 10% decrease for humid subtropical climates (Lopes; Cóstola; Labaki, 2017).

Architecture and the built environment transformed according to environmental, socio-cultural, economic, and technological constraints. As a result, the primary function of the building envelope shifted from a shelter, enclosure, structure, privacy, and security provider to a multicriteria mediator that encompasses relationships either tangible (air temperature, radiation, airflow, and humidity) or intangible (cultural and social). As most of these relationships rely on user behavior and requirements, research on energy efficiency has been increasingly redirecting towards environmental performance and human comfort provision, aiming to understand which variables, factors, or indexes interfere with human productivity and well-being.

Passive design strategies, such as solar shading, daylight admission, and natural ventilation, are practical means of naturally conditioning buildings, mainly by reducing heating and cooling demands while providing adequate human comfort levels. Out of all passive design strategies, shading devices are essential for energy conservation in buildings with large glazed envelopes as they prevent direct sunlight and radiation penetration indoors during the cooling season and allow the wanted solar gains in the heating period, helping with the homogenous distribution of daylight. In this sense, building shape and orientation play a substantial role in the device typology (Kirimtat *et al.*, 2016).

Contrary to the despoilment of adornments during the International Style, passive vernacular approaches are recently reviving as contemporary sustainable and economical alternatives to artificial techniques. Still, assuming their inherent bioclimatic suitability may be misleading, as they depend on construction typologies, materials, structural capabilities, and cultural, political, and economic factors; so, design decisions based on vernacular designs without a proper understanding of their limitations could perpetuate environmentally and healthwise unfit strategies (Cicelsky; Meir, 2014).

Hosseini *et al.* (2019) state that the building envelope's regulatory roles are changing, controlling, and responding to environmental stimuli to meet desired goals. Therefore, an optimal shape affects the quantity and quality of daylight, altering the

visual and thermal desired goals. As the sun and the sky dome are highly dynamic (e.g., various illumination directions and intensities), different strategies apply to one particular illumination scenario, normally optimal to a point in time and semi-optimal for the prevalence of times. Since the comfort concept has evolved, a notion of time-changing envelope configuration is a viable approach to improve visual comfort (Hosseini; Fadli; Mohammadi, 2021). Climate-active[1] technologies can improve building control by employing multifunctional, automatic, and reconfigurable components. Therefore, creating passive-active strategies should potentially improve occupants' comfort in real-time, responding to environmental parameters while maintaining acceptable levels of electric energy consumption (Hosseini *et al.*, 2020). Given seasonal and daily changes in solar positions and sky conditions, the combination of passive and active strategies is highly effective (Kirimtat *et al.*, 2016) and, according to Lee (2019) and Loonen (2018), coupled with computational design, they no longer have to compromise to one static state that performs acceptably under a wide range of conditions but is never optimal to any specific situation. For instance, computational design is increasingly important in improving the perception behind design creativity, providing a digital platform for creating various models with interactive environments. They encompass generative, parametric, and algorithmic designs, all of which can appropriately manage the inherent complexity in the design process.

However, active envelopes do not have a clearly defined characterization in the architectural research field (Attia *et al.*, 2018). Kolarevic (2015) states that researchers address only a few explorations on the building envelope level because the design and performance evaluation of active systems is complex. Also, existing performance assessment tools are insufficient to describe the geometrical progression generated by combining spatial motion, mechanical control, simulation/physical assessment timesteps, and performance goals (Attia *et al.*, 2018; Loonen *et al.*, 2017). In addition, according to Loonen *et al.* (2015), Building Performance Simulations need standardized procedures, more complex and precise evaluations, and better design support tools. Detailed information on design and materialization processes,

---

[1] Climate-active envelopes are a broad combination of several other classifications discussed in the theoretical framework (section four). They are passive-active solutions considering they operate either statically or kinetically (moving). Section four further discretizes Kinetic, Intelligent, Responsive, Biomimetic, Media, Smart, and Switchable typologies.

performance, physical assessment, building integration, and post-occupancy evaluations is also lacking in the literature (Attia, 2017). Most current studies focus on custom solutions to develop innovative and situational technologies that are highly specific or not replicable. Experimental studies on building envelopes are mainly small-scale (Chang; Huang; Datta, 2019; Yoon, 2019) or high-profile and high-budget (Nagy *et al.*, 2016), and despite their potential for improving building performance and the variety of technology options (from high to low-tech), the assessment of active envelopes from design to physical testing is minimal. There is still a need to address how to design, operate, and maintain active envelopes and assess their adaptation, behavior, performance parameters, and materialization. Therefore, it is essential to appraise physical geometry and structure (mechanical anchoring) and electronic subsystems (cybernetic) to support discrete motion within geometric constraints.

Among the various energy-efficient and State-of-the-Art technologies in architecture, engineering, construction, and operation, concurrent digital simulation and manufacturing processes enable geometric testing and physical/digital improvements, helping designers to develop, assess, and optimize architectural elements during the same cyclical stage, understanding construction as an integral part of the design and covering most materialization impediments.

2. Hypotheses and Research Questions

Although literature commonly focuses on façades, roofs account for significant heat gain/loss, especially in buildings with large rooftop areas. This heat transfer is significant in countries between the tropics, which describes most Brazilian territory, increasing the nearer to the Equator Line. According to preliminary investigations, research on horizontal envelopes is scarce (Park, 2016; Yang, 2020), and only a few publications combine interdisciplinary uses of computational design procedures and digital manufacturing techniques for top lighting strategies (Fang; Cho, 2019; Yang, 2020). Since a shading device's efficiency depends on the solar altitude angle, the design process for a top lighting control cell is similar to a solar control façade.

Contemplating the demand for simple, adjustable, and easily accessible solutions with well-described procedures for practical application, the author aimed to investigate a methodology for designing, simulating, optimizing, and prototyping a climate-active

top lighting cell created using computational and physical simulation for human visual (illuminance adequacy and glare prevention) and thermal comfort. This research also aimed to simplify the design workflow while incrementing the number of iterative analyses and offering various optional routes concerning simulation, design, physical assessment, and materialization for conceiving a building system that helps increase the time in comfort. This study was also meant to tackle mechatronic and cybernetic systems applied to design for manufacturing and assembly processes.

Thus, this research aimed to test the following hypothesis: **The exchange of traditionally static and opaque roof claddings with a simulation-based, climate-active, and cyber-physical top lighting cell can improve daylight admission and human visual comfort levels without compromising other comfort criteria.**

Based on this hypothesis, this research strived to answer the following questions: **How is a process for designing, simulating, and manufacturing a climate-active top lighting cell conceived through computational simulation and physical prototyping? What are the most relevant analyses behind the materialization of an active building-integrated system? Is it possible to conceive a viable physical building component using desktop manufacturing procedures?**

3. Objectives

3.1. General objective

The general objective of this work is to investigate the ideation, computational simulation, building integration, design, and digital prototyping processes for a cyber-physical top lighting cell and its potential to enhance human visual comfort.

3.2. Specific objectives

a) Formulate a State-of-the-Art Integrative Review and Bibliometric Analysis for Climate-Active Building Envelopes;

b) Calibrate a representative space for Building Performance Simulation applications;

c) Design, simulate, and optimize a parameter-based, climate-active top lighting cell for indoor daylight provision;

d) Evaluate the physicomechanical and optical properties of polymeric feedstock for desktop Fused Deposition Modeling;

e) Prototype, assess, manufacture, and assemble a minimum viable cyber-physical top lighting cell for environmental control.

4. Originality

As mentioned in the thesis overview, the **originality and justification** of this research rely on the findings shown throughout the general introduction and the theoretical framework (Chapters I and II). In this section, the author explained the software selection, envelope typology, manufacturing techniques, and cyber-physical hard robotics application to some extent, providing additional information in each chapter.

Presently, they justify this study and its originality:

Shading devices have an essential role in building energy savings and human comfort improvement, especially in climates that require selective radiation access, impacting daylight admission, light distribution, solar heat gain/loss, and reducing the likelihood of glare. Moreover, daylight improves health, awareness, and well-being, influencing the endocrine system, circadian rhythm, and other psychological aspects (Cartana, 2018; Fajkus, 2013). Nevertheless, daylight admission is not a strategy in which the higher the values, the better the performance (Reinhart; Mardaljevic; Rogers, 2013). Overshading leads to the exclusion of beneficial solar gains, and the excessive admission of daylight causes visual discomfort and undesirable heat gains. An optimal shading device should reject beam radiation when unwanted, permitting it when advantageous (Glassman; Reinhart, 2013).

The intent to design and manufacture a top lighting control element is due to the fact that roofs concentrate the most significant heat gain during the day, being the building surface most exposed to solar radiation. On a typical summer day, the incidence of solar radiation on a roof may be more than 1000 W/m^2, particularly in countries between the tropics and near the Equator line, which have higher solar radiation intensity throughout the year (4-6 kWh/m^2) and higher outdoor air temperatures[2] (Kolokotroni *et al.*, 2018).

There is also little research focusing on top lighting solutions. The author's investigations (Chapters I and II) did not return interdisciplinary uses of parametric design, building performance simulation, and digital manufacturing for modeling,

---

[2] For comparison, in a study developed for Viçosa, the highest incident radiation on a façade reached 501 W/m^2 for north orientation (Barbosa et al., 2013).

simulating, validating, and prototyping top lighting cells. Also, studies on horizontal envelopes did not associate multiple passive design strategies nor the combination of the most employed parametric modeling suite (Rhino3D+Grasshopper) and its performance simulation add-ons (Ladybug tools and sub-packages).

Although public, access to information in institutional buildings is hindered due to bureaucracy or confidentiality (normally due to eventual private funding) and is less common in research on building performance (Borgstein; Lamberts, 2014). Academic studies and publications on energy-efficiency strategies promote easy access to public information and help progress the construction sector in various spectrums.

According to Hosseini *et al.* (2019), there are many research pieces on climate-active architecture. However, interdisciplinary studies for proposing geometries that react to different environmental stimuli are rare. When allied to digital manufacturing and Design-for-Manufacture-and-Assembly (DfMA), they can be tested, edited, customized, and reproduced at a low cost. Unlike a conventional design approach (form-structure-material) (Oxman, 2017), parametric design coupled with DfMA provides viable means to explore active systems' interactive and dynamic qualities using virtual and physical media. It also allows mechatronic and cybernetic implementations. Moreover, according to Ferschin, Di Angelo, and Brunner (2015, p. 119), prototyping for active systems is "[...] only feasible when it is fast and low-cost on every level." It should allow for the re-use of prior pieces and components to test and re-design certain aspects.

Conceptually, using parametric design in conjunction with building performance simulation allows the designer to find the best solutions to a design problem. In this context, rigorous analysis and product comparison using quantitative and qualitative criteria become essential to identify good/sub-optimal solutions and improve decision-making (Landim, 2019). As mentioned above, Rhino3D+Grasshopper is the most widespread parametric modeling suite for architectural applications according to the theoretical framework and, later, the Integrative Literature Review (Chapter II). Due to Grasshopper's compatibility with many plug-ins, including the Ladybug tools and sub-packages, the digital model can employ validated simulation engines such as EnergyPlus and Radiance. Also, Arduino for Grasshopper allows real-time connection between digital simulation and physical prototypes, which creates a swift methodology for bringing digital applications into the physical world. For instance, Arduino is an easy

processing device that is readily available and designed to interact with sensors, actuators, and other devices. Simulation engines such as Grasshopper and its add-ons create a visual programming interface for combining hardware and software through ingrained C# programming.

As innovation elements, this research shifts the vertical envelope approach to horizontal surfaces, incorporating simulations for daylight admission allied with digital/physical technologies for designing and prototyping top lighting components. The author proposed a research workflow concerning digital modeling, field survey, simulation, product design, and manufacturing using the parametric computational interface and real-life building materials/properties/surroundings to devise a reality-based performance assessment, which is lacking in the literature. Furthermore, as aforementioned, static and prescriptive devices already comprise a large portion of publications on building simulation, progressively evolving into active applications and, recently, desktop prototyping (according to the integrative review in Chapter 2, from 2016 onwards).

REFERENCES

AFLAKI, A. *et al.* A review on natural ventilation applications through building façade components and ventilation openings in tropical climates. **Energy and Buildings**, [*s. l.*], v. 101, p. 153–162, 2015. DOI: http://dx.doi.org/10.1016/j.enbuild.2015.04.033.

ALVARENGA, A. **La Piel de la Arquitectura Moderna Brasileña: Las Soluciones de la envolvente a la luz de los Conceptops de la Arquitectura Bioclimática**. 2013. 138 f. - Universidad Politécnica de Cataluña, [*s. l.*], 2013.

ATTIA, S. *et al.* Current trends and future challenges in the performance assessment of adaptive façade systems. **Energy and Buildings**, [*s. l.*], v. 179, p. 165–182, 2018. DOI: https://doi.org/10.1016/j.enbuild.2018.09.017.

ATTIA, S. Evaluation of adaptive facades: The case study of Al Bahr Towers in the UAE. **QScience Connect**, [*s. l.*], n. January, 2017.

BALANÇO ENERGÉTICO NACIONAL, B. **Balanço Energético Nacional**. Rio de Janeiro: [*s. n.*], 2023.

BARBOSA, S. A. *et al.* Método de utilização do programa Energyplus para verificação de desempenho térmico de ambientes com fachadas duplas. **Ambiente Construído**, [*s. l.*], v. 13, n. 4, p. 121–134, 2013.

BAROZZI, M. *et al.* The sustainability of adaptive envelopes : developments of kinetic architecture. **Procedia Engineering**, [*s. l.*], v. 155, p. 275–284, 2016. DOI: http://dx.doi.org/10.1016/j.proeng.2016.08.029.

BENEVOLO, L. **História da arquitetura Moderna**. 3. ed. [*S. l.*]: Perspectiva, 2001.

BOLDINI, A. *et al.* Metereosensitive User-Controllable Skin for Dynamic Façades. *In*: 2017, Bern. **12th Conference on Advanced Building Skins**. Bern: [*s. n.*], 2017.

BORGSTEIN, E. H.; LAMBERTS, R. Developing energy consumption benchmarks for buildings: Bank branches in Brazil. **Energy and Buildings**, [*s. l.*], v. 82, p. 82–91, 2014. DOI: http://dx.doi.org/10.1016/j.enbuild.2014.07.028.

CARTANA, R. P. **Desempenho Térmico e Lumínico de Elementos de Controle Solar para Fachadas Desenvolvidos com Modelagem Paramétrica e Fabricação Digital**. 2018. 348 f. - Universidade Federal de Santa Catarina, [*s. l.*], 2018.

CHANG, T. W.; HUANG, H. Y.; DATTA, S. Design and fabrication of a responsive carrier component envelope. **Buildings**, [*s. l.*], v. 9, n. 4, p. 1–14, 2019.

CICELSKY, A.; MEIR, I. A. Parametric analysis of environmentally responsive strategies for building envelopes specific for hot hyperarid regions. **Sustainable Cities and Society**, [*s. l.*], v. 13, n. October, p. 279–302, 2014. DOI: http://dx.doi.org/10.1016/j.scs.2014.02.003.

CLARKE, L. *et al.* Effects of long-term climate change on global building energy expenditures. **Energy Economics**, [*s. l.*], v. 72, p. 667–677, 2018. DOI: https://doi.org/10.1016/j.eneco.2018.01.003.

DELGARM, N. *et al.* Multi-objective optimization of the building energy performance : A simulation-based approach by means of particle swarm optimization. **Applied Energy**, [*s. l.*], v. 170, p. 293–303, 2016. DOI: http://dx.doi.org/10.1016/j.apenergy.2016.02.141.

FAJKUS, M. Superficial Skins? Super Skins? Shading Structures and Thermal Impact Analysis. *In*: , 2013. **Energy Forum**. [*S. l.: s. n.*], 2013. p. 23–27.

FANG, Y.; CHO, S. Design optimization of building geometry and fenestration for daylighting and energy performance. **Solar Energy**, [*s. l.*], v. 191, n. August, p. 7–18, 2019. DOI: https://doi.org/10.1016/j.solener.2019.08.039.

FERSCHIN, P.; DI ANGELO, M.; BRUNNER, G. Rapid Prototyping for Kinetic Architecture. *In*: 2015, Cambodia. **7th International Conference on CIS & RAM**. Cambodia: IEEE 2015, 2015. p. 118–123.

GLASSMAN, E. J.; REINHART, C. Facade optimization using parametric design and future climate scenarios. **13th BS2013**, [*s. l.*], p. 1585–1592, 2013.

HERRIOTT, R. What Kind Of Research Is Research Through Design? *In*: 2019, Manchester. **IASDR: International Association of Societies of Design Research Conference**. Manchester: [*s. n.*], 2019. p. 1–11.

HOSSEINI, S. *et al.* A morphological approach for the kinetic façade design process to improve visual and thermal comfort: Review. **Building and Environment**, [*s. l.*], v. 153, p. 186–204, 2019. DOI: https://doi.org/10.1016/j.buildenv.2019.02.040.

HOSSEINI, S. *et al.* Integrating interactive kinetic façade design with colored glass to improve daylight performance based on occupants' position. **Journal of Building Engineering**, [*s. l.*], v. 31, n. April, 2020.

HOSSEINI, S.; FADLI, F.; MOHAMMADI, M. Biomimetic kinetic shading facade inspired by tree morphology for improving occupant's daylight performance. **Journal of Daylighting**, [*s. l.*], v. 8, n. 1, p. 65–82, 2021.

KIRIMTAT, A. *et al.* Review of simulation modeling for shading devices in buildings. **Renewable and Sustainable Energy Reviews**, [*s. l.*], v. 53, p. 23–49, 2016. DOI: http://dx.doi.org/10.1016/j.rser.2015.08.020.

KOLAREVIC, B. Towards an architecture of change. *In*: KOLAREVIC, B.; PARLAC, V. (org.). **Exploring the architecture of change**. New York: Routledge, 2015. p. 305.

KOLOKOTRONI, M. *et al.* Energy & Buildings Cool roofs : High tech, low-cost solution for energy efficiency and thermal comfort in low rise low-income houses in high solar radiation countries. **Energy & Buildings**, [*s. l.*], v. 176, p. 58–70, 2018. DOI: https://doi.org/10.1016/j.enbuild.2018.07.005.

LANDIM, G. R. **Programação para Arquitetura: linguagens visuais e textuais em Projeto Orientado ao Desempenho**. 2019. 161 f. - Universidade de São Paulo, [*s. l.*], 2019.

LEE, B. Heating, cooling, and lighting energy demand simulation analysis of kinetic

shading devices with automatic dimming control for Asian Countries. **Sustainability (Switzerland)**, [*s. l.*], v. 11, n. 5, 2019.

LOONEN, R. **Approaches for Computational Performance Optimization of Innovative Adaptive Façade Concepts**. 2018. 190 f. - Eindhoven University of Technology, [*s. l.*], 2018. DOI: www.tue.nl/taverne.

LOONEN, R. C. G. M. *et al.* Design for façade adaptability: Towards a unified and systematic characterization. *In*: 2015, Bern. **10th Conference on Advanced Building Skins**. Bern: [*s. n.*], 2015. p. 1284–1294.

LOONEN, R. C. G. M. *et al.* Review of current status, requirements, and opportunities for building performance simulation of adaptive facades. **Journal of Building Performance Simulation ISSN:**, [*s. l.*], v. 1493, p. 205–223, 2017. DOI: https://doi.org/10.1080/19401493.2016.1152303.

LOPES, F. D. S. D.; CÓSTOLA, D.; LABAKI, L. C. Simulação de estratégias bioclimáticas passivas para edifício de escritórios em clima tropical semiúmido. *In*: , 2017, Balneário Camburiu. **XIV**. Balneário Camburiu: [*s. n.*], 2017. p. 1–10.

MATYSEK-IMIELIŃSKA, M. **Warsaw Housing Cooperative: City in Action**. [*S. l.*]: Springer, 2020.

NAGY, Z. *et al.* The Adaptive Solar Facade: From concept to prototypes. **Frontiers of Architectural Research**, [*s. l.*], v. 5, n. 2, p. 143–156, 2016. DOI: http://dx.doi.org/10.1016/j.foar.2016.03.002.

NGUYEN, T. **Shape gramma-based adaptive building envelopes: Towards novel climate-responsive facade systems for sustainable architectural design in Vietnam**. 2019. 319 f. - University of Derby, [*s. l.*], 2019.

OXMAN, R. Thinking difference: Theories and models of parametric design thinking. **Design Studies**, [*s. l.*], v. 52, p. 4–39, 2017. DOI: http://dx.doi.org/10.1016/j.destud.2017.06.001.

PARK, J. J. **Adaptive Biomimetic Façades: compound bio-inspired design strategy for multi-functional stadiums**. 2016. 407 f. - The University of Melbourne, [*s. l.*], 2016.

REINHART, C. F.; MARDALJEVIC, J.; ROGERS, Z. Dynamic Daylight Performance Metrics for Sustainable Building Design. **LEUKOS: The Journal of the Illuminating Engineering Society of North America**, [*s. l.*], p. 37–41, 2013.

STRAUB, K. W. *et al.* Determinação da temperatura de neutralidade em salas de aula do ensino superior para as zonas bioclimáticas do estado de Mato Grosso. **Ambiente Construído**, [*s. l.*], v. 17, n. 1, p. 97–109, 2017.

YANG, C. **The Intelligent Control Strategy of Kinetic Façades for Daylight and Energy Performance**. 2020. 213 f. - University of Southern California, [*s. l.*], 2020.

YOON, J. Climate-adaptive facade design with smart materials: Evaluation and strategies of thermo-responsive smart material applications for building skins in Seoul.

In: , 2018, Hong Kong. **34th International Conference on Passive and Low Energy Architecture**. Hong Kong: [*s. n.*], 2018. p. 620–626.

YOON, J. Design-to-fabrication with thermo-responsive shape memory polymer applications for building skins. **Architectural Science Review**, [*s. l.*], v. 64, n. 1–2, p. 72–86, 2021. DOI: https://doi.org/00038628.2020.1742644.

YOON, J. SMP Prototype Design and Fabrication for Thermo-responsive Façade Elements. **Journal of Facade Design and Engineering**, [*s. l.*], v. 7, n. 1, p. 41–61, 2019.

ZHOU, J. *et al.* Investigating the impact of building's facade on the building's energy performance - a case study. **Energy Procedia**, [*s. l.*], v. 158, p. 3144–3151, 2019. DOI: https://doi.org/10.1016/j.egypro.2019.01.1016.

CHAPTER I – Building Envelopes Overview and Architecture in the Digital Age

Building Envelopes

The physical environment operates upon many components (light admission; energy gain and loss; airflow; protection from humidity, visual glare, sun, and wind; insulation; security; transparency and visual contact) with a complex relationship that the human body absorbs or counteract (Loonen, 2018; Romano *et al.*, 2018). Usually, humans strive to achieve an equilibrium between energy investment and environmental adjusting. According to Olgyay (2015), the comfort zone is their successful balance, wherein most of the energy shifts towards productivity.

Naturally, a shelter helps to fulfill these comfort requirements by adjusting the natural environment to optimum conditions, filtering, absorbing, or repelling elements according to their advantages or adversities. The settlement of all physiological needs constitutes an environmentally balanced space (Olgyay, 2015). Besides building shelter or envelope, several terms describe the zone between architectural exterior and interior, such as enclosure, façade, wall, roof, and skin. Although façades and roofs are subject to distinct weather conditions, they perform similar functions independently of shape and orientation (Nguyen, 2019). Envelopes withstand uncontrollable meteorological variations since weather conditions continuously vary with seasonal and daily changes, and occupants' needs (presence, activity, and comfort) vary with time (Loonen, 2018).

The 20_{th}-century architecture was a product of the Industrial Revolution and ever-changing technology. Building materials and techniques changed according to technological advancements, improving thermo-mechanical systems such as heating, ventilation, and air-conditioning (HVAC). As a result of the indoor mechanical control, architects interpreted the envelope as an outer surface with aesthetic significance, overlooking its function as a buffer of comfort and energy, which created high energy-consuming structures, attempting to maintain optimal indoor comfort and contributing to the greenhouse gas emissions (Reki, 2018). However, there has been a radical shift in architecture in the last few decades as sustainability concerns emerged.

Energy consumption increased as technology evolved, compelling 21st-century postmodernist buildings[3] to implement passive and active comfort strategies concomitantly. Climate change concerns obligated the construction sector to explore innovative design solutions for adequate human comfort in buildings while minimizing energy consumption. Thus, designers and architects must acknowledge passive approaches before adopting active systems. Usually, building envelopes are stationary elements and have a limited ability to respond to outdoor variations since passive design selection depends on the predetermined climate, topography, building layout, and building surroundings (Gou *et al.*, 2018). Therefore, static systems are counterproductive to the latest concept of building envelopes: a tectonic, skin-like feature with environmental and aesthetical relationships (Loonen, 2018).

In the 1920s, the International Style preached the minimalistic, rational approach to architecture, freeing it from nationalist, region-based distinctions. Architects aimed for a machine-like structure: transparent, light, and sleek forms, incorporating concrete, steel, and glass to achieve industrial modernity (Frampton, 1998, 2007; Reki, 2018) (Figure 1).

Figure 1: Richard Neutra's Lovell House.

Source: Adapted from Frampton (2007).

Figure 2: Geodesic Tensegrity structures

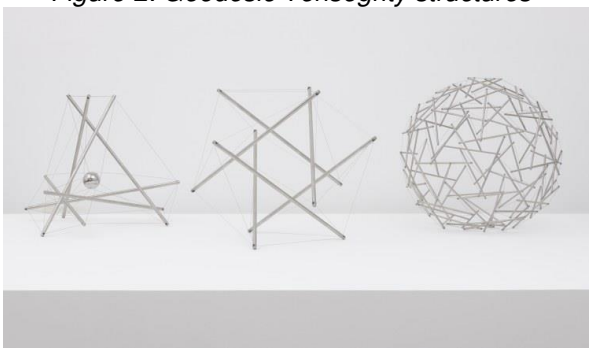

Source: Adapted from Fuller (1977).

The contemporary emphasis on environmental performance led to a revival of kinematic motion, first presented by Buckminster Fuller in his Tensegrity Theory[4] (Figure 2). The kinematics create a variety of geometric possibilities that surpass Euclidian geometries, reducing material use and increasing structural rigidity while retaining lightness. According to Nguyen (2019), the combination of kinematics

---

[3] Postmodern architecture emerged in the 1960s as a reaction to the international style, encompassing high-tech, parametricism, and sustainable architecture (Hopkins, 2014).

[4] According to Calladine (1978), in 1960, Buckminster Fuller coined the tensional integrity theory based on elements under pure tension and compression. Later, in the 1980s, hard robotics incorporated the theory due to its potential for lightweight structures (Fuller, 1977).

and standard design and crafts creates functional components that transcend the traditional design idea and improve energy moderation. Kinematic structures constitute a foundation for active approaches in architecture, i.e., products that respond to their surroundings, improve their environment, or interact with their users (Fuller, 1977). Most of them constitute a second building layer that employs several movements, including rotating, translating, and scaling (Chapter II) (Hosseini; Mohammadi; Guerra-Santin, 2019).

1. Passive design approaches

Passive design strategies concern systems, structures, features, and materials that employ natural resources to achieve a comfortable environment without using electricity or fuel (Azimi Fereidani; Rodrigues; Gaspar, 2021). According to Kirimtat *et al.* (2016) and Song *et al.* (2021), there are many conventional passive solutions (Figure 3). It is within the scope of this research to review solar and heat control strategies through shading and especially top lighting applications.

As an example of passive approaches, solar shading is one straightforward daylight-controlling technique. It also helps prevent large amounts of heat absorption in warm months while allowing heat gains during cold periods, maintaining a homogenous distribution of indoor illuminance (Kirimtat *et al.*, 2016). Large openings are fundamental to maximize natural ventilation in hot and humid climates, such as a substantial share of the Brazilian territory. However, normally, any radiation that penetrates these large windows increases human thermal discomfort.

Although shading devices effectively regulate the direct solar component, regulating the diffuse-sky component is difficult because radiation comes from large exposure angles, needing ample exterior devices, additional indoor protection, or shading within the glazing (Lechner; Andrasik, 2021). Notably, exterior devices, such as Brisé-Soleil, are more efficient than indoor shading (roller shades and Venetian blinds), reflecting and dissipating the obstructed heat into the outside air, explaining the abundance of research on their configurations. As an example, Evola, Gullo, and Marletta (2017) studied arrangements for improving thermo-luminous comfort in highly glazed buildings according to Italian standards. The authors highlighted the discrepancies between different shading systems and concluded that internal blinds

have lower performance than external systems. They also observed that the same systems are very effective on south-facing glazed envelopes in the northern hemisphere.

Figure 3: Passive design. The strategies best covered in the research's scope are in magenta.

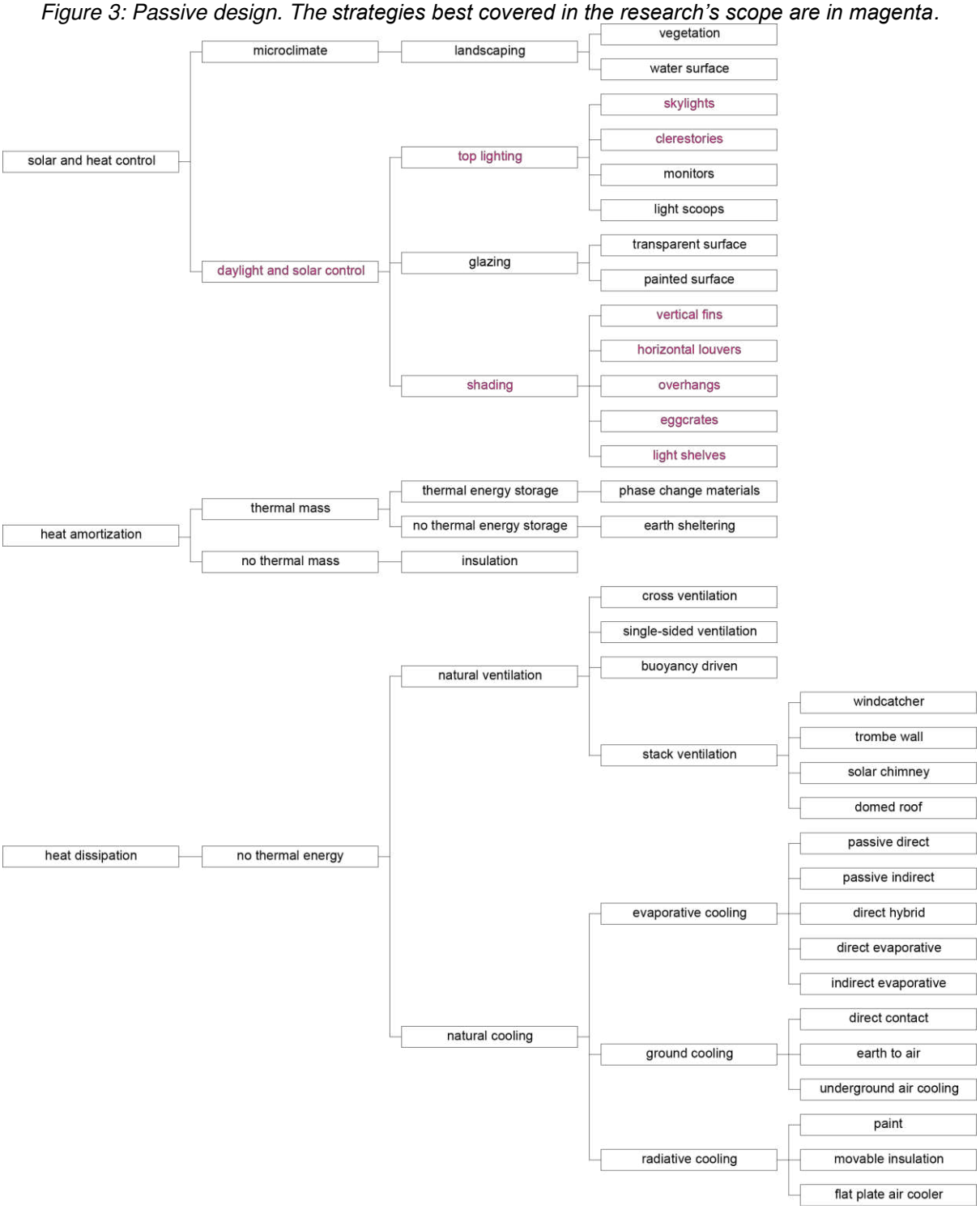

Source: The Author (2024), adapted from Mehrjardi (2016).

1.1. Side light - Vertical fins

Vertical fins or louvers provide effective shading mainly towards the east and west and near these orientations (Kirimtat *et al.*, 2016) (Figure 4). They also act as a windbreak and increase the glass insulation value during the heating season. There are two types of vertical fins: perpendicular and slanted. According to Lechner and Andrasik (2021) and Olgyay (2015), perpendicular fins must be deeper or narrow-spaced to minimize summer morning and afternoon daylight and radiation penetration since the sun's motion is as vertical as horizontal. Another obstacle with perpendicular fins is the light reflection to the right and left, while for daylight quality, the reflection should be up and off the ceiling. Slanted fins, however, are more appropriate for daylight control and for establishing outdoor visual connections.

Figure 4: Side and Top light typologies. Source: The Author.

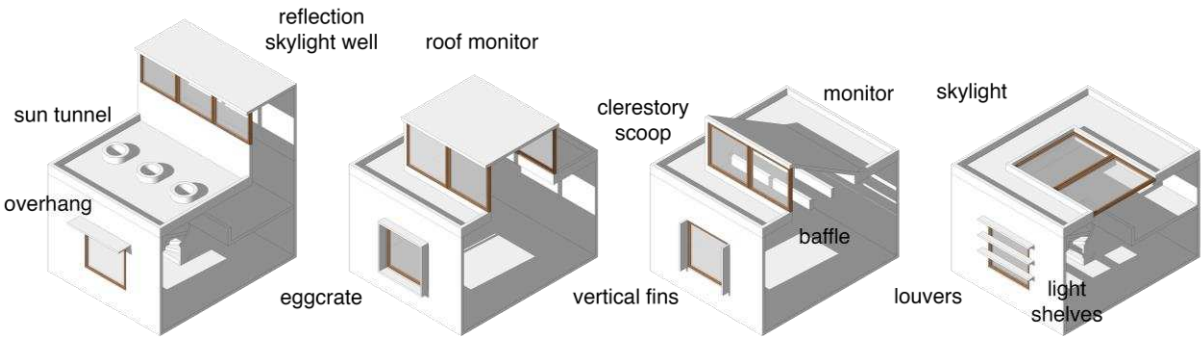

Source: The Author (2024).

For example, Rasheed *et al.* (2021) evaluated the impact of vertical fins on a building's energy consumption for a five-season semi-arid climate. Results showed a substantial reduction in energy consumption for the east and west, with a slight improvement for the south. East and west heat gain reduced from 279.4 to 245.3 kWh/m^2 and 245.3 to 226.0 kWh/m^2, respectively.

1.2. Side light - Horizontal louvers and overhangs

Horizontal louvers and overhangs are horizontal surfaces that project over or in front of a window (Figure 4). A fixed overhang can achieve both summer shading and solar radiation penetration in winter. They are most efficient toward the north or around the northern orientation of the southern hemisphere. Still, they are ineffective in the summer mornings and late afternoons, when vertical fins work best. They also minimize the accumulation of hot air below its surface (Lechner; Andrasik, 2021;

Olgyay, 2015). For instance, Fernández-Hernández *et al.* (2017) investigated the effects of horizontal southern-facing shading devices on visual comfort and energy expenditure for an office building in Spain (hot summer Mediterranean Köppen-Geiger classification). The static louvers at a 60° angle reduced energy demands for cooling by 68% compared to the base case. Even though they were adequate for reducing cooling expenses, they negatively affected daylight admission, increasing energy consumption through artificial lighting.

1.3. Side light - Egg crates

Egg crates are a hybrid of louvers and fins with a combinative shading mask projection. They work for east and west apertures for temperate climates and southeast and southwest orientations for tropical climates. According to Lechner and Andrasik (2021), egg crates can also configure small-scaled fine screens such as Islamic mashrabiya and Brazilian cobogós. Their shading effect at different scales is similar, but the view access from the inside and their outdoor appearance varies.

Even though studies on egg crates are scarce, Pilechiha, Mahdavinejad, and Beizaee (2020) appraised the energy performance and the view access of fins, louvers, and egg crates, examining more than 300 fixed configurations for a high-performance building in Iran (cold semi-arid Köppen-Geiger classification). Energy consumption of the best egg crate configurations was only 3% lower than the base case, with view access of 21%. In addition, 64% of the egg crates consumed more energy than the base case, with worse view access. However, the author highlights that their study only appraised energy performance, not considering ventilation, daylight, and thermal gains, for instance.

1.4. Side light - Light Shelves

Light shelves (Figure 4) block beam radiation while reflecting daylight onto the ceiling. Likewise, they have horizontally mounted surfaces attached to a section of a glazed opening, dividing the aperture into a lower and an upper portion. Upper portion louvers, additional light shelves, and above-eye level structures help prevent glare and improve natural light quality, increasing the depth of the daylit zone. According to Lechner and Andrasik (2021), illuminance levels can be adequate up to a depth of twice the height of the opening. As stated above, the ceiling and the back wall of the

room are more effective than the sidewalls or the floor in distributing daylight. Theoretically, they should be light-colored, but large areas of shiny surfaces can cause glare. For the southern hemisphere, light shelves are suitable for the north orientation and need to be much longer for the east and west. For south-facing surfaces, they are redundant.

Bahdad, Fadzil, and Taib (2020) developed a daylighting performance and optimization case study for typical office space in Malaysia (tropical rainforest Köppen-Geiger classification) and indicated that the optimal light shelves have great potential for illuminance improvement. Compared to reference models, useful daylight illuminance increased by 15.6% and 4.7% in June, 17.5% and 5.8% in March, and 5.8% and 11.3% in December.

1.5. Ceiling apertures or top lighting

Ceiling apertures, top lighting, or roof light (Figure 4) are openings in the horizontal portion of the building envelope and they include regular, unit, and tubular skylights, clerestories, top monitors, saw-tooth, courtyards, light wells, and atria (Al-Obaidi; Abdul Rahman, 2016). According to Lechner and Andrasik (2021), a top lighting's position, orientation, and size are as significant as selecting glazing materials and shading mechanisms.

When possible, it is always more pleasant to arrange apertures in the ceiling plane as they decrease the likelihood of glare and allow an even diffusion of daylight within the space. However, they should be out of the offending zones, which is easiest when the location of the visual task is fixed (Lechner; Andrasik, 2021). Usually, the best solution is to diffuse the light using baffles or banners to avoid veiling reflections or to adopt various smaller openings that employ the roof thickness as a skylight well. Additionally, top lighting only applies to one-story buildings or the top floor of multistory buildings and does not satisfy the need for side views (indoor-outdoor).

As for rules of thumb, top lighting strategies should be adjacent to walls for diffuse reflection and away from structural features to avoid shadows; various openings spread evenly across space create more uniform illumination (usually no more than one-and-a-half times the ceiling height apart); the higher the aperture, the more broadly the light will diffuse (therefore, low-ceiling spaces require small skylights spaced closer

together); exterior shades and reflectors can improve summer/winter illuminance balance and homogeneity (Lechner; Andrasik, 2021; Olgyay, 2015).

Top lighting designs can have horizontal (skylights), vertical (clerestories and monitors), tilted, or domed apertures. This research focuses mainly on horizontal and vertical apertures, considering their higher representativity in academic research.

Since the sun is higher during the cooling months, horizontal top lighting designs receive more direct sun in the summer (when it is usually not needed) and less in the winter (when needed). For the northern hemisphere, the opposite is true with north-facing vertical systems. Thus, for optimizing yearly heating and cooling balance, north-facing apertures tend to be most effective for the southern hemisphere. South-facing designs will receive much lower and more uniform levels of diffuse daylight and thus need to be larger than north-facing openings to achieve equivalent illuminance levels.

Skylights are horizontal or slightly sloped glazed openings in the roof. As such, they capture a large share of the unobstructed sky and transmit high light levels. Because beam radiation is usually not desirable for demanding visual tasks, they should diffuse the impinging sunlight. A significant limitation of skylights is that they face the summer sun more than the winter sun, and there is never a circumstance when more light and radiation are best in the summer than in the winter (Lechner; Andrasik, 2021). As a result, clerestories perform better than skylights in tropical and temperate climates. They can utilize louvers and fins for further shading since their vertical or near-vertical orientation is closer to window features than that of skylights.

Deciding between horizontal or vertical apertures should balance the specific building and climate demands and architectural intention and integration. For instance, Fang and Cho (2018) studied the most influential variables when designing skylights and clerestories using parametric modeling simulation for a single-story retail building in Atlanta (humid subtropical Köppen-Geiger classification). They integrated daylight and energy simulations and discovered that useful daylight Illuminances were up to 80% when adopting 50 small skylights, large clerestories on the north and south, and small apertures on the east and the west.

Other passive shading and daylight admission systems not reported in this theoretical framework comprise awnings (sunshades, tents, and shutters), balconies, perforated screens (such as mashrabiya and cobogós), trellis, and vegetation. Even

though most passive research results seem promising, Olgyay (2015) and Kirimtat *et al.* (2016) indicated that prescriptive design solutions cannot correctly respond to variable situations and achieve the required daylight conditions, increasing artificial light demand. As mentioned, these systems are only optimal at a specific time and date, lacking control and versatility over the day and year. Besides, the shading device movement can be as simple as an adjustment twice a year (late in spring and fall).

2. Active design – Controlling Techniques and Mechanical motion

According to Romano *et al.* (2018), the new frontiers of experimentation in the construction sector aim to advance the building organism to ensure autonomous human comfort. Information technology (IT) evolution increased artificial intelligence in buildings, ensured spatial regulation without human resources, and guaranteed functional and physical built space optimization. The IT advancement brought back kinematic systems based on developments in generative, parametric, and algorithmic thinking that help to understand and design active systems.

Theoretical interest in kinematic architecture emerged as part of the Futurism, Constructivism, and Expressionism movements in the first third of the 20th century. Around the 1940s, Buckminster Fuller began experimenting with tangible projects, and later, in the 1960s, material evolutions allowed the testing of inflatable and tensile structures to match the industrialized trend. The megastructure architecture style, for instance, intended to exclude static theory and functionalism, embracing social change through society's evolving needs (Schimidt III; Austin, 2016).

In the 1970s, Zuk and Clark (1970) categorized kinematic designs by their application, separating them into self-erecting, kinematic, reversible, incremental, deformable, mobile, and disposable, establishing a comprehensive view of kinematics as building systems and sub-components (Reki, 2018). Later, Nicholas Negroponte coined the concept of a responsive environment that transforms using complex or simple computations (Negroponte, 1972). Currently, architecture describes kinematics as the ability to change form or space, from a component's scale to the entire building, in response to varying conditions, negating monolithic solutions (Schimidt III; Austin, 2016) and enabling buildings to adapt by turning lights on and off, locking and unlocking doors, and adjusting cooling and heating. Only recently, "technological

research has investigated new experimentation frontiers capable of reaffirming the osmotic quality of a process of exchange concerning energy flow through the envelope" (Romano *et al.*, 2018, p.67).

According to Loonen (2018) and Tabadkani *et al.* (2021), several interchangeable terms refer to buildings with time-varying façade characteristics. The most common variations include: adaptive (Basarir; Cem Altun, 2018; Lo Verso *et al.*, 2019; Reki, 2018), kinematic (Hosseini *et al.*, 2020; Lee, 2019; Shi; Tablada; Wang, 2020), responsive (Hosseini; Mohammadi; Guerra-Santin, 2019; Tabadkani; Banihashemi; Hosseini, 2018; Yang, 2020), intelligent (Le-Thanh *et al.*, 2021; Tabadkani *et al.*, 2019; Yi *et al.*, 2020), biomimetic (Hosseini; Fadli; Mohammadi, 2021; Jahanara; Fioravanti, 2017; Sheikh; Asghar, 2019), interactive (Chang; Huang; Datta, 2019), smart (Pesenti; Masera; Fiorito, 2018; Yoon, 2019; Yoon; Bae, 2020), and switchable (Ayoub, 2018; Cannavale *et al.*, 2018; Paule *et al.*, 2017) (Chart 1).

Chart 1: Summary of Building Envelope Typologies.

		Properties	
Kinetic		Primary motion or simple, independent combinations; No or low power supplementation – self-powered; Mechatronic with no cybernetic interface; Low control with preprogrammed states; No environmental sensing; No environmental prediction; No interaction;	
Intelligent	Closed-loop	Automated control; In situ sensing, simulating, predicting, and responding; Pre-programmed Boolean operators or logic; Centralized - Offers manual control and override; Decentralized – No human interaction Demands computational power; Employs several sensors and actuators; High energy expense;	
	Open-loop	Sense and respond to environmental conditions; No outside decision-making; No human interaction; Components and actuators are one system;	
Biomimetic		Mimics organic behavior or morphology; Nature-inspired simple motion; Less energy-expenditure; Only works within thresholds; Only responds to one parameter at a time; Only appraises one environment at a time (indoors or outdoors); No user input;	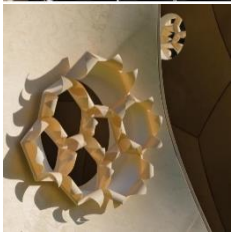

(Continues)

(Chart 1 continues): Summary of Building Envelope Typologies.

Media	Human intervention; Multiple sensors or controllers; Responds to real-time interaction. Promotes individual participation; Do not regard human comfort;	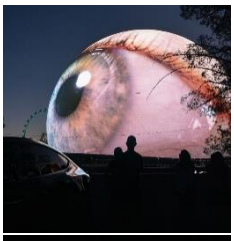
Smart	Intrinsic material properties; No need for power; Simple motion or no motion; Limited by specific material chemical and physical attributes; Limited by motion thresholds; No human interaction;	

Source: The Author (2024); Figure Sources: (a) Adapted from (Chang; Huang; Datta, 2019); (b) Reprinted from (Böke; Knaack; Hemmerling, 2020)*; (c) Adapted from "Responsive Façade," by Alani, M. (2018, Dec 18). Retrieved from: https://projecthub.arduino.cc/Mostafa7/responsive-facade-621009; (d) Reprinted from (Reichert; Menges; Correa, 2015); (e) Reprinted from "Bloomberg Business Week," by Whitmore, M. (2023, Set 12). Retrieved from: https://www.bloomberg.com/news/features/2023-09-12/james-dolan-s-vegas-sphere-cost-2-3-billion-and-might-pay-off; (f) Reprinted from "3-D printed structures remember their shapes," by Ge, K. (2016, Aug 25). Retrieved from: https://meche.mit.edu/news-media/3-d-printed-structures-%E2%80%9Cremember%E2%80%9D-their-shapes.*

In this research, the author adopts active envelopes as a comprehensive cluster, acknowledging all the terms mentioned above as smaller parties. These groups are in the scope of this framework. Other classifications include accommodating, adaptable, adjustable, advanced, controllable, living, modifying, polyvalent, reactive, reconfigurable, resilient, selective, sensitive, sentient, transformable, and transient. Chart 1 shows the main characteristics of the most employed systems and, later, Chapter II further scrutinizes each classification

Motion in architecture is either physical or visual (Mehrjardi, 2016). For instance, this research mainly focused on environmentally active large-scale physical transformations. As seen in Figure 5, geometric transformations comprise component motion or whole building action, influencing daylight, airflow, heat exchange, aesthetics, noise reduction, and energy conservation. They modify the indoor and outdoor spaces, function, form, type, size, and openness.

According to Ferschin, Di Angelo, and Brunner (2015), the first step of designing active envelopes is selecting their shape and defining their main movements and constraints. Usually, the design workflow only assesses the components' physical details and materials in the final stages. For active architecture, designers should consider the data input (location, surroundings, building geometry and orientation, and climatic factors), type of control, fabrication, assembly, and "kinetic movements [...] to

orchestrate the desired physical adaptability of buildings" (Ferschin; Di Angelo; Brunner, 2015, p.119). For instance, this framework focuses on mechanical kinematics since it offers various design configurations while maintaining physical constraints and various commercially available hardware.

Figure 5: Motion classification in architecture. The strategies best covered in this research are in magenta.

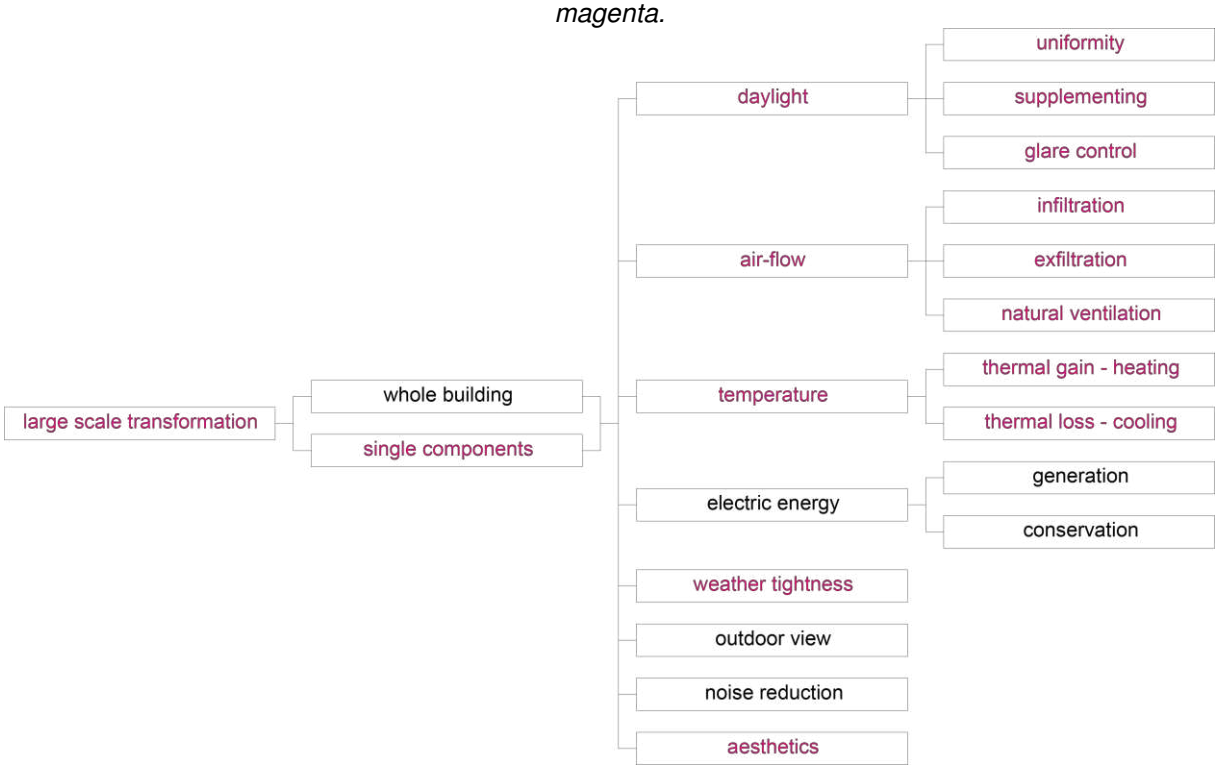

Source: The Author (2024).

Although Al-Masrani and Al-Obaidi (2019) indicate three, rigid objects present six degrees of freedom (later discussed in Chapter II). Rotation comprises pitch, yaw, and roll, and translation occurs through right, left, back, forward, up, and down sliding. In addition, combining primary motion patterns (rotation and translation, for instance) generates composite movement configurations, such as folding and rolling. Complex motion is usual in deployable structures, such as scissors and umbrella-like arrangements. Folding is standard in kinematic systems, as linear rails, rods, and hinges are commercially available products, allowing designers to create contracting and expanding synchronic mechanisms.

2.1. Mechanical components

According to Kolarevic (2015), actuation can be motor-based, hydraulic, pneumatic, or material-based, with most studies on active envelopes focusing on mechanical, motor-based motion. This actuation is either kinetic or kinematic

(Schumacher; Schaeffer; Vogt, 2012; Schumacher; Vogt; Krumme, 2020). Although the literature uses these terms arbitrarily, kinetic studies the relationship between actions and their sources (what causes motion). It explores forces and torques using analytical dynamics, where the magnitude, direction, and vector of forces actuate the system (Schumacher; Vogt; Krumme, 2020). Kinematics studies temporal motion, calculating the parameters that determine the positions, velocity, and acceleration of specific parts. According to Sierra *et al.* (2022), it is either forward or inverse. Forward kinematics describes a system's final position according to motion steps, while inverse kinematics interprets the motion path from the object's position.

Kinematic, responsive, intelligent, and biomimetic approaches are envelope typologies that often deliver macro-level adaptation. A microscale strategy considers the material molecular structure and deformations, changing optical, thermo-physical, and energetic properties. Media and smart envelopes usually employ this approach.

2.2. Controlling techniques

The standard architectural project workflow postpones material and materialization-related parameters until the later stages, which increases uncertainties in how to control active systems (Stazi, 2017). Active envelope controllers, sensors, and actuators should employ appropriate response times and enable adaptation according to collected data.

According to Tabadkani *et al.* (2021) and Alkhatib *et al.* (2021), control can be either extrinsic or intrinsic. Their main distinction somehow relates to the micro and macro scales, and the controls occur internally or externally. Intrinsic control (direct, local, feedforward, or open-loop) interprets and decides the change directly from the environmental conditions with no outside decision-making (Alkhatib *et al.*, 2021). They require less driving energy and demand fewer elements since there is no control hardware. In intrinsic systems, actuators and sensors are the same components.

Extrinsic systems (closed-loop, feedback, or central control) entail information retrieving and processing before taking action, which allows for feedback, comparing the current configuration and the desired state, and triggering adaptation. The system auto-adjusts based on sensors, processors (controllers), and actuators. According to Tabadkani *et al.* (2019), there are two levels of extrinsic control (centralized and decentralized), with subcategories (Figure 6).

Figure 6: Controlling techniques: centralized and decentralized strategies. The solutions in magenta are within the scope of this research and represent the cyber-physical system proposed later.

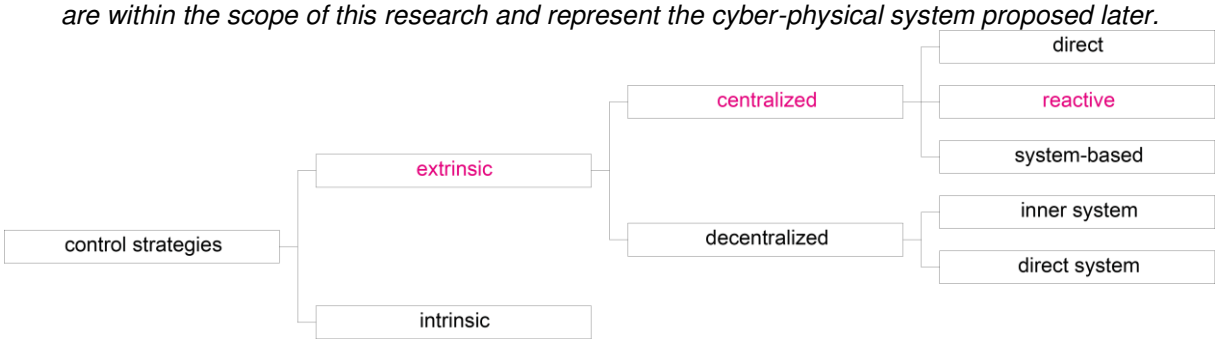

Source: The Author (2024).

A centralized control has three different scales and contemplates several components driven by a single processor. Its subcategories are direct, reactive, and system-based: direct control presents the highest user interaction and the lowest complexity, adopting a pre-programmed logic with no external inputs (sensors); a reactive system is a simple sensor-based system with Boolean expressions; and a system-based control means significant data processing and complex problems, requiring multi-objective optimization and real-time data (Tabadkani *et al.*, 2021; Velasco; Brakke; Chavarro, 2015). Decentralized controls are locally embedded processors with or without an external system, such as an information hub (Tabadkani *et al.*, 2021). They can be direct (i.e., local micro-actuators to move each kinetic element individually) or inner systems (i.e., embedded material behavior and self-adjustment). Most macro-scale envelopes employ extrinsic, centralized, direct, and reactive controls since the environmental parameters normally fall within known thresholds. In addition, human comfort is relatively subjective, and direct approaches present more override options with more uncomplicated systems (Al-Masrani; Al-Obaidi, 2019; Tabadkani *et al.*, 2021).

3. Parametric design thinking and Generative design

Since the 1980s, the continuous evolution from paper-based to computer-integrated design changed the design-thinking workflow and culminated in parametric modeling techniques complementing free-form design (Terzidis, 2015). Although the early computer-aided design (CAD) systems helped with two and three-dimensional drawings, they only allowed shape corrections and walk-throughs with no user interface for re-editing. These tools matured into generative machines that require a knowledge base, skill set, and conceptual principles, and the rework evolved to re-editing (Oxman, 2017; Yang, 2020).

In the construction sector in the 1980s, parametric architecture represented the relations between the dimensions of a design based on parameters. Then, this definition only covered parametric modeling approaches, conveying a geometric relationship that changes according to parameters, somewhat similar to the logic of repetition (Kalay, 1989; Oxman, 2006). Later, Kolarevic (2005) differentiated parametric applications, discussing parametric design as a workflow in which the inputs define the output shape but allow the prompt formulation of new solutions, i.e., a generative system, but still considering geometric modeling. In this framework, the author considers parametric design a process based on algorithmic thinking that uses variables and rules for translating designs or design properties into rationalized parameters, allowing exploration and materialization of various alternatives (Caetano; Santos; Leitão, 2020; Jabi *et al.*, 2017). This definition includes all previous descriptions without constraining its applicability to geometry-based purposes.

Still, for geometry-based models, the variables are computed in a virtual model using mathematical relationships that change the geometric element with each input, like a spreadsheet automatically recalculates changes. In this context, the use of visual programming languages (VPL) (Figure 7) allowed complex geometries with no need for textual programming languages. For instance, Figure 7 shows a snapshot of the parametric workflow later adopted in this Thesis. It concerns the simulation input parameters for thermal, daylight, and energy changes between the building to which

the cells (shown in two arrays of red shells) attach and its indoor and outdoor surroundings.

Figure 7: Visual algorithm in Grasshopper and its result on Rhino3D.

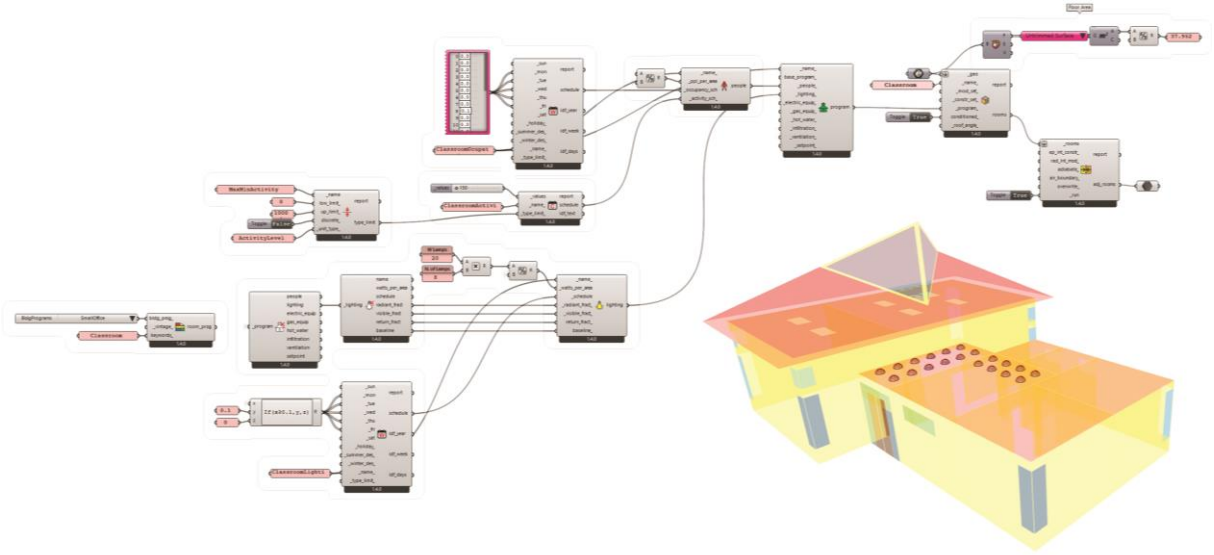

Source: The Author (2024).

VPLs have become a major component of parametric design thinking since designers use visual and interactive coding symbols (capsules) to create a model. However, scripting and developing visual codes demand cognitive and computational skills for addressing different ideas. The connection between CAD and VPL parametric modeling creates a new depth of performative design that includes building performance simulation (BPS) and evolutionary optimization and later facilitates desktop manufacturing applications. In these approaches, the designer no longer makes choices concerning single objects but a matrix of possible designs (Oxman, 2017).

The parametric design comprises explorative and cognitive refinement via an algorithmic schema with associative relationships and topological structures for editing with minimal rework. Re-editing occurs in various software and visual programming tools. For instance, Burry and Burry (2010) indicate that the first commercially successful parametric modeling software dates from 1988 (Pro/ENGINEER). Today, architects have access to various options, including Autodesk 3dsMax, Dynamo, Maya, Revit, CATIA, Generative Components, Grasshopper3D, Marionette, Modelur, and Power Surfacing. All of these options apply a similar design process and interface, i.e., a three-dimensional modeling interface on one side and, on the other, the algorithmic editor for the encoding process (Tabadkani; Banihashemi; Hosseini, 2018).

As an example, the Rhinoceros3D+Grasshopper suite enables the generation and manipulation of various shapes and a parametric workflow for multiple building simulation options depending on the enabled plug-ins. Users manipulate already-compiled coding capsules in graphic form instead of text, facilitating their use and widespread among architects and designers. This framework focuses on the Rhinoceros3D+Grasshopper suite, as it is the most employed parametric design interface (Oxman, 2017). For instance, Grasshopper capsules interconnect via data-carrying lines to build a parametric formula, visually translated into the Rhinoceros3D interface. The generation covers inputs (or start conditions), rules and algorithms, the creation, and the determination of the best variant (simulation and optimization). It connects Rhinoceros3D to other function-specific plug-ins that employ analogous coding languages, enabling the software to expand its applications. For example, Kangaroo uses computational physics to apply form-finding mechanisms; Karamba works with structural analysis; Pachyderm adds acoustical simulations; Ladybug Tools import and visually represent weather data, linking third-party engines like EnergyPlus and Radiance to perform daylight and energy simulations. As an environmental analysis plug-in, Ladybug Tools is within the scope of this framework.

Parametric design platforms coupled with third-party plug-ins also enable a generative workflow, which is a computational process that helps achieve the best possible solutions towards specific performance criteria. These approaches are particularly suited for a data-driven design that uses critical judgment to select better outputs rather than only yielding a matrix of solutions. For building-oriented applications, such as performance simulation and optimization, it can create a consistent step-by-step translation of design information, generating a database of traceable solutions with site-specific outcomes, allowing projects to take full advantage of the indoor and boundary conditions.

4. Building performance simulation (BPS) and optimization (SBO)

A limitation for achieving high-energy performance and carbon reduction in the built environment is in the design process. According to Lamberts, Dutra, and Pereira (2014), it is necessary to overview the design conception and development to incorporate human comfort conditions. Manual calculations and analog modeling demand time and multidisciplinary expertise. For this reason, an inherent feature of

technological advancement is the possibility of using computational simulations to support design decisions.

As aforementioned, parametric and generative design procedures offer a medium for Building Performance Simulations (BPS). In architecture, this approach is an algorithm-driven process in which the performance becomes the design-guiding agent (Ayoub, 2018). BPS assists in evaluating design options and assessing the various impacts of design decisions, creating high-performance buildings that possibly improve indoor or outdoor environmental quality (Nguyen; Reiter; Rigo, 2014). BPS tools rely on object-oriented languages and equation-based modeling that do not require a specific sequence of computer assignments for simulating a model. Thus, the software can generate a more effective code, integrating optimization of multiple quantifiable performances depending on the selected simulation motors (Pinheiro *et al.*, 2018; Shi; Yang, 2013). Moreover, it allows exploring geometric possibilities that perform better for defined objectives, keeping each option's performance results explicit. It can also function as a test-bed for promoting informed decision-making.

However, neither parametric design nor building simulation approaches can answer to building active components due to the computational expense of real-time simulation, prediction, and reaction. There is still limited flexibility for modeling active building elements in State-of-the-Art simulation software such as the Rhinoceros3D+Grasshopper suite (Lucarelli; Oliveira; Carlo, 2023). Simulating different control strategies covers only a limited extent of environmental performance, not allowing the full spectrum of possible outcomes behind responsive systems. Further, existing environmental simulation tools are concerned with and constantly evolve to assess static designs in which material characteristics and building components are consistent. Numerous studies demonstrated the value of combining BPS and parametric design for conventional, static envelopes (Cartana, 2018; Chen; Yang, 2018; Kirimtat *et al.*, 2019; Lucarelli; Oliveira; Carlo, 2023), but active components deepen the design complexity and demand other design approaches.

For instance, an approach for automating and reducing the computational expense of the building simulation for active components is to express the building requirements as an optimization problem. This method is an inverse strategy in which the optimization algorithms drive the search for a design until achieving the best solutions. Simulation-based optimization (SBO) is a strategy for designing components that best

fit a specific goal, dating from the 1980s. However, its applications in the construction sector started in the second half of the 21st century (Nguyen; Reiter; Rigo, 2014). It presents an iterative nature, employing computer programming to automate simulation processes, helping achieve optimal solutions to a problem with less time and labor. According to Nguyen, Reiter, and Rigo (2014), when the evaluations present multiple goals, Multi-Criteria Design Optimization methods generate and evaluate solutions through domain integration, increasing the computational expense. Apart from optimization algorithms, which can repeat the design outcomes several times and, depending on the number of simulation inputs, can be compute-intensive, simulation iterators automate all possible design solutions and deliver all simulation outputs, generating a matrix of solutions for designers to choose from. In these cases, even though the simulation process is automatic, the decision-making is a post-process.

BPS tools seem to be an essential driver for research into human comfort (Figure 8). Popular simulation tools demand users to specify building physical characteristics, occupancy, and user schedules, contemplating how occupants, constructions, materials, uses, and surrounding conditions determine the overall thermal, luminous, and energy building performance (De Dear *et al.*, 2013). According to the Integrative Literature Review presented in Chapter 2, user comfort has been discussed mainly based on quantitative thermal and visual metrics with control variables including indoor air temperature (Cheng; Zhang; Peng, 2020; Yi *et al.*, 2020), surface temperature (Fachinello Krebs; Johansson, 2021; Kolokotroni *et al.*, 2018), beam and diffuse solar radiation (Eltaweel; Su, 2017; Vlachokostas; Madamopoulos, 2017), annual sunlight exposure (Giostra *et al.*, 2019), predicted mean vote (Lucarelli; Carlo; Martínez, 2019; Wang; Morata, 2019), predicted percent dissatisfied (Jambo, 2017), physiological equivalent temperature (Lucarelli; Carlo; Martínez, 2020; Sayad *et al.*, 2021), universal thermal climate index (Lau *et al.*, 2022; Wang; Morata, 2019), adaptive comfort (Du; Bokel; van den Dobbelsteen, 2019; Fecheyr-Lippens; Bhiwapurkar, 2017), task illuminance (Tabadkani *et al.*, 2021), daylight autonomy and spatial daylight autonomy (Hosseini; Fadli; Mohammadi, 2021; Uribe *et al.*, 2019), useful daylight illuminance (Hosseini; Mohammadi; Guerra-Santin, 2019; Pesenti; Masera; Fiorito, 2018), daylight glare index (Cannavale *et al.*, 2018), and daylight glare probability (Hosseini; Mohammadi; Guerra-Santin, 2019; Pesenti; Masera; Fiorito, 2018).

Figure 8: Environmental assessment of building envelopes and the objectives covered in this framework (in magenta).

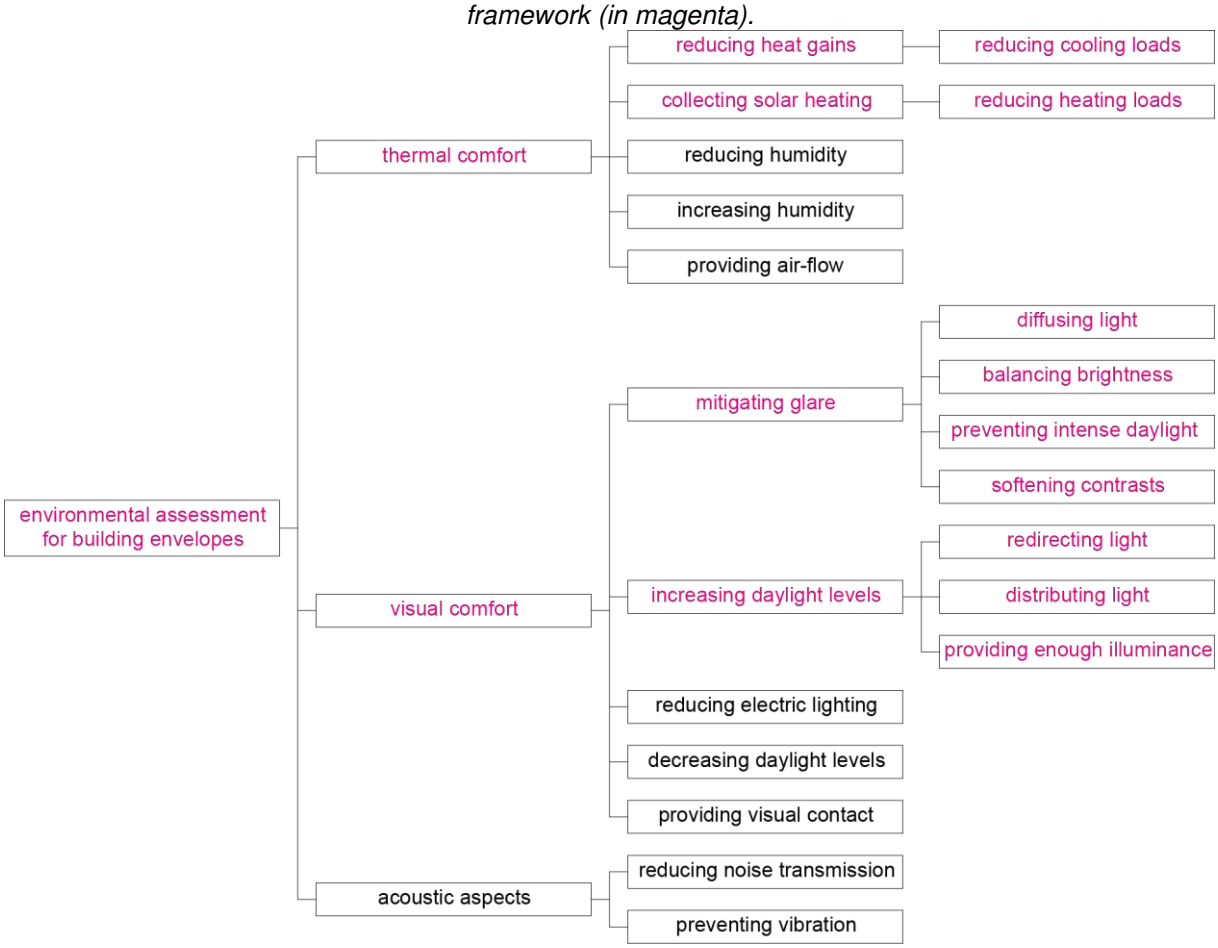

Source: The Author.

Among the literature's most accurate thermal and visual comfort bundles are the Ladybug Tools and sub-packages for Grasshopper (Ladybug, Honeybee, Butterfly, and Dragonfly)[5] (Bahdad; Fadzil; Taib, 2020; Bahdad; Syed Fadzil; Taib, 2020; Yoon; Bae, 2020). Its interface allows complex shape masking and radiation distribution visualization; Honeybee enables the user to work with daylight simulations using Radiance, energy modeling with EnergyPlus and Open Studio, and heat flow using Therm; and Butterfly and Dragonfly employ computational fluid dynamics using Open FOAM.

Even though designers have access to various human comfort indexes and software, they must apply an adequate combination of control strategies based on local weather variations, building location, and users' visual and thermal demands to ensure satisfactory indoor requirements. Furthermore, other requirements not covered in this

[5] Although Ladybug Tools for Grasshopper is not a simulation motor, it compiles various extensively validated external software within the Rhino3D+Grasshopper suite.

theoretical framework are influential when selecting suitable designs, such as aesthetics, maintenance, cost, indoor-outdoor view, and privacy (Al-Masrani; Al-Obaidi, 2019).

4.1. Thermal Comfort

According to Zhao, Lian, and Lai (2021), thermal and visual comfort studies have expanded into an independent field within the construction sector, providing important support for environmental evaluation. For instance, ASHRAE 55 (American Society of Heating, Refrigerating and Air-Conditioning Engineers, 2023) defines thermal comfort as a condition of mind that conveys satisfaction with the thermal environment, measured by objective and subjective evaluation. It is one of the most immediate and direct impacts exerted by the built environment on its occupants.

In the 1970s, Fanger (1970) created a mathematical formula using six parameters (relative humidity, airspeed and temperature, radiant temperature, metabolic rate, and clothing insulation), compared to former researchers who selected other various factors. It introduced quantitative criteria using physical environmental factors and physiological parameters for static predicted mean vote (PMV) and predicted percentage of dissatisfied (PPD) models. PMV is an index based on the mean value of occupants' votes on a seven-point thermal sensation scale based on the ASHRAE 55 Standard (American Society of Heating, Refrigerating and Air-Conditioning Engineers, 2023). PPD expresses the rate of unsatisfied subjects in a control chamber with adjustable indoor conditions. A PPD of less than 20% is acceptable, with 10% being the usual adopted threshold.

Four of Fanger's (1970) parameters are related to environmental conditions found on weather datasets: air temperature, air movement, mean radiant temperature, and relative humidity. All of these conditions influence the human body simultaneously and affect heat dissipation. For instance, the air temperature determines the heat loss rate by convection. Diurnal air temperature variations depend on sky conditions with clear days providing a large amount of incoming radiation, creating a wide daily temperature range (Olgyay, 2015). Lastly, the mean radiant temperature considers the net exchange of radiant energy between two objects.

According to Olgyay (2015), there are still few studies investigating the air temperatures that will cause occupants' heat stress, and, therefore, no temperature

metric is an isolated factor. Operative temperature combines both (air temperature and mean radiant) to represent the human-perceived temperature. Further, air movement affects heat dissipation through convection and evaporation if below the human body temperature. If above, it heats the skin by convection and cools the body by evaporation. The comfortable range for air velocities is between 0.3 to 1 m/s (above 1 m/s being disruptive). The thermal sensation is generally better when users apply natural ventilation to alleviate thermal gains and reduce mechanical ventilation (American Society of Heating, Refrigerating and Air-Conditioning Engineers, 2023).

The relative humidity interferes with perspiration, evaporation, and skin moisture. For instance, dry air can absorb the moisture from the skin, efficiently cooling the body. When relative humidity is high, moisture absorption decreases, and the cooling effect stops. The air's relative humidity should be above 20% for the whole year and below 60% and 80% for summer and winter (Olgyay, 2015). Since thermal comfort varies with culture, time of the year, health, clothing, and physical activity, comfort is not absolute, explaining why Fanger's (1970) other two parameters relate to personal factors. For instance, metabolic rates fluctuate with activity levels and environmental conditions. According to ASHRAE 55 (American Society of Heating, Refrigerating and Air-Conditioning Engineers, 2023), they are the level of chemical energy converted into heat by metabolic activities. The standard also provides met rates for a variety of activities, e.g., 1.0 met for a seated person and 1.2-1.4 met for light activities. Clothing insulation depends on the amount of clothes worn by an individual, with more insulation preventing heat loss, keeping a person warm, or leading to overheating. The thicker the garment, the greater the clo value; e.g., for trousers, a long-sleeved shirt, and a light jacket, clo equals 1. For achieving human thermal comfort, ASHRAE 55 (American Society of Heating, Refrigerating and Air-Conditioning Engineers, 2023) suggests an air temperature and a mean radiant temperature of 23 to 26 °C for the summer and 20 to 23°C for the winter. The average air velocity should be around 0.25 m/s with a 50% RH. Clothing insulation for the winter should be around 1 clo and 0.5 clo for the summer with a human metabolic rate of 1.2 met.

According to Parsons (2020), the PMV-PPD is a useful starting point for comfort appraisal. Still, it does not account for human behavior, evaluating users within uniform and steady-state air-conditioning environments. In addition to the PMV-PPD model, human comfort appraisal indices comprise the effective temperature, corrected

effective temperature, index of physiological effect, predicted four-hour sweat rate, thermal strain index, equivalent temperature, globe-thermometer temperature, and operative temperature. Percentage-based indices include the percentage outside the range and occupied hours above the reference temperature. Cumulative indices include the PPD-weighted, accumulated PPD, degree hours, and exceedance (Carlucci, 2021). Other classical models are the new-effective temperature, standard effective temperature, thermal comfort availability, two-node model, and multi-node model (Carlucci, 2021; Zhao; Lian; Lai, 2021).

Among all those thermal comfort indexes, the two and multi-node models are widely practiced and continuously developed (Parsons, 2020; Zhao; Lian; Lai, 2021). For instance, the two-node thermoregulation model simplifies the human body into a two-layered structure with outer-shell and inner-core concentric cylinders (Parsons, 2020), and the multi-node model separates the human body into various segments (skin, fat, muscle, and bones). Each layer works as a heat transfer node with thermo-physiological parameters established by energy and mass conservation equations.

Unlike indoor thermal comfort appraisal, studies on outdoor comfort indices are infrequent (Lee *et al.*, 2017). The most common examples are the physiologically equivalent temperature and the universal thermal climate index. Other metrics are the actual sensation vote, the comfort formula, the discomfort index, the thermal discomfort, the standard effective temperature, the outdoor standard effective temperature, and the temperature of equivalent perception. This framework only covers the most common thermal comfort parameters found in the Integrative Literature Review in Chapter II, as the majority of metrics are not adequate for naturally ventilated buildings, describing only air-conditioned spaces.

De Dear and Brager (1998) compiled field investigations and formalized the adaptive thermal comfort concept to complement steady-state guidelines. The adaptive hypothesis asserts that contextual factors, such as manual environmental control, influence occupants' thermal expectations. Analyzing De Dear and Brager's (1998) studies, acceptance in naturally ventilated buildings is much higher than in sealed, air-conditioned buildings because the preferred air temperature depends on outdoor circumstances. For example, people assume higher indoor temperatures in the summer than in the winter. Therefore, the indoor operative temperature rises along with the prevailing mean outdoor temperature, skewing the comfort zone.

The behavioral adaptations include operating windows and fans, adjusting blinds, wearing or changing into appropriate clothing, consuming foods or drinks, and changing the metabolism. Among these, adjusting windows to increase airflow is the most common, and according to Cândido, De Dear, and Lamberts (2011), thermal acceptability in hot and humid climates is more expressive in naturally ventilated spaces than the standards specify.

Adaptive models rely on PMV-PPD experiments and appear in several standards (American Society of Heating, Refrigerating and Air-Conditioning Engineers, 2023; European Standards, 2012; International Organization for Standardization, 2005) with different derivation methods but similar results. The larger distinction between each standard is the environmental conditioning stances, i.e., the ASHRAE 55 (American Society of Heating, Refrigerating and Air-Conditioning Engineers, 2023) adaptive standard only employs buildings with no mechanical cooling, while EN 15251 (European Standards, 2012) accepts mixed-mode buildings (given that the system is not functioning).

Bienvenido-Huertas and Rubio-Bellido (2021) state that the ASHRAE 55 (American Society of Heating, Refrigerating and Air-Conditioning Engineers, 2023) is the most internationally used adaptive comfort model, using data from various countries. It sets two limits according to an acceptability percentage: 80% and 90%. Despite not relating to a certain building typology, it requires that the space has no HVAC system, the metabolic rates are between 1 and 1.3 met, and the clothing level varies between 0.5 and 1 clo. Its main advantages are the possibility of decreasing energy consumption and approximating human comfort analysis from reality.

Currently, there are several plug-ins and add-ons for thermal comfort simulation, including DesignBuilder (Fecheyr-Lippens; Bhiwapurkar, 2017), Ecotect (Michael; Gregoriou; Kalogirou, 2018), EnergyPlus (Huo *et al.*, 2021; Tabadkani *et al.*, 2020), and TRNSYS (Fernández-Hernández *et al.*, 2017); and different three-dimensional CAD interfaces for simulation engines (e.g., Rhinoceros3D+Grasshopper, SketchUp, and Revit).

4.2. Visual Comfort

Daylight plays an important role in human well-being, especially inside buildings that are sheltered from natural conditions and potentially do not account for passive

design applications. Like thermal comfort, it involves various parameters, such as brightness, light distribution, color temperature, glare and veiling reflections, and outdoor' visual contact. In addition, both human comfort criteria are complementary since the longer light wavelengths carry heat as infrared radiation.

Evaluating the quantitative performance and qualitative expressiveness of daylight is a multi-criteria problem since poor daylighting results in inadequate illuminance levels, and excessive light admission causes over-illumination and visual strain. Improving indoor natural lighting as much as possible is an important goal to reduce artificial lighting and improve energy efficiency, but balancing visual comfort and benefiting from daylight is challenging. Considering that heat gain from solar radiation is advantageous depending on the context, the selected light control strategy needs to balance sunlight harvesting and the users' visual comfort (Hosseini *et al.*, 2019). Sunlight exposure also positively affects health, helping lessen depression symptoms, stress, eyestrain, and seasonal affective disorders (Loonen *et al.*, 2013).

Since the 1990s, studies have proposed several quantitative daylight approaches, e.g., scale models (Cartana, 2018; Yi; Kim, 2021), numerical evaluations (Jayathissa *et al.*, 2017), and software simulation (Shi; Tablada; Wang, 2020; Yi; Sharston; Barakat, 2019), with the corresponding daylight metrics being either static or dynamic. Static metrics depend only on one sky condition, while dynamic daylight metrics apply annual weather data specific to a building site and are comparatively new (Ayoub, 2019). As this study mainly concerns daylight assessment for quantitative human visual comfort, hereafter, this framework presents the fundamental inputs, indices, and metrics for daylight prediction. It is not within the scope of this Thesis to cover indoor-outdoor visual contact, directionality of light, color rendering and appearance, and flicker (European Standard 12464-1, 2021).

4.2.1. Daylight Inputs

The first step in daylight simulation is to model the sky-vault considering beam and diffuse solar radiation (Mardaljevic, 2000; Reinhart, 2018). These mathematical models normally represent continuous sky luminance patterns and present no cloud cover or weather variations. Until the 1990s, simulation and numerical calculations relied on uniform luminance models (the most simplistic representation), average overcast sky, homogenous sky, and Perraudeau's five discrete models (overcast,

intermediate overcast, intermediate, intermediate clear, and clear) (Kittler, 1985; Littlefair, 1994; Mardaljevic, 2000). In the mid-1990s, Perez, Seals, and Michalsky (1993) complemented the existing sky models with the all-weather models, divided into 15 categories. According to Ayoub (2019), all 15 classes comprised luminance distribution regarding sky clearness and brightness from global and diffuse irradiances for a given location. Perez all-weather can predict irradiances and is consistent with weather files, creating the same sky model for daylight and thermal simulations (which facilitates the building modeling and simulation workflow) and generating estimated sky luminance values through luminous efficacy models (Ayoub, 2019). For instance, EnergyPlus uses the Perez luminous efficacy model to create external illuminances (Seo, 2018). Other approaches for representing sky conditions include sky scanners and high dynamic range imaging (HDRI), with the latter using fish-eye images to capture sky fluctuations and quantify luminance levels by pixel brightness, hue, and saturation.

Another input for daylight simulation, which also appears in thermal modeling, is weather data. It compiles daily and hourly reports regarding the atmosphere state and the outdoor environmental conditions to describe the dynamic behavior of air temperature, relative humidity, irradiation, luminance, wind speed, and wind direction. Historically, the test reference year (TRY) was one of the first attempts at data compilation using matching years to assemble a multiyear sample. However, TRY did not account for solar radiance, driving simulation tools to interpolate the missing data. The inconsistent data led researchers to create other formats until the TMY3 dataset, which uses cumulative distribution functions for all assembled parameters to elect the fittest reference year (Wilcox; Marion, 2008). After TMY3, Li *et al.* (2017) report that TMY4 will depend on satellite data, rendering weather components regardless of weather stations. These weather datasets accurately portray average conditions at the hourly resolution despite their failure to represent extreme or future conditions (Crawley; Lawrie, 2015; Cui *et al.*, 2017).

The building and surrounding geometry is another input in daylight and thermal performance simulation. Shape parameters, fenestrations, materials, and constructions play an essential role in conducting thermal flow and changing the light trajectory. Outdoor reflections and sky obstructions from neighboring elements (surrounding buildings, vegetation, and ground surface) affect thermal gains and the

quantity of daylight getting to and entering the building. These parameters are fundamental for BPS since standalone geometries do not represent the complexity of the built environment and, according to Reinhart, Jakubiec, and Ibarra (2013), the commonly adopted shoebox models (Bahdad; Syed Fadzil; Taib, 2020) are only helpful for preliminary luminance/illuminance estimations. Ayoub (2019) also states that applying standard materials as baselines for initial simulation models is admissible; however, detailed fenestrations, walls with thickness and color, furniture, and shading systems affect the simulation output and deliver more accurate results. Though thermal simulations require additional variables such as air temperature, air movement, mean radiant temperature, and relative humidity, they can inherit geometries from daylight models to evade further three-dimensional modeling, which substantiates the interoperability of simulation motors (Ayoub, 2019). The opposite is also true, as the daylight simulation motors only employ the parameters adequate to their specific evaluation.

Concerning daylight simulation tools, they can employ radiosity, backward raytracing, forward raytracing, and bi-directional light transport algorithms. For instance, radiosity stores light values for surfaces and objects and renders the propagated light. Forward raytracing follows the light particles from the light source to the observer's eyes. Backward raytracing utilizes a contrary procedure, determining object visibility according to the eye distance from the view plane. The bi-directional approach (or hybrid raytracing) applies only certain levels of forward raytracing and completes the simulation with backward raytracing. Due to computational constraints, most up-to-date simulation tools apply backward raytracing or bi-directional algorithms (Ayoub, 2020). The most adopted plug-ins, add-ons, or software for daylight simulation, according to the Integrative Literature Review presented in Chapter II are DAYSIM (Gábrová, 2016; Panya; Kim; Choo, 2020), DIVA (Ayoub, 2018; Panya; Kim; Choo, 2020; Tabadkani; Banihashemi; Hosseini, 2018), Ladybug Tools (Panya; Kim; Choo, 2020; Tabadkani *et al.*, 2019; Valitabar *et al.*, 2018), and Radiance (Michael; Gregoriou; Kalogirou, 2018; Panya; Kim; Choo, 2020; Vlachokostas; Madamopoulos, 2017).

4.2.2. Daylight Characteristics

Tabadkani *et al.* (2020) state that an adequate light quantity refers to sufficient task illuminance, and, in this scenario, visual discomfort can happen due to high or low

illuminance levels. Qualitatively, contrasting light or constant light variation around the work plane diminishes light uniformity, causing visual stress due to recurrent eye adjustments between under and over-lit spaces. These significant illuminance differences between the task (visual field) and the luminance source characterize visual glare. Also, visual discomfort happens due to the angle between the luminance source and the visual field through which the light vector bounces.

Visual glare can be physiological, psychological, or veiling. Physiological glare impairs the vision without necessarily creating discomfort. It varies from blinking or squinting because of excessive light and reduced contrast to completely impaired vision (dazzle). Psychological glare occurs due to high brightness (or excess of contrast) that does not necessarily impair the vision but reduces visual performance and leads to eyestrain or headaches (Reinhart; Wienold, 2011). Veiling glare regards unwanted reflections on translucent or mirrored surfaces. Among these, daylight simulations and numerical approaches can only predict physiological glare as they employ illuminance thresholds and calculations for daylight distribution. Whereas psychological glare is subjective and relates to individual satisfaction, which is not covered in this theoretical framework and in the following Chapters.

4.2.3. Static Daylight Metrics

Sky models and weather datasets concentrate on external spatiotemporal circumstances. Contrasting, daylight calculation methods measure internal daylight, considering building geometries, materials, and occupants' visual comfort. Indoor quantitative calculation methods can be static, dynamic, or climate-based. Furthermore, qualitative means use pictures or models to create several viewports to discriminate light conditions, complementing quantitative approaches (Ayoub, 2019; Mardaljevic, 2000). Following, this framework focuses on quantitative evaluations.

The static methodology is the most widespread approach today (Ayoub, 2019; Gherri, 2015). It appraises prevailing conditions in daylighting, glare, and visual comfort in a confined environment, envisioning an optimal level of natural light through established thresholds. However, static models are more limiting and inconsistent than dynamic or climate-based approaches since they do not account for sky dynamism, internal task variability, and artificial light (Gherri, 2015). A traditional static daylight metric for quantitative evaluation in buildings is the daylight factor (DF) (Equation 1),

introduced at the beginning of the 1990s (Trotter, 1911). According to Ayoub (2019) and Mardaljevic (2000), DF is the ratio between indoor illuminance (E_{in})[6] at any point (generally one point) of a given plane and the global horizontal illuminance (E_{out}) under a sky of known luminance distribution (CIE standard overcast sky conditions) (Equation 1), expressed as a percentage.

$$DF = \frac{E_{in}}{E_{out}} \cdot 100 \qquad (1)$$

Where: DF: Daylight Factor
E_{in}: Indoor Illuminance
E_{out}: Global Horizontal Illuminance

DF does not consider direct sunlight, weather conditions, location, building orientation, or glare and, therefore, describes the worst-case scenario, only proper for estimating minimum values (Ayoub, 2019; Mardaljevic, 2000). Since "the sky luminance does not vary with azimuth, the orientation of the scene about the Z-axis [does not affect the] DF" (Mardaljevic, 2000, p.12). Each country has its requirements for DF, i.e., Brazil follows the NBR 15575-1 (Associação Brasileira de Normas Técnicas, 2013) for residential buildings.

Other static metrics found in the integrative review (Chapter II) are illuminance (E_c) (Bui *et al.*, 2020), luminance (Al Dakheel; Aoul, 2017), visual comfort probability (VCP) (El-Dabaa, 2016), and daylight glare index (DGI) (Elzeyadi, 2017).

4.2.4. Dynamic and Climate-based Methods

As aforementioned, static measures quantify absolute values of natural light using percentages and pre-established thresholds. In contrast, dynamic metrics apply realistic sky conditions and solar beam radiation, producing daylighting results for a time series at each point of the assessed space. Due to the higher accuracy in the admission and distribution of natural light, they replace static metrics (Reinhart; Wienold, 2011). For instance, in the 1980s, Tregenza and Waters prefaced the daylight coefficient (DC) metric to expedite illuminance calculations under various sky conditions, discretizing 145 sky pieces to define various luminance values. Therefore,

---

[6] According to Reinhart (2018, 2019), indoor illuminance has three components: the sky component as the proportion of illuminance due to visible sky patches; the external reflected component based on the reflected sky component; and the internal reflected component for indoor surfaces' reflection.

DC expresses the ratio between the luminance of a sky patch and the internal illuminance (Ayoub, 2019). For this metric, the contribution of indoor illuminance studies various points using matrix-based operations.

As seen in Equation 2, $DC_a(x)$ results from the indoor illuminance (E_i) of a point (x) due to a sky patch ($_a$) normalized with sky patch illuminance (L_a) and angle (S_a). Total illuminance E(x) at a point comes from a linear superposition of each DC together with luminance values and angles (Equation 3).

$$DC_a(x) = \frac{E_a(x)}{L_a \cdot \Delta S_a} \quad (2)$$

$$E(x) = \sum_{a=1}^{N} DC_a(x) \cdot L_a \cdot \Delta S_a \quad (3)$$

Where: *DC_a: Daylight Coefficient*
$_a$: Sky Patch
x: Point and orientation inside a space
E_a: Illuminance in x due to S_a
L_a: Illuminance of S_a
S_a: Sky Segment
ΔS_a: angular size of Sa
E(x): Total Illuminance
N: Number of Sky Patches

According to Nguyen (2019), daylight illuminance considers intensity and spatial distribution induced by the interaction between the sun and the sky, building geometry, location, and material attributes. It is a standard daylight metric to evaluate illuminance on the horizontal plane (Reinhart; Mardaljevic; Rogers, 2013), but it cannot represent daylight quality.

The climate-based daylight modeling further develops dynamic measures, showing many refinements relative to earlier metrics. They rely on a weather file to render daily and seasonal daylight variations throughout shifting meteorological events during the year (Gherri, 2015) and deliver predictions of absolute quantities (e.g., the illuminance levels mentioned above). Climate-based applications involve simulation environments and specific software, which makes the approach laborious and time-consuming, though accurate. They require several steps, i.e., a grid of sensors defining the evaluated space, the simulation period, the weather dataset, the luminance values, and the daylight metric (output).

Furthermore, other metrics found in the Integrative Literature Review include daylight autonomy (DA) (Cecilie *et al.*, 2017), continuous daylight autonomy (DA_{con})

(Taveres-Cachat; Goia, 2020), spatial daylight autonomy ($_{s}$DA300/50%) (Yi *et al.*, 2019), useful daylight illuminance (UDI) (Bahdad; Fadzil; Taib, 2020), annual sun exposure (ASE) (Yi *et al.*, 2019), and discomfort glare probability (DGP) (Hosseini; Mohammadi; Guerra-Santin, 2019). As most studies adopted DA, $_{s}$DA, UDI, and DGP (and variants), this framework further discusses them below.

a. Daylight autonomy (DA)

The Daylight Autonomy is a performance index based on a recorded weather dataset (Equation 4). It represents the percentage of occupied hours in a year when daylight levels are above a minimum threshold. For instance, according to the NBR ISO/CIE 8995-1 (Associação Brasileira de Normas Técnicas, 2013), minimum illuminance levels for a hallway are 100 lx; for reading spaces like libraries and conference rooms, illuminance levels increase to 500 lx. Other thresholds for work plane illuminances appear on certification records such as LEED (Nguyen, 2019).

$$DA = \frac{\Sigma_i (wf_i \cdot t_i)}{\Sigma_i t_i} \in [0,1], wf_i = \begin{cases} 1 if E_{daylight} \geq E_{limit} \\ 0 if E_{daylight} < E_{limit} \end{cases} \quad (4)$$

Where: *DA: Daylight Autonomy*
wf_i: Weighting Factor
t_i: Yearly Occupied Hours
$E_{daylight}$: Horizontal Illuminance
E_{limit}: Illuminance Limit

In the equation, wf_i is a weighting factor multiplying the annual occupied hours (t_i). $E_{daylight}$ and E_{limit} indicate the horizontal illuminance at a given point and the illuminance limit. If daylight is above the threshold, wf_i equals 1, and if below, wf_i is 0. According to Nguyen (2019), modified DA metrics comprise DA_{con}, $_{s}$DA, and UDI. DA_{con} indicates a percentage for a time step when illuminance at a given point is below the space threshold, e.g., if a point on a hallway (minimum illuminance of 100 lx) receives 25 lx, DA_{con} equals 25% (Elkhatieb, 2016).

b. Useful daylight illuminance (UDI)

According to Nabil and Mardaljevic (2006), the UDI represents the annual illuminance levels within a threshold over a task plane (considering underlit and overlit situations) (Equation 5). It is a local and long-term metric based on surveys, reports, and occupant reactions and responses. It fits large office buildings, where users experience high daylight levels and glare on display devices (Nguyen, 2019).

Compared to DA and DA_{con}, UDI offers more information to assess visual discomfort.

$$UDI = \frac{\sum_i (wf_i . t_i)}{\sum_i t_i} \in [0,1] \quad (5)$$

Where: UDI: Useful Daylight Illuminance
wf_i: Weighting Factor
t_i: Yearly Occupied Hours

According to Nabil and Mardaljevic (2006) and Loonen (2018), UDI has four classifications, i.e., fell short (<100 lx), supplementary (100-300 lx), autonomous (300-3000 lx), and exceeded (>3000 lx). Similar to DA, wf_i (weighting) changes according to the threshold. The authors only present the equation with no weighting because there is no consensus for UDI limit values (Nabil; Mardaljevic, 2006; Olbina; Beliveau, 2009). Some researchers consider the upper threshold for autonomous UDI as 2000 lx with exceeding values above 2000 lx (Reinhart; Mardaljevic; Rogers, 2013), while other authors consider UDI a three-classification index (underlit, useful, and overlit).

c. Spatial Daylight Autonomy - sDA300/50%:

$_s$DA300/50% represents the percentage of the floor area that receives at least 300 lx (the minimum illuminance according to LEED) for 50% of the annual occupied hours (Equation 6) (Ayoub, 2019).

$$sDA_{300/50\%} = \frac{\sum_i S(i)}{\sum_i Pi} \in [0,1], S(i) = \begin{cases} 1 if s_i \geq \tau t_y \\ 0 if s_1 < \tau t_y \end{cases} \quad (6)$$

Where: $_s$DA300/50%: Spatial Daylight Autonomy
S(i): Exceeding Illuminance Levels
Pi: Target Point
t: Temporal Threshold

d. Daylight Availability

Daylight availability combines DA and UDI, presenting three-evaluation criteria similar to UDI: daylit areas with at least half the time enough daylight; partially daylit for areas below useful illuminance; overlit for oversupplied daylit areas (Reinhart; Wienold, 2011).

e. Daylight glare probability (DGP)

According to Tabadkani *et al.* (2019) and Ayoub (2019), DGP is an empirical approach that combines vertical eye illuminance (E_v) and glare source luminance rather than background luminance, exhibiting a higher correlation with the perceived

discomfort glare. Therefore, it helps estimate the probability of experiencing glare using subjective evaluation based on the field of vision, the position of glare sources, and visual contrasts. If DGP is higher or equal to 45%, glare is intolerable; between 40% and 45%, disturbing; from 35% to 40%, perceptible; if below 35%, DGP is imperceptible (Reinhart; Wienold, 2011; Wienold; Christoffersen, 2006).

Similar to UDI, DGP thresholds vary. For instance, Loonen (2018) considers only three classifications, i.e., intolerable (DGP > 45%), disturbing (35% < DGP < 45%), and not disturbing (DGP < 35%). Equation 7 is valid within the DGP range of 20% to 80%, with illuminance above 380 lx. Unlike previous indices, DGP requires creating a hemispherical fisheye image at each time step, producing many images per year, which is very time-consuming for computational applications.

$$DGP = 5.87.10^{-5} + 9.18.10^{-2}.log\left(1 + \sum_{j=1}^{n} \frac{L_{s,j}^2.\omega_{s,j}}{E_v^{1.87}.P_j^2}\right) + 0.16 \qquad (7)$$

Where: *DGP: Daylight Glare Probability*
L_s: Luminance of Source
E_v: Vertical Eye Illuminance
ω_s: Solid Angle of Source
P: Position Index

5. Digital manufacturing (DM)

The Third Industrial Revolution shifted manufacturing from mechanical and analog machines to digital technologies, introducing the possibility for mass customization within the product design workflow, cutting waste, enabling manufacturers to restructure supply chains, promoting localized production, and presenting a significant social impact as it spawns new jobs and promotes new skills and greater personal satisfaction with the end product (Brandenburg *et al.*, 2014).

Digital manufacturing (DM) is a design and production process that combines digital modeling with manufacturing processes. Its first stage takes place within digital software that can perform two and three-dimensional modeling (in general, objects with volume, mass, and center of gravity), followed by the manufacturing phase, which materializes the virtual project via a machine-to-machine workflow. With digital tools, designers can directly transfer virtual data to DM machines within a Design-for-Manufacturing-and-Assembly workflow that offers control over all the design stages, consolidating terms as “making” architecture and accepting architects as “makers”,

restoring some of their involvement in product design. With DM, architects can approach the execution, intervene, and modify the design as it develops (Paio *et al.*, 2012). DM also alleviates geometry constraints and enables custom component production without increasing labor.

Parametric design and desktop digital manufacturing applications further facilitate manufacturing processes as they expedite the prototyping process, leaving the designer free to alter the virtual model according to materialization constraints and design flaws or incompatibilities.

5.1. Reductive manufacturing (RM)

Reductive manufacturing (RM) (Figure 9) processes convert CAD data into computer-aided manufacturing language to control a mechanical cutting head that removes material from a sheet or block of material near the desired final object's overall dimension. They are also known as subtractive manufacturing or machining.

Figure 9: RM materials, advantages, and drawbacks. In magenta: processes covered in this study.

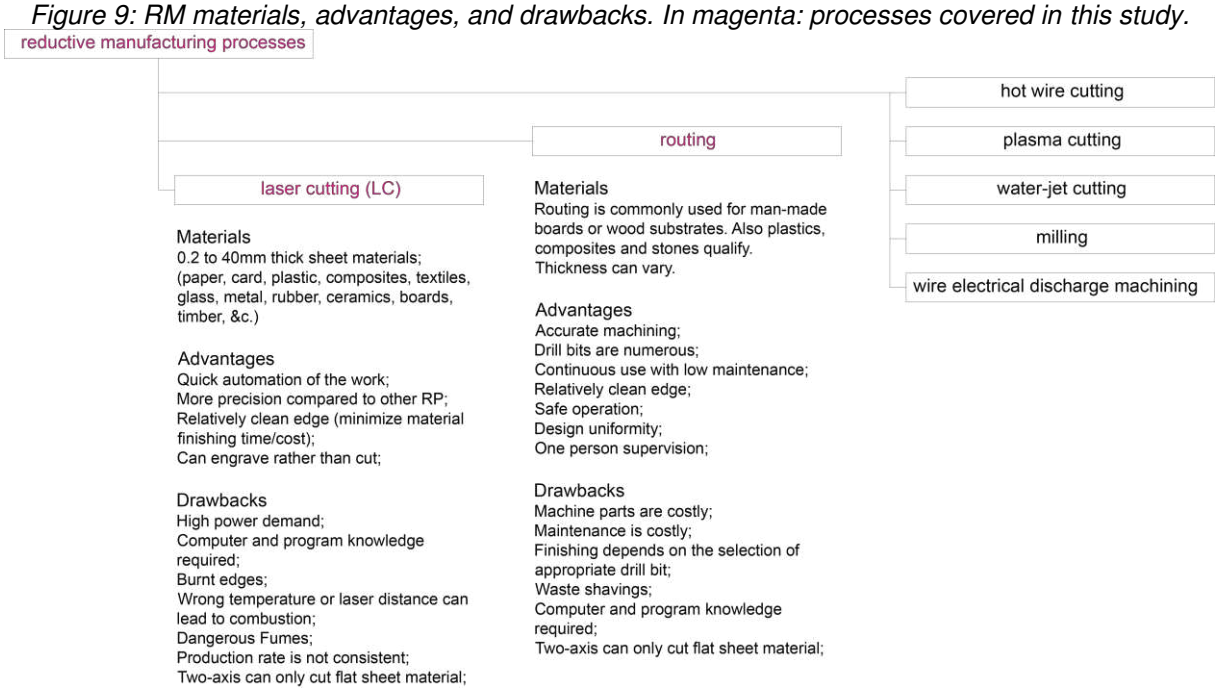

Source: The Author (2024).

According to Caneparo (2014), RM applies to any solid material, such as wood, paper, plastic, ceramic, resins, composites, and metal. RM is older than additive processes and has widespread use for both prototyping and manufacturing. It presents a wide range of applications across the manufacturing, architectural, and construction industries and provides good accuracy, good surface finish, and efficient volume fabrication. Also, RM relies on the feedstock's structural integrity and is suitable for

small to large workpieces, allowing the designer to work with end-use materials (Bryden, 2014). It encompasses various cutting machines such as milling, routing, and laser cutting (Caneparo, 2014), with most research covering desktop laser cutting as a widespread technology. In this framework, the author covers laser cutting and routing as they have access to one laser cutter, a 3-axis router, and a ZMorph Fab VX (for deposition, laser cutting, and routing).

5.1.1. Laser cutting

The CO_2 laser cutter CNC is an increasingly common machine within architecture school workshops, professional model makers, and even design practitioners. It is suitable for comparatively thin materials, usually up to 60 mm thick, and provides a high degree of accuracy and sharp cuts. Laser machines support a wide variety of materials, including paper, cards, plastics, wood, textiles, and metals (such as aluminum, brass, mild, and stainless steel). Their reductive process involves melting, burning, or vaporizing the material, producing relatively clean edges, particularly on thermoplastics, and minimizing finishing time and cost. However, it leaves a burnt edge in human-made board and timber feedstock, further subjecting the product to weathering. Further, they offer laser beam precision for cutting or engraving complex shapes and detailed elements with a typical dimension accuracy of about 12.7 µm (Bryden, 2014). Their precision attracted several model makers with the premise of creating high-quality model components. However, they vary in size and power, and not all machines are suitable for processing all materials. Most laser cutters are relatively small unless applied at an industrial scale, which places clear limits on fabricated components' size. For instance, Chart 2 presents the properties of the machine adopted in this Thesis – a two-axis CNC with a 1300x900 mm cutting area.

Chart 2: Properties for the laser cutter adopted in this study.

Machine		Work Area	Speed	Power Consump.	Laser Power	Max. Thickness	Materials	Other Features
	OMRAK 1610	1300x900 mm	0 - 500 mm/s	3200 W	130 W	18 mm	Cloth, leather, wood, acrylic, bamboo, rubber, and ceramic tile.	Adjustable laser head; XY-Axis sensor;

Source: The Author (2024). Figure Source: (a) Adapted from "Laser CO_2 1610 100w". Retrieved from: https://www.omrakcnc.com.br/produto/maquina-laser-co2-1610-100w/782031?vid=1139360.

According to Caneparo (2014), laser cutting is perhaps most analogous to conventional physical modeling and prototyping since planar components need to be assembled to represent the digital, three-dimensional model.

5.1.2. Milling and routing

Milling and routing interchangeably indicate the process of removing solid, block-shaped material using a CNC or a manually operated machine. Milling generally works for hard materials, while routing applies to human-made boards, wood substrates, and softer materials such as plastics, resins, composites, and foam (Caneparo, 2014). In this research, the author has access to a 3-axis routing machine, quicker than mills but with less torque. For this router, the feedstock remains on the cutting table, and its spindle head moves across the X, Y, and Z axes, removing layers according to a predetermined route. Other routing machines can have up to six degrees of freedom (the fourth axis yaws the workpiece, the fifth rolls it, and the sixth pitches the spindle).

Routing can generate a wide range of object sizes and allows the creation of complex forms with no required assembly. However, according to Fang *et al.* (2016), a life-cycle analysis of router machines' energy consumption compares to the CO_2-equivalent emissions of an SUV car, wasting more energy, raw materials, and resources than laser-based processes. For instance, extraction is the most energy-intensive manufacturing process, making up 70% of the process's total energy, which is not cost-effective when producing small-volume batches.

5.2. Additive manufacturing (AM)

Additive manufacturing (AM) (Figure 10) refers to a broad group of techniques that turn digital models into physical objects using CAD data. AM is also known as additive fabrication, additive layer manufacturing, layer manufacturing, free-form fabrication, and rapid prototyping. According to Bryden (2014), rapid prototyping is, often unadvisedly, a shorthand for AM instead of a general term within a family. However, additive processes are rapid only compared to traditional analog approaches.

AM expedites fabrication using a sort of materials depending on time, cost, and application. The various processes' commonality lies in the incremental build-up of material layers to produce a three-dimensional object following a general workflow, i.e., digital modeling, exporting a CAD data file, slicing the model into multiple two-dimensional cross-sectional layers using a slicing software, and printing. The thinner the layers are, the closer the printed object will be to the digital model. Such differences will determine the final part's accuracy, assembly tolerances, swelling/shrinking, and component properties (mechanical, optical, and chemical). They will also determine

production speed, post-processing needs, build volume requirements and the process and product overall costs.

Figure 10: AM materials, advantages, and drawbacks. In magenta: processes covered in this study.

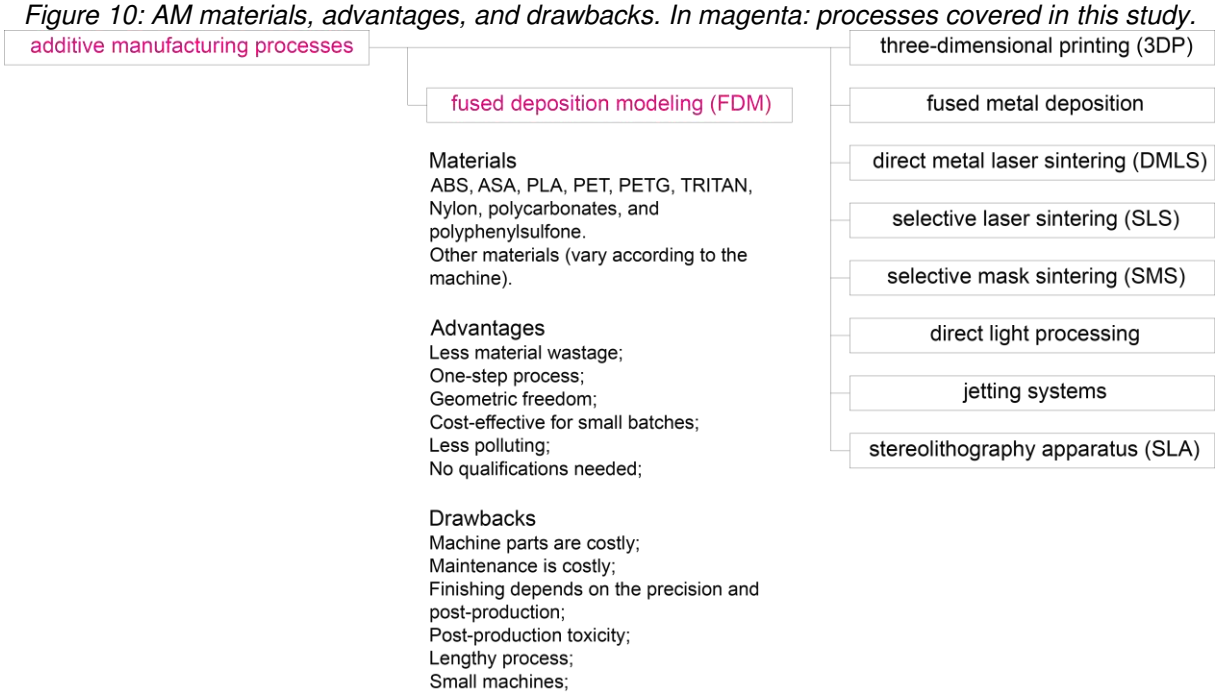

Source: The Author (2024).

Researchers still consider AM processes rapid because the prototype parts are available within several hours rather than the days or weeks required when using manual labor or industry-level production chains. For desktop applications, designers can rapidly create rough to accurate physical representations of their concepts to examine and manipulate them as physical models. According to Gibson, Rosen, and Stucker (2015), desktop AM machines have evolved to the extent that their outputs are suitable for end-use, demanding more time and explaining why the terminology changed from rapid prototyping to additive manufacturing. Among AM desktop applications, fused-deposition modeling (FDM) is the most widespread for prototyping and evaluating building components (Bayram, 2021; Yi *et al.*, 2020).

5.2.1. Fused deposition modeling (FDM)

Fused-deposition modeling (FDM) machines use an extruder carriage and a hotend to pull thin thermoplastic feedstock (normally a filament) through a print nozzle heated above the material's glass-transition point and deposit the semi-liquid molten plastic onto a heated build platform (Figure 11).

FDM machines are normally desktop-sized and can produce small to large prototypes and end-use parts (depending on the machine's build volume and print

capacity). Their depositing process is comparably clean, with no excess liquid or powder and recyclable/reusable byproducts. In case the print job stops, the machine crashes, the thermoplastic layers shift and unstick, or the product is no longer needed, the material can be shredded, re-fused, and re-spooled.

Figure 11: FDM's parts and processes. Prusa MINI+ as example.

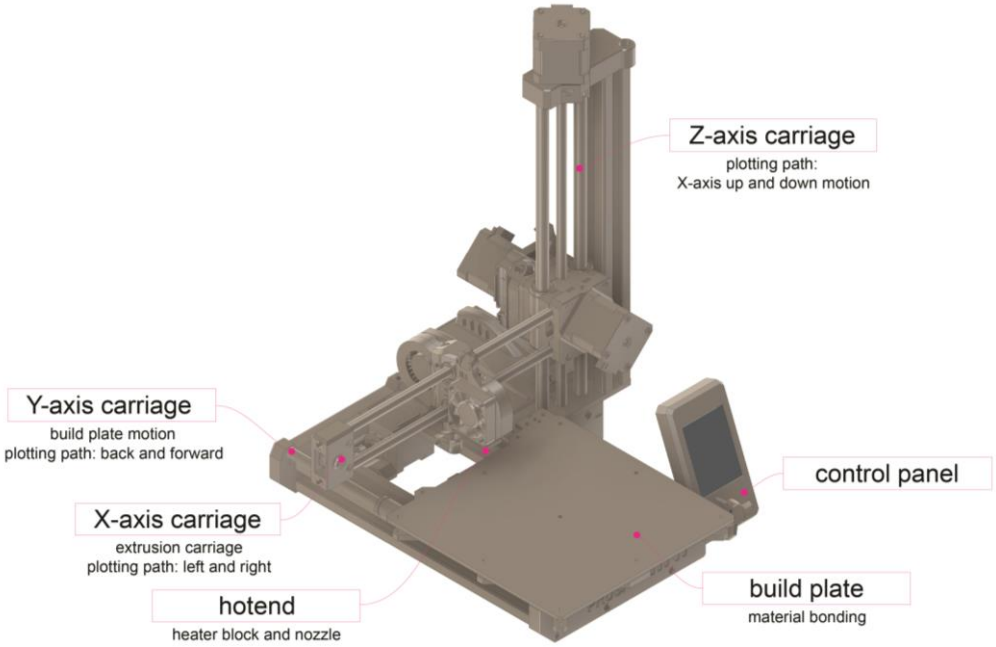

Source: The Author.

FDM's first step is to create a three-dimensional digital file of the desired object, appropriately scaled according to its physical measurements with minimum wall thicknesses larger than the print nozzle. The second step is converting the model into a .stl file (which stands for stereolithography or standard triangle language) and bringing the model into slicing software. The slicer discretizes solids into horizontal layers and these into coordinated paths for the carriages to follow (a .gcode file). After the deposition process, the designer can remove the object from the build plate, which can undergo post-processing if necessary. Although novel FDM machines can deliver ready-to-use objects without the need for post-processing, standard 0.4 mm-holed nozzles generally produce rough parts that do not have a finished feel. More recent technologies employ Artificial Intelligence-Powered Evolution (such as Bamboo Micro Lidar) with micrometric printing depths.

Thermoplastic filaments include ABS, ASA, PLA, PET, PETG, TRIRAN™, Nylon, polycarbonates, and polyphenylsulfones. According to Bryden (2014), these materials are some of the same production-grade engineering copolymers used in traditional thermoforming and plastic injection processes. They have good impact strength,

relatively high tensile strength, and good resistance to scratching and chemicals. FDM can also produce patterns for tooling and master patterns for casting.

In FDM, the nozzle size used to deposit the polymer into the build platform and the Z-axis motor and screw rod can limit the final resolution and the finish quality. Generally, FDM allows for layer resolution varying from 0.05 to 0.39 mm with nozzle holes ranging from 0.1 to 1.2 mm (given that a standard filament is 1.75 mm).

This research later employs four different FDM machines, as seen in Chart 3. Specifically, the build volume and the nozzle and table temperatures are key components. The former defines a component's maximum size and its slice orientation, while the latter determines which materials the device can employ. Layer resolution depends on the Z-axis servo motor revolution detector or encoder, which means that newer servos and better-controlling software can thin the build layers.

Currently, there are commonly three sets of printing speeds for FDM machines. The first set is at around 40 to 50 mm/s, the second prints at about 80 – 100 mm/s, and the third begins at 100 mm/s. Even though Prusa and Creality offer machines within the third printing set, when past 150 mm/s speeds, the printing quality drops noticeably, creating buckling as the filament tends to slip, anisotropy when the nozzle skips deposition, and layer shifting as the carriages and plastic parts misalign.

Chart 3: FDM machines adopted in this study.

Machine		Volume (cm^3, XYZ cm)	Speed (mm/s)	Nozzle Temp. (°C)	Nozzle Sizes (mm)	Table Temp. (°C)	Layer Res. (mm)
	Prusa MINI+	5.832 cm^3 (18x18x18 cm)	200 mm/s	280 °C	0.1 – 1.2 mm	100 °C	0.05 – 0.25 mm
	Prusa i3 MK3	11.025 cm^3 (25x21x21 cm)	200 mm/s	300 °C	0.1 – 1.2 mm	120 °C	0.05 – 0.25 mm
	Creality CR 5 – Pro H	25.080 cm^3 (22x30x38 cm)	100 mm/s	300 °C	0.1 – 1.2 mm	110 °C	0.10 – 0.25 mm
	ZMorph VX	9.775 cm^3 (23x25x17 cm)	60 mm/s	250 °C	0.3 mm	100 °C	0.05 – 0.4 mm

Source: The Author (2024). Figure Sources: (a) Reprinted from "Original Prusa MINI+" by Josef Prusa. Retrieved from: https://www.prusa3d.com/product/original-prusa-mini-semi-assembled-3d-printer-4/; (b) Reprinted from "Original Prusa i3 MK3S+ 3D", by Josef Prusa. Retrieved from: https://www.prusa3d.com/en/product/original-prusa-i3-mk3s-3d-printer-kit/?query=%3Fquery%3Dundefined; (c) Adapted from "Creality CR 5 - Pro", by Creality. Retrieved from: https://www.creality.com/products/cr-5-pro-3d-printer; (d) Reprinted from "ZMORPH FAB," by ZMorph. Retrieved from: https://zmorph3d.com/products/zmorph-fab.

Highlights and General Guides for the Thesis

Based on this theoretical framework, the author highlights the following findings that acted as guiding parameters, configurations, characteristics, or processes adopted throughout the Research-through-Design workflow within this Thesis:

a) Ceiling apertures render more homogenous light distribution and decrease the likelihood of visual glare compared to vertical openings;

b) Various openings of no more than one-and-a-half times the ceiling height apart and spread evenly across space create more uniform illumination;

c) The higher the aperture, the more broadly the light will diffuse (therefore, low-ceiling spaces require small skylights spaced closer together);

d) When positioned far from walls, zenithal openings should employ baffles or banners to avoid veiling reflections; optionally, smaller openings already have the roof thickness as a baffle-like structure;

e) Clerestories perform better than skylights in tropical and temperate climates since their vertical or near-vertical orientation is closer to window features than that of skylights;

f) Most macro-scale active components employ extrinsic, centralized, direct, and reactive controls since the environmental parameters normally fall within known thresholds (e.g., rain or no rain; adequate illuminance level or not; glare or visual comfort);

g) Human comfort is relatively subjective, and direct control approaches present more override options with simpler systems;

h) Neither parametric design nor building simulation approaches can represent active building components due to the high computational expense;

i) Simulating different point-in-time and single-configuration control strategies covers only a limited extent of environmental performance;

j) Optimization motors can automate and reduce the complexity of the real-time response, iterating all geometric configurations to achieve optimal

solutions; however, depending on the optimization algorithm, they can render local-optima or repeat design solutions several times;

k) Simulation iterators can automate the combination of all possible design solutions and deliver all simulation outputs, generating a matrix of solutions;

l) User comfort research mostly applies quantitative thermal and visual metrics and does not consider qualitative user input;

m) Parametric design and desktop digital manufacturing applications expedite the prototyping process, leaving the designer free to alter the digital model according to real-life constraints;

n) Fused-deposition modeling applications are the most widespread and still considered rapid compared to industrial mockup-alpha-beta-minimum viable product workflow.

REFERENCES

ABNT. NBR ISO/CIE 8995-1: Iluminação de ambientes de trabalho, Parte 1: Interior. [*s. l.*], p. 46, 2013. DOI: http://www.abntcatalogo.com.br/norma.aspx?ID=196479.

AGIRBAS, A. The Use of Simulation for Creating Folding Structures : A Teaching Model. *In*: 2017, Rome. **eCAADe 2017: Sharing of Computable Knowledge!** Rome: [*s. n.*], 2017. p. 325–332.

AL-MASRANI, S. M.; AL-OBAIDI, K. M. Dynamic shading systems: A review of design parameters, platforms, and evaluation strategies. **Automation in Construction**, [*s. l.*], v. 102, n. November 2018, p. 195–216, 2019. DOI: https://doi.org/10.1016/j.autcon.2019.01.014.

AL-OBAIDI, K. M.; ABDUL RAHMAN, A. M. Renewable energy and sustainable technologies for building and environmental applications: Options for a greener future. **Renewable Energy and Sustainable Technologies for Building and Environmental Applications: Options for a Greener Future**, [*s. l.*], p. 1–252, 2016.

AL DAKHEEL, J.; AOUL, K. T. Building applications, opportunities and challenges of active shading systems: A state-of-the-art review. **Energies**, [*s. l.*], v. 10, n. 10, 2017.

ALANI, M. Algorithmic investigation of the actual and virtual design space of historic hexagonal-based Islamic patterns. **International Journal of Architectural Computing**, [*s. l.*], v. 16, n. 1, p. 34–57, 2018.

ALKHATIB, H. *et al.* Deployment and control of adaptive building facades for energy generation, thermal insulation, ventilation and daylighting: A review. **Applied Thermal Engineering**, [*s. l.*], v. 185, n. January 2021, p. 116331, 2021. DOI: https://doi.org/10.1016/j.applthermaleng.2020.116331.

ASHRAE. **ASHRAE 55 - Thermal Environmental Conditions for Human Occupancy**. 2023.

AYOUB, M. 100 Years of Daylighting: A chronological review of daylight prediction and calculation methods. **Solar Energy**, [*s. l.*], v. 194, n. October, p. 360–390, 2019. DOI: https://doi.org/10.1016/j.solener.2019.10.072.

AYOUB, M. A review on light transport algorithms and simulation tools to model daylighting inside buildings. **Solar Energy**, [*s. l.*], v. 198, n. January, p. 623–642, 2020. DOI: https://doi.org/10.1016/j.solener.2020.02.018.

AYOUB, M. Adaptive façades: An evaluation of cellular automata controlled dynamic shading system using new hourly-based metrics. *In*: , 2018. **CAADRIA 2018 - 23rd International Conference on Computer-Aided Architectural Design Research in Asia: Learning, Prototyping and Adapting**. [*S. l.: s. n.*], 2018. p. 83–92.

AYOUB, M. Integrating illuminance and energy evaluations of cellular automata controlled dynamic shading system using new hourly-based metrics. **Solar Energy**, [*s. l.*], v. 170, n. April, p. 336–351, 2018. DOI: https://doi.org/10.1016/j.solener.2018.05.041.

AZIMI FEREIDANI, N.; RODRIGUES, E.; GASPAR, A. R. A review of the energy implications of passive building design and active measures under climate change in the Middle East. **Journal of Cleaner Production**, [*s. l.*], v. 305, 2021.

BAHDAD, A. A. S.; FADZIL, S. F. S.; TAIB, N. Optimization of daylight performance based on controllable light-shelf parameters using genetic algorithms in the tropical climate of malaysia. **Journal of Daylighting**, [*s. l.*], v. 7, n. 1, p. 122–136, 2020.

BAHDAD, A.; SYED FADZIL, S. F.; TAIB, N. Evaluating kinetic light-shelves and their impacts on daylighting performance. **Indonesian Journal of Electrical Engineering and Computer Science**, [*s. l.*], v. 19, n. 1, p. 476–484, 2020.

BASARIR, B.; CEM ALTUN, M. A redesign procedure to manufacture adaptive façades with standard products. **Journal of Facade Design and Engineering**, [*s. l.*], v. 6, n. 3, p. 077–100, 2018.

BAYRAM, A. K. S. Digital fabrication shift in architecture. *In*: DAL, M. (org.). **Architecture Sciences and Technology**. Lyon: Livre de Lyon, 2021. p. 173–193.

BIENVENIDO-HUERTAS, D.; RUBIO-BELLIDO, C. **Adaptive Thermal Comfort of Indoor Environment for Residential Buildings: Efficient strategy for saving energy**. [*S. l.*]: Springer, 2021. DOI: https://link.springer.com/10.1007/978-981-16-0906-0.

BÖKE, J.; KNAACK, U.; HEMMERLING, M. Prototype of a cyber-physical façade system. **Journal of Building Engineering**, [*s. l.*], v. 31, n. March, p. 101397, 2020. DOI: https://doi.org/10.1016/j.jobe.2020.101397.

BRANDENBURG, M. *et al.* Quantitative models for sustainable supply chain management: Developments and directions. **European Journal of Operational Research**, [*s. l.*], v. 233, n. 2, p. 299–312, 2014.

BRYDEN, D. **CAD and Rapid Prototyping for Product Design**. China: Laurence King Publishing Ltd, 2014.

BUI, D. *et al.* Enhancing building energy efficiency by adaptive façade: A computational optimization approach. **Applied Energy**, [*s. l.*], v. 265, n. March, 2020.

BURRY, J.; BURRY, M. **The New Mathematics of Architecture**. 1. ed. [*S. l.*]: Thames & Hudson, 2010.

CAETANO, I.; SANTOS, L.; LEITÃO, A. Computational design in architecture: Defining parametric, generative, and algorithmic design. **Frontiers of Architectural Research**, [*s. l.*], v. 9, n. 2, p. 287–300, 2020.

CALLADINE, C. R. Buckminster Fuller's "Tensegrity" structures and Clerk Maxwell's rules for the construction of stiff frames. **International Journal of Solids and Structures**, [*s. l.*], v. 14, n. 2, p. 161–172, 1978. DOI: http://dx.doi.org/10.1016/0020-7683(78)90052-5.

CÂNDIDO, C.; DE DEAR, R.; LAMBERTS, R. Combined thermal acceptability and air movement assessments in a hot, humid climate. **Building and Environment**, [*s. l.*], v.

46, n. 2, p. 379–385, 2011. DOI: http://dx.doi.org/10.1016/j.buildenv.2010.07.032.

CANEPARO, L. **Digital Fabrication in Architecture, Engineering, and Construction**. [*S. l.*]: Springer, 2014.

CANNAVALE, A. *et al.* Energy savings due to building integration of innovative solid-state electrochromic devices. **Applied Energy**, [*s. l.*], v. 225, n. April, p. 975–985, 2018. DOI: https://doi.org/10.1016/j.apenergy.2018.05.034.

CARLUCCI, F. A review of smart and responsive building technologies and their classifications. **Future Cities and Environment**, [*s. l.*], v. 7, n. 1, p. 1–12, 2021.

CARTANA, R. P. **Desempenho Térmico e Lumínico de Elementos de Controle Solar para Fachadas Desenvolvidos com Modelagem Paramétrica e Fabricação Digital**. 2018. 348 f. - Universidade Federal de Santa Catarina, [*s. l.*], 2018.

CECILIE, G. *et al.* The effect of dynamic solar shading on energy, daylighting, and thermal comfort in a nearly zero-energy loft room in Rome and Copenhagen. **Energy & Buildings**, [*s. l.*], v. 135, p. 302–311, 2017. DOI: http://dx.doi.org/10.1016/j.enbuild.2016.11.053.

CHANG, T. W.; HUANG, H. Y.; DATTA, S. Design and fabrication of a responsive carrier component envelope. **Buildings**, [*s. l.*], v. 9, n. 4, p. 1–14, 2019.

CHEN, X.; YANG, H. Integrated energy performance optimization of a passively designed high-rise residential building in different climatic zones of China. **Applied Energy**, [*s. l.*], v. 215, n. November 2017, p. 145–158, 2018. DOI: https://doi.org/10.1016/j.apenergy.2018.01.099.

CHENG, J.; ZHANG, Z.; PENG, C. Parametric modeling and simulation of an indoor temperature responsive rotational shading system design. *In*: , 2020, Hong Kong. **25th International Conference of the Association for Computer-Aided Architectural Design Research in Asia CAADRIA**. Hong Kong: [*s. n.*], 2020. p. 579–588.

CRAWLEY, D. B.; LAWRIE, L. K. Rethinking the time: Is the “typical” meteorological year best for building performance simulation? *In*: , 2015. **14th International Conference of IBPSA - Building Simulation 2015, BS 2015, Conference Proceedings**. [*S. l.: s. n.*], 2015. p. 2655–2662.

CUI, Y. *et al.* Comparison of typical year and multiyear building simulations using a 55-year actual weather data set from China. **Applied Energy**, [*s. l.*], v. 195, p. 890–904, 2017. DOI: http://dx.doi.org/10.1016/j.apenergy.2017.03.113.

DE DEAR, R. J. *et al.* Progress in thermal comfort research over the last twenty years. **Indoor Air**, [*s. l.*], v. 23, n. 6, p. 442–461, 2013.

DE DEAR, R.; BRAGER, G. S. Developing an Adaptive Model of Thermal Comfort and Preference Richard. **ASHRAE Transactions**, [*s. l.*], v. 104, p. 18, 1998.

DU, X.; BOKEL, R.; VAN DEN DOBBELSTEEN, A. Spatial configuration, building microclimate, and thermal comfort: A modern house case. **Energy and Buildings**, [*s. l.*], v. 193, p. 185–200, 2019. DOI: https://doi.org/10.1016/j.enbuild.2019.03.038.

EL-DABAA, R. A. The Use of Kinetic Facades in Enhancing Daylight Performance for Office Buildings. 2016. 118 f. Faculty of Engineering and Technology, [*s. l.*], 2016.

ELKHATIEB, M. A. **A performance-driven design model of territorial adaptive building skins (TABS) for daylighting performance optimization in office buildings in Egypt**. 2016. 338 f. - University of Liverpool, [*s. l.*], 2016.

ELTAWEEL, A.; SU, Y. Parametric design and daylighting: A literature review. **Renewable and Sustainable Energy Reviews**, [*s. l.*], v. 73, n. December 2016, p. 1086–1103, 2017.

ELZEYADI, I. The impacts of dynamic façade shading typologies on building energy performance and occupant's multi-comfort. **Architectural Science Review**, [*s. l.*], v. 60, n. 4, p. 316–324, 2017. DOI: https://doi.org/00038628.2017.1337558.

EN. **DIN EN 15251 - Indoor environmental input parameters for design and assessment of energy performance of buildings addressing indoor air quality, thermal environment, lighting, and acoustics**. 2012.

EN. **EN 12464 - Light and lighting - Lighting of work places - Part 1: Indoor work places.** 2021.

EVOLA, G.; GULLO, F.; MARLETTA, L. The role of shading devices to improve thermal and visual comfort in existing glazed buildings. **Energy Procedia**, [*s. l.*], v. 134, p. 346–355, 2017. DOI: https://doi.org/10.1016/j.egypro.2017.09.543.

FACHINELLO KREBS, L.; JOHANSSON, E. Influence of microclimate on the effect of green roofs in Southern Brazil – A study coupling outdoor and indoor thermal simulations. **Energy and Buildings**, [*s. l.*], v. 241, p. 110963, 2021. DOI: https://doi.org/10.1016/j.enbuild.2021.110963.

FANG, F. *et al.* Sustainable design and analysis of CNC machine tools: Sustainable design index-based approach and its application perspectives. *In*: , 2016, Blacksburg,. **11th International Manufacturing Science and Engineering Conference, MSEC 2016**. Blacksburg,: [*s. n.*], 2016. p. 1–10.

FANG, Y.; CHO, S. Sensitivity Analysis of Skylight and Clerestory Design on Energy and Daylight Performance of a Retail Building. *In*: 2018, Chicago. **2018 Building Performance Analysis Conference**. Chicago: [*s. n.*], 2018. p. 157–164.

FANGER, P. O. **Thermal comfort Analysis and Applications in Environmental Engineering**. [*S. l.: s. n.*], 1970.

FECHEYR-LIPPENS, D.; BHIWAPURKAR, P. Applying biomimicry to design building envelopes that lower energy consumption in a hot-humid climate. **Architectural Science Review**, [*s. l.*], v. 60, n. 5, p. 360–370, 2017. DOI: http://dx.doi.org/10.1080/00038628.2017.1359145.

FERNÁNDEZ-HERNÁNDEZ, F. *et al.* Effects of louvers shading devices on visual comfort and energy demand of an office building. A case of study. **Energy Procedia**, [*s. l.*], v. 140, p. 207–216, 2017. DOI: https://doi.org/10.1016/j.egypro.2017.11.136.

FERSCHIN, P.; DI ANGELO, M.; BRUNNER, G. Rapid Prototyping for Kinetic Architecture. *In*: 2015, Cambodia. **7th International Conference on CIS & RAM**. Cambodia: IEEE 2015, 2015. p. 118–123.

FRAMPTON, K. **The Evolution of 20th Century Architecture: A Synoptic Account**. Beijing: Springer-VerlagA/Vien and China Architecture & Building Press, 2007.

FRAMPTON, K. Towards a Critical Regionalism: Six points for an Architecture of Resistance. *In*: THE ANTI-AESTETIC: ESSAYS ON POSTMODERN CULTURE. [*S. l.: s. n.*], 1998. p. 16–30.

FULLER, R. B. **Synergetics: Explorations in the Geometry of Thinking**. Sebastopol: Macmillan Publishing Co. Inc., 1977-. ISSN 0040165X.v. 17

GÁBROVÁ, L. Comparison between Dynamic and Static Metrics for Daylight Evaluation in the Case of Obstructed Buildings. **Applied Mechanics and Materials**, [*s. l.*], v. 861, p. 477–484, 2016.

GHERRI, B. **Assessment of Daylight Performance in Buildings. Methods and design strategies**. [*S. l.*]: WIT Press, 2015.

GIBSON, I.; ROSEN, D.; STUCKER, B. **Additive manufacturing technologies: 3D printing, rapid prototyping, and direct digital manufacturing**. 2. ed. [*S. l.*]: Springer, 2015.

GIOSTRA, S. *et al.* Use of 3D tessellation in curtain wall facades to improve visual comfort and energy production in buildings. *In*: , 2019. **IOP Conference Series: Earth and Environmental Science**. [*S. l.: s. n.*], 2019.

GOU, S. *et al.* Passive design optimization of newly-built residential buildings in Shanghai for improving indoor thermal comfort while reducing building energy demand. **Energy & Buildings**, [*s. l.*], v. 169, p. 484–506, 2018. DOI: https://doi.org/10.1016/j.enbuild.2017.09.095.

HOPKINS, O. **Architectural Styles: A Visual Guide**. [*S. l.*]: Laurence King Publishing Ltd, 2014.

HOSSEINI, S. *et al.* A morphological approach for the kinetic façade design process to improve visual and thermal comfort: Review. **Building and Environment**, [*s. l.*], v. 153, p. 186–204, 2019. DOI: https://doi.org/10.1016/j.buildenv.2019.02.040.

HOSSEINI, S. *et al.* Integrating interactive kinetic façade design with colored glass to improve daylight performance based on occupants' position. **Journal of Building Engineering**, [*s. l.*], v. 31, n. April, 2020.

HOSSEINI, S.; FADLI, F.; MOHAMMADI, M. Biomimetic kinetic shading facade inspired by tree morphology for improving occupant's daylight performance. **Journal of Daylighting**, [*s. l.*], v. 8, n. 1, p. 65–82, 2021.

HOSSEINI, S.; MOHAMMADI, M.; GUERRA-SANTIN, O. Interactive kinetic façade: Improving visual comfort based on dynamic daylight and occupant's positions by 2D and 3D shape changes. **Building and Environment**, [*s. l.*], v. 165, n. August, p.

106396, 2019. DOI: https://doi.org/10.1016/j.buildenv.2019.106396.

HUO, H. *et al.* Analysis and optimization of external Venetian blind shading for nearly zero-energy buildings in different climate regions of China. **Solar Energy**, [*s. l.*], v. 223, n. January, p. 54–71, 2021. DOI: https://doi.org/10.1016/j.solener.2021.05.046.

ISO. ISO 7730 - Ergonomics of the thermal environment - Analytical determination and interpretation of thermal comfort using calculation of the PMV and PPD indices and local thermal comfort criteria. [*s. l.*], p. 52, 2005.

JABI, W. *et al.* Enhancing parametric design through non-manifold topology. **Design Studies**, [*s. l.*], v. 52, p. 96–114, 2017. DOI: http://dx.doi.org/10.1016/j.destud.2017.04.003.

JAHANARA, A.; FIORAVANTI, A. **Kinetic Shading System as a Means for Optimizing Energy Load: A Parametric Approach to Optimize Daylight Performance for an Office Building in Rome**. [*S. l.: s. n.*], 2017.

JAMBO, A. S. **The effectiveness of enviro-materially actuated kinetic facades: Evaluating the thermal performance of thermo-bimetal shading component geometries**. 2017. 151 f. - the University of Southern California, [*s. l.*], 2017.

JAYATHISSA, P. *et al.* Optimizing building net energy demand with dynamic BIPV shading. **Applied Energy**, [*s. l.*], v. 202, p. 726–735, 2017. DOI: http://dx.doi.org/10.1016/j.apenergy.2017.05.083.

KALAY, Y. E. **Modeling Objects and Environments**. 1. ed. [*S. l.*]: John Wiley & Sons, 1989.

KEATING, S.; OXMAN, N. Robotic Immaterial Fabrication. *In*: BRAUMANN, J.; BRELL-ÇOKCAN, S. (org.). **Robotic Fabrication in Architecture, Art, and Design**. [*S. l.*]: Springer, 2013.

KIRIMTAT, A. *et al.* Multi-objective energy and daylight optimization of amorphous shading devices in buildings. **Solar Energy**, [*s. l.*], v. 185, p. 100–111, 2019. DOI: https://doi.org/10.1016/j.solener.2019.04.048.

KIRIMTAT, A. *et al.* Review of simulation modeling for shading devices in buildings. **Renewable and Sustainable Energy Reviews**, [*s. l.*], v. 53, p. 23–49, 2016. DOI: http://dx.doi.org/10.1016/j.rser.2015.08.020.

KITTLER, R. Luminance distribution characteristics of homogenous skies: a measurement and prediction strategy. **Lighting Research & Technology**, [*s. l.*], p. 183–188, 1985.

KOLAREVIC, B. **Architecture in the Digital Age: Design and Manufacturing**. [*S. l.*]: Taylor & Francis Group, 2005.

KOLAREVIC, B. Towards an architecture of change. *In*: KOLAREVIC, B.; PARLAC, V. (org.). **Exploring the architecture of change**. New York: Routledge, 2015. p. 305.

KOLOKOTRONI, M. *et al.* Energy & Buildings Cool roofs : High-tech, low-cost solution

for energy efficiency and thermal comfort in low rise low-income houses in high solar radiation countries. **Energy & Buildings**, [*s. l.*], v. 176, p. 58–70, 2018. DOI: https://doi.org/10.1016/j.enbuild.2018.07.005.

LAMBERTS, R.; DUTRA, L.; PEREIRA, F. O. R. **Eficiência Energética na Arquitetura**. [*S. l.: s. n.*], 2014.

LAU, K. K. *et al.* **Outdoor Thermal Comfort in Urban Environment: Assessments and Applications in Urban Planning and Design**. [*S. l.*]: Springer, 2022.

LE-THANH, L. *et al.* Optimal design of an Origami-inspired kinetic façade by balancing composite motion optimization for improving daylight performance and energy efficiency. **Energy**, [*s. l.*], v. 219, p. 119557, 2021. DOI: https://doi.org/10.1016/j.energy.2020.119557.

LECHNER, N.; ANDRASIK, P. **Heating, Cooling, Lighting: Sustainable Design Strategies Towards Net Zero Architecture**. 5. ed. Hoboken: John Wiley & Sons, 2021.

LEE, Y. *et al.* A Review on Outdoor Thermal Comfort Evaluation for Building Arrangement Parameters. *In*: ABAS, N. H.; SALAM, N. N. A.; SHAHIDAN, S. (org.). **Sustainable Construction and Building TechnologY**. 1. ed. [*S. l.*]: Penerbit UTHM, 2017. p. 1–14.

LEE, B. Heating, cooling, and lighting energy demand simulation analysis of kinetic shading devices with automatic dimming control for Asian Countries. **Sustainability (Switzerland)**, [*s. l.*], v. 11, n. 5, 2019.

LI, W. *et al.* Modeling urban building energy use: A review of modeling approaches and procedures. **Energy**, [*s. l.*], v. 141, p. 2445–2457, 2017. DOI: https://doi.org/10.1016/j.energy.2017.11.071.

LITTLEFAIR, P. J. A comparison of sky luminance models with measured data from Garston, United Kingdom. **Solar Energy**, [*s. l.*], v. 53, n. 4, p. 315–322, 1994.

LO VERSO, V. *et al.* Photobioreactors as a dynamic shading system conceived for an outdoor workspace of the state library of Queensland in Brisbane: Study of daylighting performances. **Journal of Daylighting**, [*s. l.*], v. 6, n. 2, p. 148–168, 2019.

LOONEN, R. **Approaches for Computational Performance Optimization of Innovative Adaptive Façade Concepts**. 2018. 190 f. - Eindhoven University of Technology, [*s. l.*], 2018. DOI: www.tue.nl/taverne.

LOONEN, R. C. *et al.* Climate adaptive building shells: State-of-the-art and future challenges. **Renewable and Sustainable Energy Reviews**, [*s. l.*], v. 25, p. 483–493, 2013.

LUCARELLI, C. C.; CARLO, J. C.; MARTÍNEZ, A. C. P. Parameterization and solar radiation simulation for optimization of a modular canopy. **PARC Pesquisa em Arquitetura e Construção**, [*s. l.*], v. 10, p. e019017, 2019.

LUCARELLI, C. D. C.; CARLO, J. C.; MARTÍNEZ, A. C. P. SIMULATION-BASED

OPTIMIZATION FOR AN ORIGAMI-SHAPED CANOPY. **PARC Pesquisa em Arquitetura e Construção**, [*s. l.*], v. 11, 2020.

LUCARELLI, C. C.; OLIVEIRA, M. M.; CARLO, J. C. Climate-active building enclosures: an integrative literature review. **PARC Pesquisa em Arquitetura e Construção**, [*s. l.*], v. 14, p. e023023, 2023.

MARDALJEVIC, J. **Daylight Simulation: Validation, Sky Models and Daylight Coefficient**. 2000. 330 f. - De Montfort University, [*s. l.*], 2000.

MEHRJARDI, N. K. **Turning key knowledge exchanges within the design process of transformable shading systems**. 2016. 442 f. - Virginia Polytechnic Institute and State University In, [*s. l.*], 2016.

MICHAEL, A.; GREGORIOU, S.; KALOGIROU, S. A. Environmental assessment of an integrated adaptive system for the improvement of indoor visual comfort of existing buildings. **Renewable Energy**, [*s. l.*], v. 115, p. 620–633, 2018. DOI: https://doi.org/10.1016/j.renene.2017.07.079.

NABIL, A.; MARDALJEVIC, J. Useful daylight illuminances: A replacement for daylight factors. **Energy and Buildings**, [*s. l.*], v. 38, n. 7, p. 905–913, 2006.

NEGROPONTE, N. **The Architecture Machine**. Cambridge: MIT Press, 1972.

NGUYEN, T. **Shape gramma-based adaptive building envelopes: Towards novel climate-responsive facade systems for sustainable architectural design in Vietnam**. 2019. 319 f. - University of Derby, [*s. l.*], 2019.

NGUYEN, A. T.; REITER, S.; RIGO, P. A review of simulation-based optimization methods applied to building performance analysis. **Applied Energy**, [*s. l.*], v. 113, p. 1043–1058, 2014. DOI: http://dx.doi.org/10.1016/j.apenergy.2013.08.061.

OLBINA, S.; BELIVEAU, Y. Developing a transparent shading device as a daylighting system. **Building Research & Information**, [*s. l.*], v. 37, n. 2, p. 148–163, 2009.

OLGYAY, V. **Design with climate: Bioclimatic approach to architectural regionalism**. Princeton: Princeton University Press, 2015.

OXMAN, R. Theory and design in the first digital age. **Design Studies**, [*s. l.*], v. 27, n. 3, p. 229–265, 2006.

OXMAN, R. Thinking difference: Theories and models of parametric design thinking. **Design Studies**, [*s. l.*], v. 52, p. 4–39, 2017. DOI: http://dx.doi.org/10.1016/j.destud.2017.06.001.

PAIO, A. *et al.* Prototyping Vitruvius, New Challenges: Digital Education, Research and Practice. **Nexus Network Journal**, [*s. l.*], v. 14, n. 3, p. 409–429, 2012.

PANYA, D. S.; KIM, T.; CHOO, S. A methodology of interactive motion facades design through parametric strategies. **Applied Sciences (Switzerland)**, [*s. l.*], v. 10, n. 4, 2020.

PARK, J. J. **Adaptive Biomimetic Façades: compound bio-inspired design strategy for multi-functional stadiums**. 2016. 407 f. - The University of Melbourne, [*s. l.*], 2016.

PARSONS, K. **Human thermal comfort**. Boca Raton: Taylor & Francis Group, 2020.

PAULE, B. *et al.* Electrochromic glazings: Dynamic simulation of both daylight and thermal performance. **Energy Procedia**, [*s. l.*], v. 122, n. January, p. 199–204, 2017.

PEREZ, R.; SEALS, R.; MICHALSKY, J. All-weather model for sky luminance distribution-Preliminary configuration and validation. **Solar Energy**, [*s. l.*], v. 50, n. 3, p. 235–245, 1993.

PESENTI, M.; MASERA, G.; FIORITO, F. Exploration of Adaptive Origami Shading Concepts through Integrated Dynamic Simulations. **Journal of Architectural Engineering**, [*s. l.*], v. 24, n. 4, p. 04018022, 2018.

PILECHIHA, P.; MAHDAVINEJAD, M.; BEIZAEE, A. Simulation Assisted Design Exploration to Evaluate View and Energy Performance of Window Shading. *In*: , 2020. **5th Building Simulation and Optimization Conference**. [*S. l.: s. n.*], 2020.

PINHEIRO, S. *et al.* MVD-based information exchange between BIM and building energy performance simulation. **Automation in Construction**, [*s. l.*], v. 90, n. November 2017, p. 91–103, 2018. DOI: https://doi.org/10.1016/j.autcon.2018.02.009.

RASHEED, M. *et al.* Performance Analysis of Vertical Fins as Shading Strategy in Commercial Buildings in Lahore ; Emphasizing on the Optimal Depth of Vertical Fin. **Technical Journal**, [*s. l.*], v. 26, n. 2, 2021.

REICHERT, S.; MENGES, A.; CORREA, D. Meteorosensitive architecture: Biomimetic building skins based on materially embedded and hygroscopically enabled responsiveness. **CAD Computer Aided Design**, [*s. l.*], v. 60, p. 50–69, 2015. DOI: http://dx.doi.org/10.1016/j.cad.2014.02.010.

REINHART, C. F. Daylight Performance Predictions. *In*: HENSEN, J. L. M.; LAMBERTS, R. (org.). **Building Performance Simulation for Design and Operation**. 2. ed. [*S. l.*]: Routledge, 2019. p. 793.

REINHART, C. F. **Daylighting Handbook II**. [*S. l.*]: Building Technology Press, 2018.

REINHART, C. F.; JAKUBIEC, J. A.; IBARRA, D. Definition of a reference office for standardized evaluations of dynamic façade and lighting technologies. *In*: , 2013, Chambéry. **12th Conference of International Building Performance Simulation Association**. Chambéry: [*s. n.*], 2013. p. 3645–3652.

REINHART, C. F.; MARDALJEVIC, J.; ROGERS, Z. Dynamic Daylight Performance Metrics for Sustainable Building Design. **LEUKOS: The Journal of the Illuminating Engineering Society of North America**, [*s. l.*], p. 37–41, 2013.

REINHART, C. F.; WIENOLD, J. The daylighting dashboard e A simulation-based design analysis for daylit spaces. **Building and Environment**, [*s. l.*], v. 46, n. 2, p. 386–396, 2011. DOI: http://dx.doi.org/10.1016/j.buildenv.2010.08.001.

REKI, M. **Exploring new forms through parametric patterns in responsive facades**. 2018. 105 f. - Gazi University, [*s. l.*], 2018.

ROMANO, R. *et al.* What is an adaptive façade? Analysis of recent terms and definitions from an international perspective. **Journal of Facade Design and Engineering**, [*s. l.*], v. 6, n. 3, p. 065–076, 2018.

SAYAD, B. *et al.* Enhanced outdoor thermal comfort through natural design technique: In-situ measurement and microclimate simulation. **Instrumentation Mesure Metrologie**, [*s. l.*], v. 20, n. 3, p. 131–136, 2021.

SCHIMIDT III, R.; AUSTIN, S. **Adaptable architecture: theory and practice**. 1. ed. [*S. l.*]: Routledge, 2016.

SCHUMACHER, M.; SCHAEFFER, O.; VOGT, M. **MOVE: Architecture in Motion - Dynamic Components and Elements**. [*S. l.*]: Birkhauser, 2012.

SCHUMACHER, M.; VOGT, M.; KRUMME, L. A. C. **New Move: Architecture in Motion - New Dynamic Components and Elements**. [*S. l.*]: Birkhauser, 2020.

SEO, D. Comparative analysis of all-sky luminous efficacy models based on calculated and measured solar radiation data of four worldwide cities. **International Journal of Photoenergy**, [*s. l.*], v. 2018, 2018.

SHEIKH, W.; ASGHAR, Q. Adaptive biomimetic facades: Enhancing energy efficiency of highly glazed buildings. **Frontiers of Architectural Research**, [*s. l.*], v. 8, n. 3, p. 319–331, 2019. DOI: https://doi.org/10.1016/j.foar.2019.06.001.

SHI, X.; TABLADA, A.; WANG, L. Influence of two motion types on solar transmittance and daylight performance of dynamic façades. **Solar Energy**, [*s. l.*], v. 201, n. May, p. 561–580, 2020.

SHI, X.; YANG, W. Performance-driven architectural design and optimization technique from a perspective of architects. **Automation in Construction**, [*s. l.*], v. 32, p. 125–135, 2013. DOI: http://dx.doi.org/10.1016/j.autcon.2013.01.015.

SIERRA, S. D. *et al.* kinematics, Actuation, and Sensing Architectures for Rehabilitation and Assistive Robotics. *In*: Interfacing Humans and Robots for Gait Assistance and Rehabilitation. Gewerbestrasse: Springer, 2022. p. 43–87.

SONG, Y. I. *et al.* A review of conventional passive cooling methods applicable to arid and warm climates considering economic cost and efficiency analysis in resource-based cities. **Energy Reports**, [*s. l.*], v. 7, p. 2784–2820, 2021. DOI: https://doi.org/10.1016/j.egyr.2021.04.056.

STAZI, F. **Thermal Inertia in Energy Efficient Building Envelopes**. [*S. l.*]: Butterworth-Heinemann, 2017.

TABADKANI, A. *et al.* Analysis of the impact of automatic shading control scenarios on occupant's comfort and energy load. **Applied Energy**, [*s. l.*], v. 294, n. January, p. 116904, 2021. DOI: https://doi.org/10.1016/j.apenergy.2021.116904.

TABADKANI, A. *et al.* Design approaches and typologies of adaptive facades: A review. **Automation in Construction**, [*s. l.*], v. 121, n. April 2020, p. 103450, 2021. DOI: https://doi.org/10.1016/j.autcon.2020.103450.

TABADKANI, A. *et al.* Innovative control approaches to assess energy implications of adaptive facades based on simulation using EnergyPlus. **Solar Energy**, [*s. l.*], v. 206, n. January, p. 256–268, 2020. DOI: https://doi.org/10.1016/j.solener.2020.05.087.

TABADKANI, A. *et al.* Integrated parametric design of adaptive facades for user's visual comfort. **Automation in Construction**, [*s. l.*], v. 106, n. May, p. 102857, 2019. DOI: https://doi.org/10.1016/j.autcon.2019.102857.

TABADKANI, A. *et al.* Integrated parametric design of adaptive facades for user's visual comfort. **Automation in Construction**, [*s. l.*], v. 106, n. June, p. 102857, 2019. DOI: https://doi.org/10.1016/j.autcon.2019.102857.

TABADKANI, A.; BANIHASHEMI, S.; HOSSEINI, M. Daylighting and visual comfort of oriental sun-responsive skins: A parametric analysis. Building Simulation, [s. l.], v. 11, n. 4, pp. 663–676, 2018.

TAVERES-CACHAT, E.; GOIA, F. Co-simulation and validation of the performance of a highly flexible parametric model of an external shading system. **Building and Environment**, [*s. l.*], v. 182, n. July, p. 107111, 2020. DOI: https://doi.org/10.1016/j.buildenv.2020.107111.

TERZIDIS, K. **Permutatuion Design: Buildings, Texts, and Contexts**. [*S. l.*]: Routledge, 2015.

TROTTER, A. P. Illumination: its Distribution and Measurement. **Nature**, [*s. l.*], v. 88, p. 72–73, 1911.

URIBE, D. *et al.* Impact of different control strategies of perforated curved louvers on the visual comfort and energy consumption of office buildings in different climates. **Solar Energy**, [*s. l.*], v. 190, n. January, p. 495–510, 2019. DOI: https://doi.org/10.1016/j.solener.2019.07.027.

VALITABAR, M. *et al.* Design optimum responsive façade based on visual comfort and energy performance. *In*: , 2018, Hong Kong. **3rd International Conference on Computer-Aided Architectural Design Research in Asia CAADRIA**. Hong Kong: [*s. n.*], 2018. p. 93–102.

VELASCO, R.; BRAKKE, A. P.; CHAVARRO, D. Dynamic façades, and computation: Towards an inclusive categorization of high-performance kinetic façade systems. *In*: , 2015. **Communications in Computer and Information Science**. [*S. l.: s. n.*], 2015. p. 172–191.

VLACHOKOSTAS, A.; MADAMOPOULOS, N. Daylight and thermal harvesting performance evaluation of a liquid-filled prismatic façade using the Radiance five-phase method and EnergyPlus. **Building and Environment**, [*s. l.*], v. 126, n. October, p. 396–409, 2017. DOI: https://doi.org/10.1016/j.buildenv.2017.10.017.

WANG, C.; MORATA, A. **Adaptive Facade, the active connection between indoor**

and outdoor: Visual and Thermal evaluation of an adaptive facade in the urban context of Copenhagen. 2019. 84 f. - Lund University, [*s. l.*], 2019.

WIENOLD, J.; CHRISTOFFERSEN, J. Evaluation methods, and development of a new glare prediction model for daylight environments with the use of CCD cameras. **Energy and Buildings**, [*s. l.*], v. 38, n. 7, p. 743–757, 2006.

WILCOX, S.; MARION, W. **Users Manual for TMY3 Data Sets**. [*S. l.: s. n.*], 2008.

YANG, C. **The Intelligent Control Strategy of Kinetic Façades for Daylight and Energy Performance**. 2020. 213 f. - University of Southern California, [*s. l.*], 2020.

YI, H. *et al.* 3D-printed attachable kinetic shading device with alternate actuation: Use of shape-memory alloy (SMA) for climate-adaptive responsive architecture. **Automation in Construction**, [*s. l.*], v. 114, n. July 2019, p. 103151, 2020. DOI: https://doi.org/10.1016/j.autcon.2020.103151.

YI, H. *et al.* Rapid simulation of optimally responsive façade during schematic design phases: Use of a new hybrid metaheuristic algorithm. **Sustainability (Switzerland)**, [*s. l.*], v. 11, n. 9, 2019.

YI, H.; KIM, Y. Self-shaping building skin: Comparative environmental performance investigation of shape-memory-alloy (SMA) response and artificial intelligence (AI) kinetic control. **Journal of Building Engineering**, [*s. l.*], v. 35, n. December, p. 102113, 2021. DOI: https://doi.org/10.1016/j.jobe.2020.102113.

YI, Y.; SHARSTON, R.; BARAKAT, D. Auxetic structures and advanced daylight control systems. **Journal of Facade Design and Engineering**, [*s. l.*], v. 7, n. 1, p. 63–74, 2019.

YOON, J. SMP Prototype Design and Fabrication for Thermo-responsive Façade Elements. **Journal of Facade Design and Engineering**, [*s. l.*], v. 7, n. 1, p. 41–61, 2019.

YOON, J.; BAE, S. Performance evaluation and design of thermo-responsive SMP shading prototypes. **Sustainability (Switzerland)**, [*s. l.*], v. 12, n. 11, 2020.

ZHAO, Q.; LIAN, Z.; LAI, D. Thermal comfort models and their developments: A review. **Energy and Built Environment**, [*s. l.*], v. 2, n. 1, p. 21–33, 2021. DOI: https://doi.org/10.1016/j.enbenv.2020.05.007.

ZUK, W.; CLARK, R. **kinetic architecture**. 1. ed. [*S. l.*]: Van Nostrand Reinhold, 1970.

CHAPTER II – Climate-Active Building Enclosures: An Integrative Literature Review

Paper Doi: [https://doi.org/10.20396/parc.v14i00.8671581]

Abstract

The building energy demand and anthropogenic greenhouse gas emissions have risen since the preindustrial period, reaching the highest levels. Brazil is the eighth largest consumer of primary energy globally, with buildings accounting for 51.2% of the total electric energy consumption. In this sense, the building enclosure has substantial potential and the lowest cost for reducing energy expenditure. The dynamicity of environmental factors allows for many design approaches, and since the user comfort analysis evolved, time-varying building skin configurations emerged. When coupled with computational design, the building's skins no longer must compromise to one stationary condition that is never optimal to any particular condition. These climate-active envelopes need a seemingly conveyed characterization or a straightforward design process as a relatively new technique. We aimed to differentiate climate-active building typologies and gather the latest compositions and performance assessment metrics, rendering an integrative literature review, state-of-the-art, and bibliometric analysis. As the main results, we assembled tabular data on 100 research pieces considering various study methodologies, climate-active typologies, movement categories, actuation styles, simulation engines, and performance criteria, demonstrating that most studies evaluated facade typologies, concerned temperate climates and adopted simple, binary movement characterizations. Furthermore, the design process for active building enclosures needs to be clearer and well-structured, and the available computational tools still need improvement.

Keywords: *climate-active. Bibliometric analysis. state-of-the-art. building performance.*

1. Introduction

Buildings are among the largest energy consumers worldwide, with up to 40% of the total energy requirement and 36% of carbon emissions (Zhou; Nazi; Wang; Roskilly, 2019). Despite the growth of emerging economies, developing countries are still responsible for an unbalanced energy consumption per capita (Clarke *et al.*, 2018). Besides, the extensive implementation of building equipment for heating, ventilation, and air-conditioning facilitates reaching user comfort requirements indoors, overlooking building passive design strategies. As a result, buildings assume a conspicuous energy expense, and the conventional building enclosure does not function efficiently enough to handle the matter. Therefore, roofs, walls, and windows perform separately (Yang, 2020).

Postmodernist[7] climate-concerned architecture shifted the primary function of the building envelope into a many-criteria mediator that encompasses tangible (e.g., air temperature, radiation, etc.) or intangible (e.g., cultural and social) relationships. This connection with the outdoors plays a considerable role in indoor performance, presenting the building enclosure with significant potential and the lowest cost among building operations for reducing energy demand and carbon emissions (Delgarm; Sajardi; Kowsary; Delgarm, 2016).

Passive design approaches, such as solar shading, daylighting, natural ventilation admittance, and thermal mass, are essential enclosure-related tactics for boosting comfort. However, passive strategies alone are counterproductive to the latest concept of building enclosure: a tectonic, skin-like feature with environmental and aesthetical relationships (Oxman, 2006, 2017; Schumacher; Vogt; Krumme, 2020).

As the environmental performance metrics evolved, time-changing envelopes became a viable strategy for enhancing visual and thermal comfort (Hosseini *et al.*, 2019a). Given seasonal and daily changes in solar positions and sky conditions, climate-active envelopes[8] are highly effective for managing daylight and solar radiation

---

[7] Postmodern architecture emerged in the 1960s in response to the International Style, encompassing High-Tech, Contemporary, Sustainable, etc. architecture (Hopkins, 2014).

[8] We adopt climate-active envelopes as a broad combination of several other classifications (kinetic, intelligent, responsive, biomimetic, and smart typologies). We accept them as passive-active solutions considering they operate either statically (optimally fixed shading devices) or kinetically (moving devices).

based on indoor requirements (Kirimtat; Koyunbaba; Chatzikonstantinoi; Sariyildiz, 2016). Coupled with computational design, they no longer have to compromise to one static state that performs acceptably under a wide range of situations but is never optimal.

Climate-active envelopes need a clear definition in the architectural research field (Attia *et al.*, 2018). Researchers address only a few geometric and motion explorations on the enclosure level because active systems' design and performance evaluation are complex, and existing performance assessment tools are insufficient (Kolarevic, 2015; Loonen, 2018). We aim to investigate literature-found climate-active enclosures, documenting the methodologies, study's location and weather classification, active typology and mechanical movement, modeling, simulation, optimization software, and simulation objectives and metrics to outline architectural responsiveness.

Systematic, narrative, and integrative reviews on the topic are scarce and only present a global perspective on responsiveness, failing to describe, organize, and scrutinize computational simulation, experiments, mathematical calculation, and case studies (Alkhati; Lemarchand Norton; O'Sullivan, 2021; Hosseini *et al.*, 2019a; Tabadkan; Valinejad Shoubi; Soflaei; Banihashemi, 2021). They provide a base for future studies but do not clearly define methodological procedures, leading researchers to misinterpret motion categories due to background-lacking research pieces.

Hence, we strive to answer the following questions: How to distinguish climate-active building enclosures? What are the latest envelope configurations, environmental assessment methodologies, and performance metrics? What are the next steps in building performance simulations for enclosures? Consequently, this study assembles the most applied climate-active envelope terminologies and design strategies to distinguish climate-active skins. We also address the advances in climate-active building envelope research, tabulating literature-missing data for evaluating and improving building performance.

2. Theoretical frameworks

This section clarifies unfamiliar terms, presenting geometric, mechanical, and control approaches for various climate-active typologies, i.e., kinetic, intelligent,

responsive, biomimetic, and smart. We focus on large-scale kinetic transformations (i.e., changing function, form, and size) and small-scale, material-related deformations that generate motion.

2.1. Building envelope overview

The physical environment operates upon multiple parameters (e.g., light admission and blockage, energy gain and loss, etc.) with a complex relationship that the human body absorbs or counteracts (Tabadkani; Roetzel; Xian; Tsangrassoulis, 2021). Humans seek a balance between energy investment and environmental adjusting. The comfort zone is the successful balance between both (Olgyay, 2015). A shelter helps meet these comfort requirements by adjusting the indoor space to optimal conditions by filtering environmental factors.

20th-century architecture was a product of the Industrial Revolution and ever-changing technology (Benevolo, 2001). The new engineering methods from the 19th century striped buildings from passive thermal comfort techniques and electromechanical ventilation improvement compelled architects to pay more attention to their role as a buffer of comfort and energy (Reki, 2018). Consequently, energy consumption increased, forcing 21st-century postmodernist architects to reimplement passive strategies and explore innovative design solutions for adequate human comfort, leading to a revival of kinetic motion.

2.2. Active envelope approaches

Theoretical interest in kinetic architecture arose with Futurism, Constructivism, and Expressionism in the first third of the 20th century. In the 1960s, Megastructure architecture planned to exclude static Functionalism, embracing change and motion through society's evolving needs (Schimidt III; Austin, 2016). In the 1970s, Zuk and Clarke (1970) classified kinetic structures by their application, separating them into static, kinetically controlled, self-erecting, reversible, incremental, deformable, mobile, and disposable. Later, Nicholas Negroponte coined the concept of a responsive environment utilizing computation (Negroponte, 1973).

Still, building components that could react to environmental conditions would only appear later in the 20th century. Information technology and data retrieval improved, and artificial intelligence facilitated spatial change without human resources. The

developments in generative, parametric, and algorithmic thinking supported the surge of kinetic systems, helping to comprehend and conceive responsive systems (Schumacher, 2016).

Nowadays, several interchangeable terms depict buildings with time-varying façade characteristics (Loonen, 2018). The most common variations include adaptive (Lo Verso *et al.*, 2019), kinetic (Shi; Tablada; Wang, 2020), responsive (Hosseini; Mohammadi; Guerra-Santin, 2019; Yang, 2020), intelligent (Yi *et al.*, 2020), biomimetic (Augustin, 2018; Sheikh; Asghar, 2019), and smart (Yoon, 2019).

We employ climate-active enclosures as a compilation, acknowledging all the classifications as smaller groups. We define climate-active envelopes as self-adjusting surfaces that contain systems with mechanical, moving, or advanced electronics or materials with varying intrinsic characteristics. These envelopes can change according to indoor and outdoor parameters, building performance criteria, weather sensing and prediction, environmental stimuli, user needs and interactions, and so on.

2.3. Architectural components – geometry and motion

The first step of designing active envelopes is selecting their geometrical form and defining their primary movements (Ferschin; Di Angelo; Brunner, 2015). Moloney (2011) developed the basic kinetic patterns, which depict single movements and variations according to anchor points (Figure 1). The primary motion patterns were translation, rotation, and scaling. Other typologies could emerge from these simple patterns based on degrees of freedom, geometric restrictions, and coordinate axes. Also, combining primary patterns can generate composite configurations such as folding and rolling.

Kinetic, responsive, intelligent, and biomimetic approaches (following sections) often deliver rigid or mechanic macro-level adaptation. Conversely, a microscale strategy considers material molecular structure and deformations. Smart and seldom biomimetic systems employ microscale transformation.

2.3.1. Kinetic typology

The kinetic architecture comprises technological systems in constant transformation driven by variable stimuli over a stipulated interval (Nguyen, 2019). These systems change building environmental performance according to outdoor

conditions rather than indoor requirements. Other names for kinetic devices are deployable, retractable (Heinzelmann, 2018), dynamic (Schielke, 2019), convertible (Wang; Perez Morata, 2019), transformable (Matheou; Couvelas; Phocas, 2020), and shape-shifting (Kolarevic, 2015).

Figure 1: Geometric motion classification - spatial movement vocabulary.

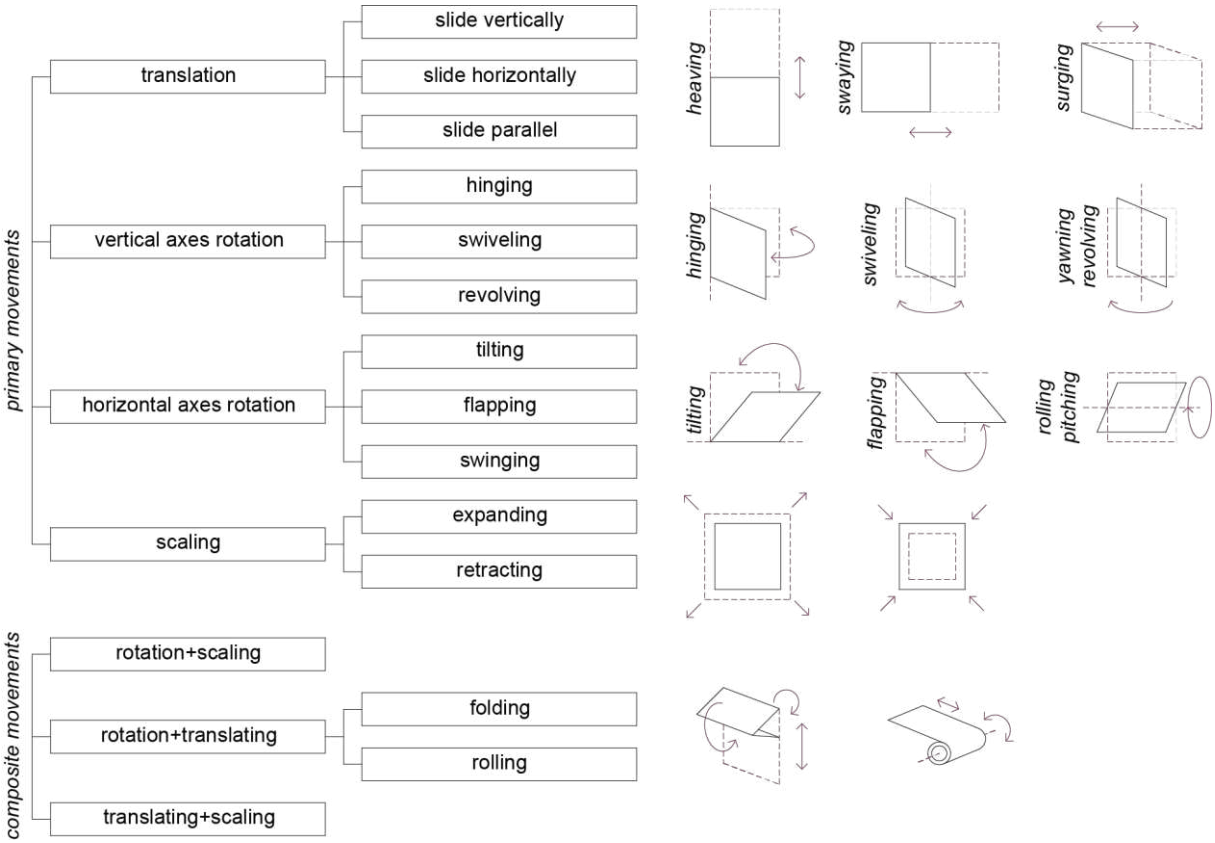

Source: The Authors (2023), adapted from Moloney (2011).

Kinetic systems can be either conventional or complex. A conventional device displays one moveable element, a single motion pattern, or several identical components (such as Venetian blinds). Complex systems present more innovative forms with composite movement patterns.

2.3.2. Intelligent typology

The term ‘Intelligent’ gained widespread in the 1980s, accompanied by ‘smart architecture’ indiscriminately referring to capabilities of materials, structures, and buildings. Nowadays, intelligence conveys functionality for building structures that understand indoor and outdoor conditions and selects the most convenient operation for achieving a comfortable environment based on predictive models and minimal user intervention. Intelligent envelopes comprise perception, logic, and action, applying sensors and computational protocols to re-balance the indoor space without manual

interference. Unlike kinetic models, a smart system can use future weather fluctuation to learn from occupants' reactions (Knaack *et al.*, 2014).

For instance, Böke, Knaack, and Hemmerling (2020) developed a cyber-physical intelligent skin with various modules for selecting solar shading, natural and mechanical ventilation, and heating and cooling, creating a system that allows all processes to intercommunicate.

2.3.3. Responsive typology

Responsiveness indicates that building enclosures can adapt to weather oscillations instead of shutting the environment out. These envelopes benefit from the natural energy sinks and sources in their surroundings, improving functional building requirements (Loonen, 2018).

The first applications of contemporary responsiveness emerged in the early 21st century (Knaack *et al.*, 2014), complementing the broader and misleading intelligent definition from the 80s. For Bui *et al*. (2020) and Loonen (2018), responsiveness means changing properties over time to decrease energy consumption. Other terms are adaptive (Lee; Cho; Jo, 2021), interactive (Panya; Kim; Choo, 2020), and interchangeable.

We adopt the latest definition of responsiveness as a climate-active typology able to "deliver multi-objective comfort [...] under uncertain environmental conditions by changing its physical characteristics [to match people's needs] within a short-timing scale" (Tabadkani *et al.*, 2021, p.2).

Responsive envelopes are an evolution of kinetic and are not so different from intelligent systems. Like the former, they employ sensor networks, controllers, and actuators but respond to an action rather than moving according to programming. As the latter, responsive systems include real-time perception, building automation, and user-oriented operations. However, they can learn to self-adjust by progressively instructing the building and users, offering the manual override possibility, which is minimal in intelligent systems.

In responsive designs, the outdoors influence, reprogram, and reconfigure the building envelope. "Rather than the designer predetermining appropriate responses to

user inputs, the system measures reactions to its outputs and continually modifies its actions according to these responses" (Velikov; Thün, 2017, p.70).

2.3.4. Biomimetic typology

The biomimetic design incorporates biological compositions and processes into technological applications. A direct biomimetic approach copies the observed functionality for responding to changes in environmental situations. In contrast, the indirect technique abstracts the biological principle, loosely basing the result on the natural aesthetic (Pawlin, 2019; Romano *et al.*, 2018). Plant structure, growth, and development contemplate biomimetic envelopes as they perform similarly, responding to daylight (phototropism), radiation (heliotropism), and humidity.

Unlike the previous typologies, biomimetic systems can apply macro (mechanical movement) or microscale adaptation. They respond to environmental conditions within certain thresholds rather than complying with a parameter-based movement (Reichert; Menges; Correa, 2015).

2.3.5. Smart typology

Smart typologies correlate to kinetic, intelligent, and responsive classifications, as their main concept is adapting to external stimuli. The terms intelligent and smart were interchangeable in the 1980s. Their biggest difference is that intelligence relates to computation and automation, whereas smart features result from material intrinsic properties. Smart typologies can appear in any other active classification, enhancing mechanical actuation with material-imbued qualities.

For instance, an external force or energy supply can deform or modify their initial configuration; a subsequent exposure to an environmental agent will return the material to its primary shape. Their activity is typically binary and limited but is self-powering and self-actuating (Heinzelmann, 2018). Examples of smart materials include stimulus-responsive materials (SRMs), phase change materials (PCMs), color-changing paints, and building-integrated photovoltaics (BIPV).

3. Materials and methods

This section details the methodology for executing an Integrative Literature Review (ILR), electing the state-of-the-art, and presenting a bibliometric analysis. We cover

multi-disciplinary analyses of climate activity regarding study procedures, research locations, design solutions, active typology, movement characterization, and building performance simulation software and metrics.

An ILR is an extensive investigation that contributes to deepening discussions on research methods and results, helping future studies on a distinct issue. It “reviews, critiques, and synthesizes representative literature on a topic [...] [to generate] new frameworks and perspectives [...]” (Moher *et al.*, 2009, p.1). They normally apply to “dynamic topics that experience rapid growth in the literature” (Moher *et al.*, 2009, p.1), especially because these are relatively unexplored and have not yet undergone an exhaustive examination.

ILRs incorporate different methodologies (i.e., literature review, mathematical calculations, physical experiments, etc.) into a single research object, allowing a combination of theoretical and empirical applications. Bibliometric analysis is a means for quantitatively interpreting a considerable volume of scientific information, graphically depicting the latest research breakthroughs and developments. Also, we portray state-of-the-art as the congregation of the most up-to-date research on a topic to uncover new research subjects, methods, and sub-topics.

3.1. Integrative literature review stages

For the ILR, we applied the Preferred Reporting Items for Systematic Reviews and Meta-Analyses (PRISMA) workflow and the State-of-the-art through Systematic Review software (StArt v. 3.4) (Fabbri *et al.*, 2016; Moher *et al.*, 2009). The StArt Tool separates the research process similarly to the PRISMA methodology, making both approaches compatible (Figure 2).

Figure 2: PRISMA and StArt methodological steps.

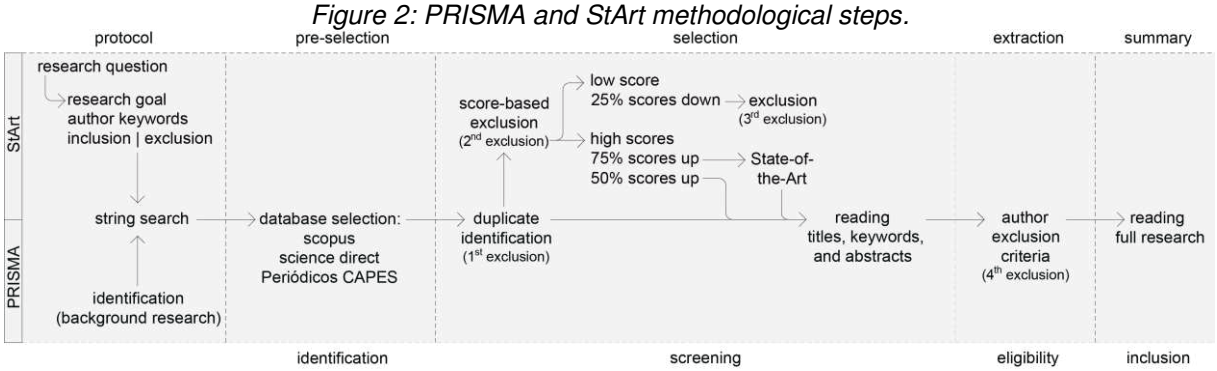

Source: The Authors (2023).

StArt helps organize data, filter duplicate productions, score publications according to user-selected keywords (title, abstract, and keywords), and identify recurrent authors and topics. It also outputs BibTex and RIS files (research information and plain bibliography style), later utilized in the bibliometric analysis as input for VOSviewer 1.6.1.7's authors and co-authors network and keyword analysis.

Our review process comprises five stages (Figure 2): protocol (StArt exclusive), pre-selection or identification, selection or screening, extraction or eligibility, and summary or inclusion. In the first stage of the StArt/PRISMA workflow, we state our "research goal, research questions, [and] search and selection strategies […]" (Moher *et al.*, 2009, p.2). Our ILR questions are: What are the latest envelope configurations and environmental assessment methodologies and metrics? What are the next steps in building performance simulation for active enclosures?

This research aims to survey and discuss the characteristics, potentials, restrictions, approaches, and main results of state-of-the-art research on kinetic, intelligent, responsive, biomimetic, and smart applications. We considered papers, conference proceedings, dissertations, and thesis published in English and Portuguese from 2016 to 2022. We selected Scopus, Science Direct, and *Periódicos CAPES* as databases. We designated a set of synonyms, inclusions, and exclusions for searching criteria, using the most general terms in all string search attempts (Chart 1): buildings or enclosure typologies.

Chart 1: Search strings and results for the protocol and pre-selection stages.

Language	Database	Date	Search String	n° of pieces
en	Scopus	07/16/2022	(TITLE-ABS-KEY("awning" OR "build* envelope" OR "build* enclosure" OR "canopy" OR "façade" OR "roof*" OR "shade*") AND TITLE-ABS-KEY ("active" OR "adaptive" OR "automatic" OR "biomimetic" OR "dynamic" OR "interactive" OR "kinetic" OR "responsive") AND TITLE-ABS-KEY ("daylight*" OR "light*" OR "energy" OR "glare" OR "illuminance" OR "radiation" OR "thermal comfort") AND TITLE-ABS-KEY ("generative" OR "algorithm*" OR "optimize*" OR "parameter*" OR "simulation" OR "fabrication" OR "manufacture*")) AND PUBYEAR>2015	709
en	Science Direct	07/16/2022	("build* enclosure" OR "façade" OR "shade*") AND ("kinetic" OR "responsive" OR "intelligent") AND ("thermal comfort" OR "optimize*" OR "simulation") AND PUBYEAR>2015	249
en	*Periódicos CAPES*	07/18/2022		152
pt	*Periódicos CAPES*	07/19/2022	*("edifica*" OU "fachada" OU "sombra*) E ("cinético" OU "responsivo" OU "inteligente") E ("conforto térmico" OU "otimiza*" OU "simulação") E ANO>2015*	10
Total				1120

Source: The Authors (2023).

Then, we added performance-related terms, such as simulation, parameterization, optimization, and manufacturing, or envelope-related terms, such as façade, canopy, roofing, etc. Afterward, we selected adjectives such as dynamic, active, kinetic,

movable, responsive, interactive, and intelligent (Tabadkani *et al.*, 2021). Database search compositions differ, and therefore, we adjusted the strings accordingly. The string search incorporated terms within the same keyword category using the Boolean operator OR. The operator AND appeared between different keyword categories (Chart 1). We applied the Portuguese version of all the keywords using the same Boolean operators. Chart 1 also presents the number of research pieces found for each database.

The protocol stage in StArt has an embedded feature for scoring publications according to author-selected keywords. If the designated keyword appears on the collected publication title, StArt grants five points; if the word appears in the keyword section, three points; if it appears on the abstract, StArt assigns two points. All keywords appear in the search strings in Chart 1.

The next step is pre-selection (PRISMA identification) (item 1 in Table 1), in which the researcher loads the bibliographic information (publication title, authors, keywords, and abstract) into the StArt Tool. We collected 1120 research pieces based solely on the string search inclusion/exclusion criteria. Removing the duplicated files also occurred during the pre-selection stage. As seen in Table 1, item 2, we excluded 55 occurrences.

Table 1: Pre-selection, selection, and extraction stages.

		(1)	(2)	(3)	(4)	(5)	(6)	(7)
language	**database**	**pre-selection stage**	**duplicated**	**selection stage**	**rejected researches**	**extraction stage**	**rejected researches**	**total research pieces**
en	Scopus	709	12	697	601	96	53	40
en	Science Direct	229	25	204	171	33	18	15
en	*Periódicos CAPES*	172	18	154	25	129	85	44
pt	*Periódicos CAPES*	10	0	10	9	1	0	1
Total		1120	55	1065	706	259	126	100

Source: The Authors (2023).

The following stage is the selection (screening) (item 3 in Table 1), in which we rejected papers based on StArt scoring and author-defined criteria. We assessed all 1065 studies through titles, keywords, and abstracts, eliminating any irregular occurrence or duplicated pieces (not accounted for by StArt). For the selection, we adopted four exclusion criteria: (i) research has a low StArt score; (ii) the study is not available; (iii) the study is a peer-reviewed publication; (iv) the study covers only prescriptive design solutions (passive or analog strategies with no active motion).

Scoring in StArt grants five, three, or two points for each author-selected keyword appearance. The highest publication score in this research was 224. We consider any score below 25% (56 points) ineligible, as most did not cover climate adaptiveness. As seen in Table 1, we rejected 706 papers.

We read all 259 papers for the extraction (eligibility) stage (item 5 in Table 1) and removed further passive technologies that did not convey motion. We also rejected studies with no building performance evaluation and others not complying with the inclusion/exclusion criteria established in the screening phase. We separated our findings into two datasets (Appendix II and III) (Lucarelli; Oliveira; Carlo, 2023). Dataset 1 (Appendix II) (Lucarelli; Oliveira; Carlo, 2023) presents all 23 scores above 112 StArt points (50% of the highest score, 224) and within the last three years (2019, 2020, and 2021, since 2022 returned no papers) and composes the state-of-the-art. Among these 23 studies, we addressed and further scrutinized the most promising investigations.

Our qualitative selection concerns methodology complexity, combined research methods, novel approaches, distinct geometric compositions, and interesting results. Although we did not discuss the remaining 77 studies, they are listed in Dataset 2 (Appendix III) (Lucarelli; Oliveira; Carlo, 2023). Therefore, both datasets present each study with its methodology, location, weather classification, active typology, movement classification, modeling suite, simulation software, optimization motor, and StArt score based on our keyword selection.

4. Results

With the highest StArt score (224) (Appendix II) (Lucarelli; Oliveira; Carlo, 2023), Hosseini, Mohammadi, and Guerra-Santin (2019b) presented quali-quantitative research on daylight systems. Using Google Scholar and Scopus as academic research databases, the authors offered a brief literature review on light redirecting systems (from 1974 to 2017). As the highest-ranked research based on StArt scoring, their study is a complete composition that combines literature review and building performance simulation, addressing literature gaps, and adopting the most up-to-date software and performance metrics. However, the authors presented anidolic components, redirecting mirrors, diamond-shaped domes, perforated metal sheets, etc. as innovative static systems. Even though these strategies provide sunlight

redirection, they only present technological innovation when coupled with computational methods for shape prediction, optimization, simulation, motion, etc.

Furthermore, Hosseini, Mohammadi, and Guerra-Santin (2019b) referred to kinetic systems as dynamic, encompassing tracking systems, PCMs, and other dynamic configurations. Tracking systems would better describe intelligent or responsive architecture (depending on user-oriented operations), and PCMs would better fit the smart category. The authors also provided various geometric classifications (i.e., flapping, folding, translating, expanding, and extracting) but failed to clarify the primary motion types and composite arrangements. Regardless, they presented interesting tabular data on light redirecting configurations, rightly distinguishing the kinetic system typology and simulation objective. They also pointed out that daylight control strategies interact with sun radiation, interior space requirements, and occupant position and demands.

Hosseini, Mohammadi, and Guerra-Santin (2019b) developed a parametric algorithm for two and three-dimensional shape-changing façades to assess visual comfort and field of view in response to the sun's position. The authors discovered that although both configurations present significant potential for meeting visual comfort requirements, the three-dimensional façades deliver better useful daylight illuminance levels.

Although thermal metrics did not appear in their study, the authors affirmed that the façade could also prevent thermal discomfort, decreasing more than 98% solar heat gain compared to the base case. They concluded the study by declaring that the next step in the climate-active façade assessment would be applying the simulation logic to a real kinetic device. However, their three-dimensional façade presented scaling and transforming motion that did not translate to real-world materialization constraints. The authors might rework the selected geometry, utilizing rotating and translating motion for a similar geometric approach.

Yang (2020) applied a systematic approach to daylight evaluation using intelligent façades and skylight systems. Yang (2020) was the first study in this ILR that involved top lighting strategies. We only found four other investigations, emphasizing the need for other active top lighting applications. He simulated a cuboid (7 mx7 m) and shoebox model (6mx8m) using a parametric workflow for evaluating indoor illuminance through

useful daylight illuminance, glare through daylight glare probability, and solar heat gain, similar to Hosseini, Mohammadi, and Guerra-Santin (2019b).

The simulations run for June 21st, September 21st, and December 21st, representing the northern hemisphere's hot, cool, and cold seasons. Adopting three or four representative days is typical in several other investigations in our ILR. The small representativity of simulation days is normally due to computational expense. An appropriate evaluation of indoor daylight and thermal performance should include complete annual indices, which is not feasible using the available simulation tools. Despite the few simulation days, we comprehend Yang's (2020) study as a noteworthy takeoff on building performance simulation and active approaches. Based on our ILR, the author could have proposed optimization states for various days, interpolating hour-specific simulation results with pre-determined geometric conditions. Besides, the control process only assessed environmental constraints, not involving the occupant's feedback.

Shi, Tablada, and Wang (2020) investigated the influence of two motion typologies on building performance simulation for active façades, evaluating energy expenditure and daylight. In this ILR, they are the first authors to address energy expenditure and human comfort parameters. Their research comprised modeling, simulation, and analysis within a single procedure. The authors applied the Rhino3D+Grasshopper suite, creating a fan-like skin. We consider the object an innovative approach to geometrical characterization since it encompasses various motion axes, creating other classifications such as scaling, expanding, and retracting within material constraints.

They adopted a theoretical office space with a typical open floorplan instead of a cuboid or shoebox model. They applied daylight autonomy and useful daylight illuminance as visual comfort calculation indexes. They evaluated three simulation models (base case, dynamic folding motion, and dynamic rotating motion) for four days (March, June, September, and December 22nd) and three hours (9 am, noon, and 3 pm). They employed the hourly energy consumption in Wh/m^2 using Honeybee for energy examination.

Daylight autonomy and useful daylight illuminance were typical visual metrics improved with active applications, rendering static envelopes inefficient in all investigations with stationary base cases. However, Shi, Tablada, and Wang's (2020)

simulation results showed that not all façade configurations positively affect daylight performance due to the various parametric combinations.

Therefore, all studies covered some environmental analysis tools (experiment, simulation, case study, etc.). However, we selected Hosseini *et al.'s* (2019a) research as an example of a literature review on various approaches to active design processes. Likewise, we also point to Tabadkani, Roetzel, Xian, and Tsangrassoulis (2021) paper as a state-of-the-art example of building performance classification for various active systems, even though their study ranked 23rd.

Hosseini *et al.'s* (2019a) study covered six complementary subjects: kinetic systems, biomimicry, building geometry, energy efficiency, comfort conditions, and parametric design thinking. After the systematic research, the authors concluded that, until 2019, studies for proposing kinetic façades were relatively rare, principally when coupled with visual requirements. However, we found 72 research pieces analyzing, simulating, or proposing active shading systems; among those, 43 are kinetic (Heinzelmann, 2018; Nguyen, 2019; Tabadkani; Banihashemi; Hosseini, 2018), and 60 concern visual analysis (Elkhatieb, 2016; Yi; Sharston; Barakat, 2019). Hosseini *et al*. (2019a) also stated that generative and parametric studies could help respond to climate fluctuations with high adaptability and create a framework for designing active façades. Nonetheless, they did not consider façade categories, only addressing biomimicry and kinetics, later revised in Tabadkani *et al.'s* (2021) and Alkhatib *et al.'s* (2021) research. Likewise, the authors did not acknowledge dynamic daylight measures (e.g., daylight autonomy, spatial daylight autonomy, useful daylight illuminance, etc.) or adaptive comfort strategies.

Yi, Sharston, and Barakat (2019) investigated the effects of auxetic shading systems with varying shapes for daylight and glare. In this ILR, we consider their approximation very innovative, applying an interpretation of Iranian patterns to a kinetic structure. Even though pattern inspiration is a common approach for design, they developed an interesting geometry that applies rotation and translation, causing scaling transformation. We only consider translational, rotational, and scaling movement as the base geometry modifications because the transformation is mechanical, not intrinsic; their study is the first to apply all three basic movements. The authors also developed an equation to find the number of vertices according to the façade angulation, facilitating the simulation process. Yi, Sharston, and Barakat (2019)

stated that the geometry responds to varying outdoor and sky conditions. We consider the structure kinetic since it did not involve any sensors and only relied on simulation data.

Tabadkani *et al.* (2019) developed a comprehensive literature review to create an origami-based active system using three numerical timing patterns. As we commended Yi, Sharston, and Barakat's (2019) research, we also acknowledge Tabadkani *et al.* (2019) for their approach to digital modeling.

The authors used ‘adaptive’ to signify a “potential to react or benefit from external climatic conditions to meet occupant comfort and well-being requirements” (Tabadkani *et al.*, 2021, p. 3). Our study classifies their approach as responsive since the design reacted to real-time weather conditions and assessed user needs. We also note that the authors would later rectify the proposed adaptive category, establishing a theoretical background for each active typology (Tabadkani *et al.*, 2021). They aimed to design a modular hexagonal responsive origami-inspired shading design, highly integrated with the dynamic building system. Since origami is a folding-based technique, the geometry showed a composite movement (rotation + translation). The authors created 1800 design examples in the modeling stage based on several variables, including rotation, indoor view, and transmittance properties.

To evaluate daylight and glare, Tabadkani *et al.* (2019) ran useful daylight illuminance, daylight glare index, and daylight glare probability simulations for each building skin configuration on March, June, September, and December 21st. They considered four days instead of three (which all authors have done until now). For daylight metrics, both equinoctial days would present comparable results. Unlike the other studies, they applied other simulation parameters such as glazing ratio, task area height, space width, length and height, wall, ceiling, floor reflectance, etc. The authors selected proper daylight illuminance maximization as optimization criteria, maintaining daylight glare probability below the perceptive range. Compared to Yang (2020), they did not prioritize glare over illuminance values.

Yi and Kim (2021) used smart materials to study a self-shaping building skin. Even though they presented their study as a first approximation to kinetic motion using these materials, other studies have already experimented with smart actuation and even employed digital manufacturing techniques (Yoon, 2019, 2021; Yoon; Bae, 2020). However, as the previous authors did, they evaluated shape-memory alloy applications

instead of shape-memory polymers. They investigated the controllability of shape memory alloys in building performance applications, reverting the scope of Yoon's (2019) research that evaluated the benefits of shape memory polymers instead of managing indoor conditions through controlled transformations.

Yi and Kim (2021) are the first authors to couple simulation, materialization, and environmental survey techniques in our state-of-the-art. Although Yoon (2019) applied prototyping techniques and assessed materialization parameters, Yi and Kim (2021) assembled physical thermal and daylight data to validate their simulation. They created two 1:20 building models: one with a motor-controlled shading and the other with an actuated shading as a test case, demonstrating that thermo-mechanical shape memory alloy applications could achieve comparable results to kinetically-actuated devices.

4.1. Further research pieces on active envelopes

All 100 research pieces in this ILR are essential for developing up-to-date research on active building envelopes (Appendix III) (Lucarelli; Oliveira; Carlo, 2023). The studies that did not comply with our state-of-the-art criteria (scores above 112 points and within the last three years) are still very representative and fulfilled all inclusion criteria. We followed a specific methodology for creating the state-of-the-art, which upholds the remaining studies. As we see in Dataset 1 (Appendix III) (Lucarelli; Oliveira; Carlo, 2023), all studies scored at least 56 points, present one or more building performance criteria, depict a specific movement and actuation (macro or micro), and are within the time limit set in the search strings.

4.2. Bibliometric analysis

We used VOSviewer 1.6.1.7 to create a co-authorship cluster analysis (first authors and co-authors) considering all studies (Figure 3). We adopted ten maximum authors per document and a minimum of 3 papers per author. Wider circles and larger names represent higher name occurrences; the lines indicate the author networks and co-authorships; different colors represent research groups. Some authors have no connections, representing no coincident research. Although important for this ILR, some authors have limited or no co-authorship connections (de Dear; Brager, 1998; Kirimtat *et al.*, 2016; Kolarevic, 2015; Oxman, 2017).

Most wider circles adequately represent our state-of-the-art and ILR and describe the higher-scored research pieces (Fiorito *et al.*, 2016; Loonen, 2018; Nagy *et al.*, 2016; Svetozarevic *et al.*, 2019; Tabadkani *et al.*, 2020).

Figure 3: Co-authorship analysis.

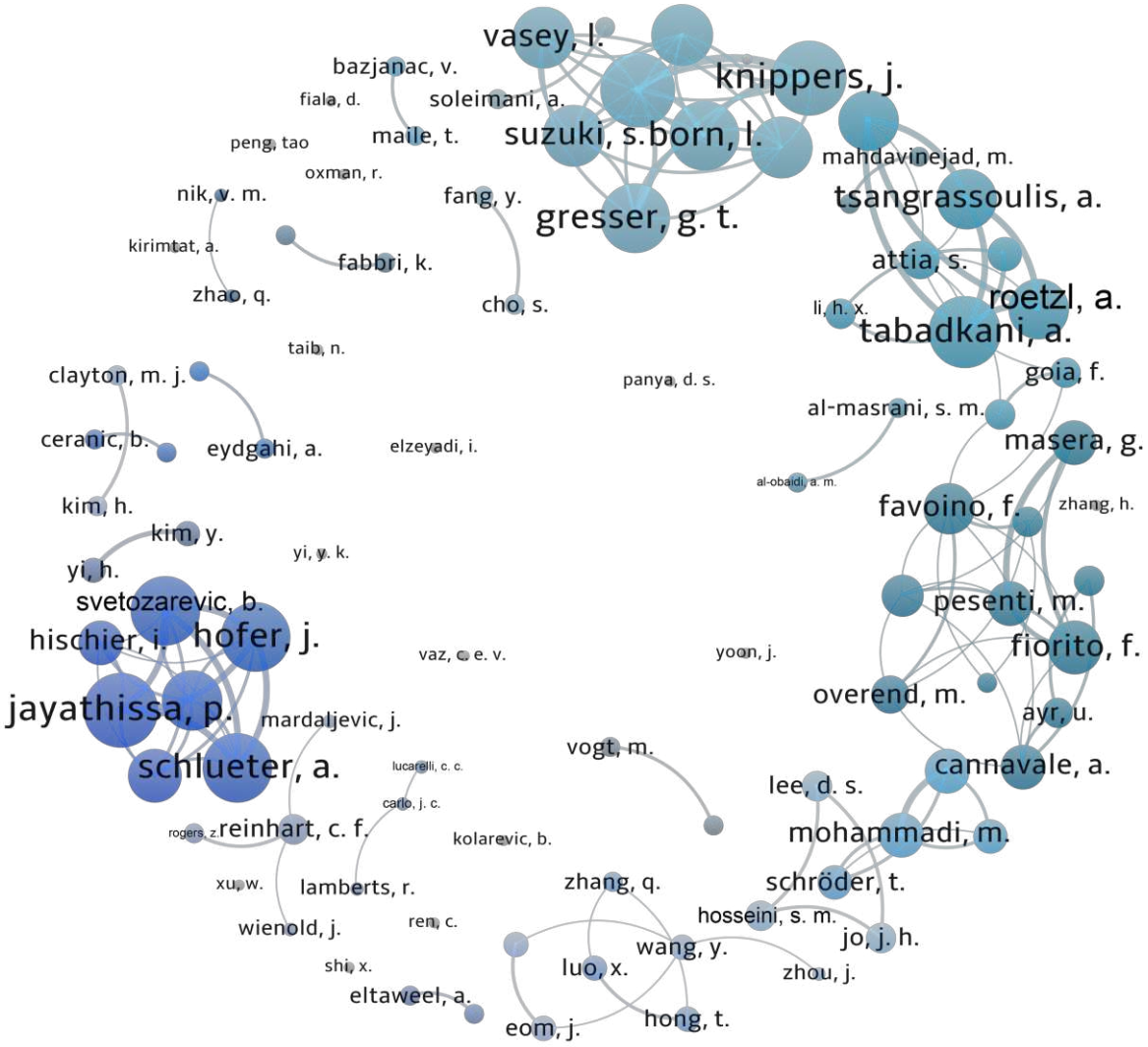

Source: The Authors (2023).

Furthermore, Figure 4 displays the most usual terms on selected research titles, abstracts, and keywords. The analysis criteria are similar for both cluster analyses. The most recurrent words are ‘façade, building, envelope, thermal comfort, visual comfort, occupant, and energy.’ They are also part of our string search. Some of our classifications do not appear among the wider circles or in the cluster, indicating that active, kinetic, intelligent, and smart typologies are the most employed in building performance simulation studies.

Figure 4: Keyword clustering.

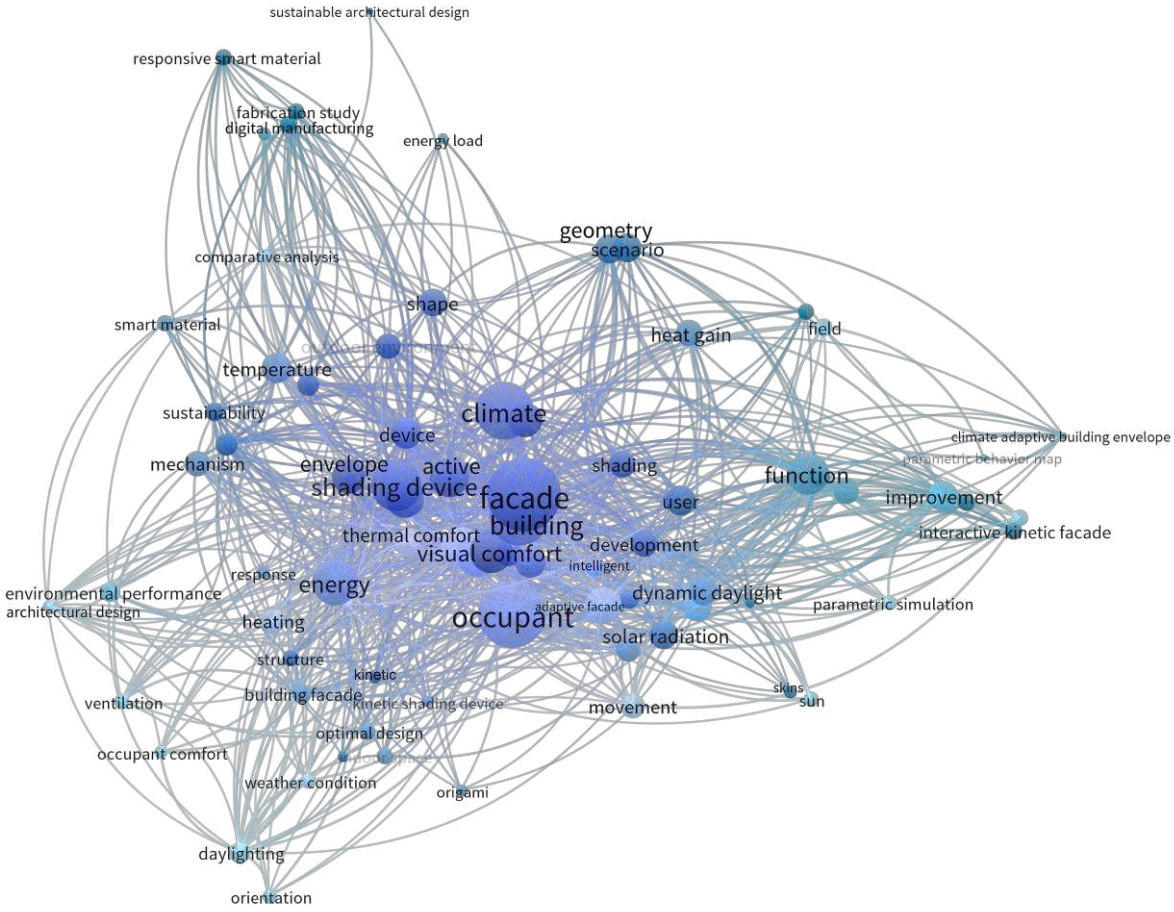

Source: The Authors.

Based on these analyses, some keywords, such as heat, mechanism, occupant, and temperature, can be new additions to the search string since they show good representativity in the clustering.

We also gathered study methodologies and location, active typologies, type of movement, modeling suite, simulation motor, and simulation metrics and presented a bibliometric analysis below. Although we only considered studies from 2016, the literature suggests that active façade systems are an uprising research topic. Even in a limited period, we observe an increasing publication pattern in building simulation modeling for climate-active envelopes per year (Alkhatib *et al.*, 2021; Tabadkani *et al.*, 2020) (Figure 5). We understand that 2020 and 2021 were pandemic-ravaged (COVID-19), diminishing scientific publications in some academic fields, and, therefore, 2018 and 2019 appeared as the peak production years among the collected research pieces.

Even though our investigation encompassed all envelope typologies, façades appear to be the most common research approach with 89% of the studies. We only

found five studies concerning top light strategies and three stand-alone physical prototypes. For instance, all physical prototypes are part of experimental studies. Experiments appeared in 25% of the research pieces, and software simulation is the most common research approach, appearing in 80% of all investigations.

Figure 5: Research publication per year.

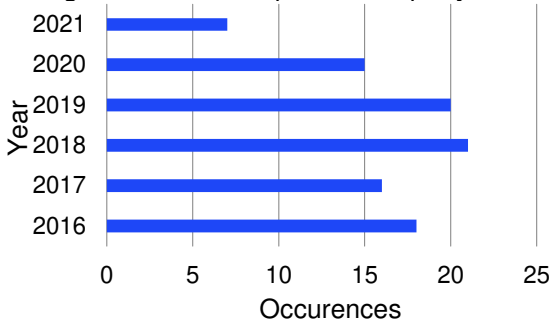

Source: The Authors (2023).

Figure 6: Active Typology. Source: The Authors.

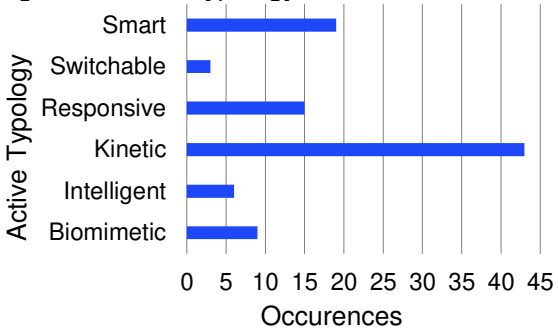

Source: The Authors (2023).

According to Figure 6, kinetic envelopes are the most common research subject in this ILR. Since building performance simulation and building modeling suites for active envelopes are still being developed, most studies simplify all possible input parameters (motion patterns, deformation, simulation days, performance metrics, etc.). We understand that kinetic designs are simpler than the other typologies, requiring only outdoor sensing and no user inputs. Furthermore, mechanical biomimetic, intelligent, responsive, and kinetic typologies better fit the building simulation framework since they generate motion according to predictable weather/user parameters. Smart or smart-actuated systems are usually binary and unpredictable, limiting building simulation applications.

Also, most kinetic investigations employed further simplifications such as primary movement selection or single-objective simulation criteria. They commonly presented thermal or energy simulations since they do not necessarily provide comfort. More comprehensive studies (intelligent, smart, and biomimetic typologies) considered visual objectives but rarely offered user override options (responsiveness). Figure 6 also indicates that smart approaches are the second-largest publication group. Smart applications are usually experimental and function as binary kinetic actuators. Most studies on smart typologies presented shape-memory polymers, followed by shape-memory alloys. For polymers, there are various studies in additive manufacturing and self-assembled structures. Most alloy research pieces use spring alloys with a simple

mechanical motion as base-case. Biomimetic approaches applying alloys were also recurrent.

Even though more advanced than intelligent systems, responsive applications appeared third, with approximately 70% of publications after 2018. Responsive research also involved one simulation objective in most studies. Visual (daylight and glare) simulations were the most frequent as they considered the user directly.

We do not present a graphical representation for mechanical and non-mechanical actuation since non-mechanical approaches only appeared in 18% of studies. The shape memory systems are mainly responsible for non-mechanical procedures. The primary motion typologies in Figure 7 are more recurrent than composite movement patterns, appearing in 54% of the publications. We point out that folding mechanisms (rotating + translating) occur in 25% of the research pieces and normally appear as origami designs.

Figure 7: Primary movement appearances.

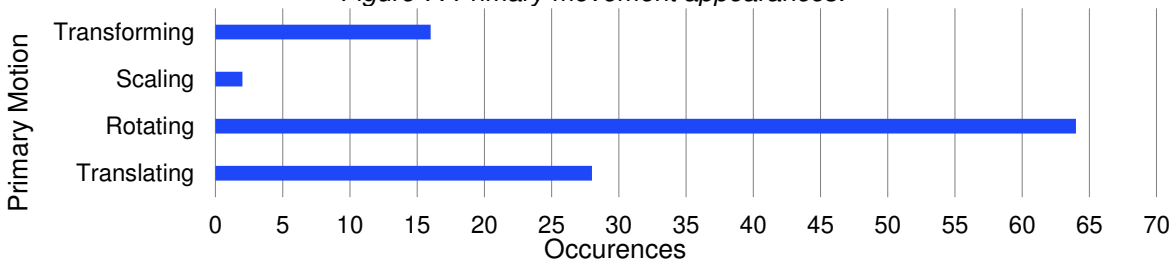

Source: The Authors (2023).

Adaptability through rotation is the most used among active envelopes, followed by translational motion. Passive strategies are well established and normally apply simple geometries (fins, louvers, and egg crates); therefore, the transposition of passive geometries into active strategies preserves the shape simplicity, offering one-axis motion, demonstrating that normal shapes perform similarly to non-conventional geometries. Transformational patterns appear in software simulation studies that are not concerned with physical/material properties and only regard building performance optimization to the detriment of materialization. They also occur for tensile modules (which can present elastic action) and some shape memory materials.

Most reviews do not characterize studies' location and climate classification. However, it is essential to comprehend the climatic conditions from several viewpoints. For instance, heat gains during the winter could be desirable in locations with large seasonal outdoor temperature fluctuation, while shading is imperative in tropical

climates throughout the year. Another issue is the prevalent atmospheric conditions, i.e., regions with high precipitation rather than arid climates have more cloudy sky conditions; thus, less illuminance and more diffuse natural light are available.

We use the Köppen-Geiger weather classification to categorize the studies; we pin all studies' locations on the Köppen map (Figure 8). Most investigations found in our ILR occur in temperate regions (42%) and dry weather (36%). Furthermore, 36 studies are in regions with no dry season (subclassification f); 22 studies appear in desertic climates (subclassification W); and 15 research pieces are in dry winter locations (subclassification w). Most studies are also in hot or hot summer areas. So, we confirm that most research pieces consider mild temperatures, humid regions, and warm summer months. Tropical climates are the least representative, with seven investigations (disregarding the polar group - classification E).

Figure 8: Köppen-Geiger classification and studies' location.

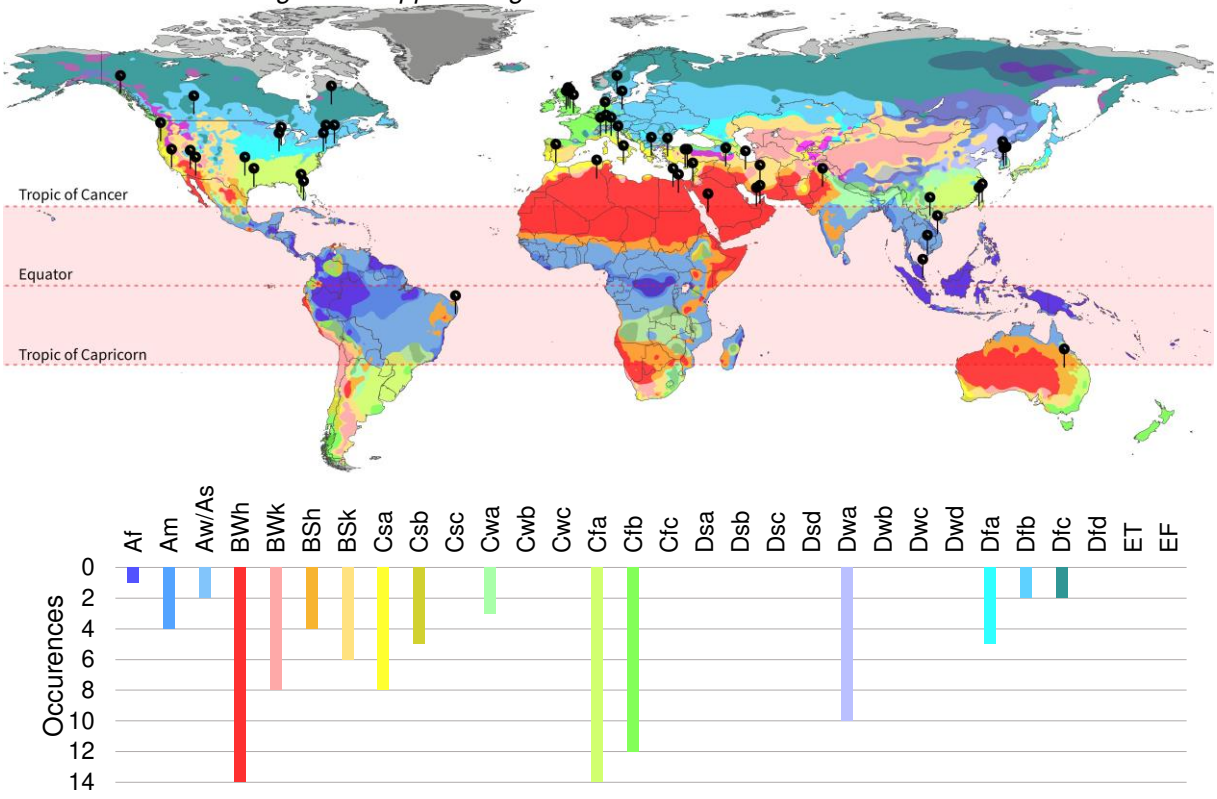

Source: The Authors (2023).

Among the 86 pins, only six are between the tropics, and only one is below the Tropic of Capricorn. Most research appears in the northern hemisphere, mainly in Asia, with 36 studies; North America is second with 24 locations, only in the United States; Europe (mainly in the Mediterranean) has 14 studies; the African continent appears 11

times (mainly northern portion). As mentioned above, Latin America only has one study in South America.

We found five distinct modeling software: Design Builder, Revit, Rhinoceros3D, SketchUp, and SolidWorks. Among those, two are parametrically-coupled modeling suites: Rhino3D+Grasshopper and Revit+Dynamo. The Rhino3D+Grasshopper appears in 78% of our literature pieces, followed by Revit with 8%. Also, Revit+Dynamo only appeared in building information modeling research. The high adhesion of Grasshopper is due to the coupled plug-ins for environmental, mechanical, structural, fabrication, etc. investigation. We only included environmental analysis and performance criteria in our search strings.

Figure 9: Simulation engine employment.

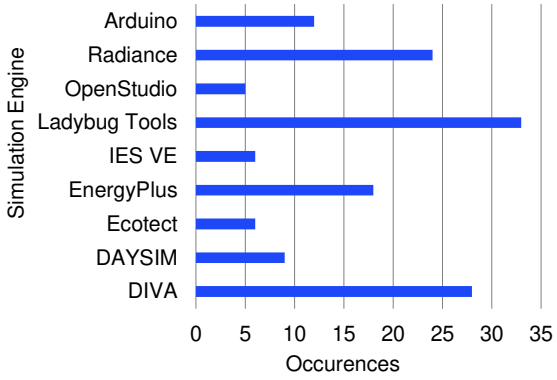

Source: The Authors (2023).

Figure 10: Performance Criteria adoption according to the ILR.

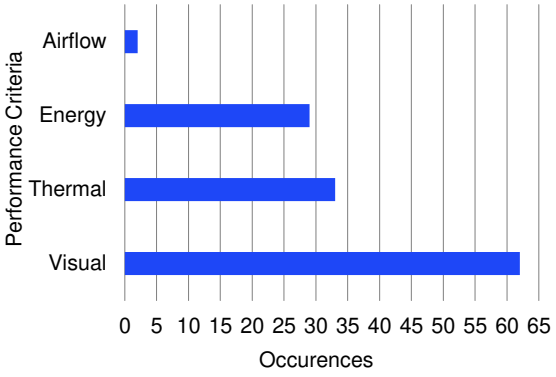

Source: The Authors (2023).

We consider all simulation software (Figure 9) autonomously, i.e., research pieces can apply DIVA unaided or through Ladybug Tools. The Ladybug Tools, including Honeybee, is the most employed simulation software. Other engines include DIVA (20% of research pieces), Radiance (17%), and EnergyPlus (13%). We recognize that Arduino is not software; however, since some investigations did not apply computational simulation, we accepted the Arduino peripherals and sensors as environmental data collectors.

Concerning simulation objectives (Figure 10), we observe that visual metrics are the most common. They appear in 49% of all research, and in 23%, they are the only simulation objective. Thermal and energy analysis are also very representative, with 26% and 23% appearances. The most common association is visual and thermal, appearing in 11% of the studies.

Some daylight studies focused exclusively on glare, especially in simplified, single-occupancy office units. The authors adopted static daylight metrics in these investigations to estimate illuminance levels. They require only one point-in-time and unchangeable sky conditions, consuming less computational time. However, they do not represent the dynamism of active building shading and only appear in approximately 12% of the investigations. Regarding daylight evaluation, daylight levels (25%), useful daylight illuminances (20%), spatial daylight autonomy (17%), annual sunlight exposure (9%), and daylight autonomy (8%) are the most frequent. The daylight glare probability (DGP) also appears in 19% of studies. We also found modified daylight glare probability, daylight glare index, predicted mean vote, and percentage of people dissatisfied.

Energy appraisal mostly considered heat and cooling loads (7%) and photovoltaic generation (3%). Generally, most evaluations relied on specific days and hours, representing different seasons with the same time step.

Even though we show simulation motors and objectives, we acknowledge other research typologies apart from computational simulation. Although fast and economically effective, we also note that they require no field measurements and are prone to low accuracy due to design simplifications. Experiments were the most accurate among the reviewed studies, although relatively high-cost and time-consuming. We found examples of full-scale objects, large-scale mockups, physical measurements, and surveys appearing right before simulation approaches with 27 occurrences. They allow accurate weather characterization, physical materialization, design revision, microcontroller applications, etc. We also found experiment research coupled with numerical calculations (3 studies) or software simulations (22 studies). The latter presented the best results and thorough research pieces.

5. Conclusion

This study developed a comprehensive theoretical background on climate-active skins, creating a preamble for future building enclosure classifications. We also conducted an Integrative Literature Review with a state-of-the-art selection on active building envelopes, compiling study methodologies, geographical location, weather

classification, design solution, active typologies, movement characterization, software application, and simulation metrics and objectives.

We applied a novel methodology coupling StArt v. 3.4 and the Preferred Reporting Items for Systematic Literature Reviews and Meta-Analysis's (PRISMA) selection criteria. The methodology description also supports future studies, guiding and suggesting new keyword insertions. As a drawback, we point out that a permissive string search offers many results, leading to time-consuming analysis.

Even though Scopus conveyed 40% of the selected studies, we indicate Periódicos CAPES as the best scholarly search engine since it represented 30% of research outcomes, with 61% of research pieces as state-of-the-art studies. Furthermore, the superposition of Scopus and Science Direct returned several duplicated research pieces and deviant studies.

We found no nomenclature standardization, so we adopted the most used classifications according to building envelope theoreticians and systematic literature reviews. Since some groups have similar characteristics, we only presented the most occurrent. We also conclude that active strategies mainly concern passive reinterpretations as kinetic systems, explaining the abundance of kinetic research. There is no clear correlation between geometry and active control strategy. Studies mostly applied top-down approaches for selecting envelope shapes. Typically, geometric choices are related to case studies or cultural aspects. Further geometric analysis showed that most researchers apply one-axis rotation or simple motion techniques. Only a few studies considered complex motion typologies that did not comply with mechanical actuation. Also, there is no typical room typology for conducting simulation-based methodologies.

Among our findings, one of the most important factors is the occupant's daylighting preference (illuminance levels and glare). Other representative simulation objectives were thermal and energy assessment. Only two studies did not adopt one of these objectives. We found several studies confirming that users can endure short periods of glare discomfort if adequate lighting is available. We recommend correlating daylight levels with glare analysis. However, glare evaluation research only considered one or two reference points due to simulation limitations (which corresponds to most of our findings).

We consider the simulation workflow as a significant limitation. Active systems lack simulation-based control strategies and cannot predict long-term energy performance or comfort levels in early design stages, limiting their applicability. As a solution, associating simulation with physical experimentation rectifies some drawbacks. For instance, various experimental research with digital manufacturing or prototyping techniques appeared in our state-of-the-art. We consider empirical validation under real climate conditions imperative for simulation approaches.

Experimentation also allowed digital controlling techniques, such as Arduino-based prototypes, to provide a good indication of the system's performance, allowing controlling adjustments and materialization discussions. Another solution for automatizing simulations is the optimization approach. However, we only found 13 research pieces that applied optimization motors.

Following, we pinpoint some major conclusions of this research:

a) Building envelope research primarily focuses on façades to the detriment of other envelope geometries and stand-alone projects, mainly due to the predominancy of evaluations on high latitudes. Most investigations occur above the Tropic of Cancer, with 8% below/between the tropics. Furthermore, only a few studies considered more than one location with different weather classifications, presenting no comparable results.

b) Overall, climate-active enclosures are more effective than optimized static geometries. Building retrofitting and simulation studies demonstrated that even seasonally actuated envelopes perform better than a point-in-time geometry.

c) Recent research offers more intricate adaptation parameters, shifting from kinetic motion (very representative until 2018) into responsive or intelligent systems. Some authors focus on smart actuation without mechanical components or further energy expenditure. However, smart applications require market-ready products or specific fabrication technologies.

d) Simulation motors do not offer a straightforward methodology for assessing active approaches, explaining the lack of standardization. Research pieces also adopt diverse simulation motors and different input parameters and optimization objectives. Therefore, we can analyze the studies

independently, but comparing all approaches is difficult. Besides, a successful simulation procedure involves multiple or many criteria parameters such as indoor activity, climatic zoning, and user requirements. So, current simulation software needs substantial efforts from developers to offer a real-time evaluation of active elements under variable weather conditions, considering potential scenarios in controlling and automation.

e) The primary XY or ZY-axis rotation is the most frequent mechanical motion. Most studies considered hinging and swiveling motion. The second recurring motion pattern is the translation (especially horizontal sliding). The folding motion is also very present. We assume primary movements have a low initial cost, are more mechanically feasible, and rely on market-ready pieces.

f) Daylight simulations with illuminance-based objectives are the most common and frequent combinations comprise visual+thermal and thermal+energy analysis.

Acknowledgments

This study was financed by Coordenação de Aperfeiçoamento de Pessoal de Nível Superior – Brasil (CAPES) – Finance Code 001 and by Fundação de Amparo à Pesquisa de Minas Gerais (FAPEMIG), financing notice N° 001/2021 Universal Demand - under process code APQ-00266-21.

REFERENCES

ALKHATIB, H.; LEMARCHAND, P.; NORTON, B.; O'SULLIVAN, D. Deployment and control of adaptive building facades for energy generation, thermal insulation, ventilation and daylighting: A review. **Applied Thermal Engineering,** v. 185, p. 116331, Feb. 2021. DOI: https://doi.org/10.1016/j.applthermaleng.2020.116331.

ATTIA, S.; BILIR, S.; SAFY, T.; STRUCK, C.; LOONEN, R.; GOIA, F. Current trends and future challenges in the performance assessment of adaptive façade systems. **Energy and Buildings,** v. 179, p. 165–182, Nov. 2018. DOI: https://doi.org/10.1016/j.enbuild.2018.09.017.

AUGUSTIN, N. **Motion with Moisture:** Creating Passive Dynamic Envelope Systems Using the Hygroscopic Properties of Wood Veneer**.** 2018. 130 f. Thesis (Master of Architecturel) - University of Waterloo, Ontario, 2018. Disponível em: https://uwspace.uwaterloo.ca/handle/10012/12953. Acesso em: 20 maio 2022.

BENEVOLO, L. **História da Arquitetura Moderna.** 3. ed. São Paulo: Perspectiva, 2001. 813 p.

BÖKE, J.; KNAACK, U.; HEMMERLING, M. Prototype of a cyber-physical façade system. **Journal of Building Engineering,** v. 31, p. 101397, Sept. 2020. DOI: https://doi.org/10.1016/j.jobe.2020.101397.

BUI, D.; NGUYEN, T.; GHAZLAN, A.; NGO, N.; NGO, T. Enhancing building energy efficiency by adaptive façade: A computational optimization approach. **Applied Energy,** v. 265, May 2020. DOI: https://doi.org/10.1016/j.apenergy.2020.114797.

CLARKE, L.; EOM, J.; MARTEN, E.; HOROWITZ, R.; KYLE, P.; LINK, R.; MIGNONE, B.; MUNDRA, A.; ZHOU, Y. Effects of long-term climate change on global building energy expenditures. **Energy Economics,** v. 72, p. 667–677, May 2018. DOI: https://doi.org/10.1016/j.eneco.2018.01.003.

DE DEAR, R.; BRAGER, G. Developing an Adaptive Model of Thermal Comfort and Preference. **ASHRAE Transactions,** v. 104, Part 1, p. 145-167, 1998.

DELGARM, N.; SAJADI, B.; KOWSARY, F.; DELGARM, S. Multi-objective optimization of the building energy performance: A simulation-based approach by means of particle swarm optimization (PSO). **Applied Energy,** v. 170, p. 293–303, May 2016. DOI: https://doi.org/10.1016/j.apenergy.2016.02.141.

ELKHATIEB, M. A. **A performance-driven design model of territorial adaptive building skins (TABS) for daylighting performance optimization in office buildings in Egypt.** 2016. 338 f. Thesis (Ph.D.) - School of Architecture, University of Liverpool, Liverpool, 2016. Disponível em: https://livrepository.liverpool.ac.uk/3007311/. Acesso em: 20 Nov. 2022.

FABBRI, S.; SILVA, C.; HERNANDES, E.; OCTAVIANO, F.; DI THOMMAZO, A.; BELGAMO, A. Improvements in the StArt tool to better support the systematic review process. *In:* INTERNATIONAL CONFERENCE ON EVALUATION AND ASSESSMENT IN SOFTWARE ENGINEERING, 20., 2016, Limerick. **Proceedings**

[...]. Limerick: Association for Computing Machinery, 2016. DOI: https://doi.org/10.1145/2915970.2916013.

FERSCHIN, P.; DI ANGELO, M.; BRUNNER, G. Rapid Prototyping for Kinetic Architecture. *In*: INTERNATIONAL CONFERENCE ON CYBERNETICS AND INTELLIGENT SYSTEMS; CONFERENCE ON ROBOTICS, AUTOMATION AND MECHATRONIC, 17., 2015, Siem Reap. **Proceedings [...]**. Siem Reap: IEEE, 2015. p. 118-123.

FIORITO, F.; SAUCHELLI, M.; ARROYO, D.; PESENTI, M.; IMPERADORI, M.; MASERA, G.; RANZI, G. Shape morphing solar shadings: A review. **Renewable and Sustainable Energy Reviews,** v. 55, p. 863–884, Marc. 2016. DOI: https://doi.org/10.1016/j.rser.2015.10.086.

HEINZELMANN, F. **Design method for adaptive daylight systems for buildings covered by large (span) roofs.** 2018. 301 f. Thesis (Ph.D.) - Faculty of Architecture, Building and Planning, Eindhoven University of Technology, Eindhoven, 2018. Disponível em: https://pure.tue.nl/ws/portalfiles/portal/96860270/20180612_Heinzelmann.pdf. Acesso em: 20 out. 2022.

HOSSEINI, S.; MOHAMMADI, M.; GUERRA-SANTIN, O. Interactive kinetic façade: Improving visual comfort based on dynamic daylight and occupant's positions by 2D and 3D shape changes. **Building and Environment,** v. 165, p. 106396, Nov. 2019b. DOI: https://doi.org/10.1016/j.buildenv.2019.106396.

HOSSEINI, S.; MOHAMMADI, M.; ROSEMANN, A.; SCHRÖDER, T.; LICHTENBERG, J. A morphological approach for kinetic façade design process to improve visual and thermal comfort: Review. **Building and Environment,** v. 153, p. 186–204, Apr. 2019a. DOI: https://doi.org/10.1016/j.buildenv.2019.02.040.

KIRIMTAT, A.; KOYUNBABA, B. K.; CHATZIKONSTANTINOU, I.; SARIYILDIZ, S. Review of simulation modeling for shading devices in buildings. **Renewable and Sustainable Energy Reviews,** v. 53, p. 23–49, Jan. 2016. DOI: https://doi.org/10.1016/j.rser.2015.08.020.

KNAACK, U.; KLEIN, T.; BILOW, M.; AUER, T. **Façades:** principles of Construction. Basel: Birkhäuser, 2014. 135 p.

KOLAREVIC, B.; PARLAC, V. Towards architecture of change. In: KOLAREVIC, B.; PARLAC, V. (ed.). **Exploring the architecture of change.** Boca Raton: Routledge, 2015. p. 1-16.

LEE, D.; CHO, Y. H.; JO, J. H. Assessment of control strategy of adaptive façades for heating, cooling, lighting energy conservation, and glare prevention. **Energy and Buildings,** v. 235, p. 110739, Mar. 2021. DOI: https://doi.org/10.1016/j.enbuild.2021.110739.

LO VERSO, V. R. M.; JAVADI, M. H. S.; PAGLIOLICO, S.; CARBONARO, C.; SASSI, G. Photobioreactors as a dynamic shading system conceived for an outdoor workspace of the state library of Queensland in Brisbane: Study of daylighting performances. **Journal of Daylighting,** v. 6, n. 2, p. 148–168, Dec. 2019. DOI: https://dx.doi.org/10.15627/jd.2019.14.

LOONEN, R. C. G. **Approaches for Computational Performance Optimization of Innovative Adaptive Façade Concepts.** 2018. 190 f. Thesis (Ph.D.) - Department of the Built Environment, Eindhoven University of Technology, Eindhoven, 2018.

LUCARELLI, C. D. C.; OLIVEIRA, M. M.; CARLO, J. C. Dataset for Climate-Active Building Enclosures. Genève: Zenodo, 2023. DOI: https://doi.org/10.5281/zenodo.8316380.

MATHEOU, M.; COUVELAS, A.; PHOCAS, M. C. Transformable building envelope design in architectural education. **Procedia Manufacturing,** v. 44, p. 116–123, 2020. DOI: https://doi.org/10.1016/j.promfg.2020.02.212.

MOHER, D.; LIBERATI, A.; TETZLAFF, J.; ALTMAN, D. Preferred Reporting Items for Systematic Reviews and Meta-Analyses: The PRISMA Statement. **Plos Medicine,** v. 6, n. 7, e1000097, July. 2009. DOI: https://doi.org/10.7326/0003-4819-151-4-200908180-00135.

MOLONEY, J. **Designing Kinetics for Architectural Facades:** State Change. Boca Raton: Routledge, 2011. 192 p.

NAGY, Z.; SVETOZAREVIC, B.; JAYATHISSA, P.; BEGLE, M.; HOFER, J.; LYDON, G.; WILLMANN, A.; SCHLUETER, A. The Adaptive Solar Facade: From concept to prototypes. **Frontiers of Architectural Research,** v. 5, n. 2, p. 143–156, June 2016. DOI: https://doi.org/10.1016/j.foar.2016.03.002.

NEGROPONTE, N. **The Architecture Machine.** Cambridge: MIT Press, 1973. 164 p.

NGUYEN, T. N. S. **Shape gramma-based adaptive building envelopes: Towards a novel climate-responsive** facade system for sustainable architectural design in Vietnam. 2019. 319 f. Thesis (Ph.D.) - University of Derby, England, Derby, 2019.

OLGYAY, V. **Design with climate:** Bioclimatic approach to architectural regionalism. Princeton: Princeton University Press, 2015. 224 p.

OXMAN, R. Theory and design in the first digital age**. Design Studies**, v. 27, n. 3, p. 229–265, May 2006. DOI: https://doi.org/10.1016/j.destud.2005.11.002.

OXMAN, R. Thinking difference: Theories and models of parametric design thinking. **Design Studies,** v. 52, p. 4–39, 2017. DOI: https://doi.org/10.1016/j.destud.2017.06.001.

PANYA, D. S.; KIM, T.; CHOO, S. A methodology of interactive motion facades design through parametric strategies. **Applied Sciences**, v. 10, n. 4, Feb. 2020. DOI: https://doi.org/10.3390/app10041218.

PAWLIN, M. **Biomimicry in Architecture.** Newcastle upon Tyne, 2nd. Ed. London: RIBA, 2016. 176 p.

REICHERT, S.; MENGES, A.; CORREA, D. Meteorosensitive architecture: Biomimetic building skins based on materially embedded and hygroscopically enabled responsiveness. **Computer Aided Design,** v. 60, p. 50–69, Mar. 2015. DOI: https://doi.org/10.1016/j.cad.2014.02.010.

REKI, M. **Exploring new forms through parametric patterns in responsive facades.** 2018. 105 f. Dissertation (MPhil) - Graduate School of Natural and Applied Sciences, Gazi University, Ankara, 2018.

ROMANO, R.; AELENEI, L.; AELENEI, D.; MAZZUCCHELLI, E. What is an adaptive façade? Analysis of recent terms and definitions from an international perspective. **Journal of Facade Design and Engineering,** v. 6, n. 3 - Special Issue FAÇADE 2018, p. 65-76, 2018. DOI: https://doi.org/10.7480/jfde.2018.3.2478.

SCHIELKE, T. Dynamic design with light: Media facades. *In:* SCHUMACHER, M.; VOGT, M. M.; KRUMME, L. A. C. **New MOVE:** Architecture in Motion - New Dynamic Components and Elements. Basel: Birkhaüser, 2019. p. 90-93.

SCHIMIDT III, R.; AUSTIN, S. **Adaptable architecture:** theory and practice. Boca Raton: Routledge, 2016. 296 p.

SCHUMACHER, M.; VOGT, M.; KRUMME, L. A. C. **New MOVE:** Architecture in Motion - New Dynamic Components and Elements. Basel: Birkhauser, 2020. 216 p.

SCHUMACHER, P. (ed.). **Parametricism 2.0:** Rethinking Architecture's Agenda for the 21st Century, Architectural Design. Cambridge: Academic Press, 2016. 136 p.

SHEIKH, W. T.; ASGHAR, Q. Adaptive biomimetic facades: Enhancing energy efficiency of highly glazed buildings. **Frontiers of Architectural Research,** v. 8, n. 3, p. 319–331, Sept. 2019. DOI: https://doi.org/10.1016/j.foar.2019.06.001.

SHI, X.; TABLADA, A.; WANG, L. Influence of two motion types on solar transmittance and daylight performance of dynamic façades. **Solar Energy,** v. 201, p. 561–580, May 2020. DOI: https://doi.org/10.1016/j.solener.2020.03.017.

SVETOZAREVIC, B.; BEGLE, M.; JAYATHISSA, P.; CARANOVIC, S.; SHEPHERD, R. F.; NAGY, Z.; HISCHIER, I.; HOFER, J.; SCHLUETER, A. Dynamic photovoltaic building envelopes for adaptive energy and comfort management. **Nature Energy,** v. 4, p. 671–682, July 2019. DOI: https://doi.org/10.1038/s41560-019-0424-0.

TABADKANI, A.; BANIHASHEMI, S.; HOSSEINI, M. R. Daylighting and visual comfort of oriental sun responsive skins: A parametric analysis. **Building Simulation,** v. 11, p. 663–676, Feb. 2018. DOI: https://doi.org/10.1007/s12273-018-0433-0.

TABADKANI, A.; ROETZEL, A.; XIAN LI, H.; TSANGRASSOULIS, A. A review of automatic control strategies based on simulations for adaptive facades. **Building and Environment,** v. 175, Jan. 2020. DOI: https://doi.org/10.1016/j.buildenv.2020.106801.

TABADKANI, A.; ROETZEL, A.; XIAN LI, H.; TSANGRASSOULIS, A. Design approaches and typologies of adaptive facades: A review. **Automation in Construction,** v. 121, p. 103450, Jan. 2021. DOI: https://doi.org/10.1016/j.autcon.2020.103450.

TABADKANI, A.; VALINEJAD SHOUBI, M.; SOFLAEI, F.; BANIHASHEMI, S. Integrated parametric design of adaptive facades for user's visual comfort. **Automation in Construction,** v. 106, p. 102857, Oct. 2019. DOI: https://doi.org/10.1016/j.autcon.2019.102857.

VELIKOV, K.; THÜN, G. Responsive Building Envelopes: Characteristics and Evolving Paradigms. *In*: TRUBIANO, F. (ed.). **Design and Construction of High-Performance Homes:** Building Envelopes, Renewable Energies and Integrated Practice**.** Abingdon: Routledge, 2017. p. 75–92.

WANG, C.; PEREZ MORATA, A. **Adaptive Facade, the active connection between indoor and outdoor:** Visual and Thermal evaluation of an adaptive facade in the urban context of Copenhagen. 2019. 84 f. Master thesis (MPhil) - Faculty of Engineering, Lund University, Lund, 2019. Disponível em: https://lup.lub.lu.se/luur/download?func=downloadFile&recordOId=8968027&fileOId=8969098. Acesso em: 20 out 2022.

YANG, C. **The Intelligent Control Strategy of Kinetic Façades for Daylight and Energy Performance.** 2020. 213 f. Thesis (Ph.D.) - Faculty of the USC School for Architecture, University of Southern California, Los Angeles, 2020.

YI, H.; KIM, D.; KIM, Y.; KIM, D.; KOH, J.; KIM, M. 3D-printed attachable kinetic shading device with alternate actuation: Use of shape-memory alloy (SMA) for climate-adaptive responsive architecture. **Automation in Construction,** v. 114, p. 103151, June 2020. DOI: https://doi.org/10.1016/j.autcon.2020.103151.

YI, H.; KIM, Y. Self-shaping building skin: Comparative environmental performance investigation of shape-memory-alloy (SMA) response and artificial intelligence (AI) kinetic control. **Journal of Building Engineering,** v. 35, p. 102113, Mar. 2021. DOI: https://doi.org/10.1016/j.jobe.2020.102113.

YI, Y. K.; SHARSTON, R.; BARAKAT, D. Auxetic structures and advanced daylight control systems. **Journal of Facade Design and Engineering,** v. 7, n. 1 Special Issue Powerskin 2019, p. 63–74, 2019. DOI: https://doi.org/10.7480/jfde.2019.1.2620.

YOON, J. Design-to-fabrication with thermo-responsive shape memory polymer applications for building skins. **Architectural Science Review,** v. 64, n. 1–2, p. 72–86, Mar. 2021. DOI: https://doi.org/10.1080/00038628.2020.1742644.

YOON, J. SMP Prototype Design and Fabrication for Thermo-responsive Façade Elements. **Journal of Facade Design and Engineering,** v. 7, n. 1, Special Ussie Power, p. 41–61, Jan. 2019. DOI: 10.7480/jfde.2019.1.2662. DOI: https://doi.org/10.7480/jfde.2019.1.2662.

YOON, J.; BAE, S. Performance evaluation and design of thermo-responsive SMP shading prototypes. **Sustainability,** v. 12, n. 11, May 2020. DOI: https://doi.org/10.3390/su12114391.

ZHOU, J.; NAZI, W. I. W. M.; WANG, Y.; ROSKILLY, A. Investigating the impact of building's facade on the building's energy performance - a case study. **Energy Procedia,** v. 158, p. 3144–3151, Feb. 2019. DOI: https://doi.org/10.1016/j.egypro.2019.01.1016.

ZUK, W.; CLARK, R. H. **Kinetic Architecture**. New York: Van Nostrand Reinhold, 1970. 163 p.

CHAPTER III – Assessing Human Comfort for Active Building Enclosures: A Novel Simulation Workflow for Environmentally Active Top Lighting Cells

Abstract

This study examines the impact of top lighting cells in a low-latitude city. It hypothesizes that an environmentally active control system enhances indoor illuminance without causing glare or jeopardizing the user's thermal comfort. It proposes a parametric procedure based on two simulation stages using UDI/UDI_{avg}, Image-based, and Imageless DGP. The first stage is a simplified approach considering representative dates for selecting the most contributing motion parameters through an Analysis of Variance. The second expands the system's complexity for year-round cases. Results indicate hinging motion as the most contributing factor for daylight control. Furthermore, the cells supplement daylight indoors, rendering a minimal increase of approximately 30% of the hours within the adequate illuminance range compared to the base case with no roof openings. The systems ultimately achieve 100% of the hours in compliance with the selected daylight thresholds without significantly increasing glare or notably altering user thermal comfort levels.

Keywords: *climate-active building shells; top lighting; visual comfort; adaptive thermal comfort*.

1. Introduction

Daylighting is a fundamental aspect of architecture that significantly affects building occupants' comfort, health, and well-being. Buildings designed to optimize natural light can reduce energy consumption, improve occupant satisfaction, and increase productivity (Straub *et al.*, 2017). Nonetheless, daylight admission is not a strategy in which the higher the values, the better the performance (Reinhart; Mardaljevic; Rogers, 2013). Overshading excludes beneficial solar gains, and the excessive admission of daylight causes visual discomfort and undesirable heat gains (Glassman; Reinhart, 2013).

The evolution of Information Technology (IT) enabled the potential increase of artificial intelligence in buildings, ensuring spatial regulation without human resources and functional and physical optimization of built space (Romano *et al.*, 2018). The advancement of IT reintroduced the concept of kinetic systems based on recent developments in generative, parametric, and algorithmic thinking (Hosseini *et al.*, 2020). These developments aid in understanding and designing environmentally active systems.

Environmentally active architecture uses movable elements such as louvers, shades, and panels to control natural light entering a space. This approach allows occupants to customize the amount of daylight in a room according to their preferences and needs. Kinetic architecture can also mitigate glare and control solar heat gain, enhancing overall comfort levels in the building (Hosseini; Fadli; Mohammadi, 2021).

While literature frequently concentrates on façades, roofs play a crucial role in the heat gain/loss and daylight admission in buildings, particularly in those with large rooftop areas. This heat transfer and natural light selection is particularly relevant in countries between the tropics, and the closer a building is to the Equator, the greater the impact of solar irradiation.

This study developed a parametric modeling and simulation process to determine an environmentally active top lighting cell's revolving and tilting mechanical control states based on illuminance supplementing. The author adopted a previously calibrated institutional building in Viçosa, Brazil (Lucarelli; Oliveira; Carlo, 2022) (Appendix I), placing a matrix of circular roof openings (with 30 cm diameter) above its transitional spaces. The first simulation stage adopts the average results of the

Honeybee Useful Daylight Illuminance (UDI) module. It comprises compute-intensive image-based analysis using Honeybee Daylight Glare Probability (DGP) for 3600 scenarios. Based on these UDI_{avg} and DGP results, the author employed a two-factor Variance-based Sensitivity Analysis (ANOVA) to select the most contributing motion parameters, reducing the shape iterations (i.e., revolving and tilting combinations) and increasing the number of simulation time steps. The second simulation stage adopted grid-based UDI_{avg} and imageless DGP simulations to define the adequate top lighting tilting position to enhance indoor illuminance levels.

2. Theoretical Framework

2.1. Environmentally Active Building Enclosures

Non-flexible enclosures lead to modifications over the building life cycle, reducing the anticipated indoor comfort and energy savings (Barozzi *et al.*, 2016; Lucarelli; Oliveira; Carlo, 2023). A conventional fenestration may be enough to allow natural light indoors, but providing consistent and uniform daylight usually demands more advanced design alternatives. Static shading systems have limited potential to respond to indoor or outdoor environmental variations throughout the day and seasons, which decreases their performance if the operating requirements vary over time. Computational tools offer more freedom in planning environmentally active building structures, causing traditional louvers to seem ineffective (Barozzi *et al.*, 2016).

Several interchangeable terms refer to time-varying building features. The most common variations include adaptive (Basarir; Cem Altun, 2018; Lo Verso *et al.*, 2019), kinetic (Hosseini *et al.*, 2020; Shi; Tablada; Wang, 2020), responsive (Hosseini *et al.*, 2020; Tabadkani; Banihashemi; Hosseini, 2018), intelligent (Le-Thanh *et al.*, 2021; Yi *et al.*, 2020), biomimetic (Jahanara; Fioravanti, 2017; Sheikh; Asghar, 2019), interactive (Chang; Huang; Datta, 2019), smart (Pesenti; Masera; Fiorito, 2018), and switchable (Ayoub, 2019; Cannavale *et al.*, 2018; Paule *et al.*, 2017), and each one has a different definition. Active envelopes can adjust to various internal and external factors, such as user comfort parameters, building performance criteria, weather sensing and prediction, environmental stimuli, and user interactions (Böke, 2020).

Most building performance simulation (BPS) studies on active enclosures occur in temperate climates, dry weather regions, and mostly above the tropics (Lucarelli;

Oliveira; Carlo, 2023). The Brazilian Köppen-Geiger weather classification mainly comprises tropical (megathermal, group A), with some temperate (mesothermal, group C) occurrences, which only appear in 7% of studies concerning active enclosures from 2015 until 2023 (Lucarelli; Oliveira; Carlo, 2023). Furthermore, only 8% of these publications are below or between the tropics. Even though research pieces often focus on active facades (Kirimtat *et al.*, 2016), roofs concentrate the most significant heat gain during the day, being the surface most exposed to solar radiation in low latitudes. On a typical summer day, the incidence of solar radiation on a horizontal surface may be more than 1000 W/m[2][9], particularly in countries between the tropics and near the Equator, which have higher solar radiation intensity throughout the year (4-6 kWh/m^2) and higher outdoor air temperatures (Kolokotroni *et al.*, 2018). Additionally, top lighting provides a more uniform and balanced light distribution than side or down lighting, reducing the likelihood of harsh shadows that can be distracting or uncomfortable for users (Lechner; Andrasik, 2021).

Only a few research pieces focus on the interdisciplinary use of parametric design and BPS for top lighting solutions. The BPS studies on top lighting do not associate multiple environmental analysis criteria and whole-year simulations nor combine the most employed parametric modeling suite (Rhino3D+Grasshopper) and its performance simulation add-ons (Ladybug Tools and sub-packages) (Lucarelli; Oliveira; Carlo, 2023). Yang (2020) is one of the few authors who discussed active skylights, applying model-based predictive control algorithms. For instance, Lucarelli, Oliveira, and Carlo (2023) only found four other investigations on top lighting strategies, emphasizing the need for additional applications.

Yang (2020) evaluated indoor illuminance (minimum and maximum of 500 lx and 1500 lx), Daylight Glare Probability (DGP), and solar heat gain, running simulations for three specific dates: June, September, and December 21st, representing hot, cool, and cold seasons. The author recommended avoiding 70°, 80°, and 90° angles between noon and 3 p.m. and indicated that illuminances at a 10° tilt angle in June, September, and December are always below 100 lx. Although this study represents significant advances in active top lighting approaches, it offered no clear correlation between

---

[9] In a study developed for Viçosa, Brazil, the highest incident radiation on a façade reached 501 W/m^2 (Barbosa et al., 2013).

geometry, operational control strategy, and weather classification, and the optimization problem only delivered one cell opening instead of a matrix of solutions.

Research on environmentally active building envelopes lacks standardization, is compute-intensive, and does not offer a straightforward methodology for assessing the continuous motion of active envelope approaches (Lucarelli; Oliveira; Carlo, 2023). Multicriteria simulation-based optimization problems can mimic a real-time evaluation but are time-consuming, require high computational processing, and are prone to 'local optima' results. Regarding motion constraints, researchers often apply one-axis rotation (XY or ZY-axis panning or tilting) or translation (Moloney 2011; Lee, Cho, and Jo 2021; Yi and Kim 2021). These are primary movements compatible with physical applications and market available products, representing a low cost for future materialization. Only a few studies considered complex motion typologies that did not comply with mechanical actuation by simplifying other simulation inputs, i.e., selecting fewer representative days and moving states (Hosseini; Fadli; Mohammadi, 2021; Nguyen, 2019).

Furthermore, BPS on building active typologies mainly concerns visual metrics, especially static daylight metrics (such as the Daylight Factor) (Lucarelli; Oliveira; Carlo, 2023). However, they do not represent the dynamism of active components, estimating illuminance levels for a specific time and sky condition.

2.2. Computational Simulation for Visual and Thermal Comfort

Concerning active systems, the parametric modeling workflow generates a suitable medium for performative approaches, automatically changing input parameters (such as analysis period, building occupation and use, and surrounding shade geometry). This approach is an algorithm-driven process in which the performance becomes the design guiding agent (Ayoub, 2019), and each input parameter change triggers new simulations with corresponding outcomes.

In architecture, engineering, construction, and operation (AECO), daylight plays a vital role, involving various parameters such as brightness, light distribution, color temperature, glare and veiling reflections, visual contact, and individual control. The assessment of daylight's performance and expressiveness is a multi-criteria analysis considering architectural and environmental contexts. Poor daylighting can lead to inadequate illuminance or over-illumination, affecting visual and thermal comfort.

However, balancing visual comfort and daylight maximization can be challenging (Hosseini *et al.*, 2019). Solar gains can be advantageous in certain situations, but the selected daylighting strategy must offset the risks of discomfort and excessive solar heat gain. Daylight is also a potential energy reduction technique since it is a renewable energy and light source at high luminous effectiveness, which makes it more compelling than traditional electric lighting (Konis 2017). Furthermore, solar energy control effectively reduces cooling loads, prevents heating loads from surpassing the capacity of the HVAC system (Yang, 2020), and positively affects well-being and health, helping lessen depression symptoms, stress, eye strain, and seasonal affective disorders (Loonen *et al.*, 2013).

Since the 1990s, several quantitative daylighting approaches have been proposed, such as scale models (Cartana 2018; Yi and Kim 2021), numerical methods (Jayathissa *et al.*, 2017), and software simulation (Shi, Tablada, and Wang 2020; Yi, Sharston, and Barakat 2019). They apply calculation methods to measure internal daylighting, considering building geometries, materials, occupants' visual comfort, and &c. These can be either static or dynamic, requiring fundamental inputs for predicting illuminance levels. Static models, such as the Daylight Factor (DF), appraise daylighting, glare, and visual comfort prevailing conditions in a confined environment, defining optimal thresholds. They are more limiting than dynamic or climate-based approaches since they do not account for sky dynamism, internal task variability, and artificial light (Ayoub, 2020; Gherri, 2015). Dynamic metrics apply realistic sky and regional weather conditions, delivering daylighting results for a time series at each point of a grid-based space with higher accuracy, thus superseding static metrics (Nabil; Mardaljevic, 2006; Reinhart; Wienold, 2011). The Daylight and Spatial Daylight Autonomy (DA and $_{s}$DA), the Useful and the Average Useful Daylight Illuminance (UDI and UDI_{avg}), and the Annual Sunlight Exposure (ASE) are the most employed metrics for visual comfort simulation (Liu *et al.*, 2023; Yu; Wennersten; Leng, 2020).

For instance, UDI represents a percentage of the occupied time in a year during which illuminance levels fall within an illuminance threshold[10] (Mardaljevic *et al.*, 2011; Nabil; Mardaljevic, 2005, 2006). It identifies the frequency in which the indoor

[10] Nabil and Mardaljevic (Nabil; Mardaljevic, 2006) first indicated 2000 lx as the upper illuminance threshold. Mardaljevic et al. (Mardaljevic et al., 2011) raised the maximum illuminance to 3000 lx. In both indications, the minimum illuminance value is 100 lx.

illuminance levels are appropriate for building occupants, not too dim (less than 100 lx) or bright (greater than 2000 lx or 3000 lx). The upper threshold also indicates instances where an excess of daylight might cause visual discomfort (Nabil; Mardaljevic, 2005). UDI is a local and long-term metric based on surveys, reports, and occupant reactions. It suits office buildings, where users experience high daylight levels and glare (Nguyen, 2019), and compared to other dynamic daylight metrics, it offers more details to assess visual comfort.

Although Liu *et al.* (2023) indicate a lack of consensus on selecting daylight metrics for specific geographical locations, climates, building types, and occupants, Konis, Gamas, and Kensek (2016) state that spatial and average climate-based metrics can further describe the architectural space by analyzing a work plane instead of one given point, for instance, the Spatial UDI ($_{s}$UDI) is the percentage of floor space that receives 100 lx to 2000 lx (a proxy indicator of glare) for 50% of the working hours, while the average UDI (UDI_{avg}) is the mass addition of point-in-time UDI within a space, divided by the number of evaluation points. In Zhang *et al.'s* (2017) and *Zheng et al.'s* (2023) research, UDI_{avg} showed better results, steadily adjusting according to the glazing ratio, while $_{s}$UDI presented a less accurate variation.

Although the UDI_{avg} upper threshold indicates a likelihood of visual impairment, discomfort glare can occur due to saturation (i.e., extreme brightness) and contrast (i.e., excessive range of luminance in the field of view) (Wienold; Christoffersen, 2006). Daylight Glare Probability (DGP) integrates vertical eye illuminance (E_v) and glare source luminance, considering both effects through luminance maps and simulation-based renderings (image-based high dynamic range analysis) (Pierson *et al.*, 2021). It requires creating a hemispherical fisheye image at each time step, producing many images, which is very time-consuming. Therefore, it is a considerably validated metric for daylighting simulation but is subject to computer accuracy and power (Jones, 2019; Wienold; Christoffersen, 2006).

If DGP is higher or equal to 45%, glare is intolerable; between 40% and 45%, disturbing; from 35% to 40%, perceptible; if below 35%, DGP is imperceptible (Reinhart; Wienold, 2011; Wienold; Christoffersen, 2006). Similar to UDI, DGP thresholds vary. For instance, Loonen (Loonen 2018) considers only three classifications, i.e., intolerable (DGP>45%), disturbing (35%<DGP<45%), and not disturbing (DGP<35%).

Since active building typologies rely on parametric modeling and simulation approaches, the Honeybee plug-in for Grasshopper is a widespread bridge between energy, thermal, and daylight simulation motors. Its Image-based Daylight Coefficient module uses a 2-phase dynamic daylight simulation to calculate indoor illuminance by summing direct and indirect illuminance from the sun and the sky. Unlike an illuminance-only strategy, it also analyses the angular distribution of light, requiring time-consuming, high-quality renderings (Jones, 2019). Even though Jones and Reinhart (2017) indicated that low-quality renderings produce similar DGP results, the rendering time required for annual calculation or multiple views remains prohibitive for most applications (Jones, 2019).

Imageless DGP uses normalized daylight coefficients to represent flux transfer from patches of the sky to various viewing positions (Subramaniam, 2017). It modifies DGP's equation, reducing the computational expense by replacing illuminance and luminance with daylight coefficient-based calculations (Equation 1) while maintaining Wienold and Christoffersen's (2006) acceptance thresholds.

$$E_v = kD_{total}S$$

$$L_s = k\frac{d_{direct}s_i}{\omega \cos\theta} \quad (1)$$

Where: E_v*: Vertical Eye Illuminance*
S*: Point in time sky luminance vector of sky patches*
d_{direct}*: Daylight coefficient of direct component for sky patch i*
s_i*: Point in time sky luminance value of sky patch i*
k*: 179 lumens per watt – luminous efficacy of white light*

Visual metrics are environmentally active building enclosure studies' most common simulation objective since 2015 (Lucarelli; Oliveira; Carlo, 2023). The users' thermal comfort appraisal is also a representative analysis, especially when associated with visual comfort. For comfort evaluation, the adaptive theory asserts that human thermal comfort depends not solely on the surrounding environment's physical conditions but also on individual physiological and social factors. Adaptive models appear in several standards with different derivation methods but similar results (American Society of Heating, Refrigerating and Air-Conditioning Engineers, 2023; European Standards, 2012, 2021; International Organization for Standardization, 2005).

ASHRAE 55's (American Society of Heating, Refrigerating and Air-Conditioning Engineers, 2023) adaptive model concerns only buildings with no mechanical cooling (or mixed conditioning), human metabolic rates between 1 and 1.3 met, and clothing insulation between 0.5 and 1 clo. It considers indoor comfort based on outdoor conditions, including prevailing mean outdoor air temperatures, by weighting the mean outdoor temperatures from Typical Meteorological Year weather files. For instance, de Dear and Brager (1998) indicate a higher comfort acceptance threshold in naturally ventilated buildings as a user's preferred air temperature depends on outdoor circumstances. Furthermore, according to Cândido, de Dear, and Lamberts (2011), thermal acceptability percentages in hot and humid climates are more expressive due to higher air velocities (between 0.3 m/s and 1 m/s). Attia and Carlucci (2015) compared the different adaptive models, concluding that ASHRAE 55's (2023) is better suited for non-air-conditioned buildings in hot climates and can predict a wider range of comfort temperatures than Fanger's model (Fanger, 1970).

3. Methodology

3.1. Building Performance Simulation (BPS)

The modeling process employed the Rhino3D+Grasshopper suite. The building is the head office of *Universidade Federal de Viçosa's Architecture Graduation Program (PPG.au)* (Viçosa/MG 20°45'14''S and 42°52'54''W), calibrated in Lucarelli, Oliveira, and Carlo (2022) research (Figure 1a, b, and c). Viçosa is warm and temperate (Köppen Cwa) with hot and humid summers and cool to mild winters. Its fittest weather file is an edited version of the TMY3 that compiles south-facing *in situ* air dry-bulb temperature and humidity (Appendix I) (Lucarelli; Oliveira; Carlo, 2023). The building is a 110 m^2, one-story, hip/Dutch-like roof with eight thermal zones (Figure 1d). It is wind-exposed for Northwest, North, and Northeast orientations and shows an expressive microclimate caused by a mass of vegetation and lawn for South and West. Soil conditions are mud-like, and ventilation is single-flow. The walls, floor, and ceiling are opaque, with separate color absorptance (α) of 0.35 (light plaster walls), 0.65 (terracotta-painted walls), and 0.80 (clay tiles and exposed concrete floors) with 0.85 overall emissivity (ε).

Figure 1: (a) Head office of Universidade Federal de Viçosa's Architecture Graduation Program (PPG.au); (b and c) Entrance Hall and Kitchen marked as 'c' and 'd' - spaces modeled for the simulation process; (d) Building with Honeybee Thermal Zones, cell positioning above entrance hall and kitchen area and work planes within the same spaces.

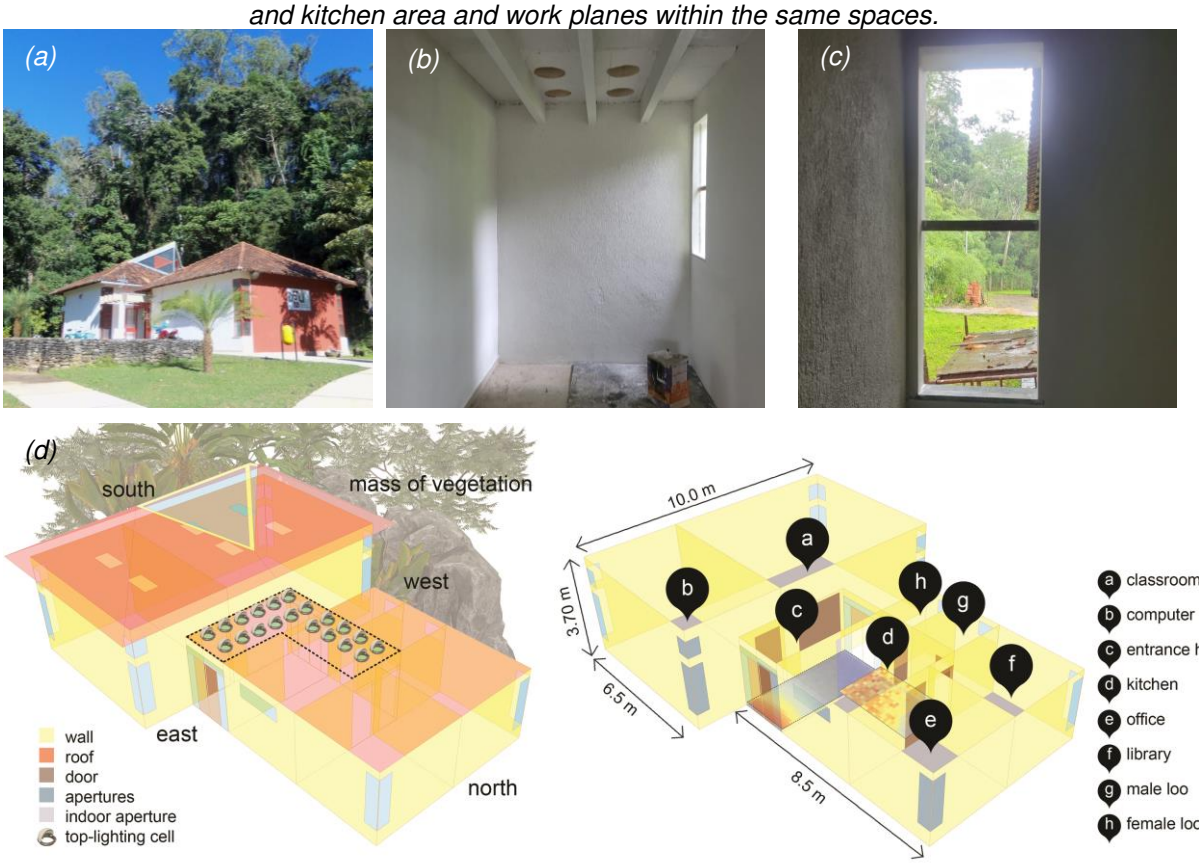

Source: The Author (2024).

The roof apertures in which the cells attach are clear, uncoated, single-pane glass with 0.88 transmittance and 30 cm diameter (Figures 1d and 2). They are above the building's transitional space (hall and kitchen corridor) (Figure 1d), and their arrangement followed a 2 by 6 grid for the hall and a 2 by 5 grid for the kitchen corridor according to the respective thermal zones' sizing.

Figure 2: The base case for the top lighting cell.

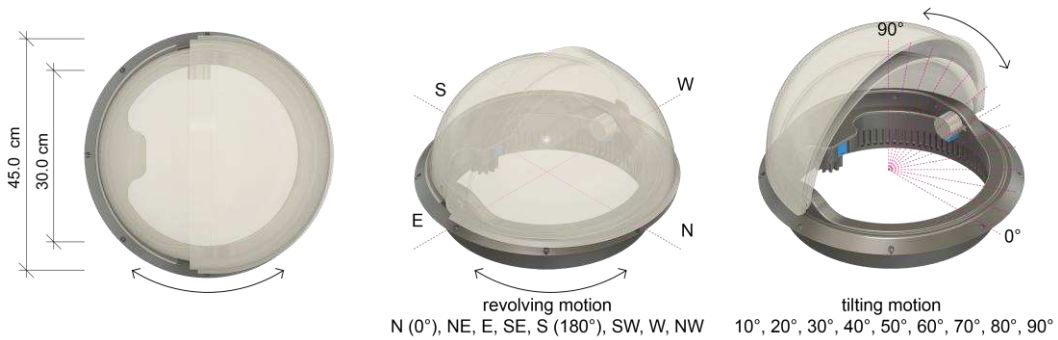

Source: The Author (2024).

As shading geometries in Honeybee radiance, they do not require shell thicknesses. They are hollow half-spheres covering the 30 cm diameter circular roof

openings (Figures 1d and 2). The environmentally active cell is a copolymer with 0.2 absorptance, 0.9 emissivity, and 0.1 roughness. Further, top lighting shape parameters comprise vertical axis tilting and horizontal axis revolving (Figure 2).

As seen in Figure 1d, the hall work plane is 20 cm above the floor, compatible with a walking activity, and the kitchen corridor is 90 cm, consistent with a kitchen counter height. The author adopted both work planes as input geometries, using 'HB sensor grids from rooms' to generate a 10 cm x 10 cm grid, or 796 analysis points (European Standards, 2021). As the hall and kitchen are contiguous, the author considered both rooms as a joint space. Honeybee radiance outputs Useful Daylight Illuminance (UDI), which the author converted to average UDI (UDI_{avg}) by summing all results and dividing by the number of analysis points (Nabil; Mardaljevic, 2006). Its glare analysis component uses a point-in-time view-based model connected directly to the surveyed room, outputting luminance values translated to the Daylight Glare Probability index (DGP). The observer is in the left-most corner of the Hall, looking at both analyzed spaces. The sky model is climate-based, following Viçosa TMY3's weather file. It fluctuates from clear to overcast, affecting daylight transmission and solar radiation toward the evaluated space.

This research considered two simulation stages. Since image-based DGP simulations are time-consuming, the first stage only comprises 3600 scenarios to identify the most representative shape parameters for daylight control (24 days; three hours per day – 09 a.m., 12 p.m., and 03 p.m.; eight revolving stages – 0°, 45°, 90°, 135°, 180°, 225°, 270°, 315°; and three tilting positions – 30°, 60°, and 90°). After selecting the fittest positions, the second stage assesses 40150 scenarios (11 working hours, 365 days, and 10 tilting positions).

3.2. Preliminary daylight and thermal simulations

The first daylight simulations served as a preliminary analysis for tuning motion parameters. They occurred every 15 days (24 days), three hours per day (09 a.m., noon, and 03 p.m.), rendering 72 points in time for each tilting and revolving combination. The cell presented eight revolution stages (45° rotations) and three tilting positions (30°, 60°, and 90°), rendering 24 stages and a base case (cell closed) (Figure 3). These grid and image-based simulations generated 3600 results (1800 UDI_{avg} and 1800 DGP).

Figure 3: Preliminary simulation delineation.

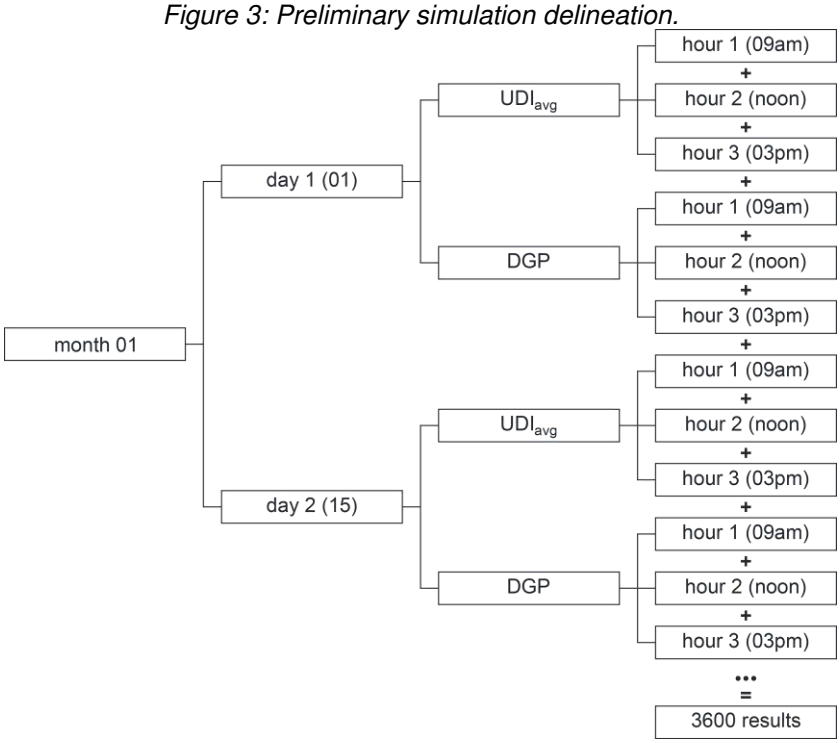

Source: The Author (2024).

To understand which input parameters rendered the highest daylight contribution, reduce the computational time, and increase the number of simulations, the author used Minitab to assemble a two-factor Variance-based Sensitivity Analysis (ANOVA) with three replications adopting the 3600 simulation results. The two factors were the tilting states (30°, 60°, and 90°) and the cardinal/collateral orientations (0°, 45°, 90°, 135°, 180°, 225°, 270°, and 315°; N, NE, E, SE, S, SW, W, NW), and the replicates were the hours (9 a.m., noon, and 3 p.m.). The author considered P-values significant for alpha levels below 0.05.

3.2.1. Daylight simulation

After selecting the most contributing motion through the sensibility analysis, the author fixed the northeast-facing rotation, which presented a higher sky luminance availability, increased the tilting stages to nine (10°-based tilt angles with one closed state as the base case), and adopted grid-based UDI_{avg} and imageless DGP simulations. The author simulated the whole year, from 08 a.m. to 06 p.m. (working hours), adopting TT Toolbox Colibri for Grasshopper to iterate all possible input combinations (day, hour, month, and cell tilt angle).

The author compared simulation results from stage one and stage two using the Root-Mean-Square-Error (RMSE) (Equation 2) to identify possible correlations

between different methodologies and potentially simplify the simulation workflow. They also compared stage two tilt angle correlations to evaluate the impact of increasing the number of openings to 9.

$$RMSE = \sqrt{\frac{\sum_{i=1}^{n}(stage1_i - stage2_i)^2}{n}} \quad (2)$$

Where: RMSE - Root-Mean-Square Error
$stage1_i$ – stage 1 UDI_{avg} and DGP simulation values
$stage2_i$ – stage 2 UDI_{avg} and DGP simulation values
n - total number of observations

3.2.2. Adaptive Thermal Comfort Assessment

The second simulation stage also employed the Honeybee adaptive thermal comfort component to assess the consequences of installing various top lighting apertures. Thermal comfort simulation appears in the iteration process as a verification output rather than as a design decision criterion or an optimization problem because a previous study concerning the same building indicated the low impact of airflow and radiation on indoor air temperatures and humidity (Lucarelli; Oliveira; Carlo, 2022). Furthermore, the low thermal comfort percentage in the selected space (without the top lighting) during winter is due to misapplied passive design strategies: heavy walls, low glazing ratio, ceramic roof with attic vents, and massive surrounding shading geometries.

The author selected the ASHRAE 55 (2023) adaptive model with 90% acceptability. The space is occupant-controlled and naturally conditioned. The prevailing outdoor air temperature is between 10 °C and 33.5 °C. Users' metabolic rates are 1.0 met, and clothing insulation ranges from 0.6 to 1.0 clo.

4. Results

4.1. First Stage

The first stage investigated UDI_{avg} and Image-based DGP for 24 days, three hours per day, culminating in 300 monthly results (150 for the first day and 150 for the fifteenth) (Figure 3). Figures 4, 5, and 6 (9 a.m., noon, and 3 p.m.) display UDI_{avg} and DGP percentages for all the simulated days. The red dashed line indicates the limit of the DGP's imperceptible band (Reinhart; Wienold, 2011). The author considered UDI

as the percentage of time when at least 50% of the analysis points have illuminance levels above 200 lx instead of 100 lx, defined as the minimum threshold for walking and eating activities by the NBR/ISO 8995 (ABNT, 2013), and below 2000 lx. The Y-axis represents the DGP for each case. As the increase in indoor natural light admission can lead to glare, the top lighting cell's most appropriate tilting and revolving positions are the points closest to the graph's lower-left corner. They exhibit higher illuminance values with minimum DGP (Figure 4).

Figure 4: Yearly UDI_{avg} and DGP at 9 a.m.

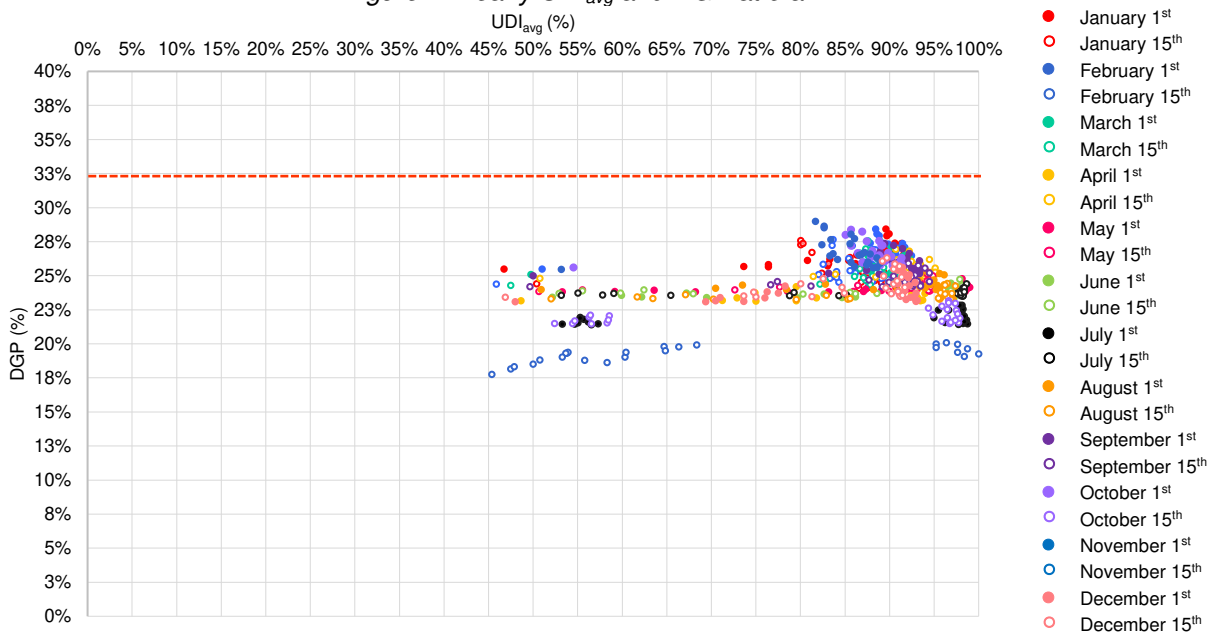

Source: The Author (2024).

Tables 1, 2, and 3 (9 a.m., noon, and 3 p.m., respectively) show UDI_{avg} and DGP for the base case and each motion combination for four representative months (one for each season). For 9 a.m., DGP did not exceed the imperceptibility band; therefore, the results closest to the left side are all adequate, with no significant glare increase (Figure 4). In Viçosa, the minimum solar altitude at this hour is approximately 25°, which causes the roof slab thickness to block most of the direct sunlight, preventing it from reaching the work planes. The UDI_{avg} increased for the 60°, indicating greater daylight admission, even when compared to larger angles (Table 1). It is the highest percentual gain compared to the base case. DGP hardly changed, confirming that the influence of the existing fenestrations is more substantial than that of the cells. Due to the lower sun altitude at 9 a.m., the kitchen window and the entrance door are responsible for most of the daylight. The summer months presented the lowest UDI_{avg} (Table 1). The UDI_{avg} increase through the top lighting is higher in summer when the

daylight does not reach the work plane through the doors and windows, resulting in an average increase of 36%, with a maximum improvement of 45.6% for a 60° opening facing northeast.

Table 1: UDI_{avg} and DGP for base case and the cell positions on four representative months at 9 a.m.

			Fall				Winter				Spring				Summer			
			March				June				September				December			
			1		15		1		15		1		15		1		15	
Tilt.	Revo.		UD_{avg}	DGP	UD_{avg}	DGP	UD_{avg}	DGP	UD_{avg}	DGP	UD_{avg}	DGP	UD_{avg}	DGP	UD_{avg}	DGP	UD_{avg}	DGP
Base Case			49.7%	25.1%	47.5%	24.3%	52.1%	23.4%	52.9%	23.7%	50.0%	25.0%	49.6%	24.2%	48.0%	23.1%	46.9%	23.4%
30°	180°	30°	90.1%	25.2%	82.2%	24.4%	69.5%	23.4%	68.0%	23.7%	88.8%	25.1%	81.2%	24.2%	70.5%	23.2%	73.6%	23.5%
	225°	SE	92.7%	25.3%	87.8%	24.3%	79.6%	23.4%	80.3%	23.7%	93.3%	25.2%	89.2%	24.2%	69.3%	23.1%	75.0%	23.4%
	270°	E	92.8%	25.3%	90.7%	24.4%	84.7%	23.4%	86.2%	23.7%	93.3%	25.3%	92.6%	24.2%	73.6%	23.1%	81.3%	23.5%
	315°	NE	93.1%	25.5%	91.6%	24.6%	86.2%	23.4%	88.6%	23.7%	93.1%	25.4%	92.6%	24.4%	76.0%	23.4%	84.9%	23.7%
	0°	N	92.8%	25.6%	90.6%	24.9%	82.7%	23.7%	85.6%	23.8%	93.0%	25.5%	93.1%	24.6%	77.5%	23.7%	84.7%	24.2%
	45°	NW	93.2%	25.7%	89.4%	25.1%	67.2%	23.7%	62.4%	24.0%	92.8%	25.5%	87.7%	24.7%	78.3%	24.3%	82.5%	24.8%
	90°	W	88.6%	25.6%	86.1%	25.0%	59.9%	23.6%	55.5%	23.9%	87.4%	25.4%	77.4%	24.6%	76.3%	23.8%	80.0%	24.4%
	135°	SW	87.9%	25.3%	82.8%	24.6%	62.2%	23.5%	59.8%	23.7%	83.2%	25.2%	76.6%	24.4%	71.0%	23.4%	74.7%	23.8%
60°	180°	60°	92.2%	25.6%	90.8%	24.6%	97.0%	23.4%	98.1%	23.7%	92.8%	25.4%	93.5%	24.3%	92.8%	23.3%	91.2%	23.7%
	225°	SE	91.3%	25.6%	89.9%	24.4%	97.2%	23.4%	97.9%	23.7%	92.5%	25.6%	93.5%	24.3%	93.0%	23.1%	91.2%	23.5%
	270°	E	91.0%	25.8%	90.3%	24.5%	97.1%	23.4%	97.6%	23.7%	91.7%	25.8%	92.0%	24.3%	93.1%	23.2%	91.5%	23.6%
	315°	NE	90.6%	26.1%	89.4%	25.0%	97.0%	23.7%	97.6%	23.9%	91.5%	26.1%	92.1%	24.7%	93.0%	23.7%	91.7%	24.2%
	0°	N	91.5%	26.4%	89.3%	25.6%	97.4%	23.8%	97.7%	24.2%	92.0%	26.3%	92.8%	25.0%	92.8%	24.5%	91.3%	24.9%
	45°	NW	91.7%	26.9%	90.2%	26.4%	97.1%	23.9%	98.4%	24.1%	92.2%	26.6%	94.0%	25.6%	92.2%	25.1%	91.1%	25.7%
	90°	W	92.2%	26.4%	90.5%	25.9%	97.2%	23.8%	97.9%	24.1%	93.3%	26.1%	94.5%	25.2%	92.1%	24.9%	90.5%	25.5%
	135°	SW	93.0%	25.8%	90.6%	25.1%	96.7%	23.6%	97.7%	23.8%	93.3%	25.5%	94.5%	24.6%	91.7%	23.9%	90.5%	24.4%
90°	180°	90°	90.3%	26.2%	88.1%	25.0%	96.9%	23.5%	97.5%	23.8%	91.0%	26.0%	91.7%	24.5%	91.1%	23.6%	89.6%	24.1%
	225°	SE	88.7%	26.2%	87.3%	24.7%	96.9%	23.4%	97.0%	23.7%	90.2%	26.1%	90.8%	24.4%	91.8%	23.3%	90.2%	23.7%
	270°	E	87.6%	26.5%	87.1%	24.9%	96.6%	23.5%	96.7%	23.8%	89.2%	26.4%	89.9%	24.5%	92.3%	23.4%	91.0%	23.9%
	315°	NE	87.7%	26.9%	86.7%	25.5%	96.6%	23.8%	96.9%	23.9%	88.9%	26.8%	90.5%	25.0%	92.2%	24.3%	90.8%	24.6%
	0°	N	87.6%	27.6%	86.7%	26.7%	96.7%	24.0%	97.6%	24.2%	89.4%	27.4%	91.0%	25.8%	91.6%	25.2%	90.6%	25.9%
	45°	NW	88.9%	27.6%	87.3%	27.0%	96.6%	24.1%	97.9%	24.7%	90.5%	27.2%	92.1%	25.9%	91.5%	25.6%	89.7%	26.3%
	90°	W	90.2%	27.1%	87.9%	26.8%	96.9%	24.5%	98.1%	24.3%	91.5%	27.0%	93.2%	25.8%	91.0%	25.4%	89.2%	26.1%
	135°	SW	90.2%	26.5%	88.2%	25.7%	97.0%	23.7%	98.0%	24.0%	91.6%	26.2%	92.5%	24.9%	91.0%	24.4%	89.3%	25.0%

Source: The Author (2024).

Figure 5 presents each cell's positioning with their respective UDI_{avg} and DGP values. The best cases should consider the highest UDI_{avg}, provided they are within the imperceptible glare range. In this case, the most satisfactory results are closer to the right-most axis and below the red dashed line.

Figure 5: Yearly UDI_{avg} and DGP at noon.

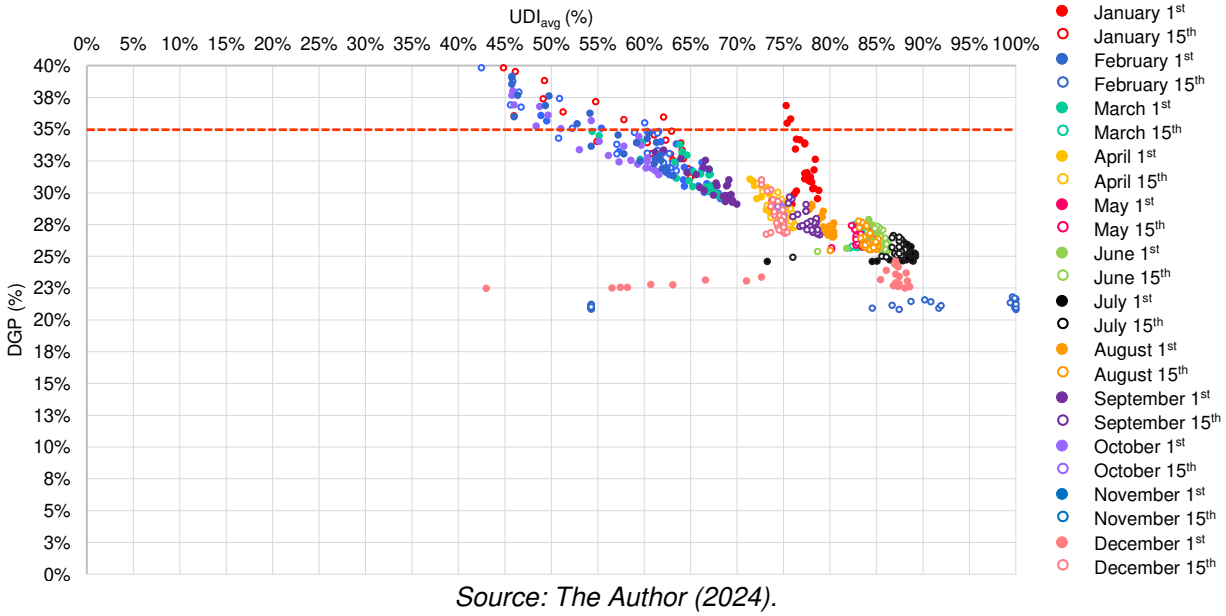

Source: The Author (2024).

Table 2: UDI_{avg} and DGP for base case and the cell positions on four representative months at noon.

			Fall				Winter				Spring				Summer			
			March				June				September				December			
			1		15		1		15		1		15		1		15	
Tilt.	Revo.		UD_{avg}	DGP	UD_{avg}	DGP	UD_{avg}	DGP	UD_{avg}	DGP	UD_{avg}	DGP	UD_{avg}	DGP	UD_{avg}	DGP	UD_{avg}	DGP
Base Case			68.3%	29.6%	82.2%	25.7%	81.8%	25.6%	78.6%	25.4%	70.0%	29.1%	78.9%	26.7%	43.0%	22.5%	73.1%	26.7%
30°	180°	S	82.8%	25.7%	85.2%	25.7%	85.7%	25.4%	68.7%	29.3%	78.5%	26.8%	57.4%	22.6%	73.6%	26.9%	73.6%	23.5%
	225°	SE	82.9%	25.7%	85.3%	25.7%	85.6%	25.4%	69.5%	29.3%	78.6%	26.8%	56.5%	22.5%	75.1%	26.8%	75.0%	23.4%
	270°	E	83.9%	25.7%	85.8%	25.7%	86.2%	25.4%	69.5%	29.4%	78.6%	26.8%	58.2%	22.6%	75.3%	26.9%	81.3%	23.5%
	315°	NE	83.7%	26.0%	85.8%	26.0%	86.3%	25.7%	69.3%	29.9%	78.5%	27.2%	63.1%	22.8%	75.0%	27.5%	84.9%	23.7%
	0°	N	83.7%	26.3%	85.7%	26.2%	86.3%	25.9%	69.0%	30.6%	78.5%	27.6%	71.0%	23.1%	74.6%	28.2%	84.7%	24.2%
	45°	NW	83.7%	26.5%	85.7%	26.3%	86.1%	26.0%	69.1%	31.0%	78.5%	28.0%	72.6%	23.4%	74.9%	28.7%	82.5%	24.8%
	90°	W	83.4%	26.2%	85.7%	26.2%	86.3%	25.9%	68.8%	30.5%	78.3%	27.7%	66.6%	23.1%	75.0%	28.1%	80.0%	24.4%
	135°	SW	82.4%	25.8%	85.7%	25.9%	85.6%	25.6%	69.1%	29.8%	78.6%	27.1%	60.7%	22.8%	74.7%	27.2%	74.7%	23.8%
60°	180°	S	83.3%	25.8%	84.9%	25.9%	86.1%	25.6%	68.5%	29.7%	78.1%	27.0%	86.8%	22.7%	74.9%	27.1%	91.2%	23.7%
	225°	SE	83.5%	25.7%	85.3%	25.8%	85.8%	25.5%	68.7%	29.5%	78.1%	26.9%	88.1%	22.5%	75.4%	26.9%	91.2%	23.5%
	270°	E	83.4%	25.9%	85.4%	25.9%	85.9%	25.5%	68.7%	29.8%	78.0%	27.1%	88.6%	22.6%	75.0%	27.3%	91.5%	23.6%
	315°	NE	83.4%	26.3%	85.3%	26.3%	86.1%	26.0%	67.7%	30.8%	77.9%	27.7%	88.3%	23.1%	74.0%	28.3%	91.7%	24.2%
	0°	N	83.4%	26.9%	85.1%	26.8%	85.9%	26.4%	66.3%	32.0%	77.4%	28.6%	88.2%	23.7%	73.9%	29.5%	91.3%	24.9%
	45°	NW	83.2%	27.2%	84.8%	27.2%	85.7%	27.1%	66.6%	32.6%	77.4%	29.1%	87.3%	24.2%	73.6%	30.2%	91.1%	25.7%
	90°	W	83.3%	26.7%	84.7%	26.9%	85.4%	26.6%	67.0%	31.9%	77.4%	28.6%	86.1%	23.9%	74.4%	29.3%	90.5%	25.5%
	135°	SW	83.2%	26.1%	84.8%	26.2%	85.6%	25.9%	67.8%	30.5%	77.5%	27.6%	85.4%	23.2%	74.7%	27.8%	90.5%	24.4%
90°	180°	S	82.9%	25.8%	84.0%	26.1%	85.1%	25.7%	66.5%	30.2%	76.8%	27.3%	87.1%	22.9%	74.4%	27.3%	89.6%	24.1%
	225°	SE	83.3%	25.8%	84.7%	25.9%	85.4%	25.6%	67.5%	29.8%	77.5%	27.1%	87.3%	22.6%	74.5%	27.1%	90.2%	23.7%
	270°	E	83.2%	26.0%	84.7%	26.1%	85.4%	25.7%	66.0%	30.4%	77.0%	27.4%	87.4%	22.8%	74.2%	27.6%	91.0%	23.9%
	315°	NE	83.0%	26.6%	84.3%	26.6%	85.4%	26.3%	64.6%	31.6%	76.5%	28.3%	87.4%	23.4%	73.6%	28.9%	90.8%	24.6%
	0°	N	82.8%	27.5%	84.5%	27.5%	85.3%	27.2%	61.2%	33.2%	75.9%	29.5%	87.2%	24.3%	72.6%	30.7%	90.6%	25.9%
	45°	NW	82.7%	27.5%	84.2%	27.9%	85.1%	27.4%	62.1%	33.4%	75.6%	29.7%	87.1%	24.6%	72.6%	31.0%	89.7%	26.3%
	90°	W	82.7%	27.1%	83.9%	27.3%	84.8%	27.2%	63.9%	32.7%	75.5%	29.2%	86.9%	24.4%	73.2%	30.1%	89.2%	26.1%
	135°	SW	82.9%	26.3%	84.3%	26.6%	84.7%	26.2%	65.6%	31.4%	76.0%	28.1%	87.1%	23.6%	74.0%	28.5%	89.3%	25.0%

Source: The Author (2024).

The results for 3 p.m. (Figure 6) have the lowest UDI_{avg} and DGP, as the dense vegetation towards the west obstructs the afternoon sun. The few cases that resulted in almost 100% of the time within the selected illuminance band occurred from November to January when the sun's altitude was higher and partially obstructed by context geometry. The base cases already demonstrated very low UDI_{avg} and DGP due to the limited availability of unobstructed sky during the afternoon. However, larger openings resulted in an average increase of 15.7% throughout the year, with the best cases facing northwest and mainly due to diffuse radiation (Table 3).

Figure 6: Yearly UDI_{avg} and DGP at 3 p.m.

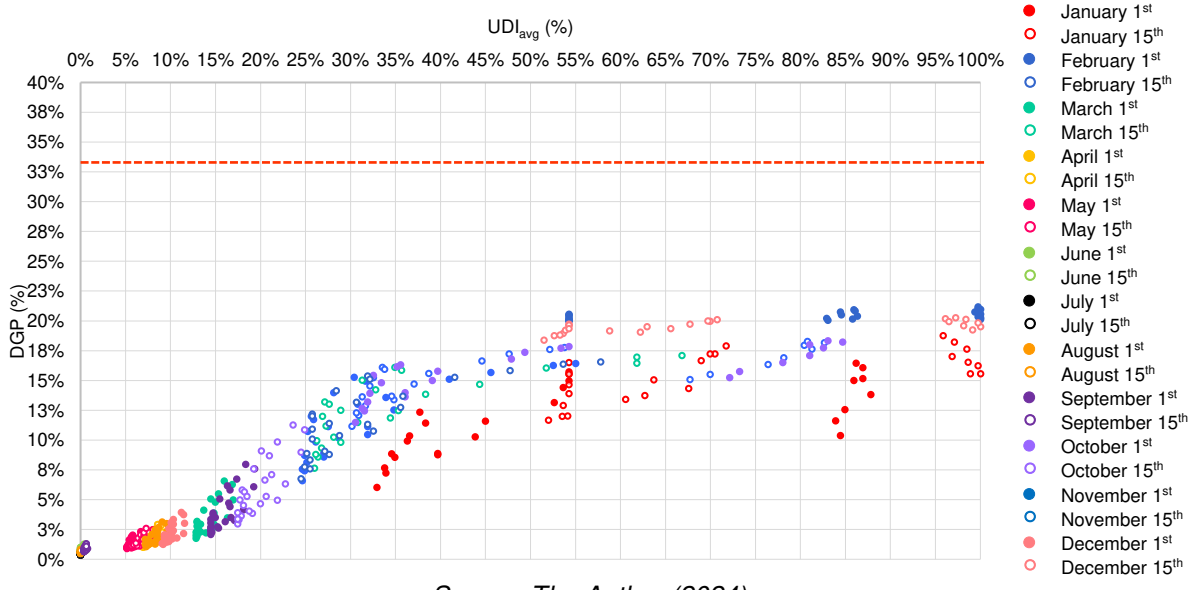

Source: The Author (2024).

By 9 a.m., the cell rotation was primarily towards the northeast, north, and northwest, tracking the largest portion of the unobstructed sky. Context geometries, such as the classroom and computer lab roof or the surrounding mass of vegetation, predominantly shade the east, southeast, south, and southwest orientations. The tilting ranges between 30° to 60°, being narrower during seasons with higher solar positions and more open during seasons with lower solar altitudes.

For noon, the cell was mainly towards the sky portion with the highest diffuse daylight availability and the lowest beam radiation incidence. The openings were consistently smaller to avoid glare. The base case remained the best option in many cases, especially in months with lower solar altitudes when sunlight through doors and windows was already sufficient (Table 2). During these months, the contribution of the top lighting cell is minimal, as shown in Tables 1, 2, and 3.

Table 3: UDI_{avg} and DGP for base case and the cell positions on four representative months at 3 p.m.

			Fall				Winter				Spring				Summer			
			March				June				September				December			
			1		15		1		15		1		15		1		15	
Tilt.	Revo.		UD_{avg}	DGP	UD_{avg}	DGP	UD_{avg}	DGP	UD_{avg}	DGP	UD_{avg}	DGP	UD_{avg}	DGP	UD_{avg}	DGP	UD_{avg}	DGP
Base Case			**1.3%**	**1.8%**	**1.5%**	**0.6%**	0.0%	**0.6%**	**0.1%**	**0.6%**	**14.4%**	**2.1%**	**0.4%**	**0.7%**	**9.2%**	**1.3%**	**51.5%**	**18.4%**
30°	180°	S	1.5%	0.8%	0.0%	0.6%	0.3%	0.7%	14.4%	2.5%	0.4%	0.7%	9.5%	1.4%	53.6%	19.0%	73.6%	23.5%
	225°	SE	1.3%	0.6%	0.0%	0.6%	0.4%	0.7%	14.6%	2.3%	0.4%	0.7%	9.0%	1.4%	52.6%	18.8%	75.0%	23.4%
	270°	E	0.3%	0.2%	0.0%	0.6%	0.1%	0.7%	14.4%	2.4%	0.4%	0.7%	9.2%	1.4%	53.3%	18.8%	81.3%	23.5%
	315°	NE	1.1%	0.1%	0.0%	0.6%	0.0%	0.7%	14.4%	2.7%	0.4%	0.7%	9.3%	1.5%	53.9%	19.2%	84.9%	23.7%
	0°	N	1.4%	0.1%	0.0%	0.7%	0.0%	0.8%	14.4%	3.4%	0.4%	0.8%	9.3%	1.8%	54.3%	19.6%	84.7%	24.2%
	45°	NW	1.3%	0.2%	0.0%	0.7%	0.3%	0.9%	14.7%	3.9%	0.4%	0.9%	9.3%	2.1%	54.3%	19.8%	82.5%	24.8%
	90°	W	1.3%	0.7%	0.0%	0.7%	0.0%	0.8%	14.7%	3.8%	0.4%	0.9%	9.5%	2.0%	54.3%	19.7%	80.0%	24.4%
	135°	SW	1.3%	1.2%	0.0%	0.7%	0.3%	0.8%	14.4%	3.1%	0.4%	0.8%	9.5%	1.7%	54.3%	19.4%	74.7%	23.8%
60°	180°	S	1.0%	1.5%	0.0%	0.7%	0.4%	0.8%	16.1%	3.2%	0.5%	0.8%	10.2%	1.7%	65.6%	19.4%	91.2%	23.7%
	225°	SE	1.1%	1.1%	0.0%	0.6%	0.4%	0.7%	15.3%	2.6%	0.5%	0.7%	9.8%	1.5%	62.2%	19.1%	91.2%	23.5%
	270°	E	1.0%	0.4%	0.0%	0.6%	0.4%	0.7%	15.2%	2.7%	0.4%	0.7%	9.7%	1.6%	58.8%	19.2%	91.5%	23.6%
	315°	NE	0.8%	0.2%	0.0%	0.7%	0.4%	0.8%	14.9%	3.5%	0.4%	0.8%	9.5%	1.9%	62.9%	19.5%	91.7%	24.2%
	0°	N	1.1%	0.1%	0.0%	0.8%	0.4%	1.0%	15.5%	5.1%	0.4%	1.0%	9.8%	2.6%	70.0%	20.0%	91.3%	24.9%
	45°	NW	1.0%	0.4%	0.0%	0.9%	0.3%	1.1%	16.3%	6.2%	0.5%	1.1%	10.1%	3.1%	70.7%	20.1%	91.1%	25.7%
	90°	W	0.9%	1.0%	0.0%	0.9%	0.4%	1.1%	16.6%	5.8%	0.6%	1.1%	10.3%	2.9%	69.7%	20.0%	90.5%	25.5%
	135°	SW	0.6%	1.8%	0.0%	0.8%	0.5%	0.9%	16.6%	4.4%	0.6%	0.9%	10.2%	2.3%	67.7%	19.7%	90.5%	24.4%
90°	180°	S	0.5%	1.9%	0.0%	0.8%	0.6%	0.9%	18.1%	4.2%	0.8%	0.9%	11.4%	2.2%	98.1%	19.6%	89.6%	24.1%
	225°	SE	0.5%	1.4%	0.0%	0.7%	0.6%	0.8%	17.1%	3.3%	0.6%	0.8%	10.7%	1.8%	99.1%	19.3%	90.2%	23.7%
	270°	E	0.8%	0.7%	0.0%	0.7%	0.5%	0.8%	16.7%	3.5%	0.6%	0.8%	10.2%	1.9%	100.0%	19.5%	91.0%	23.9%
	315°	NE	0.0%	0.0%	0.0%	0.8%	0.4%	1.0%	16.5%	4.7%	0.6%	1.0%	10.3%	2.4%	99.7%	19.9%	90.8%	24.6%
	0°	N	0.0%	0.0%	0.0%	0.9%	0.4%	1.2%	17.3%	6.7%	0.6%	1.2%	10.3%	3.4%	98.4%	20.2%	90.6%	25.9%
	45°	NW	0.0%	0.0%	0.0%	1.0%	0.4%	1.3%	18.3%	8.0%	0.6%	1.3%	11.2%	4.0%	97.2%	20.3%	89.7%	26.3%
	90°	W	0.0%	0.0%	0.0%	1.0%	0.5%	1.2%	19.3%	7.6%	0.6%	1.3%	11.4%	3.8%	96.1%	20.2%	89.2%	26.1%
	135°	SW	0.0%	0.0%	0.0%	0.9%	0.6%	1.1%	19.2%	6.1%	0.6%	1.1%	11.6%	3.0%	96.5%	20.0%	89.3%	25.0%

Source: The Author (2024).

Since the portion of the unobstructed sky and the availability of beam radiation are low by 3 p.m., the openings only rendered substantial illuminance gains for the maximum tilt angle, mainly due to the reduced contribution from doors and windows. For such cases, the orientation with the highest availability of natural lighting was southwest. Table 4 shows the most adequate tilting and revolving positions with higher UDI_{avg} and glare below the perceptible range. When the variation in illuminance is minimal, or the cells cause glare, the selected geometry is the base case.

Table 4: Configurations with highest UDI_{avg} and imperceptible DGP.

		Jan.		Feb.		March		April		May		June		July		Aug.		Sept.		Oct.		Nov.		Dec.	
		1	15	1	15	1	15	1	15	1	15	1	15	1	15	1	15	1	15	1	15	1	15	1	15
9	Revo.	NE	E	SE	NE	NE	NE	NE	N	NW	W	N	NW	E	NW	S	NW	SE	SE	E	NW	NW	E	E	NE
	Tilt	60°	30°	30°	30°	30°	30°	60°	30°	60°	60°	60°	60°	30°	60°	60°	60°	30°	60°	30°	60°	60°	60°	60°	60°
12	Revo.	SE	BC	BC	BC	BC	E	BC	SE	NE	E	E	NE	NE	N	NE	NE	BC	BC	BC	BC	BC	SE	E	E
	Tilt	60°					30°		30°	30°	30°	30°	30°	30°	30°	30°	30°						90°	60°	30°
15	Revo.	NE	W	NE	NW	NW	NW	SW	SW	S	SW	BC	SE	BC	BC	SW	BC	W	SW	SW	SW	SE	NW	SW	E
	Tilt	90°	90°	90°	90°	90°	90°	90°	90°	90°	90°		90°			90°		90°	90°	90°	90°	90°	90°	90°	90°

Source: The Author (2024).

4.2. Second Stage - ANOVA

According to Tables 1, 2, and 3, altering the cardinal/collateral orientation for the same opening angles causes little variation in UDI_{avg}, which does not occur between cases with different tilt angles. In order to test the contribution of each variable, the author applied an Analysis of Variance (ANOVA), considering that: (a) the dependent data answers to an interval scale; (b) population distribution is normal; (c) the error variance follows the homoscedasticity assumption; and (d) there is no multicollinearity among independent variables.

Table 5's contribution column shows the percentage that each source in the ANOVA contributes to the sequential sums of squares (SeqSS). Higher rates demonstrate that the source accounts for more of the variation. Therefore, the tilt angle factor is the main contributing source, with 89.5%, followed by the error with 5.67%, and the revolution states with 4.83%. Tilting displays the highest F-values.

Table 5: ANOVA experiment.

Results versus Opening, Rotation (from MINITAB)			
Factor	**Type**	**Levels**	**Values**
Tilt Angle	Fixed	3	30°, 60°, 90°
Revolution Angle	Fixed	8	0°, 45°, 90°, 135°, 180°, 225°, 270°, 315°

Analysis of Variance						
Source of Variation	**SeqSS**	**Contribution**	**AdjSS**	**AdjMS**	**F-Value**	**P-Value**
Tilt Angle	975.29	89.50%	975.29	487.647	489.43	0.001
Revolution Angle	52.68	4.83%	52.68	7.525	7.55	0.001
Error	61.77	5.67%	61.77	0.996	*	*
Lack of fit	41.49	3.81%	41.49	2.964	7.01	0.464
Pure error	20.28	1.86%	20.28	0.423	*	*
Total	1089.74	**100.00%**				

S	**R-Sq**	**R-Sq (adj)**	**R-Sq (pred)**	**AICc**	**BIC**
0.998174	94.33%	93.51%	92.36%	219.7	240.34

Source: The Author (2024).

Since this experiment considered P-values significant when the alpha levels are below 0.05, the model tilting and revolving factors have statistically influential associations. Both factors indicate a less than 0.1% risk that the model does not correctly specify the relationship between the response and the predictors. Furthermore, the lack of fit is negligible as it displays a 46% risk. The R^2, adjusted R^2 and predicted R^2 values are above 90%, indicating a fit model. In addition, the predicted R^2 implies a high ability to anticipate new observations, such as new tilting angles.

Since the glare results remained consistently below the perceptible band in the first simulation stage and, in 99% of cases, the DGP was imperceptible, time-consuming, computationally expensive simulations such as image-based methods are not justifiable for this BPS workflow. Therefore, the next simulation stage only employed grid-based and imageless glare simulations. The author fixed the northeast-facing orientation and expanded the tilting motion to nine stages (10°, 20°, 30°, 40°, 50°, 60°, 70°, 80°, and 90°) complying with the ANOVA results.

4.3. Second Stage – Daylight Simulations

Figure 7 indicates a maximum increase of 44.2% on UDI_{avg} compared to the base case[11]. Despite observing three opening clusters (highlighted with dashed lines - from 10° to 30°, 40° to 60°, and 70° to 90°) with leaps in averages and quartiles, 30°, 60°, and 90° angles simulated in the second stage did not statistically correspond to the same conditions simulated in the first stage. In contrast, when comparing the results solely for the second simulation stage, the RMSEs within the same aperture grouping shown in Figure 7 and Table 6 exhibit low discrepancies and suggest that employing only three apertures, as done in the initial phase, would create fit predictions.

Table 6 shows the correlation between all tilt angles adopted in stage two. Therefore, a tilt angle of 10° presents no error when compared to itself, rendering a RMSE of 0. Among the assessed values, the first cluster with smaller apertures showed higher RMSEs compared to the other circled groupings highlighted in bold (maximum of 4.99%). These tilt angle clusters are likely due to the minimal increase in

---

[11] The author adopted UDI_{avg} and DGP with the top lighting minus UDI_{avg} and DGP for the base case to assess the sole influence of the daylight strategy.

the useful illumination area; also, the cell's opening is not the sole determining factor for daylight admission.

Figure 7: UDI_{avg} relative to the base case (with no top lighting).

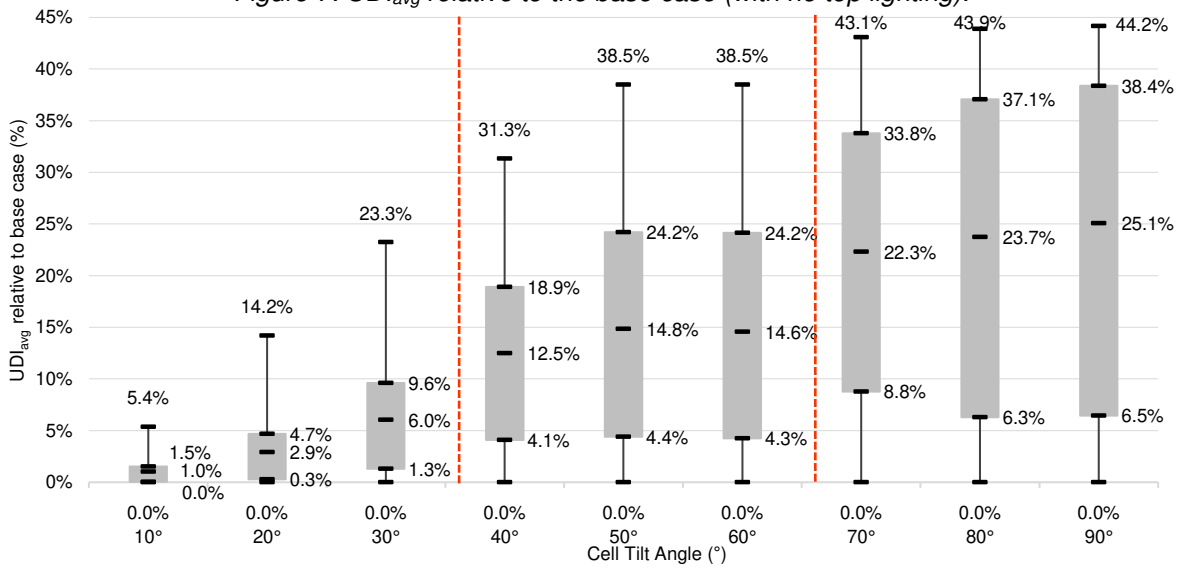

Source: The Author (2024).

Table 6: Clustering RMSEs.

Cell tilt angle – stage 2	Cell opening angle – stage 2								
	10°	**20°**	**30°**	**40°**	**50°**	**60°**	**70°**	**80°**	**90°**
10°	-	**2.97%**	**4.55%**	11.59%	17.76%	17.43%	25.68%	27.36%	28.71%
20°	**2.97%**	-	**4.99%**	9.66%	15.77%	15.46%	23.79%	25.65%	27.07%
30°	**4.55%**	**4.99%**	-	5.72%	12.44%	12.20%	20.69%	22.39%	23.88%
40°	11.59%	9.66%	5.72%	-	**2.40%**	**3.10%**	16.97%	18.75%	20.37%
50°	17.76%	15.77%	12.44%	**2.40%**	-	**1.18%**	10.59%	13.20%	15.21%
60°	17.43%	15.46%	12.20%	**3.10%**	**1.18%**	-	10.68%	13.34%	15.34%
70°	25.68%	23.79%	20.69%	16.97%	10.59%	10.68%	-	**3.24%**	**3.68%**
80°	27.36%	25.65%	22.39%	18.75%	13.20%	13.34%	**3.24%**	-	**2.74%**
90°	28.71%	27.07%	23.88%	20.37%	15.21%	15.34%	**3.68%**	**2.74%**	-

Source: The Author (2024).

Despite the increase in the cell opening, the thickness of the roof slab (modeled as a shading geometry) consistently acts as a barrier to natural light, reducing the illuminance on the work plane. Additionally, the cell's internal surface is concave. It only contributes to the beam radiation reflection (fixed at 10 bounces) when the opening is between 45° and 50° (due to solar altitude in Viçosa, Brazil).

The three groupings shown for UDI_{avg} (Figure 7) did not occur for the glare analysis (Figure 8), which exhibited an exponential increase according to the cell's opening, likely due to the limited influence of horizontal surfaces in increasing glare, as they only allow beam radiation to reach the work planes during months with higher solar angles. The higher the tilt angle, the higher the DGP increase compared to the base case. Higher opening areas displayed a more prolonged interquartile range, indicating a predominance of the middle half of the DGP distribution. They also showed divergent

maximum values, mainly due to the occasional circumstances when the top lighting cell cannot block beam radiation.

Figure 8: DGP relative to the base case (with no top lighting opening).

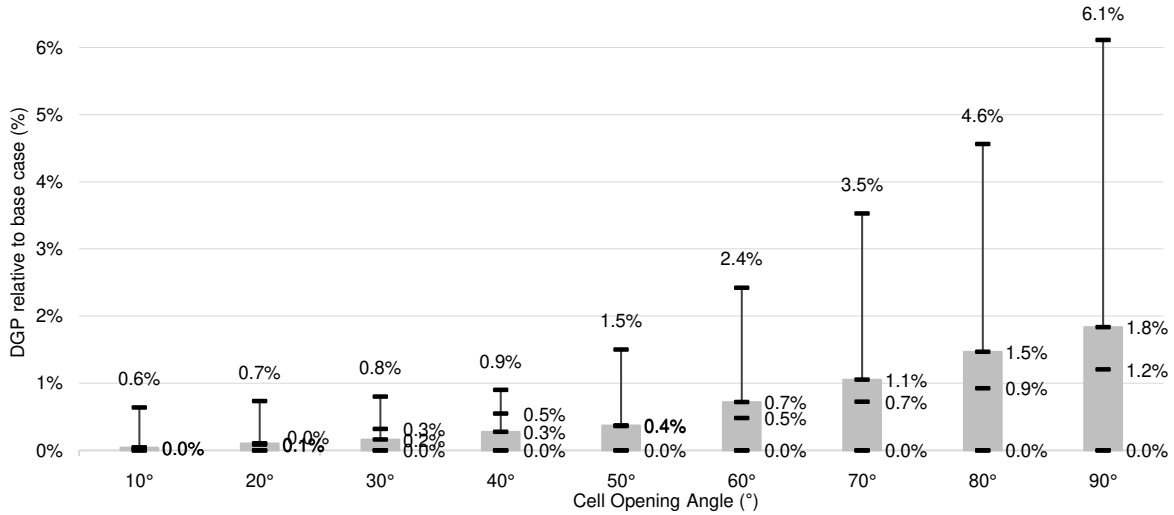

Source: The Author (2024).

Consistently, the openings could not supplement the illuminance requirement for 8 a.m. and had a low effect for 3 p.m., mainly due to the limited daylight availability in the sky dome, not solely due to the cell's design. Installing a convex surface inside the cell could enhance solar capture for these situations.

Considering the entire set of building fenestration, i.e., the summing of UDI_{avg} for the base case and the UDI_{avg} for the various top lighting applications, the cell has the potential to achieve 100% of hours within the appropriate illuminance range (or an UDI_{avg} of 100%). When discounting the beginning and end of the day when daylight levels are low (8 a.m. and 3 p.m.), the minimum UDI_{avg} is 28.7%. The author did not evaluate individual cell influences as the simulations sought to assess a real situation to be later replicated in the actual building.

Higher percentages of hours within the appropriate illuminance did not necessarily entail higher glare percentages, and higher glare percentages are not always due to larger openings. The internal reflections of multiple concave surfaces resulted in nonlinear gains. The maximum rate of hours with perceptible DGP considering the base case is 19.8% for 2 p.m. and 3 p.m. when there is higher daylight availability and lower cloudiness. Figures 9 and 10 indicate the most suitable cell tilt angles in two situations: (a) 0% DGP through the top lighting with the highest UDI_{avg}; (b) the highest UDI_{avg} with a maximum DGP of 35%. The author presents both options because adopting 0% DGP results in 28% of cases at 0° tilt angles (base case) and a maximum

UDI_{avg} increase of 55% from January to April. By allowing DGP gains above 0% and below 35%, the 0° opening occurrences decreased to approximately 13%, lessening the variability of opening positions and generating less movement and lower complexity, with 100% UDI_{avg} (Figure 10).

Figure 9: Tilt angle for 0% DGP.

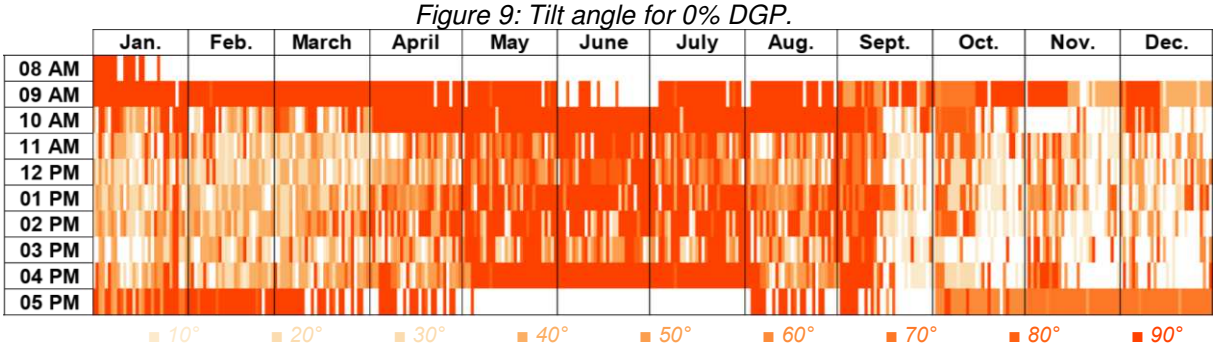

Source: The Author (2024).

Figure 10: Tilt angle allowing DGP below 35%.

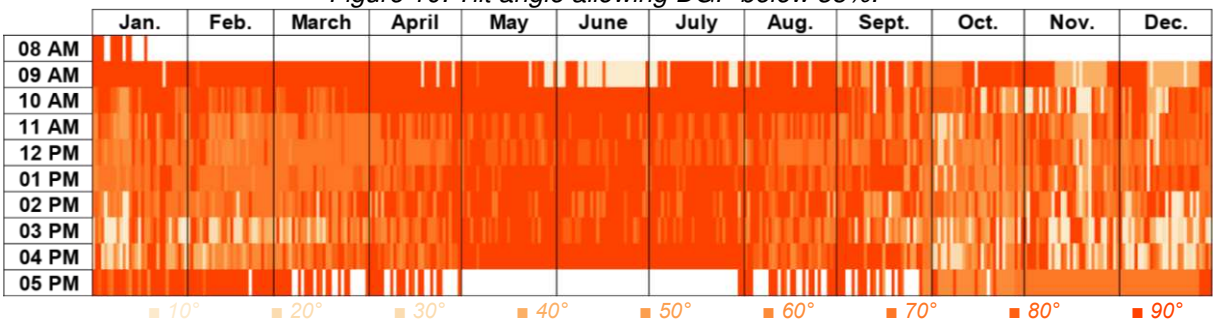

Source: The Author (2024).

From May to July, the cell was at 90° in 68% of the hours in both situations, indicating a higher illuminance gain with minimal glare. Despite the low daylight availability in the sky dome after 5 p.m., the top lighting aperture remained open between August and April in approximately 80% of cases. In contrast, from May to July, the cell was at 0° 98% of the time. During these months, the inability to provide adequate UDI_{avg} at the end of the day is also due to the boundary conditions, provided there is a mass of vegetation to the west obstructing the sun below sun altitudes of 50° (Figure 10). December had the highest glare rates due to increased beam radiation and less cloudiness, typical of summer in low latitudes. Therefore, when adopting the 0% DGP option, the cell remains closed for 41% of the time (Figure 9).

Figures 9 and 10 are relatively symmetrical, with higher correlations in the fall and winter due to comparable clear sky conditions, i.e., medium and low solar altitudes resulting in less radiation incidence on the work plane and more daylight redirection from the cell. Despite the visually proportional apertures due to the symmetry of solar movement, the boundary conditions and the construction of the weather file used in

the simulation do not allow analyses to be restricted to only half of the year. As discussed earlier, the months with lower solar altitudes are more consistent, while the RMSE between late summer and early winter reaches 18.7%.

Finally, the adaptive thermal comfort simulations did not indicate considerable variations in the percentage of comfortable hours for building users (Table 7). The base case without the top lighting appears to be the best scenario for the fall, winter, and spring months, with only a 0.2% increase in comfortable hours during the summer.

Table 7: Adaptive Thermal Comfort hours per season.

	Adaptive Thermal Comfort Percent Per Season							
	Hall				Kitchen			
	Summer	Fall	Winter	Spring	Summer	Fall	Winter	Spring
Base	94.7%	36.7%	10.0%	51.9%	96.5%	54.1%	6.3%	69.5%
10°	94.7%	36.6%	9.9%	51.6%	96.5%	53.7%	6.1%	69.4%
20°	94.6%	37.1%	10.2%	52.1%	96.5%	54.0%	6.3%	69.5%
30°	94.7%	36.6%	9.9%	51.6%	96.5%	53.7%	6.1%	69.3%
40°	94.7%	36.7%	10.0%	52.1%	96.5%	54.1%	6.3%	69.5%
50°	94.5%	36.9%	10.1%	52.1%	96.5%	53.8%	6.1%	69.4%
60°	94.6%	37.3%	10.3%	52.2%	96.5%	54.0%	6.3%	69.5%
70°	94.5%	37.1%	10.2%	52.1%	96.5%	53.8%	6.1%	69.4%
80°	94.5%	35.9%	9.8%	51.4%	96.6%	53.5%	6.0%	69.2%
90°	94.5%	36.1%	9.9%	51.5%	96.7%	53.5%	6.0%	69.1%

Source: The Author (2024).

For the Hall, cases with smaller apertures generally exhibit slightly better thermal comfort percentages, but the improvements are also minimal. Due to the surrounding microclimate, discomfort in the winter is significantly higher and remains unchanged even with the top lighting. Although horizontal surfaces are more susceptible to thermal loads, the aperture's size is not large enough to cause a significant thermal gain and alter the hours in thermal comfort. When comfort hours slightly increase, the author attributes it to radiation intake, particularly during months other than summer. Conversely, when comfort worsens, airflow reduces thermal inertia in the space.

5. Conclusions

This study presented a parametric modeling and computational simulation process based on daylight performance for the optimal positioning of a top lighting cell in an institutional building in a low-latitude climate. The methodology employed considered simulations for the entire year with hourly tilt motion for natural light admission. Due to the computational demand of image-based simulations for Daylight Glare Probability (DGP) and the high variability of motion combinations, the first part of this research developed a simplified process to assess the feasibility of grid and image-based simulations and identify the most contributing motion parameters through a Variance-

based Sensibility Analysis (ANOVA). The author expanded the number of simulations generally adopted by related studies developing year-round analysis instead of using representative dates (Lucarelli; Oliveira; Carlo, 2023). A comparison between both simulation workflows indicated that the first step (with 3600 cases) requires further simulations since the few representative days failed to portray the year. Therefore, using only representative days for environmentally active building applications is an unreliable approach.

The first stage, low DGP values with 1% results above the perceptible range, suggest that computationally expensive methods may not be justified for the adopted latitude (20°45'14''S). However, there is a need to evaluate the representativeness of image-based simulations for latitudes where solar altitudes are higher and direct radiation more easily reaches the working plane.

The ANOVA conducted for the tilting and revolving motion contribution indicated that the aperture is the most significant factor influencing natural light gain, as Lucarelli and Carlo (2019) suggested, accounting for 89.50% of the model contribution. Consequently, for the second stage of simulations, the author considered all hours with available natural light throughout the year, fixed the northeast orientation, and expanded the cell aperture steps to multiples of 10°. The second stage solely applied grid-based and imageless simulations to select the appropriate top lighting position based on UDI_{avg} and DGP.

Despite adopting multiple apertures, the simulations demonstrated the potential of the previously selected opening angles (30°, 60°, and 90°) to meet the daylight requirements. The comparability within similar opening clusters (10°, 20°, and 30°; 40°, 50°, and 60°; 70°, 80°, and 90°) is high, while displaying visible shifts between different clusters. Therefore, using only the three tilt angles from the first stage would decrease the number of simulations from 40150 to 16060, a 60% decrease.

Regardless of the aperture, most applications could increase the UDI_{avg}. Only during 8 a.m. and 5 p.m. is the opening position stuck on 0°. From 8 a.m. to 9 a.m., the daylight availability is relatively low, and between late autumn and early spring, the boundary conditions obstruct the low-altitude sun. Eliminating 8 a.m. and 5 p.m. for the selected latitude would further decrease the number of simulations by 25%.

As predicted by the initial simulations, the cell's contribution to glare increase is relatively low, reaching a maximum DGP increase of 6.1% (relative to the base case) for the largest aperture and higher solar altitude. In general, there was no glare increase for most cases, mainly due to the work plane position and the prevailing inability of beam radiation to reach it.

The author adopted two scenarios for choosing the optimal cell opening. Given the high variability in the cell's position when adopting 0% DGP and the constant variation in lighting conditions, which may cause discomfort, the author proposed adopting scenarios in which DGP is existing but imperceptible (below 35%), based on the continuous 1.2% averages and invariable 0% first quartiles for glare intake. Besides, the more permissive option averages 75% UDI_{avg}, with 45% of scenarios above 90% UDI_{avg}.

Acknowledgments

This study was financed by Coordenação de Aperfeiçoamento de Pessoal de Nível Superior – Brasil (CAPES) – Finance Code 001 and by Fundação de Amparo à Pesquisa de Minas Gerais (FAPEMIG), financing notice N° 001/2021 Universal Demand - under process code APQ-00266-21.

REFERENCES

ABNT. NBR ISO/CIE 8995-1: Iluminação de ambientes de trabalho, Parte 1: Interior. [*s. l.*], p. 46, 2013. DOI: http://www.abntcatalogo.com.br/norma.aspx?ID=196479.

ASHRAE. **ASHRAE 55 - Thermal Environmental Conditions for Human Occupancy**. 2023.

ATTIA, S.; CARLUCCI, S. Impact of different thermal comfort models on zero energy residential buildings in hot climate. **Energy and Buildings**, [*s. l.*], v. 102, p. 117–128, 2015. DOI: http://dx.doi.org/10.1016/j.enbuild.2015.05.017.

AYOUB, M. 100 Years of Daylighting: A chronological review of daylight prediction and calculation methods. **Solar Energy**, [*s. l.*], v. 194, n. October, p. 360–390, 2019. DOI: https://doi.org/10.1016/j.solener.2019.10.072.

AYOUB, M. A review on light transport algorithms and simulation tools to model daylighting inside buildings. **Solar Energy**, [*s. l.*], v. 198, n. January, p. 623–642, 2020. DOI: https://doi.org/10.1016/j.solener.2020.02.018.

BARBOSA, S. A. *et al.* Método de utilização do programa Energyplus para verificação de desempenho térmico de ambientes com fachadas duplas. **Ambiente Construído**, [*s. l.*], v. 13, n. 4, p. 121–134, 2013.

BAROZZI, M. *et al.* The sustainability of adaptive envelopes : developments of kinetic architecture. **Procedia Engineering**, [*s. l.*], v. 155, p. 275–284, 2016. DOI: http://dx.doi.org/10.1016/j.proeng.2016.08.029.

BASARIR, B.; CEM ALTUN, M. A redesign procedure to manufacture adaptive façades with standard products. **Journal of Facade Design and Engineering**, [*s. l.*], v. 6, n. 3, p. 077–100, 2018.

BÖKE, J. **Thinking- Skins**. 2020. 286 f. - Delft University of Technology, [*s. l.*], 2020. DOI: https://journals.open.tudelft.nl/abe/article/view/5035.

CÂNDIDO, C.; DE DEAR, R.; LAMBERTS, R. Combined thermal acceptability and air movement assessments in a hot, humid climate. **Building and Environment**, [*s. l.*], v. 46, n. 2, p. 379–385, 2011. DOI: http://dx.doi.org/10.1016/j.buildenv.2010.07.032.

CANNAVALE, A. *et al.* Energy savings due to building integration of innovative solid-state electrochromic devices. **Applied Energy**, [*s. l.*], v. 225, n. April, p. 975–985, 2018. DOI: https://doi.org/10.1016/j.apenergy.2018.05.034.

CARTANA, R. P. **Desempenho Térmico e Lumínico de Elementos de Controle Solar para Fachadas Desenvolvidos com Modelagem Paramétrica e Fabricação Digital**. 2018. 348 f. - Universidade Federal de Santa Catarina, [*s. l.*], 2018.

CHANG, T. W.; HUANG, H. Y.; DATTA, S. Design and fabrication of a responsive carrier component envelope. **Buildings**, [*s. l.*], v. 9, n. 4, p. 1–14, 2019.

DE DEAR, R.; BRAGER, G. S. Developing an Adaptive Model of Thermal Comfort and Preference Richard. **ASHRAE Transactions**, [*s. l.*], v. 104, p. 18, 1998.

EN. **DIN EN 15251 - Indoor environmental input parameters for design and assessment of energy performance of buildings addressing indoor air quality, thermal environment, lighting, and acoustics**. 2012.

EN. **EN 12464 - Light and lighting - Lighting of work places - Part 1: Indoor work places.** 2021.

FANGER, P. O. **Thermal comfort Analysis and Applications in Environmental Engineering**. [*S. l.: s. n.*], 1970.

GHERRI, B. **Assessment of Daylight Performance in Buildings. Methods and design strategies**. [*S. l.*]: WIT Press, 2015.

GLASSMAN, E. J.; REINHART, C. Facade optimization using parametric design and future climate scenarios. **13th BS2013**, [*s. l.*], p. 1585–1592, 2013.

HOSSEINI, S. *et al.* A morphological approach for the kinetic façade design process to improve visual and thermal comfort: Review. **Building and Environment**, [*s. l.*], v. 153, p. 186–204, 2019. DOI: https://doi.org/10.1016/j.buildenv.2019.02.040.

HOSSEINI, S. *et al.* Integrating interactive kinetic façade design with colored glass to improve daylight performance based on occupants' position. **Journal of Building Engineering**, [*s. l.*], v. 31, n. April, 2020.

HOSSEINI, S.; FADLI, F.; MOHAMMADI, M. Biomimetic kinetic shading facade inspired by tree morphology for improving occupant's daylight performance. **Journal of Daylighting**, [*s. l.*], v. 8, n. 1, p. 65–82, 2021.

ISO. ISO 7730 - Ergonomics of the thermal environment - Analytical determination and interpretation of thermal comfort using calculation of the PMV and PPD indices and local thermal comfort criteria. [*s. l.*], p. 52, 2005.

JAHANARA, A.; FIORAVANTI, A. **Kinetic Shading System as a means for Optimizing Energy Load: A Parametric Approach to Optimize Daylight Performance for an Office Building in Rome**. [*S. l.: s. n.*], 2017.

JAYATHISSA, P. *et al.* Optimizing building net energy demand with dynamic BIPV shading. **Applied Energy**, [*s. l.*], v. 202, p. 726–735, 2017. DOI: http://dx.doi.org/10.1016/j.apenergy.2017.05.083.

JONES, N. L. Fast climate-based glare analysis and spatial mapping. **Building Simulation Conference Proceedings**, [*s. l.*], v. 2, p. 982–989, 2019.

JONES, N. L.; REINHART, C. F. Experimental validation of ray tracing as a means of image-based visual discomfort prediction. **Building and Environment**, [*s. l.*], v. 113, p. 131–150, 2017. DOI: http://dx.doi.org/10.1016/j.buildenv.2016.08.023.

KIRIMTAT, A. *et al.* Review of simulation modeling for shading devices in buildings. **Renewable and Sustainable Energy Reviews**, [*s. l.*], v. 53, p. 23–49, 2016. DOI: http://dx.doi.org/10.1016/j.rser.2015.08.020.

KOLOKOTRONI, M. *et al.* Energy & Buildings Cool roofs : High tech, low-cost solution for energy efficiency and thermal comfort in low rise low-income houses in high solar radiation countries. **Energy & Buildings**, [*s. l.*], v. 176, p. 58–70, 2018. DOI: https://doi.org/10.1016/j.enbuild.2018.07.005.

KONIS, K. A novel circadian daylight metric for building design and evaluation. **Building and Environment**, [*s. l.*], v. 113, p. 22–38, 2017.

KONIS, Kyle; GAMAS, Alejandro; KENSEK, Karen. Passive performance and building form: An optimization framework for early-stage design support. **Solar Energy**, [*s. l.*], v. 125, p. 161–179, 2016. DOI: http://dx.doi.org/10.1016/j.solener.2015.12.020.

LE-THANH, L. *et al.* Optimal design of an Origami-inspired kinetic façade by balancing composite motion optimization for improving daylight performance and energy efficiency. **Energy**, [*s. l.*], v. 219, p. 119557, 2021. DOI: https://doi.org/10.1016/j.energy.2020.119557.

LECHNER, N.; ANDRASIK, P. **Heating, Cooling, Lighting: Sustainable Design Strategies Towards Net Zero Architecture**. 5. ed. Hoboken: John Wiley & Sons, 2021.

LEE, D.; CHO, Y.; JO, J. Assessment of control strategy of adaptive façades for heating, cooling, lighting energy conservation, and glare prevention. **Energy and Buildings**, [*s. l.*], v. 235, p. 110739, 2021. DOI: https://doi.org/10.1016/j.enbuild.2021.110739.

LIU, Binyan, *et al.* A study on daylighting metrics related to the subjective evaluation of daylight and visual comfort of students in China. **Energy and Buildings**, [*s. l.*], v. 287, p. 113001, 2023. DOI: https://doi.org/10.1016/j.enbuild.2023.113001.

LO VERSO, V. *et al.* Photobioreactors as a dynamic shading system conceived for an outdoor workspace of the state library of Queensland in Brisbane: Study of daylighting performances. **Journal of Daylighting**, [*s. l.*], v. 6, n. 2, p. 148–168, 2019.

LOONEN, R. **Approaches for Computational Performance Optimization of Innovative Adaptive Façade Concepts**. 2018. 190 f. - Eindhoven University of Technology, [*s. l.*], 2018. DOI: www.tue.nl/taverne.

LOONEN, R. *et al.* Climate adaptive building shells: State-of-the-art and future challenges. **Renewable and Sustainable Energy Reviews**, [*s. l.*], v. 25, p. 483–493, 2013.

LUCARELLI, C. D. C.; CARLO, J. C. Parametric modeling simulation for an origami-shaped canopy. **Frontiers of Architectural Research**, [*s. l.*], v. 9, n. 1, p. 67–81, 2019. DOI: https://doi.org/10.1016/j.foar.2019.08.001.

LUCARELLI, C. D. C.; OLIVEIRA, M. M.; CARLO, J. C. Climate-active building enclosures: an integrative literature review. **PARC Pesquisa em Arquitetura e Construção**, [*s. l.*], v. 14, p. e023023, 2023.

LUCARELLI, C. C.; OLIVEIRA, M. M.; CARLO, J. C. Thermal calibration of an existing institutional building. *In*: , 2022, Porto Alegre. **XIX Encontro Nacional De Tecnologia Do Ambiente Construído**. Porto Alegre: [*s. n.*], 2022.

MARDALJEVIC, J. *et al.* Daylighting metrics for residential buildings. *In*: , 2011. **CIE International Conference 1**. [*S. l.: s. n.*], 2011. p. 93–111.

MOLONEY, J. **Designing kinetics for architectural facades: state change**. [*S. l.*]: Routledge, 2011.

NABIL, A.; MARDALJEVIC, J. Useful daylight illuminance: a new paradigm for assessing daylight in buildings. **Lighting Research and Technology**, [*s. l.*], v. 37, n. 1, p. 21–59, 2005.

NABIL, A.; MARDALJEVIC, J. Useful daylight illuminances: A replacement for daylight factors. **Energy and Buildings**, [*s. l.*], v. 38, n. 7, p. 905–913, 2006.

NGUYEN, T. **Shape gramma-based adaptive building envelopes: Towards novel climate-responsive facade systems for sustainable architectural design in Vietnam**. 2019. 319 f. - University of Derby, [*s. l.*], 2019.

PAULE, B. *et al.* Electrochromic glazings: Dynamic simulation of both daylight and thermal performance. **Energy Procedia**, [*s. l.*], v. 122, n. January, p. 199–204, 2017.

PESENTI, M.; MASERA, G.; FIORITO, F. Exploration of Adaptive Origami Shading Concepts through Integrated Dynamic Simulations. **Journal of Architectural Engineering**, [*s. l.*], v. 24, n. 4, p. 04018022, 2018.

PIERSON, C. *et al.* Tutorial: Luminance Maps for Daylighting Studies from High Dynamic Range Photography. **LEUKOS - Journal of Illuminating Engineering Society of North America**, [*s. l.*], v. 17, n. 2, p. 140–169, 2021. DOI: https://doi.org/10.1080/15502724.2019.1684319.

REINHART, C. F.; MARDALJEVIC, J.; ROGERS, Z. Dynamic Daylight Performance Metrics for Sustainable Building Design. **LEUKOS: The Journal of the Illuminating Engineering Society of North America**, [*s. l.*], p. 37–41, 2013.

REINHART, C. F.; WIENOLD, J. The daylighting dashboard e A simulation-based design analysis for daylit spaces. **Building and Environment**, [*s. l.*], v. 46, n. 2, p. 386–396, 2011. DOI: http://dx.doi.org/10.1016/j.buildenv.2010.08.001.

ROMANO, R. *et al.* What is an adaptive façade? Analysis of recent terms and definitions from an international perspective. **Journal of Facade Design and Engineering**, [*s. l.*], v. 6, n. 3, p. 065–076, 2018.

SHEIKH, W.; ASGHAR, Q. Adaptive biomimetic facades: Enhancing energy efficiency of highly glazed buildings. **Frontiers of Architectural Research**, [*s. l.*], v. 8, n. 3, p. 319–331, 2019. DOI: https://doi.org/10.1016/j.foar.2019.06.001.

SHI, X.; TABLADA, A.; WANG, L. Influence of two motion types on solar transmittance and daylight performance of dynamic façades. **Solar Energy**, [*s. l.*], v. 201, n. May, p. 561–580, 2020.

STRAUB, K. W. *et al.* Determinação da temperatura de neutralidade em salas de aula do ensino superior para as zonas bioclimáticas do estado de Mato Grosso. **Ambiente Construído**, [*s. l.*], v. 17, n. 1, p. 97–109, 2017.

SUBRAMANIAM, S. **Daylighting Simulations with Radiance using Matrix-based MethodsLawrence Berkeley National Laboratory**. [*S. l.: s. n.*], 2017. DOI: https://unmethours.com. .

TABADKANI, A.; BANIHASHEMI, S.; HOSSEINI, M. Daylighting and visual comfort of oriental sun-responsive skins: A parametric analysis. Building Simulation, [s. l.], v. 11, n. 4, pp. 663–676, 2018.

WIENOLD, J.; CHRISTOFFERSEN, J. Evaluation methods, and development of a new glare prediction model for daylight environments with the use of CCD cameras. **Energy and Buildings**, [*s. l.*], v. 38, n. 7, p. 743–757, 2006.

YANG, C. **The Intelligent Control Strategy of Kinetic Façades for Daylight and Energy Performance**. 2020. 213 f. - University of Southern California, [*s. l.*], 2020.

YI, H. *et al.* 3D-printed attachable kinetic shading device with alternate actuation: Use of shape-memory alloy (SMA) for climate-adaptive responsive architecture. **Automation in Construction**, [*s. l.*], v. 114, n. July 2019, p. 103151, 2020. DOI: https://doi.org/10.1016/j.autcon.2020.103151.

YI, H.; Kim, Y. Self-shaping building skin: Comparative environmental performance investigation of shape-memory-alloy (SMA) response and artificial intelligence (AI) kinetic control. **Journal of Building Engineering**, [*s. l.*], v. 35, n. December, p. 102113, 2021. DOI: https://doi.org/10.1016/j.jobe.2020.102113.

YI, Y.; SHARSTON, R.; BARAKAT, D. Auxetic structures and advanced daylight control systems. **Journal of Facade Design and Engineering**, [*s. l.*], v. 7, n. 1, p. 63–74, 2019.

YU, Fei; WENNERSTEN, Ronald; LENG, Jiawei. A state-of-art review of concepts, criteria, methods, and factors for reaching 'thermal-daylighting balance.' **Building and Environment**, [*s. l.*], v. 186, n. September, p. 107330, 2020. DOI: https://doi.org/10.1016/j.buildenv.2020.107330.

ZHANG, Anxiao *et al.* Optimization of thermal and daylight performance of school buildings based on a multi-objective genetic algorithm in the cold climate of China. **Energy and Buildings**, [*s. l.*], v. 139, p. 371–384, 2017. DOI: http://dx.doi.org/10.1016/j.enbuild.2017.01.048.

ZHENG, Chi *et al.* Multi-objective optimization of energy, thermal, and visual comfort for dormitory buildings in the cold climate of China. **Indoor and Built Environment**, [*s. l.*], v. 0, n. 92, p. 1–19, 2023.

CHAPTER IV – Structural and Optical Behavior of Rapidly-Aged and Unaged Engineering-Grade Copolymers Produced via Fused Deposition

Abstract

Thermoplastic copolymers often show good physicomechanical properties, undergoing extensive deformation and maintaining chemical resistance. However, they can experience physical and optical fluctuations when exposed to harsh environmental conditions. This study compares the optical and structural changes of engineering-grade FMD-compatible copolymers (PETG, ASA, and TRITAN™) through uniaxial tensile and compressive stress before and after accelerated aging processes. The author evaluated 120 test coupons, obtaining the ultimate tensile and compressive stresses (UTS and UCS), resulting strains, and Young's Moduli before and after 90 8-hour semi-controlled weathering cycles. This research also evaluated visual changes using the CIE L*a*b* space and reflectance values. For all coupons, the temperature increase from UVA exposure boosted the material's elasticity and elongation, leading to higher UTSs and lower Young's Moduli. The opposite is not true for compressive scenarios. White materials reached lower UTS than transparent due to pigment addition, slight distinctions in print settings, and higher thermal energy gain. Overall, unaged PETG exhibited the highest UTSs, averaging 24.5 MPa and 28.11 MPa for white and transparent shades, respectively. After aging, the pattern persists, with PETG reaching 25.58 MPa and 28.90 MPa for the mentioned hues. ASA, which consistently had the lowest average UTS, showed the highest UCS for both colors. However, PETG remained relatively invariant, reducing 0.97 MPa for white and 1.55 MPa for transparent. Comprehensively, the FDM-induced phase change and the aging resulted in darkening and loss of gloss. Ultimately, this study indicates PETG as the most suitable material for tensile and compressive applications, showing the least color variation.

Keywords: *Polymers; uniaxial strength; structural analysis; chromatic variance; accelerated aging.*

1. Introduction

According to Gershenfeld (2012), the first numerically controlled machine dates from 1952, with a rudimentary computer connected to manual milling machines. Until then, a design's materialization through the conventional manufacturing process relied on analog information. Technological evolution and the emergence of integrated digital tools for visualization, representation, and fabrication have played crucial roles in architectural design as a new paradigm for education, academic research, and architectural practice, opening precedents to new design methodologies and theories (Oxman, 2006, 2017).

During the last two decades, the debate about the impact of digital culture on architecture has shifted towards fabrication. Digital manufacturing (DM) is relatively recent and appeared due to the widespread use of computer numerically controlled machines (CNC) (Caneparo, Luca, 2014; Scheurer, 2010). Specifically, additive manufacturing (AM) is a broad group of techniques that turn digital models into functioning components using computer-aided design (CAD) data. AM decreases the lead time for creating and producing functional components, stimulates complex geometries' materialization, and enables highly customized and low-volume elements (Menezes *et al.*, 2022). As a subcategory of AM, polymer-based fused-deposition modeling (FDM) expedites the fast production of objects from various materials.

Among these, thermoplastic polymers present good physicomechanical properties and can undergo large deformation, are lightweight, bond with various polymers, and retain good chemical and solvent resistance (Awasthi; Banerjee, 2021). However, they can experience physical and chemical fluctuations if subjected to environmental degradation, e.g., loss of structural characteristics, reduced durability, and spectrophotometric or chromatic variation. Standard environmental factors affecting polymer attributes include "liquid or vapor water, aqueous solutions, oxygen, UV/solar radiations, [temperature variation], chemicals, acid or alkaline environments, fuels, pollutants […]" (Frigione; Rodríguez-Prieto, 2021, p.1). Most happen simultaneously, leading to faster degradation for outdoor-exposed cases.

Even though Frigione and Rodríguez-Prieto (2021) indicate that natural polymer aging provides the most reliable results, on-field studies demand long-time analysis to deliver statistically representative data. Therefore, it is necessary to expedite the aging

process using accelerated aging techniques to intensify one or more environmental factors and simulate long-term exposure.

This study compares the structural integrity of unaged and rapidly-aged additive-manufactured samples of polyethylene terephthalate glycol (PETG), acrylonitrile styrene acrylate (ASA), and Eastman Commercial TRITAN™ copolymer (terephthalic acid - tetramethylcyclobutanediol/cyclohexanedimethanol TPA-TMCD/CHDM) through uniaxial tensile and compressive stress and strain and chromaticity analysis. Section 2 presents an overview of polymer-based FDM processes, the adopted thermoplastics, and a description of mechanical testing and polymer degradability. Section 3 details the samples' preparation and experimental tests (i.e., thermal aging, mechanical tests, and chromaticity evaluation). We present the results in Section 4 and a summary and conclusions in Section 5.

2. Theoretical Frameworks

2.1. Digital (DM) and Additive Manufacturing (AM)

The manufacturing paradigm derives from a long process of manual crafting. Mass production became possible in the early 20th century through the Industrial Revolution, and the manufacturing system has economically evolved through technology development (Ham; Lee, 2019). Digital manufacturing (DM) is a descendant of MIT's first numerically controlled mill and presents a broad range of applications, extending beyond aiding the generation of planar drawings and three-dimensional models, combining digital modeling and manufacturing processes. It consists of two phases: the first one is the two and three-dimensional modeling (in general, solids and surfaces, objects with volume, mass, and center of gravity) within the digital space; the second one is the manufacturing phase, which transforms the virtual design into a real object through DM machines.

DM reduces the time and cost needed for designing, assembling, and assessing prototypes and final products, allowing creators to directly transfer information to machines, alleviating geometry constraints on mass production strategies, and enabling custom production without increasing labor. According to Agirbas (2017) and Keating and Oxman (2013), DM can be reductive (milling, cutting, and eroding), additive (automated assembly, lamination, extrusions, and other forms of 3D printing),

formative, composite or hybrid, immaterial, and informed. Firstly, ASTM F2792 (American Society for Testing and Materials, 2012) and lastly, ISO/ASTM 52900 (International Organization of Standardization/ American Society for Testing and Materials, 2021) defined the standard terminology for additive manufacturing (AM) processes. AM is also known as 3D printing (3DP) or rapid prototyping (RP). These processes gradually build two-dimensional material layers to produce a three-dimensional object.

FDM machines use a thin filament of solid thermoplastic polymer, heated above the melting point (i.e., glass transition temperature) and extruded through a small nozzle, which deposits the semi-liquid melted plastic onto the build platform. A major advantage of 3D printing lies in producing components where conventional manufacturing techniques have reached their limits. AM processes are ‘rapid’ due to several reasons. The prototype parts are available within several hours, rather than the days or weeks required using conventional manufacturing. Designers can rapidly create accurate physical representations of their design concepts to examine and manipulate them as physical models.

According to Gibson, Rosen, and Stucker (2015), recently, AM evolved to the extent that the output is suitable for end-use, explaining why the terminology evolved from rapid prototyping to additive manufacturing. The mechanical properties of FDM-printed parts depend on the material, structural parameters (i.e., raster angle, infill density, printing orientation, and stacking sequence), and manufacturing variables (i.e., printing and nozzle speed, extrusion temperature and rate, and bed temperature) (Ansari; Kamil, 2021; Khosravani *et al*., 2022). FDM allows control over the structural matrix (shape, size, branching, bridging, orientation, etc.) and filament settings, which vary according to the material. Due to the assortment of polymer-based materials, many studies assess how to enhance printing quality (Alafaghani; Qattawi, 2018).

2.2. Thermoplastic Materials

FDM applies several polymers, including acrylonitrile butadiene styrene (ABS), polylactide (PLA), polyethylene terephthalate (PET), and copolymers such as acrylonitrile styrene acrylate (ASA), polyethylene terephthalate glycol-modified (PETG) and terephthalic acid-tetramethylcyclobutanediol/cyclohexanedimethanol polyester (TRITAN^{TM}). According to Callister Jr. and Rethwisch (2020), the mechanical

properties of polymers in high temperatures classify them as thermoplastic polymers or thermoset materials. The former presents reversible and repeatable cycles and softens or liquefies when heated and hardens when cooled. The molecular motion diminishes bonding forces, facilitating pressure deposition from the FDM machines' heated extrusion block. When raised above the glass transition temperature, the molten plastic undergoes irreversible degradation. The latter comprises network polymers that permanently harden and do not soften upon heating due to the high-density cross-linkages (Callister Jr.; Rethwisch, 2020; Wang *et al.*, 2020).

For instance, petroleum-based (e.g., ABS, ASA, and PET) and biodegradable (e.g., PLA) thermoplastics and blends are generally FDM's most frequently encountered materials. Most thermosetting polymers are viscous liquids cured using a photo or thermal polymerization process and do not apply to FDM techniques (Wang *et al.*, 2020).

According to Bryden (2014) and Jafferson and Chatterjee (2021), thermoplastics and thermosets can be general-purpose, engineering-grade, and ultra-performance materials. Excepting general-purpose materials, these polymers have good impact strength, high tensile force, and good resistance to scratching and chemicals (Fig. 1) (Jafferson; Chatterjee, 2021).

Figure 1: Thermoplastics and thermosets.

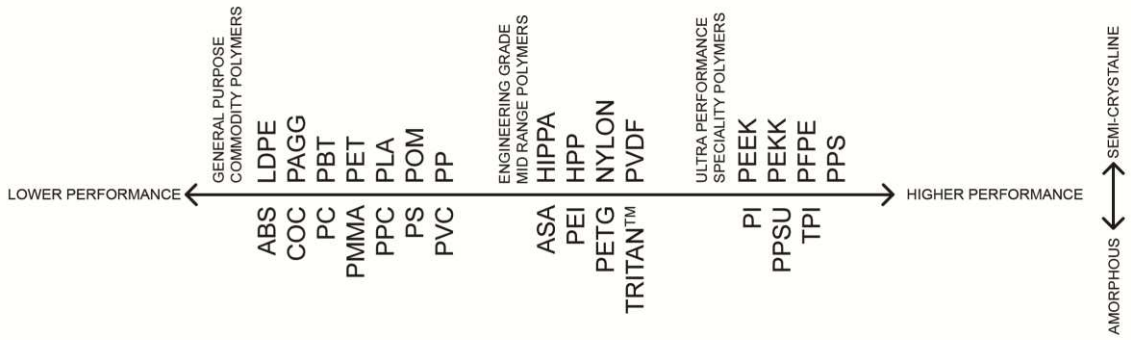

Source: The Author (2024).

Another polymer classification ranges from amorphous to crystalline regimes depending on the cooling rate during solidification. As deformation relies on the degree of crystallinity, the higher the crystallinity, the more rigid the polymer. Crystallinity enhances polymer strength and toughness, influencing chemical, mechanical, electrical, and optical properties and causing brittleness. Conversely, amorphous polymers are malleable, exhibit relatively low heat resistance (principally when close

to the glass transition temperature), are less prone to shrinkage, and can satisfactorily bond to substrates. For copolymers, “the more irregular and random the repeat unit arrangements, the greater the tendency for the development of noncrystallinity” (Callister Jr.; Rethwisch, 2020, p.555).

FDM’s filament properties (such as ductility, viscosity, and crystallinity) and printing parameters (such as orientation, raster angle, layer thickness, infill pattern and density, and printing speed) profoundly influence the final objects’ mechanical properties, affecting isotropy, surface smoothness, and fabrication time (Braconnier; Jensen; Peterson, 2020; Popescu *et al.*, 2018). For instance, tensile strength improves with infill density and smaller layer thicknesses, reaching the highest value when the raster direction is parallel to the direction of the applied force (Popescu *et al.*, 2018; Vukasovic *et al.*, 2019).

Several studies detail the influence of print settings on the mechanical properties of FDM-printed parts, emphasizing the effect of printing orientation surface quality, geometric precision, and time and cost of manufacturing. Li *et al.* (2018), Chacón *et al.* (2017), and Hanon *et al.* (2020) showed that increasing the total number of printing layers contributes to higher tensile strengths. For instance, Hanon *et al.* (2020) demonstrated that 0.1 mm layer thicknesses increased elongation at break and ultimate tensile strength. Zieman *et al.* (2015) and Hanon *et al.* (2020) indicated that 45/90° raster angle specimens (aligned along the longest dimension) had the highest tensile strength, declining below 45° as the perpendicular test load leads to dismantling the print lines with modest strength and elongation. Unlike Vukasovic *et al.’s* (2019), compression tests indicated that the printing orientation does not affect the specimens’ performance.

Each research selects the best-fit polymer for a specific FDM machine or design application, hindering comparisons. Different polymers will perform differently according to filament brand, composition, color, conditioning procedures, printing parameters (e.g., layer thickness, build orientation, feed rate), machine specificities (i.e., cartesian, delta, or polar), etc. Even though previous studies show how they should perform, understanding their mechanical properties in each situation is paramount. Polymers and copolymers are highly sensitive to temperature and the chemical nature of the environment (presence of water, oxygen, organic solvents, etc.) and, considering the lack of specific standards on test methods and the large variety

of FDM machines and materials, there is not a set of optimal parameters for a machine/polymer/application combination (Popescu *et al.*, 2018).

2.3. Engineering-grade copolymers: ASA, PETG, and TRITAN™

2.3.1. ASA

According to Kamran and Saxena (2016), acrylonitrile butadiene styrene (ABS) was one of the first materials in polymer printing, patented and presented to commercial markets in 1954. It is cheap, withstands high temperatures, and has good impact resistance, toughness, and rigidity. It can also be post-processed in various ways (sanding, gluing, filling, and chemical smoothing). Its great disadvantages are its melting temperatures of about 215 °C to 250 °C (ABS is amorphous and has no true melting point), which demands a hotbed print surface and enclosure to prevent warping, and its lack of resistance to ultraviolet light (UV), which potentially decreases its mechanical properties during exposure to harsh environmental conditions (Ansari; Kamil, 2021; Cano-Vicent *et al.*, 2021; Pertuz; Díaz-Cardona; González-Estrada, 2020).

Acrylonitrile styrene acrylate or acrylic styrene acrylonitrile (ASA) is an amorphous thermoplastic and rubber-modified copolymer alternative to ABS. ASA is significantly more resistant to environmental stress cracking and presents a lower glass transition temperature of about 200 °C, providing better low-temperature properties (Ansari; Kamil, 2021; Cano-Vicent *et al.*, 2021). It is easy to print, has good dimensional stability and layer-to-layer adhesion, is UV-stable, can withstand extreme temperature swings, and retains gloss, color, and mechanical properties during exposure to outdoor conditions (Guessasma *et al.*, 2016). According to Izdebska-Podsiadły (2022), “ASA [has] the best aesthetics of any of FDM thermoplastic […] with a [high-quality] surface-finish” (Izdebska-Podsiadły, 2022, p.182).

ABS and ASA printing settings are similar (Chart 1), demanding high nozzle temperatures, a heated bed with good bonding, and no cooling fan during printing. The printed parts need vapor-smoothing (controlled exposure to acetone) and drying since unfinished ABS and ASA prints have very high-temperature sensitivity, provoking warping, cracking, and shrinkage under less-than-ideal conditions (Izdebska-Podsiadły, 2022).

Chart 1: Typical properties of generic ABS and ASA filaments.

			ABS	ASA
Filament Properties	Density (g/cm^3)		1.03 - 1.08	1.05 - 1.07
	Thermal conductivity (W/mK)		0.173 - 0.202	0.173
	Visual appearance	Gloss (%)	15.0 - 78.0	21.0 - 96.5
		Reflectance (%)	83.7 - 93.0	85.5 - 90.0
		Haze (%)	1.46 - 4.02	1.0 - 8.0
	Water absorption	50% relative humidity (%)	0.70	0.35
		Immersed (%)	0.27 - 0.31	0.30 - 0.32
	Tensile strength	Yield (MPa)	39	29
		Break (MPa)	33.9	26.8
	Tensile elongation	Yield (%)	3.5	2
		Break (%)	4.8	3.5
	Tensile modulus (GPa)		1.50 - 3.14	1.78 - 2.58
	Flexural strength (MPa)		53.9 - 86.2	55.3 - 80.0
	Flexural modulus (GPa)		1.86 - 2.96	1.81 - 2.67
Print settings	Melt flow rate (MRF) (g/10min)		41	14.2
	Melting temperature (°C)		225 - 245	200 - 250
	Bed temperature (°C)		80 - 110	90 - 110
	Print speed (mm/s)		30 - 80	35 - 70
	Bed adhesion		PEI or PET tape, ABS slurry, hairspray, glue sticks	PEI or PET tape/sheet ABS/ASA slurry
	Cooling fan		Not required	
	Enclosure		Required for heated bed temperatures below 100 °C	

Source: Adapted from Izdebska-Podsiadły (2022) +Overview of materials for Acrylonitrile/Styrene/Acrylate (ASA), Unreinforced, Molded (matweb.com) + Overview of materials for Acrylonitrile Butadiene Styrene (ABS), Extruded (matweb.com)

2.3.2. PETG

Polyesters (PESs) are engineering thermoplastic semicrystalline polymers that contain the ester functional group in their main chain (Mendivil-Escalante *et al.*, 2015). Polyethylene terephthalate (PET) is the most common thermoplastic polymer. It is hard, stiff, strong, and highly shatter and deformation-resistant, with a good strength-to-weight ratio (Izdebska-Podsiadły, 2022, p.196). PET can be highly transparent and colorless, with thicker sections usually opaque.

PESs are as easy to use as PLA filaments and have the strength and durability of ABS with melting temperatures ranging from 160 °C to 250 °C. Unlike ABS and ASA, PESs are not prone to warping and are highly adhesive, easily sticking to heated beds, glass, or painter's tape. Raw PET is normally applied for textiles and food packaging. It is not as typical as a printing filament as its glycol-modified version, PETG (polyethylene terephthalate glycol-modified) (Cano-Vicent *et al.*, 2021). The cyclohexanedimethanol addition reduces the opaqueness, bubbling, and crystallinity of PETG, lowering the glass transition temperature compared to PET. Therefore, PETG maintains many desirable mechanical (formability, resistance to brittleness and shock, and high flexibility and toughness) and chemical properties (glasslike

appearance, waterproofness, and good chemical resistance) of PET while being easier to use. The glycol in the polymer structure prevents visible hazing, warping, crystallization, and hygroscopy (Callister Jr.; Rethwisch, 2020; Valvez; Silva; Reis, 2022).

PETG is mostly odorless, unlike ABS and ASA, so printing with an enclosure is unnecessary. Even though PETG is a PES, it requires high nozzle temperatures, usually between 220 °C and 260 °C, and moderately heated bed temperatures of about 70°C (Chart 2) (Izdebska-Podsiadły, 2022). Due to its bonding ease, PETG can damage the print surface if not coated with glue or hairspray (due to vinyl acetate and crotonic acid monomers).

Chart 2: Typical properties of generic PET and PETG filaments.

			PET	PETG
Filament Properties	Density (g/cm^3)		1.34	1.27
	Thermal conductivity (W/mK)		0.30	0.21
	Visual appearance	Reflectance (%)	87.5 - 90.1	82.0 - 91.0
		Haze (%)	0.25 - 4.93	0.20 - 1.00
	Water absorption	50% relative humidity (%)	0.2 -0.5	0.13
		Immersed (%)	0.40 -0.70	0.13 - 0.20
	Tensile strength	Yield (MPa)	54.3 - 84.8	50.0
		Break (MPa)	70	28
	Tensile elongation	Yield (%)	4.0 - 4.1	4.0 - 8.4
		Break (%)	9	10
	Tensile modulus (GPa)		2.3	2.1
	Flexural strength (MPa)		80.7 - 121.4	68
	Flexural modulus (GPa)		1.1 - 2.2	2
Print settings	Melt flow rate (MRF) (g/10min)		14 - 60	34 - 39
	Melting temperature (°C)		210 - 230	220 - 250
	Bed temperature (°C)		50 - 60	60 - 80
	Print speed (mm/s)		40 - 80	30 - 90
	Bed adhesion		Glue stick, blue painter's tape	PEI, blue painter's tape, hairspray
	Cooling fan		Required	
	Enclosure		Not required	

Source: Adapted from Izdebska-Podsiadły (2022) + Mitsubishi Chemical Advanced Materials Ertalyte® PET-P, Polyester-semi-crystalline thermoplastic, extruded (ASTM Product Data Sheet) (matweb.com) + Overview of materials for PETG Copolyester (matweb.com)

2.3.3. TRITAN™

According to Guarda and Augusto (2020), TRITAN™ is the most resistant and durable copolyester. It is a new-generation copolyester with further advantages, including easier processing, higher temperature resistance, and significantly higher impact resistance (Lim, 2017). It also withstands high pressure and alkaline, acidic, or aqueous solutions. Like PETG copolyester, TRITAN™ displays good in-between layer adhesion and comparable tensile strength, ductility, and, consequently, tenacity

(Cavalcanti; Banea; de Queiroz, 2020; Lim, 2017). It is also much more durable and flexible than ABS and ASA.

TRITAN™ originates from the melt phase copolymerization of 2,2,4,4-tetramethyl-1,3-cyclobutanediol (TMCD) or poly(1,4-cyclohexylenedimethylene terephthalate) (PCT) and 1,4 cyclohexanedimethanol (CHDM) with dimethyl terephthalate (DMT) (Lim, 2017). Incorporating TMCD results in higher glass transition temperatures, causing TRITAN™ to crystallize very slowly compared to ABS, ASA, and PET, making it easier to mold into amorphous transparent parts even in thicker sections, unlike other copolyesters. It also experiences lower residual stress, which causes warpage, shrinkage, distortion, stress cracking, and poor chemical resistance. Consequently, TRITAN™ has one of the highest chemical resistances in organic solvents such as adhesives, paints, and printing inks (Erokhin; Gordeev; Ananikov, 2019; Farias, 2022). Its printing temperature ranges from 260 °C to 290 °C, with heated bed temperatures starting at 100 °C (Chart 3). Furthermore, TRITAN™ filaments present a higher level of light transmission than multiphasic transparent ABS with a water-like, neutral color.

Chart 3: Typical properties of TRITAN™ HT filament.

			TRITAN™
Filament Properties	Density (g/cm^3)		1.18
	Thermal conductivity (W/mK)		0.21
	Visual appearance	Reflectance (%)	90
		Haze (%)	0 - 0.8
	Water absorption	50% relative humidity (%)	0.13
		Immersed (%)	0.18
	Tensile strength	Yield (MPa)	47
		Break (MPa)	58
	Tensile elongation	Yield (%)	7
		Break (%)	185
	Tensile modulus (GPa)		15.5
	Flexural strength (MPa)		59
	Flexural modulus (GPa)		14.9

Print settings	Melt flow rate (MRF) (g/10min)	14 - 60
	Melting temperature (°C)	260 - 290
	Bed temperature (°C)	100 - 120
	Print speed (mm/s)	40 - 60
	Bed adhesion	PEI, blue painter's tape, hairspray
	Cooling fan	Not required
	Enclosure	Required

Source: Adapted from Izdebska-Podsiadły (2022) + Eastman 1223 Copolyester (matweb.com) + Material Data Center | Datasheet TRITAN™ GX100 + Eastman TRITAN™ Copolyester TX1000 | TDS | Eastman Chemical Company

2.4. Mechanical testing

As every mechanical system is subject to loads during operation, it is necessary to comprehend how the materials that make up those mechanical systems behave.

Callister Jr. and Rethwisch (2020) state that the axial forces (tensile and compressive stress and strain) are the most relevant loading types in polymer research.

The ISO/ASTM 52901 (International Organization of Standardization/American Society for Testing and Materials, 2017) standard defines the general guidelines and prerequisites for purchased AM parts. Still, there is no specific international standard for FDM-printed pieces. The American Society for Testing and Materials (ASTM) and the International Organization for Standardization (ISO) primarily specify standard plastic tests, including sample preparation and plastic product subclassification (Kawalkar; Dubey; Lokhande, 2021). Even though many plastic families have their own ASTM and ISO guidelines, currently, there is no published standard or specification for polymeric FDM mechanical characterization, mainly due to the anisotropic properties generated by layer deposition (Kawalkar; Dubey; Lokhande, 2021).

According to Fernandes (2022) and Popescu *et al.* (2018), mechanical testing for metals and plastics can apply to FDM parts, even if they do not consider voids and anisotropy. According to Vukasovic *et al.* (2019), most studies evaluate the tensile properties of unreinforced plastics according to the ASTM D638-22 (American Society for Testing and Materials, 2022; Alafaghani; Qattawi, 2018; Braconnier; Jensen; Peterson, 2020; Hsueh *et al.*, 2021; Li; Lou, 2020), flexural strength according to ISO 178-19 (International Organization of Standardization, 2019; Tosto *et al.*, 2020; Wang *et al.*, 2021), and uniaxial compression according to ASTM D695-15 (Guessasma *et al.*, 2016; Vukasovic *et al.*, 2019). Chart 4 presents all ASTM/ISO standards published to date.

Chart 4: ASTM and ISO Standards for Additive Manufacturing.

Standard	
ISO 17296-2	General guidelines in AM process categories and feedstock
ISO 17296-3	General guidelines for AM characteristics for testing methods
ISO 27547-1	General guidelines for laser sintering of testing specimens of thermoplastic materials using AM technology
ISO/ASTM 52900	General theories in AM Terminologies
ISO/ASTM 52901	General theories for buying AM parts
ISO/ASTM 52902	Testing artifact guidelines for additive manufacturing systems
ISO/ASTM 52903-1	Guidelines for feedstock plastic materials used in the extrusion process
ISO/ASTM 52903-2	Guidelines for process equipment plastic materials used in the extrusion process
ISO/ASTM 52904	General guidelines for process characteristics and performance, including application for metal PBF process
ISO/ASTM 52907	Guidelines to characterize metal powders

(Continues)

(Chart 4 continues): ASTM and ISO Standards for Additive Manufacturing.)

ISO/ASTM 52910	Requirements and recommendations for AM design
ISO/ASTM 52911-1	Design guidelines for Metal LPBF processes
ISO/ASTM 52911-2	Design guidelines for Polymer LPBF processes
ISO/ASTM TR52912	Recommendations for grading AM
ISO/ASTM 52915	Guidelines for AM file format Version 1.2 in AMF type
ISO/ASTM 52921	Guidelines for determining coordinate systems and testing methodologies in AM processes
ISO/ASTM 52941	Guidelines for AM system performance for testing LPBF machines for metal powders in the aerospace industry
ISO/ASTM 52942	Guidelines for qualified machine operators of LPBF machines for metal powders and application of parts used in the aerospace industry
ISO/ASTM 52950	Guidelines for data processing in AM

Source: The Author (2024).

Even though there is a myriad of FDM printers and raw materials from different manufacturers, generally, mechanical evaluation processes lead to comparable results for filaments such as PLA (Oviedo *et al.*, 2020; Santana *et al.*, 2018), ABS (Abeykoon; Sri-Amphorn; Fernando, 2020; D'Amico; Debaie; Peterson, 2017; Khabia; Jain, 2019), PETG (Tanikella; Wittbrodt; Pearce, 2017; Valvez; Silva; Reis, 2022), ASA (Grabowik *et al.*, 2017; Guessasma *et al.*, 2016), etc., consistently adopting rigid plastic standards (Chart 5) (Kawalkar; Dubey; Lokhande, 2021).

Chart 5: ASTM and ISO Standards for rigid plastics.

	Measurement	American Society for Testing and Materials (ASTM)	International Organization for Standardization (ISO)
Standard Mechanical Tests	Coefficient of friction	ASTM D1894-14	-
	Compressive modulus	ASTM D695-15	ISO 604:2002
	Compressive strength	ASTM D695-15	ISO 604:2002
	Deformation under load	ASTM D621	-
	Flexural creep	ASTM D2990-17	-
	Flexural modulus	ASTM D2990-17	ISO 178:2019
	Flexural strength	ASTM D2990-17	ISO 178:2019
	Flexural strength at break	ASTM D2990-17	-
	Flexural strength at yield	ASTM D2990-17	-
	Poisson's ratio	ASTM E132-17	-
	Shear modulus	ASTM E132-17	-
	Shear strength	ASTM E132-17	-
	Tensile creep modulus	-	ISO 527:2019
	Tensile elongation at break	ASTM D638-22	ISO 527:2019
	Tensile elongation at yield	ASTM D638-22	ISO 527:2019
	Tensile modulus	ASTM D638-22	ISO 527:2019
	Tensile strength	ASTM D638-22	ISO 527:2019
	Tensile strength at break	ASTM D638-22	ISO 527:2019
	Tensile strength at yield	ASTM D638-22	ISO 527:2019
	Ultimate tensile strength	ASTM D638-22	ISO 527:2019

Source: The Author (2024).

Material selection for structural applications requires precise mechanical measurements to create safety-critical designs. Mechanical properties represent the material behavior at loads that do not produce failure, defined by the stress divided by the strain employing different loading modes such as tension, compression, flexure,

shear, or torsion. Generally, the moduli of polymeric materials rely on temperature and time, reported in two different loading directions (stress and strain), Young's modulus or Poisson's Ratio (Hibbeler, 2019; Ward; Sweeney, 2004-). For instance, uniaxial stress is expressed by force acting on an area (Equation 1). A material's compressive strength represents its ability to withstand a mechanical pushing force that tends to shorten its size (as opposed to tensile strength, which withstands pulling loads that, ultimately, lead to elongation). The deformation created by mechanical stress is the 'strain.' A positive strain represents an object under tension, possibly lengthened, and a negative pressure occurs in compressive scenarios (Hibbeler, 2019; Ward; Sweeney, 2004).

$$\sigma = \frac{F}{A} \qquad (1)$$

Where: σ *= uniaxial stress*
F *= force in N*
A *= area in* m^2

Normally, polymers can endure large linear elastic deformation up to a certain load, in which the deformity becomes plastic. As the curve shifts from elastic to plastic, peak stress (yield stress) typically occurs. Below the yield stress, polymeric materials follow Hooke's Law, in which the applied pressure is a product of an elastic modulus (Young's modulus) and the resulting strain (Equation 2). Young's modulus measures tensile or compressive stiffness when a force is applied lengthwise and quantifies the linear elastic region's relationship between tensile/compressive stress (σ) and axial strain (ε) (Hibbeler, 2019).

$$\sigma = E\varepsilon \qquad (2)$$

Where: σ *= uniaxial stress*
E *= Young's modulus*
ε *= resulting strain*

When unloaded, plastically deformed objects do not completely return to their original size and shape. Beyond the yield point, they experience a strain hardening and begin to neck as the cross-sectional region becomes significantly smaller. The heterogeneous concentration of forces in a small section leads to fracture. Material strength parameters include yield and fatigue strength, crack resistance, etc., as seen in Chart 5. The most employed standards for polymeric mechanical characterization are ASTM D695-15 (American Society for Testing and Materials, 2015; Bonada; Pastor; Buj-Corral, 2021; Vukasovic *et al.*, 2019), which aids in determining the

compressive properties of un-reinforced and reinforced plastics, alongside ASTM D638-22 (American Society for Testing and Materials, 2022; Bonada; Pastor; Buj-Corral, 2021; Fernandes, 2022), the equivalent tensile test standard (Popescu *et al.*, 2018).

ASTM D695-15 supports obtaining the properties of a material's compressive strength, compressive yield point, and modulus (Chart 5). It also defines the standard specimen for strength determination as a cylinder or prism whose length is twice its principal width or diameter (American Society for Testing and Materials, 2016). ASTM D638-22 introduces the basic elements of a plastic tensile test, including an overview of the equipment, software, and samples, helping measure tensile strength and modulus, elongation, and Poison's Ratio. The most common specimen type is Type I (dog bone or dumbbell), with an overall length of 165 mm and width of 13 mm, with a gauge length of 50 mm, which ensures that the break appears in the center of the sample rather than at the clamping spots (American Society for Testing and Materials, 2022).

For instance, Brischetto and Torre (2020) developed tensile and compression tests to assess the main mechanical properties of PLA components utilizing ASTM 695-16. The authors conducted a statistical and capability analysis to gather test coupon geometrical data and calculate acceptable structural limits. Results showed a linear elastic Young's modulus of 2549.03 MPa for tensile applications and 2035.01 MPa for compression scenarios, indicating that it is fundamental to pre-define the accurate acting forces beforehand. Even though the authors covered compression applications, they did not comply with any standard and presented less information than obtained for tensile tests.

Vukasovic *et al.'s* (2019) investigations are one of few that fully assess tension and compression. They indicated the tensile, compressive, and bending behavior of flat and upright printed ABS and PLA test coupons, determining Young's modulus, yield, and maximum stresses. The upright-printed specimens showed lower values for tensile applications than the corresponding horizontal coupons. Compression test coupons showed no significant difference for vertical and flat prints. The distinctions between tensile and compressive behavior characterize the materials as bimodular, demanding additional tests for other loading conditions (including shear and torsion).

2.5. Polymer Degradability

Due to their low density, flexibility, and simple processing, structural polymer applications have contributed to the exponential growth of the polymer industry (Jasso-Gastinel; Soltero-Martínez; Mendizábal, 2017). However, plastics are subject to degradation at all life cycle stages; thermoplastics are especially sensitive to degradation than thermosets. “Many applications require that plastics retain critical properties, such as strength, toughness, or appearance, during and after exposure to natural environmental conditions” (Speight, 2020, p. 627-628), principally due to resource management and end-of-life analysis. Degradation represents a change of properties, such as strength, color, shape, and weight, under one or more environmental factors, including applied force and exposure to oxygen, water, heat, light, and chemicals. Their combination is often generalized as weathering due to a chemical or physical change in the polymer chain that leads to fragmentation. The main permanent deterioration agents are thermal, thermo-mechanical, thermo-oxidative, oxidative, photo-oxidative, ozone-induced, bio-degradative, and hydrolysis-induced (Frigione; Rodríguez-Prieto, 2021; Speight, 2020).

Under lenient loading circumstances, polymers experience only elastic deformation, returning to their original shape after withdrawing the load. However, they deform and flow similarly to highly viscous liquids under long-term heavy loads or elevated temperatures. They can also experience creep deformation (cold flow) if subjected to constant stress at a consistent temperature, stress cracking when exposed to hostile environmental conditions, and crazing due to chemical embrittlement (Jasso-Gastinel; Soltero-Martínez; Mendizábal, 2017; Speight, 2020). Exposure to UV light (mainly from sunlight) adds thermal energy to the polymer, causing thermal and thermo-mechanical degradation. It also excites the electrons, weakening chemical bonds and generating brittleness. UV light exposure can also interfere with light transmission and modify properties such as color, gloss, absorptance, reflectance, and refractive index (Kockott, 2022; Tocháček; Vrátníčková, 2014).

Thermoplastic polymers are also susceptible to hydrolysis reactions and the permeation of gases and liquids. Even though these reactions are slow, most plastics are hygroscopic and extremely sensitive to high humidity (Daminabo *et al.*, 2020; Speight, 2020). This leads to water absorption and swelling, which potentializes

solvation reactions, causing weight gain and environmental stress cracking. In real environmental conditions, many agents exist simultaneously as a synergistic action. Their synchronicity (e.g., UV light and temperature) can dramatically affect the polymer's lifespan, justifying why plastics degrade faster when exposed to outdoor conditions that normally present harsher UV irradiation and air temperature (Frigione; Rodríguez-Prieto, 2021; Ishida; Kitagaki, 2021). Since outdoor conditions are unpredictable and inconsistent, depending on the location (e.g., on altitude, latitude, and distance from the sea), the season, and the weather conditions, the most reliable representation of polymer degradation is natural aging based on field exposure (Frigione; Rodríguez-Prieto, 2021). However, as they require long-term analysis (over decades) to accumulate representative data, existing studies with relatively short durations (usually less than 3 years) are biased and do not accumulate enough data (Kockott, 2022).

Accelerated aging techniques are a straightforward method for predicting long-term material changes, done by amplifying one or more environmental parameters (e.g., radiation, heat, and humidity) to represent real environmental exposure in a condensed period of alternating weather cycles. According to Frigione and Rodríguez-Prieto (2021, p. 3), rapid aging techniques can make "[...] reliable previsions of the on-field long-term durability of a polymer".

According to Khosravani *et al.* (2022), there is no standard for investigating rapid aging for FDM-produced parts. Studies often adopt guidelines for plastics, such as ISO 4892:2016, or propose new methods for lifetime predictions based on reasonable correlation to natural exposure tests (Celina *et al.*, 2019). Generally, UV light exposure, temperature, and humidity are the most investigated aging factors (Celina *et al.*, 2019; Kockott, 2022). Although the temperature is the main driver of degradation (Celina *et al.*, 2019), an aging test should present coexisting parameters to depict environmental synergies. For instance, various studies simultaneously subject polymers to UV radiation (from xenon, mercury, metal halide or carbon arc, and fluorescent tube light sources) and moisture or wetting (Ishida; Kitagaki, 2021; Menezes *et al.*, 2022; Tocháček; Vrátníčková, 2014).

Ishida and Kitagaki (2021) investigated the year-round natural aging of polycarbonates (PC) based on appearance (yellowing and loss of gloss) at five exposure sites (Tokyo, Kagoshima, Okinawa, Florida, and Arizona) to reproduce their

behavior using environmental datasets. Their prediction curves followed the natural aging data, revealing that UV irradiation and temperature contribute more than humidity levels. Since Frigione (2020) indicates that on-field analyses should be the most reliable, as opposed to Kockott (2022), Ishida and Kitagaki's (2021) research presents a good approximation, weighing different environmental factors to obtain a statistically representative prediction.

Furthermore, Khosravani *et al.* (2022) investigated the end-of-life mechanical behavior of FDM-produced PLA coupons using accelerated thermal aging methods. The authors adopted 5-hour temperature cycles ranging from −5 °C to 35 °C over 10 days. Consistently, thermal aging decreased the failure loads of intact specimens by 10.15% and increased surface roughness with no change in color and gloss. Although chromaticity evaluation was not part of their study, the authors indicate that color variation may appear after a lengthier span.

3. Methodology

3.1. Materials, FDM printers, and specimen preparation

The author adopted the thermoplastic copolymers acrylonitrile styrene acrylate (ASA), polyethylene terephthalate glycol-modified (PETG), and terephthalic acid-tetramethylcyclobutanediol/cyclohexanedimethanol polyester (TRITAN™) due to the amorphous attributes, engineering grade category, and filament-compatible applications (used in fused-deposition) with market-ready products.

The materials are 1.75 mm thick, purchased from 3DFila in 1 kg coils, and conditioned according to ASTM D618 (American Society for Testing and Materials, 2022). Filaments are TRITAN™ HT White Milk, TRITAN™ HT Clear Water, ASA WP Natural, ASA WP Transparent, PETG Snow White, and PETG XT Glass Colorless. Coupon fabrication obeyed the flowchart in Figure 2.

Based on Hsueh *et al.* (2021), Hanon, Dobos, and Zsidai (2020), Popescu *et al.* (2018), and Vukasovic *et al.'s* (2019) studies, the author produced 60 coupons for tensile testing with flat printing orientation (oriented along the y-axis to prevent the nozzle from contacting the coupons and disrupting the printing process), aligned rectilinear 90° raster angle (collinear to the applied force), and 100% infill density. The

test coupons followed ASTM D638 (American Society for Testing and Materials, 2022) Type I dog bone, as seen in Figure 3.

Figure 2: Coupon counting.

Source: The Author (2024).

The author also fabricated 60 test coupons for compression with the same raster angle, infill density, and printing orientation perpendicular to the applied force. The coupons conform to ASTM D695 (American Society for Testing and Materials, 2016) and are cylindrical with a length twice its principal width diameter (Figure 3). Chart 6 displays further printing configurations.

Figure 3: Test coupons' print placement and size.

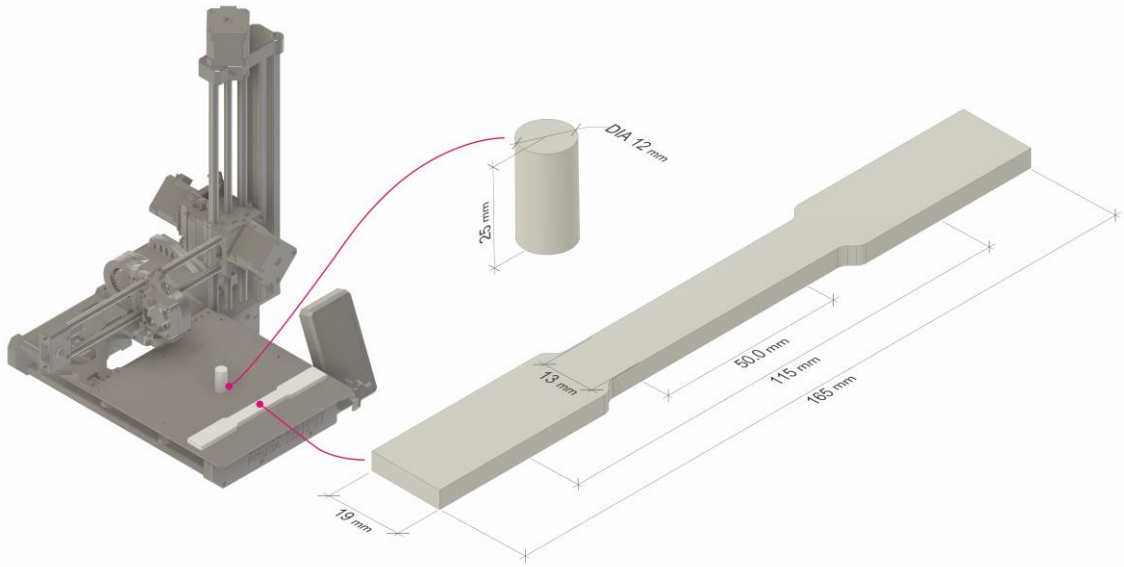

Source: The Author (2024).

Chart 6: Copolymer print settings.

		Copolymer		
		ASA	PETG	TRITAN™
Infill	Fill density (%)	100		
	Fill pattern	Align rectilinear		
	Top fill pattern	Monotonic		
	Bottom fill pattern	Monotonic		
	Fill angle (°)	90	90	90
Layers	Layer height (mm)	0.05	0.05	0.05
	Skirt loops	5	0	0
	Skirt height	0.05	-	-
	Brim (mm)	10	0	0
Printer settings	First layer - nozzle temperature (°C)	260	220	280
	Other layers - nozzle temperature (°C)	250	220	260
	First layer - bed temperature (°C)	100	80	100
	Other layers - bed temperature (°C)	100	60	100
	Bed adhesive	ABS slurry	None	ABS slurry
	Cooling fan	Off	Always on	Off
	Perimeter speed (mm/s)	30	50	40
	Infill speed (mm/s)	30	70	60
	Travel speed (mm/s)	120	150	120

Source: The Author (2024).

The author adopted Autodesk Fusion360 for modeling the specimens and producing the stereolithography file. Prusa Slicer 2.5.0 is the slicing software compatible with Prusa MINI+, the FDM printer employed in this study. Prusa's maximum build volume is 180x180x180 mm, its printing carriage travels at 200+ mm/s, and the default printing nozzle is 0.4 mm, heating up to 280 °C, extruding with a 3:1 gearing Bowden system. Its heated bed's maximum temperature is 100 °C, compatible with smooth (used for ABS and TRITAN™) and satin (used for PETG) PEI sheets.

3.2. Mechanical tests

ASTM D638 (American Society for Testing and Materials, 2022) suggests producing duplicate specimens for anisotropic materials. However, studies show that layer deposition normal to the applied force presents the best mechanical properties. Therefore, this research only adopted one set of coupons, following the printing guidelines outlined in the studies discussed throughout the theoretical framework (Hsueh *et al.*, 2021; Vukasovic *et al.*, 2019) (Figure 2).

The author marked the tensile specimen's gauge length, the distance between grips, and the center with India ink (Braconnier; Jensen; Peterson, 2020). They measured the width and thickness of each sample to the nearest 0.5 mm using a micrometer caliper, following the ASTM D5947 (American Society for Testing and Materials, 2018) (Figure 4a and b).

Figure 4: (a and b) PETG test coupons marked with India Ink; (c) aging chamber configuration.

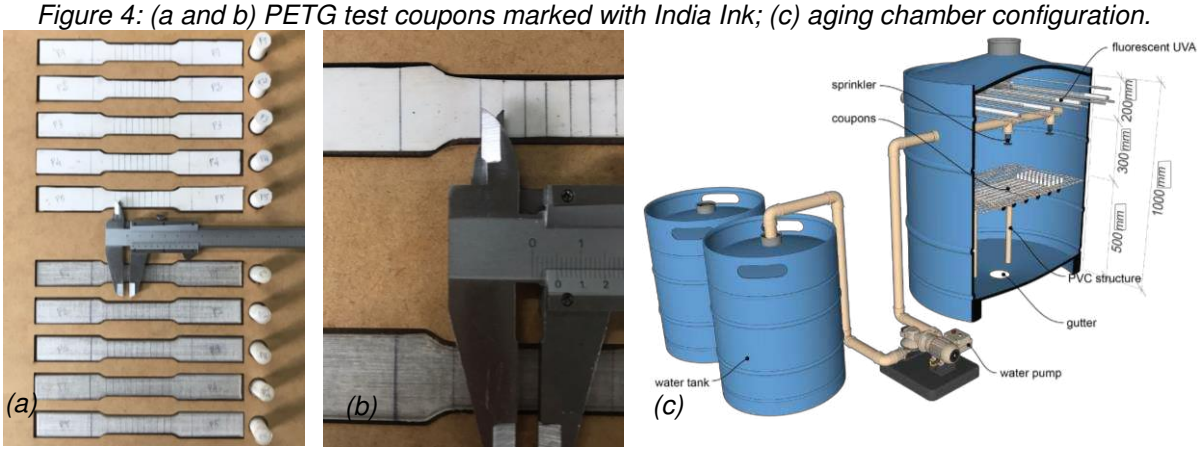

Source: The Author (2024).

The tensile and compression tests follow their specific standards, ASTM D638-22 (American Society for Testing and Materials, 2022) and ASTM D695-15 (American Society for Testing and Materials, 2016), respectively. The author used a 50 KN Instron Emic DL60000 universal testing machine with a 5 KN load cell at fixed load speeds of 0.1 mm/sec and 0.005 mm/sec for the tensile tests; the compression tests employed an analog unconfined compression-testing machine with a 696 KgF/mm proving ring. The author processed the experimental data to obtain tensile and compressive stress and resulting strain to obtain Young's modulus (E) before and after the aging process.

3.3. Accelerated Aging

The adopted age-acceleration chamber simulates solar radiation (fluorescent UV light), humidity, dew, and rain (water sprinkling), exposing the coupons to repetitive cycles under semi-controlled environmental conditions, according to ASTM G154 (American Society for Testing and Materials, 2023), ASTM G151 (American Society for Testing and Materials, 2019), ISO 4892 (International Organization of Standardization, 2016) (Figure 4c). For solar radiation simulation, the chamber has four long-wave (350-400 nm) UVA fluorescent lamps, model Tlk 40W/10R, with 7.4 W radiation (fitting the solar radiation spectrum) and 2000 hours of average service life. Their irradiance of 9.76 W/mm² is above 7.8 W/mm², matching the ASTM D5208 (American Society for Testing and Materials, 2022) and the ISO 4892 (International Organization of Standardization, 2016) standards.

Since UV lamps emit relatively lower infrared radiation than the sun, the surface heating in the test specimens is primarily by convection of heated air. The author monitored the air temperature inside the chamber using an Arduino-compatible thermocouple and measured humidity levels inside the aging chamber, controlling the rain and dew from micro-sprinklers. Exposure cycles were 8 hours long, 6 hours simulating the daytime and 2 hours emulating the nighttime as recommended by ASTM G154 (American Society for Testing and Materials, 2023), ASTM G151 (American Society for Testing and Materials, 2019), and ISO 4892 (International Organization of Standardization, 2016). The 6 daytime hours consisted of 4 hours of UVA radiation exposure solely, 1 hour and 45 minutes of condensation, and 15 minutes of rain. The aging process ran for 30 days, or 90 8-hour cycles, collecting temperature, humidity, and irradiance data every 5 minutes. ISO 4892 (International Organization of Standardization, 2013) indicates that “at least three replicates of each material [should] be exposed in each test to allow statistical evaluation” (International Organization of Standardization, 2013, p. 12). The author employed 60 test coupons, 5 of each color and material (Figure 2), placed 30 cm below the fluorescent lamps.

This research evaluated optical degradability and color variation between the base-case (unaged specimens) and aged coupons of the same color and material after the 30-day experiment using L*a*b* space based on CIE Standard illuminant D65 (Carter *et al.*, 2018; ISO, 2017). For instance, L*a*b* expresses color in coordinates according to human vision. L* represents perceptual lightness from 0 (black) to 100

(diffuse white); a* indicates the color position between red and green; and b* represents the position between yellow and blue. The author obtained L*a*b* values using Adobe Photoshop CC's color picker on before and after photographs taken with an EOS Rebel T7+ (18-55 mm lens) with f/22 aperture and 'daylight white-balance' setting, using an LED-lit booth to minimize environmental interference (Figure 5a). They collected three L*a*b* values between each marking, mixed each three hues using the smudge tool, and generated nine hues for each coupon; subsequently, they combined the nine hues into one swatch for coupon (Figure 5b). This study also assessed and compared the tension and compression of aged and unaged coupons, following the methodology discussed in section 3.2.

*Figure 5: (a) LED-lit booth for L*a*b* analysis; (b) Adobe Photoshop color picker and L*a*b* compilation.*

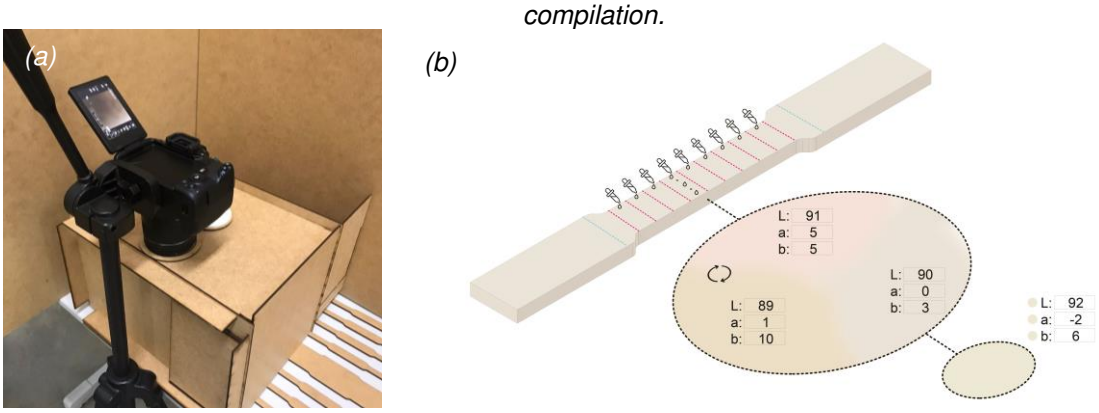

Source: The Author (2024).

The author measured reflectance values using an ALTA II portable spectrometer following the methodology outlined in Pereira et al. (2017) and the points indicated in Figure 5b. The equipment collects spectral values in millivolts (mV) for 11 wavelengths (nm), converted to reflectance values (%) using Equation 3. The voltage and reflectance adopted as a reference are relative to a sheet of white paper (75 g/m^2) (Pereira; Hirashima; Oliveira, 2021), and the dark current is the value displayed when on standby. Subsequently, the author calculated the reflectance values in the visible range using Equation 4.

$$\rho_{\lambda,sample} = \left(\frac{V_{\lambda,sample} - V_{f,sample}}{V_{\lambda,reference} - V_{f,reference}}\right) * \rho_{f,reference} \qquad (3)$$

Where: $\rho_{\lambda,sample}$*: sample's reflectance for a specific wavelength (%)*
$\rho_{\lambda,reference}$*: known reference reflectance for a specific wavelength (%)*
$V_{\lambda,sample}$*: sample's voltage for a specific wavelength (mV)*
$V_{\lambda,reference}$*: known reference voltage for a specific wavelength (mV)*
$V_{f,sample}$*: dark current for the sample*
$V_{f,reference}$*: dark current for the reference model*

$$\rho_{vis} = 5.12695 + (0.25417 * \rho_{470}) + (0.6542 * \rho_{585}) \quad (4)$$

Where: ρ_{vis}*: visible reflectance (%)*
ρ_{470}*: reflectance obtained using Equation 3 for 470nm wavelength (%)*
ρ_{585}*: reflectance obtained using Equation 3 for 585nm wavelength (%)*

4. Results

4.1. ASA

The author gathered the digital universal testing machine's data output in a stress-strain curve, finding the Ultimate Tensile Strength (UTS), percent elongation, fracture (rupture), and Young's modulus. Following Hooke's Law, the author analyzed the curves' linear region to obtain the curve's equation and the Elastic Modulus. Figures 6 and 7 depict the behavior of white and transparent ASA samples with and without accelerated aging. The terminology used for the result and discussion sections is FilamentType_CouponNumber_Color_AgedOrUnaged.

Figure 6: Unaged ASA tensile stress coupons.

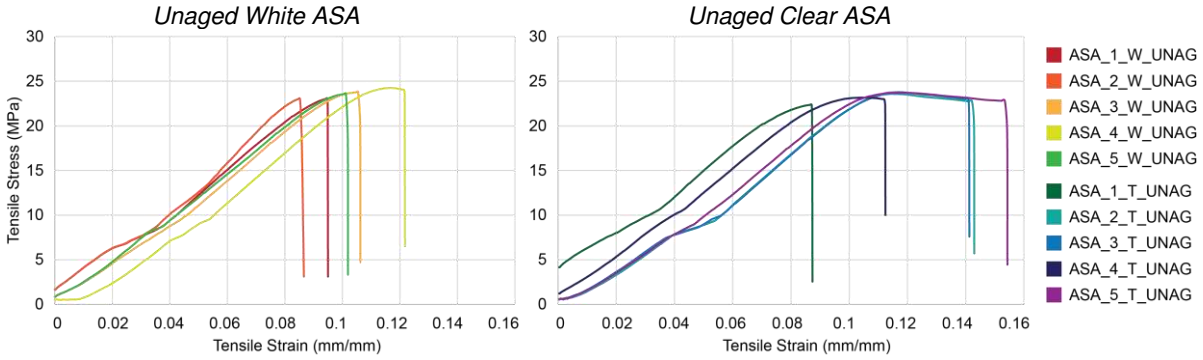

Source: The Author (2024).

Overall, under displacement-controlled loading, a nearly linear rise occurs until reaching the peak load. The initial strain increases without a corresponding stress growth, typically observed at the beginning of the curves, which is a toe point resulting from specimen misalignment due to slipping in the grips. This phenomenon is a characteristic of the mechanical test, not the material. ASTM D638 (American Society for Testing and Materials, 2022) acknowledges toe points and recommends calculating the Elastic Modulus using the linear physiological range (with lower R^2).

The transparent coupons exhibited higher elongation, ranging from 0.0857 mm/mm to 0.1518 mm/mm. In comparison, the maximum strain for the white specimens was 0.1199 mm/mm, resulting in higher elasticity coefficients (Figure 6).

Nevertheless, the max tensile stress for both is relatively similar (24.21 MPa for the white and 23.70 MPa for the transparent), with an average difference of 1.67%. The UTS for white and transparent specimens were 7.6% and 9.55% lower than the reference values provided by the manufacturer. It is essential to note that the reference values are filament properties and loosely apply to FDM-produced parts.

All samples exhibited elastic behavior for most of the experiment, with a small range of plastic behavior, particularly in transparent specimens (ASA_2_T_UNAG, ASA_3_T_UNAG, and ASA_5_T_UNAG), followed by rupture. Table 1 indicates the strain interval that Hooke's Law applies, the curve equation, the Elastic Modulus for each coupon, and the maximum stress and strain. ASA_1_T_UNAG and ASA_4_T_UNAG specimens displayed distinctive strains, as expected in FDM-produced test cells, which are anisotropic due to manufacturing quality (e.g., nozzle clogging, scorching, heated bed vibration or detachment, and temperature variations during printing). Due to low yielding and minimal decrease in transverse dimension (necking), it is not possible to calculate the Poisson's ratio.

Table 1: Mechanical properties of ASA tensile coupons.

	Linear Strain Interval		Linear Equation	Young's Modulus	UTS (MPa)	Avg. Stress (MPa)	Fracture (mm/mm)	Avg. Strain (mm/mm)
ASA_1_W_UNAG			y=278.24x-1.3249	278.24	22.97		0.094	
ASA_2_W_UNAG			y=253.14x-1.7896	253.14	23.87		0.110	
ASA_3_W_UNAG	0.04	0.08	y=272.68x-2.1305	272.68	23.70	23.65	0.105	0.106
ASA_4_W_UNAG			y=256.7x-3.4653	256.7	24.20		0.120	
ASA_5_W_UNAG			y=261.76x-0.7617	261.76	23.51		0.100	
ASA_1_T_UNAG			y=221.74x+4.6475	221.74	22.29		0.086	
ASA_2_T_UNAG			y=283.11x-5.3609	283.11	23.53		0.141	
ASA_3_T_UNAG	0.05	0.08	y=273.47x-4.7716	273.47	23.70	23.25	0.139	0.126
ASA_4_T_UNAG			y=263.19x-0.1923	263.19	23.11		0.110	
ASA_5_T_UNAG			y=269.16x-3.3431	269.16	23.64		0.152	
ASA_1_W_AG			y=278.24x-1.3249	243.1	23.51		0.109	
ASA_2_W_AG			y=253.14x-1.7896	243.1	23.51		0.109	
ASA_3_W_AG	0.04	0.08	y=272.68x-2.1305	250.09	25.07	24.38	0.117	0.119
ASA_4_W_AG			y=256.7x-3.4653	256.83	24.84		0.134	
ASA_5_W_AG			y=261.76x-0.7617	235.1	24.99		0.122	
ASA_1_T_AG			y=221.74x+4.6475	252.78	24.01		0.107	
ASA_2_T_AG			y=283.11x-5.3609	258.61	24.56		0.106	
ASA_3_T_AG	0.05	0.08	y=273.47x-4.7716	250.09	24.74	24.3	0.115	0.113
ASA_4_T_AG			y=263.19x-0.1923	256.83	23.86		0.106	
ASA_5_T_AG			y=269.16x-3.3431	265.14	24.74		0.126	

Source: The Author (2024).

Since the heat gain within the aging chamber is predominantly through convection, it is unreliable to correlate thermal gain with color. Despite having similar chemical compositions (i.e., transparent ASA has a methyl methacrylate addition, which decreases impact resistance), white ASA exhibited a greater variation in the Elastic Coefficient, elevating the UTS. This increase after thermal aging aligns with the findings of Khosravani *et al.* (2022), which indicated an increment of up to 10.15% in

UTS (Figure 7).

Figure 7: Aged ASA tensile stress coupons.

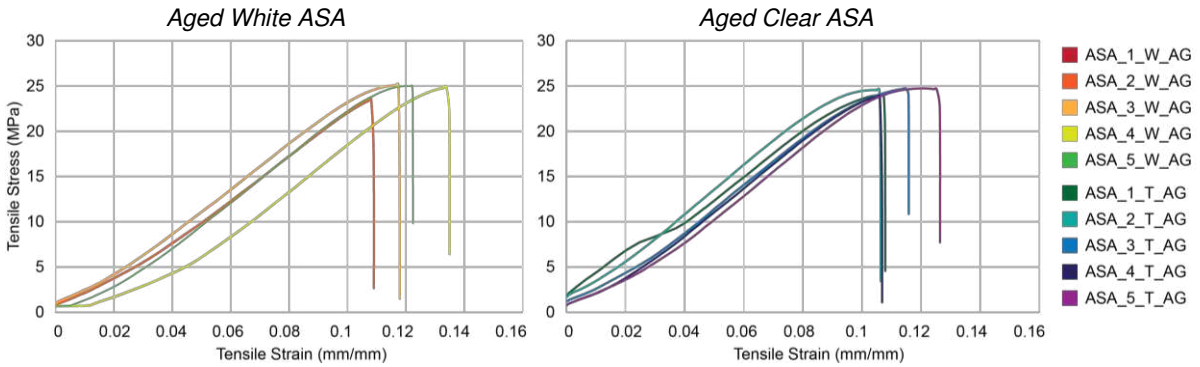

Source: The Author (2024).

In contrast to the UTS values that increased with weather exposure, the ultimate compressive strength (UCS) was lower for all cases (Table 2). The specimens were under the same conditions; thus, reducing Young's modulus entails less compressive stress to generate the same deformation. Unaged specimens performed similarly for white and transparent samples, with an average compressive stress variation of 0.24%. The difference in average UCS between color groupings in aged specimens was approximately 2.18%. The loss of mechanical strength due to thermal aging was 12.7% and 10.51% for white and transparent filaments, respectively.

Table 2: Mechanical properties of ASA compression coupons.

Unaged Coupons	Read (mm)	Force (KgF)	Force (N)	Stress (MPa)	Avg. Stress (MPa)	Aged Coupons	Read (mm)	Force (KgF)	Force (N)	Stress (MPa)	Avg. Stress (MPa)
ASA_1_W_UNAG	0.81	563.7	5528.6	48.8		ASA_1_W_AG	0.73	508.0	4982.5	44.0	
ASA_2_W_UNAG	0.82	570.7	5596.8	49.4		ASA_2_W_AG	0.72	501.1	4914.3	43.4	
ASA_3_W_UNAG	0.82	570.7	5596.8	49.4	49.4	ASA_3_W_AG	0.68	473.2	4641.2	41.0	43.2
ASA_4_W_UNAG	0.84	584.6	5733.3	50.6		ASA_4_W_AG	0.75	522.0	5119.0	45.2	
ASA_5_W_UNAG	0.81	563.7	5528.6	48.8		ASA_5_W_AG	0.7	487.2	4777.8	42.2	
ASA_1_T_UNAG	0.81	563.7	5528.6	48.8		ASA_1_T_AG	0.72	501.1	4914.3	43.4	
ASA_2_T_UNAG	0.82	570.7	5596.8	49.4		ASA_2_T_AG	0.73	508.0	4982.5	44.0	
ASA_3_T_UNAG	0.81	563.7	5528.6	48.8	49.3	ASA_3_T_AG	0.74	515.0	5050.8	44.6	44.1
ASA_4_T_UNAG	0.83	577.6	5665.1	50.0		ASA_4_T_AG	0.77	535.9	5255.5	46.4	
ASA_5_T_UNAG	0.82	570.7	5596.8	49.4		ASA_5_T_AG	0.7	487.2	4777.8	42.2	

Source: The Author (2024).

Regardless of the chemical additive for gloss, color, and mechanical properties retention during exposure to outdoor conditions (Guessasma *et al.*, 2016), ASA specimens proved sensitive to high temperatures, resulting in variations in tensile strength, ductility, and, consequently, tenacity. Also, despite the predictions of Ishida and Kitagaki (2021), which suggested little yellowing of aged copolymers, exposure to UV, temperature, and humidity showed changes in various wavelengths (Table 3).

Table 3: Chromaticity variation for tensile ASA samples.

	ALTA II voltage (mV)											ρ_{vis} (%)	CIE L*a*b* and Color			
	470 (nm)	525 (nm)	560 (nm)	585 (nm)	600 (nm)	645 (nm)	700 (nm)	735 (nm)	810 (nm)	880 (nm)	940 (nm)					
REFERENCE	**587**	**637**	**732**	**495**	**453**	**707**	**680**	**780**	**809**	**880**	**668**	**78.3**				
1_W_UNAG																
2_W_UNAG																
3_W_UNAG	484	593	681	475	429	631	602	692	729	788	630	**88.8**	98	0	8	
4_W_UNAG																
5_W_UNAG																
1_T_UNAG																
2_T_UNAG																
3_T_UNAG	408	592	585	458	418	624	624	595	647	684	548	**81.0**	85	-2	-3	
4_T_UNAG																
5_T_UNAG																
1_W_AG	445	556	657	470	420	608	574	672	702	756	592	**85.3**	68	-1	2	
2_W_AG	412	517	597	423	378	571	544	640	694	715	517	**77.5**	79	1	-2	
3_W_AG	409	518	596	430	379	575	560	650	702	738	584	**78.0**	72	-1	-4	
4_W_AG	451	560	666	465	415	592	557	648	694	735	573	**85.0**	71	-1	-4	
5_W_AG	422	532	631	457	407	602	581	662	702	730	584	**82.1**	69	-2	-2	
1_T_AG	388	432	483	336	303	492	494	583	640	670	529	**66.4**	68	-1	-4	
2_T_AG	384	497	595	410	371	555	536	650	680	732	559	**73.9**	68	-1	-3	
3_T_AG	379	435	503	344	323	534	540	612	622	642	533	**66.5**	67	-1	-3	
4_T_AG	388	440	505	350	320	540	541	599	636	629	526	**67.7**	63	-1	-3	
5_T_AG	351	440	528	372	340	538	532	625	639	646	522	**67.3**	63	-1	-4	

Source: The Author (2024).

The L*a*b* analysis indicated the darkening of all aged pieces compared to the new samples. In most cases, the yellow and red spectra reflected less radiation, with an average reflectance decrease of 12.33% for white specimens and 17.76% for transparent ones. There was a loss of gloss, but contrary to what Ishida and Kitagaki (2021) indicated, yellowing occurred in only one case (ASA_1_W_AG).

4.2. PETG

White unaged PETG tensile tests demonstrated a considerable toe point (Figure 8). Despite being anticipated in the ASTM D638 (American Society for Testing and Materials, 2022) standard, as discussed earlier, the slippage was more pronounced due to the extremely smooth finish provided by the white material. This phenomenon did not occur for any of the other cases due to the distinct characteristics of the transparent filaments and the aging process on both filaments that resulted in increased roughness and porosity due to moisture action. Unlike the tensile test coupons produced in ASA, both PETG colors exhibited a significant variation in average tensile stress after aging, with the transparent filament showing a 12.88% rise in average UTS (Figure 9).

Figure 8: Unaged PETG tensile stress coupons.

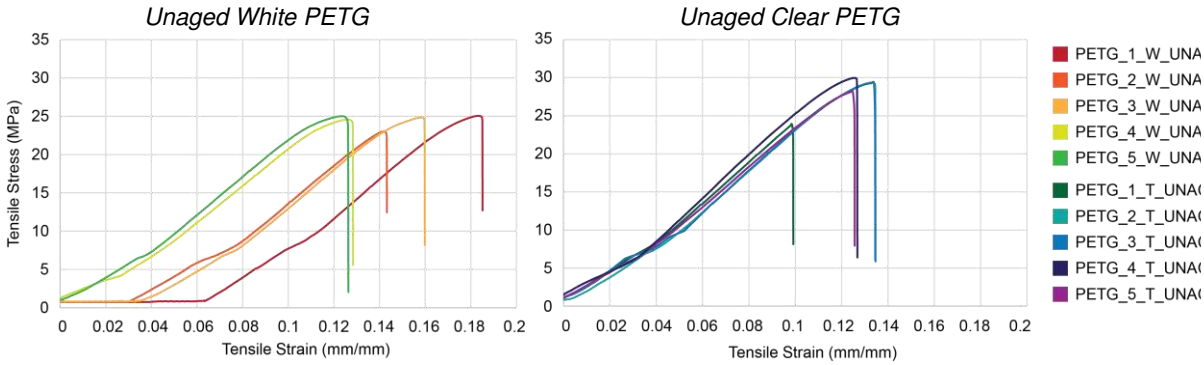

Source: The Author (2024).

Figure 9: Aged PETG tensile stress coupons.

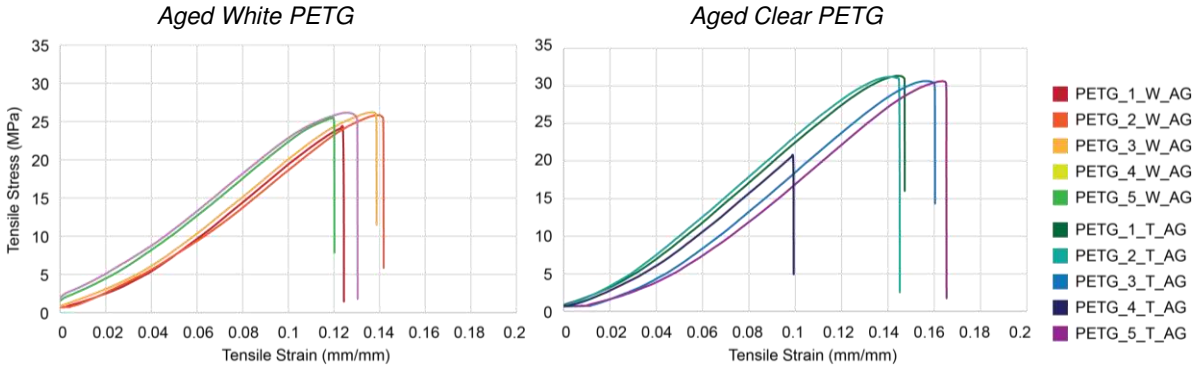

Source: The Author (2024).

Nevertheless, the strain for both colors is similar when removing the toe points (Table 4). Similarly, one of the specimens behaved very differently from the others within the same group, rupturing upon reaching 23.87 MPa (a value 15% below the average) (Figures 8 and 9).

Table 4: Mechanical properties of PETG tensile coupons.

	Linear Strain Interval		Linear Equation	Young's Modulus	UTS (MPa)	Avg. Stress (MPa)	Fracture (mm/mm)	Avg. Strain (mm/mm)
PETG_1_W_UNAG			y=185.22x-10.893	185.22	25.08		0.125	
PETG_2_W_UNAG			y=220.55x-8.4517	220.55	23.03		0.113	
PETG_3_W_UNAG	0.04	0.08	y=220.83x-9.0734	220.83	24.83	24.50	0.129	0.124
PETG_4_W_UNAG			y=229.96x-2.5362	229.96	24.58		0.128	
PETG_5_W_UNAG			y=226.34x-1.1141	226.34	24.99		0.126	
PETG_1_T_UNAG			y=269.42x-3.8318	269.42	29.34		0.134	
PETG_2_T_UNAG			y=270.79x-2.7628	270.79	23.87		0.099	
PETG_3_T_UNAG	0.05	0.08	y=279.81x-4.5869	279.81	29.27	28.11	0.134	0.124
PETG_4_T_UNAG			y=262.58x-2.7384	262.58	28.13		0.125	
PETG_5_T_UNAG			y=286.95x-3.0554	286.95	29.94		0.126	
PETG_1_W_AG			y=240.57x-4.8206	240.57	24.27		0.124	
PETG_2_W_AG			y=236.37x-5.0703	236.37	25.84		0.141	
PETG_3_W_AG	0.04	0.08	y=239.19x-3.9969	239.19	26.23	25.58	0.138	0.131
PETG_4_W_AG			y=220.8x+0.3853	220.8	26.15		0.13	
PETG_5_W_AG			y=231.15x-1.0208	231.15	25.41		0.12	
PETG_1_T_AG			y=262.26x-3.8609	262.26	31.33		0.147	
PETG_2_T_AG			y=264.81x-3.2727	236.37	31.20		0.145	
PETG_3_T_AG	0.05	0.08	y=241.55x-6.0879	239.19	30.63	28.90	0.16	0.143
PETG_4_T_AG			y=253.47x-4.5855	253.47	20.74		0.099	
PETG_5_T_AG			y=220.23x-5.7278	220.8	30.61		0.165	

Source: The Author (2024).

The UTS indicated by the manufacturer is 28 MPa, close to the average UTS for the transparent group. The white coupons reached UTS 12.53% lower than the supplier-indicated properties (Chart 2). Overlooking the outlier (PETG_1_T_UNAG), the average UTS becomes 4% stronger than the product's standard properties. The stress-strain curves for both filaments behaved similarly, mainly occupying the range of elastic deformation. The Young's moduli for white PETG specimens are consistently lower than the values for white ASA, while the contrary occurs for transparent specimens. Therefore, white PETG is more resistant to elastic deformation than white ASA, and the opposite is true for transparent filaments. The transparent coupons exhibited higher elongation, ranging from 0.0857 mm/mm to 0.1518 mm/mm. In comparison, the maximum strain for the white specimens was 0.1199 mm/mm, resulting in higher elasticity coefficients (Table 4). Nevertheless, the max tensile stress for both is relatively similar (24.21 MPa for the white and 23.70 MPa for the transparent), with an average difference of 1.67%.

In contrast to the tensile coupons, samples produced for compression exhibited a decrease in compressive strength after aging (Table 5). The reduction was 1.6% for the white filament and approximately 17% for the transparent. The latter already showed improved performance for tension, thus exhibiting a higher decline for compressive scenarios. PETG has the lowest moisture absorption coefficient among all filaments and experiences the smallest reduction in average compressive stress.

Table 5: Mechanical properties of PETG compression coupons.

Unaged Coupons	Read (mm)	Force		Stress (MPa)	Avg. Stress (MPa)	Aged Coupons	Read (mm)	Force		Stress (MPa)	Avg. Stress (MPa)
		(KgF)	(N)					(KgF)	(N)		
PETG_1_W_UNAG	0.62	431.5	4231.7	37.4		PETG_1_W_AG	0.61	424.5	4163.5	36.8	
PETG_2_W_UNAG	0.63	438.4	4300.0	38.0		PETG_2_W_AG	0.61	424.5	4163.5	36.8	
PETG_3_W_UNAG	0.62	431.5	4231.7	37.4	37.2	PETG_3_W_AG	0.63	438.4	4300.0	38.0	36.8
PETG_4_W_UNAG	0.60	417.6	4095.2	36.2		PETG_4_W_AG	0.58	403.6	3958.7	35.0	
PETG_5_W_UNAG	0.61	424.5	4163.5	36.8		PETG_5_W_AG	0.62	431.5	4231.7	37.4	
PETG_1_T_UNAG	0.65	452.4	4436.5	39.2		PETG_1_T_AG	0.64	445.4	4368.2	38.6	
PETG_2_T_UNAG	0.64	445.4	4368.2	38.6		PETG_2_T_AG	0.64	445.4	4368.2	38.6	
PETG_3_T_UNAG	0.64	445.4	4368.2	38.6	38.9	PETG_3_T_AG	0.62	431.5	4231.7	37.4	32.3
PETG_4_T_UNAG	0.63	438.4	4300.0	38.0		PETG_4_T_AG	0.65	452.4	4436.5	39.2	
PETG_5_T_UNAG	0.66	459.3	4504.7	39.8		PETG_5_T_AG	0.62	431.5	4231.7	37.4	

Source: The Author (2024).

Concerning the chromaticity evaluations (Table 6), white PETG demonstrates higher reflectances than ASA due to the former's intrinsic yellow hue. Also, the manufacturer indicates lower reflectances for transparent PETG, with lower transmittances and a hazier appearance. The white groups showed reflectance differences of about 5%, while the transparent reached 16.5% after aging.

Table 6: Chromaticity variation for tensile PETG samples.

	ALTA II voltage (mV)												CIE L*a*b* and Color		
	470 (nm)	525 (nm)	560 (nm)	585 (nm)	600 (nm)	645 (nm)	700 (nm)	735 (nm)	810 (nm)	880 (nm)	940 (nm)	ρ_{vis} (%)			
REFERENCE	**587**	**637**	**732**	**495**	**453**	**707**	**680**	**780**	**809**	**880**	**668**	**78.3**			
1_W_UNAG															
2_W_UNAG															
3_W_UNAG	552	596	678	459	420	648	624	710	720	770	607	**92,2**	87	-1	1
4_W_UNAG															
5_W_UNAG															
1_T_UNAG															
2_T_UNAG															
3_T_UNAG	410	408	444	304	282	493	492	532	543	560	479	**64,5**	81	-2	-5
4_T_UNAG															
5_T_UNAG															
1_W_AG	497	548	615	402	367	569	564	672	702	763	600	**81,8**	52	1	2
2_W_AG	495	569	658	456	403	627	606	687	729	770	604	**87,4**	66	-1	-4
3_W_AG	508	587	686	473	427	639	616	735	744	797	618	**90,2**	74	-1	-5
4_W_AG	486	562	670	466	420	637	620	721	740	770	603	**87,8**	70	-2	-3
5_W_AG	576	544	633	401	447	662	629	740	754	806	624	**87,7**	75	-2	-4
1_T_AG	405	410	458	309	291	499	493	539	549	569	482	**64,7**	73	-2	-5
2_T_AG	372	392	429	288	277	477	468	520	538	580	488	**59,9**	73	-2	-5
3_T_AG	404	400	444	297	283	492	489	535	546	572	484	**63,3**	71	-2	-5
4_T_AG	408	402	434	288	281	497	491	524	533	571	486	**62,4**	72	-2	-6
5_T_AG	410	408	434	305	291	492	491	532	542	571	486	**64,6**	74	-2	-6

Source: The Author (2024).

Overall, the darkening of ASA pieces was much more pronounced, with an average reduction in reflectance of about 7.2%. For the transparent group, the average reduction for PETG filament was 1.5%, compared to 12.6% for ASA. Despite the weather resistance additive added to the former filament, other copolymers (such as PETG) appear more suitable for weather-exposed applications. Analyzing CIE L*a*b*, yellowing occurred in only one specimen (PETG_1_W_AG), with a greater increase in the predominance of blue tones, with little variation in the green and red spectra.

4.3. TRITAN™

White TRITAN™ had the poorest tensile performance among all the filaments, reaching a maximum UTS of 20.474 MPa for TRITAN_2_W_UNAG. Compared to the previous unaged white filaments, its average tensile stress is 13.44% lower than ASA and 16.41% lower than PETG. As seen in Figure 10, TRITAN_5_T_UNAG had discrepant stress among the specimens in the same group, skewing the tensile stress.

The average tensile stress reaches 25.383 MPa when omitting the measured data for this specimen (different from the 26.29 MPa shown in Table 7). Thus, transparent TRITAN™ is an intermediate filament among the previous filaments. Young's moduli for both filaments are lower than the previous ones, indicating that TRITAN™ is less deformable under the same applied load. TRITAN™'s increased elasticity after aging is more pronounced than any other coupon (Figure 11).

Figure 10: Unaged TRITAN™ tensile stress coupons.

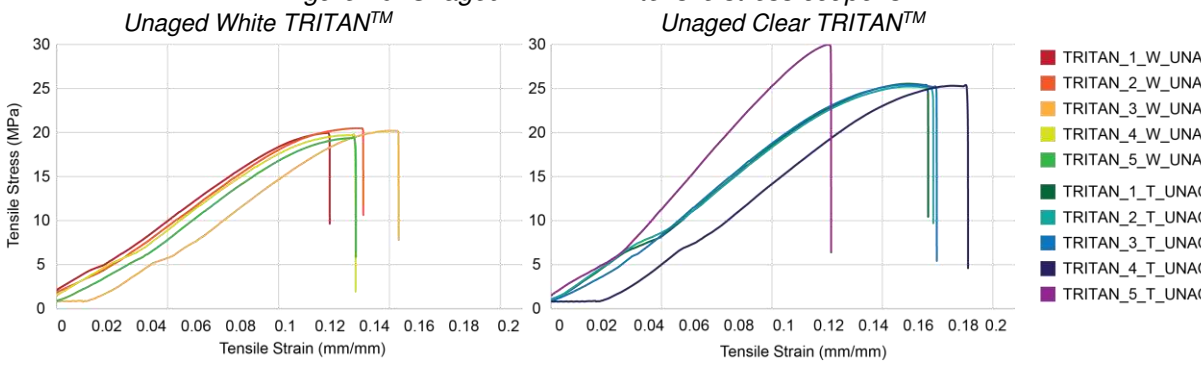

Source: The Author (2024).

Figure 11: Aged TRITAN™ tensile stress coupons. Source: The Author.

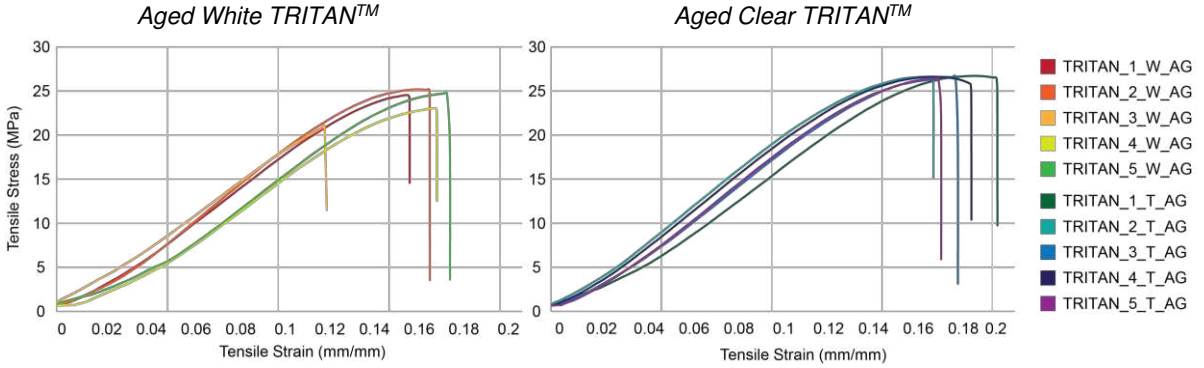

Source: The Author (2024).

Disregarding the isolated case of the TRITAN_5_T_UNAG, all UTS values increased, reaching average gains of 15.80% for white specimens and 4.40% for transparent ones. Due to the augmented deformation under a similar force, Young's modulus also raised (Table 7).

Table 7: Mechanical properties of PETG tensile coupons.

	Linear Strain Interval		Linear Equation	Young's Modulus	UTS (MPa)	Avg. Stress (MPa)	Fracture (mm/mm)	Avg. Strain (mm/mm)
TRITAN_1_W_UNAG			y=131.31x+4.895	131.31	19.94		0.123	
TRITAN_2_W_UNAG			y=144.53x+3.3027	144.53	20.47		0.138	
TRITAN_3_W_UNAG	0.05	0.12	y=181.31x-3.5688	181.31	20.21	19.94	0.154	0.13704
TRITAN_4_W_UNAG			y=138.44x+3.4317	138.44	19.70		0.134	
TRITAN_5_W_UNAG			y=148.51x+1.6644	148.51	19.36		0.134	
TRITAN_1_T_UNAG			y=195.21x-1.1687	195.21	25.54		0.170	
TRITAN_2_T_UNAG			y=193x-1.0931	193.00	25.23		0.173	
TRITAN_3_T_UNAG	0.05	0.12	y=198.18x-1.1847	198.18	25.45	26.29	0.174	0.16681
TRITAN_4_T_UNAG			y=253.21x-0.3093	253.21	25.31		0.188	
TRITAN_5_T_UNAG			y=201.31x-6.0172	201.31	29.99		0.126	
TRITAN_1_W_AG			y=190.84x-1.8658	190.84	24.52		0.159	
TRITAN_2_W_AG			y=201.56x-2.3153	201.56	25.16		0.168	
TRITAN_3_W_AG	0.05	0.12	y=182.86x-0.4905	182.86	20.98	23.68	0.121	0.159687
TRITAN_4_W_AG			y=186.11x-4.0896	186.11	23.03		0.171	
TRITAN_5_W_AG			y=191.63x-4.2786	191.63	27.71		0.177	
TRITAN_1_T_AG			y=186.57x-3.3154	186.57	26.71		0.202	
TRITAN_2_T_AG			y=196.16x-0.6572	196.16	26.61		0.173	
TRITAN_3_T_AG	0.05	0.12	y=197.29x-2.6003	197.29	26.57	26.56	0.184	0.185461
TRITAN_4_T_AG			y=197.54x-1.3126	197.54	26.61		0.190	
TRITAN_5_T_AG			y=199.05x-2.48	199.05	26.30		0.176	

Source: The Author (2024).

For compression, TRITAN™ remained intermediate to the previous filaments. Its average compressive stress is 19.50% lower than that of white ASA and 16.63% lower than that of transparent ones (Table 8). Compared to PETG, the compressive stress increased by 6.67% for the white group and 5.56% for the transparent ones. The pattern of higher average compressive stress compared to tensile stress persisted, and, as in all other aged cases, there was a drop of 8.18% for the white filament and 9.67% for the transparent ones.

Table 8: Mechanical properties of PETG compression coupons.

Unaged Coupons	Read (mm)	Force		Stress (MPa)	Avg. Stress (MPa)	Aged Coupons	Read (mm)	Force		Stress (MPa)	Avg. Stress (MPa)
		(KgF)	(N)					(KgF)	(N)		
TRITAN_1_W_UNAG	0.64	445.4	4368.2	38.6		TRITAN_1_W_AG	0.62	431.5	4231.7	37.4	
TRITAN_2_W_UNAG	0.66	459.3	4504.7	39.8		TRITAN_2_W_AG	0.58	403.6	3958.7	35.0	
TRITAN_3_W_UNAG	0.71	494.1	4846.0	42.8	39.8	TRITAN_3_W_AG	0.60	417.6	4095.2	36.2	36.6
TRITAN_4_W_UNAG	0.63	438.4	4300.0	38.0		TRITAN_4_W_AG	0.59	410.6	4027.0	35.6	
TRITAN_5_W_UNAG	0.66	459.3	4504.7	39.8		TRITAN_5_W_AG	0.64	445.4	4368.2	38.6	
TRITAN_1_T_UNAG	0.70	487.2	4777.8	42.2		TRITAN_1_T_AG	0.61	424.5	4163.5	36.8	
TRITAN_2_T_UNAG	0.66	459.3	4504.7	39.8		TRITAN_2_T_AG	0.63	438.4	4300.0	38.0	
TRITAN_3_T_UNAG	0.73	508.0	4982.5	44.0	41.2	TRITAN_3_T_AG	0.61	424.5	4163.5	36.8	37.2
TRITAN_4_T_UNAG	0.65	452.4	4436.5	39.2		TRITAN_4_T_AG	0.58	403.6	3958.7	35.0	
TRITAN_5_T_UNAG	0.67	466.3	4573.0	40.4		TRITAN_5_T_AG	0.65	452.4	4436.5	39.2	

Source: The Author (2024).

Farias's (2022) report that TRITAN™ filaments are water-like compared to ASA was imprecise for samples subjected to fusion deposition processes. Farias' (2022) study possibly considered the filaments as marketed and not after fused deposition, which reduced transparency and increased haziness. Although the visible reflectance of white TRITAN™ is higher than that of ASA (mainly due to the yellow hue caused by the weather resistance additives), the transparent filament has a 4.4% lower visible reflectance (Table 9).

The coloration of unaged white TRITAN™ is similar to that of PETG, while the transparent filament has much lower reflectance than the other filaments. Despite this, transparent specimens' aging caused little color variation, with reflectance reduced due to loss of gloss. For white specimens, darkening was pronounced compared to unaged pieces but was the lowest among all specimens (mainly due to the lower reflectance of the unaged filament). Once again, the yellowing indicated in Ishida and Kitagaki's (2021) research did not occur, with a slight reflection reduction between 585 nm and 645 nm. For instance, Figures 12 a through c display the discoloration after the ageing process.

Table 9: Chromaticity variation for tensile TRITAN™ samples.

	ALTA II voltage (mV)												CIE L*a*b* and Color			
	470 (nm)	525 (nm)	560 (nm)	585 (nm)	600 (nm)	645 (nm)	700 (nm)	735 (nm)	810 (nm)	880 (nm)	940 (nm)	ρ_{vis} (%)				
REFERENCE	**587**	**637**	**732**	**495**	**453**	**707**	**680**	**780**	**809**	**880**	**668**	**78.3**				
1_W_UNAG																
2_W_UNAG																
3_W_UNAG	567	692	775	465	483	709	677	770	777	837	648	**94**	89	-1	0	
4_W_UNAG																
5_W_UNAG																
1_T_UNAG																
2_T_UNAG																
3_T_UNAG	458	492	540	381	358	571	561	560	572	606	503	**76,6**	74	-1	-5	
4_T_UNAG																
5_T_UNAG																
1_W_AG	541	637	730	463	453	679	563	743	763	807	624	**91,8**	67	-1	-3	
2_W_AG	504	608	687	462	403	627	606	687	729	770	604	**88,9**	71	-1	-3	
3_W_AG	518	570	651	442	393	602	616	750	770	833	643	**87,8**	75	-1	-1	
4_W_AG	541	623	717	440	445	666	633	721	751	808	621	**89,3**	75	-1	-3	
5_W_AG	533	624	730	448	444	660	634	741	762	813	631	**89,5**	73	-1	-4	
1_T_AG	381	422	467	311	297	503	483	539	549	569	482	**63,1**	69	-1	-2	
2_T_AG	426	465	527	350	330	544	535	588	590	619	513	**70,8**	72	-2	-4	
3_T_AG	407	436	498	335	317	531	520	560	576	608	507	**67,7**	73	-2	-4	
4_T_AG	380	432	493	330	311	517	508	566	583	618	512	**65,1**	73	-2	-4	
5_T_AG	415	451	496	341	314	531	513	558	598	615	514	**68,9**	69	-2	-4	

Source: The Author (2024).

Figure 12: (a) White and Clear PETG before and after aging process; (b) white and Clear ASA before and after aging process; (c) white and Clear TRITAN™ before and after aging process.

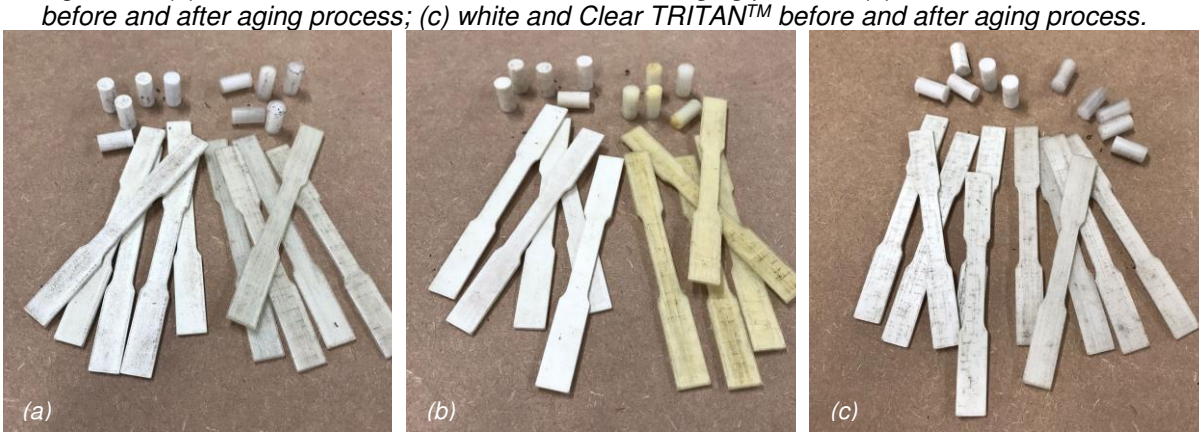

Source: The Author (2024).

5. Conclusion

This study evaluated the structural and optical integrity of three engineering-grade copolymers produced for fluid deposition modeling (FDM) applications before and after accelerated aging. The research assumed the best printing guidelines for coupon production (Hanon; Dobos; Zsidai, 2020; Hsueh *et al.*, 2021; Popescu *et al.*, 2018; Vukasovic *et al.*, 2019) for uniaxial tensile and compressive strength. The author produced 120 test coupons, 60 assessed after the FDM process and 60 after accelerated aging following ASTM G154 (American Society for Testing and Materials, 2016), ASTM G151 (American Society for Testing and Materials, 2019), ASTM D5208

(American Society for Testing and Materials, 2022), and ISO 4892 (International Organization for Standardization, 2016).

Despite the absence of standards for evaluating anisotropic polymers, it is common in the literature to adopt ASTM D638 (American Society for Testing and Materials, 2022) and ASTM D695 (American Society for Testing and Materials, 2016) for obtaining Young's Modulus, ultimate tensile and compressive strength (UTS and UCS), and fracture. This study operated a universal testing machine for tensile applications and an analog unconfined testing machine for compression tests. Thus, tension measurements were more thorough and reliable. Additionally, for optical variation analysis, the author adopted L*a*b* CIE Standard Illuminant D65 (Carter *et al.*, 2018) and reflectance measurements using a portable spectrometer.

For all tensile specimens, the increase in temperature resulting from exposure to UVA fluorescent lamps raised the material's elasticity and elongation, consequently leading to higher UTS and lower Young's Moduli. The opposite is not true for compression specimens. All white filaments reached lower UTS compared to transparent filaments, which may be correlated with chemical composition (due to pigment addition), slight differences in the printing settings indicated by the manufacturer (despite following standard printing properties for each color in this study), or lower reflectance and consequent higher thermal energy gain.

PETG exhibited the highest UTS among the unaged coupons, averaging 24.5 MPa and 28.11 MPa for white and transparent filaments, respectively. For the white filament, this represents UTS 3.45% higher than that achieved by ASA and 18.51% higher than that of TRITAN™. For the transparent filament, ASA is 17.27%, and TRITAN™ is 6.46% more fragile. After aging, the pattern persists, with PETG reaching 25.58 MPa and 28.90 MPa for white and transparent coupons, respectively. ASA reaches 24.28 MPa for both colors, and TRITAN™ ranges between 23.67 MPa (white) and 26.55 (transparent). The plastic behavior of the materials is consistently more visible in transparent filaments (which in some cases displayed necking, albeit negligibly pronounced), giving them lower Elastic Moduli.

For compression studies, ASA, which consistently had the lowest average UTS, showed the highest average ultimate compressive stress (UCS) for both colors, a characteristic generally attributed to brittle materials (despite polymers and copolymers being ductile materials). Lower UTS for ASA may indicate micro-fissures in the

specimen that, when analyzed under compression, do not cause issues but generate fissure elongation when subjected to tension. This pattern was observed in the specimens after elongation, with ASA specimens being the only coupons showing stretcher-strain marks. White ASA had an average UCS 18.39% higher than PETG specimens and 19.18% higher than those made from TRITAN™. For transparent specimens, PETG was 19.18% more fragile, while TRITAN™ only reached 79.70% of the UCS demonstrated by ASA. After aging, all specimens had reduced UCS values. Although ASA continued to demonstrate higher average UCS values, its loss was the greatest among all filaments (12.68 MPa for white and 10.51 MPa for transparent). PETG was the material that remained the most consistent, with a reduction of only 0.97 MPa for white specimens and 1.55 MPa for transparent ones.

Regarding colorimetric analysis, it is worth noting that no specimen is truly transparent after the deposition process, despite its high transmittance before the FDM process (as indicated by the manufacturer). This transmittance loss occurs because the edges between the different layers generated by the gradual construction of the piece refract light separately, generating significant distortion and giving the final piece a milky and grayish appearance. Despite this, the possibility of light transmission and the milky appearance give transparent filaments lower reflectances, as seen in the L*a*b* and visible reflectance classification. Among transparent specimens, the highest reflectances occurred for ASA, with PETG being the filament with the highest light transmission capacity and TRITAN™ showing the lowest values for L (in L*a*b*, L represents luminosity; lower values indicate colors closer to the black spectrum). For white filaments, ASA exhibits higher reflection in the yellow spectrum, which, along with the less glossy finish of the pieces after heating, causes lower reflectances.

The phase change (from solid filament to a viscous liquid during deposition and subsequent solidification) and aging of all materials resulted in darkening (decrease in L*) and visual reduction of the pieces' luster. In this study, the author only quantitatively assessed reflectance values, so the pieces' brightness variation is only qualitative. Despite the indications of Ishida and Kitagaki (2021), yellowing was not the main cause of reflectance fluctuation, with all specimens showing greater variations toward the blue and green spectra. The filament with the greatest hue variation was ASA for both colors, indicating that, despite additives to reduce aging, the filament still displays the worst decline in optical properties.

Thus, this study indicates PETG as the most suitable filament for tensile applications, regardless of color variation. For compression, the best choice would be ASA, which still demonstrated higher UCS even after aging and significant variation in structural stability. If the piece's exposure is lengthened (not evaluated in this study), PETG would be the best choice, displaying a slower structural decline. Regarding coloration, if the filaments' application depends on color maintenance, PETG, with the least variation, is also the best choice.

Acknowledgments

This study was financed by Coordenação de Aperfeiçoamento de Pessoal de Nível Superior – Brasil (CAPES) – Finance Code 001; by Fundação de Amparo à Pesquisa de Minas Gerais (FAPEMIG) – financing notice N° 001/2021 Universal Demand - under process code APQ-00266-21; and by Conselho Nacional de Desenvolvimento Científico e Tecnológico (CNPQ) – financing notice N° 59/2022 – under process code 406426/2022-8.

The author also wants to acknowledge the Construction Materials Laboratory and the Mechanical Testing Laboratory (LEC) - Civil Engineering Department - Federal University of Viçosa.

REFERENCES

ABEYKOON, C.; SRI-AMPHORN, P.; FERNANDO, A. Optimization of fused deposition modeling parameters for improved PLA and ABS 3D printed structures. **International Journal of Lightweight Materials and Manufacture**, [*s. l.*], v. 3, n. 3, p. 284–297, 2020. DOI: https://doi.org/10.1016/j.ijlmm.2020.03.003.

AGIRBAS, A. The Use of Simulation for Creating Folding Structures : A Teaching Model. *In*: 2017, Rome. **eCAADe 2017: Sharing of Computable Knowledge!** Rome: [*s. n.*], 2017. p. 325–332.

ALAFAGHANI, A.; QATTAWI, A. Investigating the effect of fused deposition modeling processing parameters using Taguchi design of experiment method. **Journal of Manufacturing Processes**, [*s. l.*], v. 36, n. June, p. 164–174, 2018. DOI: https://doi.org/10.1016/j.jmapro.2018.09.025.

ANSARI, A. A.; KAMIL, M. Effect of print speed and extrusion temperature on properties of 3D printed PLA using fused deposition modeling process. **Materials Today: Proceedings**, [*s. l.*], v. 45, p. 5462–5468, 2021. DOI: https://doi.org/10.1016/j.matpr.2021.02.137.

ASTM. ASTM D5208 - Standard Practice for Fluorescent Ultraviolet (UV) Exposure of Photodegradable Plastics. [*s. l.*], p. 5, 2022.

ASTM. ASTM D5947 - Standard Test Methods for Physical Dimensions of Solid Plastics Specimens. [*s. l.*], p. 10, 2018.

ASTM. ASTM D638 - Standard test method for tensile properties of plastics. [*s. l.*], p. 16, 2022. DOI: http://scholar.google.com/scholar?hl=en&btnG=Search&q=intitle:Standard+Test+Method+for+Tensile+Properties+of+Plastics#0.

ASTM. ASTM D638 - Standard Test Method for Tensile Properties of Plastics. [*s. l.*], p. 16, 2022.

ASTM. ASTM D695 - Standard Test Method for Compressive Properties of Rigid Plastics. [*s. l.*], p. 8, 2016.

ASTM. ASTM F2792 - Standard Terminology for Additive Manufacturing Technologies. [*s. l.*], p. 3, 2012.

ASTM. ASTM G151 - Standard Practice for Exposing Nonmetallic Materials in Accelerated Test Devices that Use Laboratory Light Sources. [*s. l.*], p. 15, 2019.

ASTM. ASTM G154 - Standard practice for operating fluorescent light apparatus for UV exposure of nonmetallic materials. [*s. l.*], 2016.

ASTM. ASTM G154 - Standard Practice for Operating Fluorescent Ultraviolet (UV) Lamp Apparatus for Exposure of Materials. [*s. l.*], p. 12, 2023.

AWASTHI, P.; BANERJEE, S. S. Fused deposition modeling of thermoplastic elastomeric materials: Challenges and opportunities. **Additive Manufacturing**, [*s. l.*],

v. 46, n. June, p. 102177, 2021. DOI: https://doi.org/10.1016/j.addma.2021.102177.

BONADA, J.; PASTOR, M. M.; BUJ-CORRAL, I. Influence of infill pattern on the elastic mechanical properties of fused filament fabrication (FFF) parts through experimental tests and numerical analyses. **Materials**, [*s. l.*], v. 14, n. 18, 2021.

BRACONNIER, Daniel J.; JENSEN, Robert E.; PETERSON, Amy M. Processing parameter correlations in material extrusion additive manufacturing. **Additive Manufacturing**, [*s. l.*], v. 31, n. October 2019, p. 100924, 2020. DOI: https://doi.org/10.1016/j.addma.2019.100924.

BRISCHETTO, Salvatore; TORRE, Roberto. Tensile and Compressive Behavior in the Experimental Tests for PLA Specimens Produced via Fused Deposition Modelling Technique. **Journal of Composites Science**, [*s. l.*], v. 4, n. 3, p. 140, 2020. DOI: https://www.mdpi.com/2504-477X/4/3/140.

BRYDEN, D. **CAD and Rapid Prototyping for Product Design**. China: Laurence King Publishing Ltd, 2014.

CALLISTER JR., W. D.; RETHWISCH, D. G. **Ciência e engenharia de materiais: Uma introdução**. 10. ed. [*S. l.*]: LTC, 2020.

CANEPARO, Luca. **Digital Fabrication in Architecture, Engineering and Construction Foreword by Antoine Picon**. [*S. l.: s. n.*], 2014.

CANO-VICENT, A. *et al.* Fused deposition modeling: Current status, methodology, applications, and prospects. **Additive Manufacturing**, [*s. l.*], v. 47, n. October, 2021.

CARTER, E. C.; *et al.* **CIE 015 - Colorimetry**. 4. ed. [*S. l.: s. n.*], 2018.

CAVALCANTI, D. K. K; BANEA, M. D.; DE QUEIROZ, H. F. M. Effect of material on the mechanical properties of additive-manufactured thermoplastic parts. In: 2020. **Dunarea de Jos University of Galati**. [*S. l.: s. n.*], 2020. p. 9.

CELINA, M. *et al.* Overview of accelerated aging and polymer degradation kinetics for combined radiation-thermal environments. **Polymer Degradation and Stability**, [*s. l.*], v. 166, p. 353–378, 2019. DOI: https://doi.org/10.1016/j.polymdegradstab.2019.06.007.

CHACÓN, J. M. *et al.* Additive manufacturing of PLA structures using fused deposition modeling: Effect of process parameters on mechanical properties and their optimal selection. **Materials and Design**, [*s. l.*], v. 124, p. 143–157, 2017. DOI: http://dx.doi.org/10.1016/j.matdes.2017.03.065.

D'AMICO, A. A.; DEBAIE, A.; PETERSON, A. M. Effect of layer thickness on irreversible thermal expansion and interlayer strength in fused deposition modeling. **Rapid Prototyping Journal**, [*s. l.*], v. 23, n. 5, p. 943–953, 2017.

DAMINABO, S. C. *et al.* Fused deposition modeling-based additive manufacturing (3D printing): techniques for polymer material systems. **Materials Today Chemistry**, [*s. l.*], v. 16, p. 100248, 2020. DOI: https://doi.org/10.1016/j.mtchem.2020.100248.

EROKHIN, K. S.; GORDEEV, E. G.; ANANIKOV, V. P. Revealing interactions of layered polymeric materials at the solid-liquid interface for building solvent compatibility charts for 3D printing applications. **Scientific Reports**, [*s. l.*], v. 9, n. 1, p. 1–14, 2019.

FARIAS, A. M. **estudo sobre a utilização de dispositivos de fixação para usinagem fabricados pela tecnologia de modealgem por fusão e deposição**. 2022. 66 f. - Universidade Tecnológica Federal do Paraná, [*s. l.*], 2022.

FERNANDES, T. F. **Avaliação das propriedades mecânicas e dimensionais de diferentes polímeros processados pelo método FDM**. 2022. 109 f. - Universidade Federal de Santa Catarina, [*s. l.*], 2022. DOI: https://www.who.int/news-room/fact-sheets/detail/autism-spectrum-disorders.

FRIGIONE, M.; RODRÍGUEZ-PRIETO, Alvaro. Can accelerated aging procedures predict the long-term behavior of polymers exposed to different environments? **Polymers**, [*s. l.*], v. 13, n. 16, 2021.

GERSHENFELD, Neil. How to make almost anything. **Foreign Affairs**, [*s. l.*], v. 91, n. 6, p. 16, 2012.

GIBSON, I.; ROSEN, D.; STUCKER, B. **Additive manufacturing technologies: 3D printing, rapid prototyping, and direct digital manufacturing**. 2. ed. [*S. l.*]: Springer, 2015.

GRABOWIK, C. *et al.* Tensile tests of specimens made of a selected group of filament materials manufactured with the FDM method. **MATEC Web of Conferences**, [*s. l.*], v. 112, p. 1–6, 2017.

GUARDA, T.; AUGUSTO, M. F. The Competitive Advantage of Additive Manufacturing in the Naval Sector. *In*: DEVELOPMENTS AND ADVANCES IN DEFENSE AND SECURITY. [*S. l.*]: Springer Nature Singapore Pte Ltd., 2020. v. 181, p. 473–481.

GUESSASMA, S. *et al.* Anisotropic damage inferred to 3D printed polymers using fused deposition modeling and subject to severe compression. **European Polymer Journal**, [*s. l.*], v. 85, p. 324–340, 2016. DOI: http://dx.doi.org/10.1016/j.eurpolymj.2016.10.030.

HAM, Namhyuk; LEE, Sanghyo. Project Benefits of Digital Fabrication in Irregular-Shaped Buildings. **Advances in Civil Engineering**, [*s. l.*], v. 2019, 2019.

HANON, M. M.; DOBOS, J.; ZSIDAI, L. The influence of 3D printing process parameters on the mechanical performance of PLA polymer and its correlation with hardness. **Procedia Manufacturing**, [*s. l.*], v. 54, p. 244–249, 2020. DOI: https://doi.org/10.1016/j.promfg.2021.07.038.

HIBBELER, R. C. **Resistencia dos Materiais**. 10. ed. [*S. l.*]: Pearson Universidades, 2019.

HSUEH, M. H. *et al.* Effect of printing parameters on the tensile properties of 3D-printed polylactic acid (Pla) based on fused deposition modeling. **Polymers**, [*s. l.*], v. 13, n. 14, 2021.

ISHIDA, Takato; KITAGAKI, Ryoma. Mathematical modeling of outdoor natural weathering of polycarbonate: Regional characteristics of degradation behaviors. **Polymers**, [*s. l.*], v. 13, n. 5, 2021.

ISO/ASTM. ISO/ASTM 52900 - Additive manufacturing — General principles — Fundamentals and vocabulary. [*s. l.*], p. 28, 2021.

ISO/ASTM. ISO/ASTM 52901 — Additive manufacturing — General principles — Requirements for purchased AM parts. [*s. l.*], p. 11, 2017.

ISO. ISO 4582 — Plastics — Determination of changes in color and variations in properties after exposure to glass-filtered solar radiation, natural weathering, or laboratory radiation sources. [*s. l.*], p. 16, 2017.

ISO. ISO 4892 - Plastics: Methods of exposure to laboratory light sources. [*s. l.*], p. 20, 2013.

ISO. ISO 4892 — Plastics — Methods of exposure to laboratory light sources. [*s. l.*], p. 25, 2016.

IZDEBSKA-PODSIADŁY, J. **Polymers for 3D Printing: Methods, Properties, and Characteristics**. [*S. l.: s. n.*], 2022.

JAFFERSON, J. M.; CHATTERJEE, D. A review on polymeric materials in additive manufacturing. **Materials Today: Proceedings**, [*s. l.*], v. 46, p. 1349–1365, 2021.

JASSO-GASTINEL, Carlos F.; SOLTERO-MARTÍNEZ, J. F.A.; MENDIZÁBAL, E. Introduction: Modifiable Characteristics and Applications. *In*: MODIFICATION OF POLYMER PROPERTIES. [*S. l.*]: Elsevier Inc., 2017. p. 1–21.

KAMRAN, M.; SAXENA, A. A Comprehensive Study on 3D Printing Technology. **MIT International Journal of Mechanical Engineering**, [*s. l.*], v. 6, n. 2, p. 63–69, 2016. DOI: https://www.researchgate.net/publication/310961474_A_Comprehensive_Study_on_3D_Printing_Technology%0Ahttps://www.researchgate.net/publication/310961474.

KAWALKAR, R.; DUBEY, H. K.; LOKHANDE, Satish P. A review for advancements in standardization for additive manufacturing. **Materials Today: Proceedings**, [*s. l.*], v. 50, p. 1983–1990, 2021. DOI: https://doi.org/10.1016/j.matpr.2021.09.333.

KEATING, S.; OXMAN, N. Robotic Immaterial Fabrication. *In*: BRAUMANN, J.; BRELL-ÇOKCAN, S. (org.). **Robotic Fabrication in Architecture, Art, and Design**. [*S. l.*]: Springer, 2013.

KHABIA, S.; JAIN, K. K. Comparison of mechanical properties of components 3D printed from different brand ABS filament on different FDM printers. **Materials Today: Proceedings**, [*s. l.*], v. 26, p. 2907–2914, 2019. DOI: https://doi.org/10.1016/j.matpr.2020.02.600.

KHOSRAVANI, M. *et al.* Failure analysis of 3D-printed PLA components: Impact of manufacturing defects and thermal aging. **Engineering Failure Analysis**, [*s. l.*], v. 136, n. November 2021, 2022.

KOCKOTT, D. New method for accelerated testing of the aging behavior of polymeric materials as a function of radiation and temperature. **Polymer Testing**, [*s. l.*], v. 110, n. April, p. 107550, 2022. DOI: https://doi.org/10.1016/j.polymertesting.2022.107550.

LI, H. *et al.* The effect of process parameters in fused deposition modeling on bonding degree and mechanical properties. **Rapid Prototyping Journal**, [*s. l.*], v. 24, n. 2, p. 80–92, 2018. DOI: https://doi.org/10.1108/RPJ-06-2016-0090.

LI, Y.; LOU, Y. Tensile and bending strength improvements in peek parts using fused deposition modeling 3D printing considering multi-factor coupling. **Polymers**, [*s. l.*], v. 12, n. 11, p. 1–14, 2020.

LIM, Henry C.A. Thermoplastic Polyesters. *In*: BRYDSON'S PLASTICS MATERIALS. [*S. l.*]: Elsevier Ltd, 2017. p. 527–543. DOI: http://dx.doi.org/10.1016/B978-0-323-35824-8.00020-7.

MENDIVIL-ESCALANTE, J. M. *et al.* Synthesis and characterization of PET polymer resin for your application in concrete. **International Journal of Structural Analysis & Design**, [*s. l.*], v. 2, n. 1, p. 105–109, 2015. DOI: http://upcommons.upc.edu/handle/2117/27717.

MENEZES, O. *et al.* Performance of additively manufactured polylactic acid (PLA) in prolonged marine environments. **Polymer Degradation and Stability**, [*s. l.*], v. 199, p. 109903, 2022. DOI: https://doi.org/10.1016/j.polymdegradstab.2022.109903.

OVIEDO, A. M. *et al.* Mechanical evaluation of polymeric filaments and their corresponding 3D printed samples. **Polymer Testing**, [*s. l.*], v. 88, n. November 2019, 2020.

OXMAN, R. Theory and design in the first digital age. **Design Studies**, [*s. l.*], v. 27, n. 3, p. 229–265, 2006.

OXMAN, R. Thinking difference: Theories and models of parametric design thinking. **Design Studies**, [*s. l.*], v. 52, p. 4–39, 2017. DOI: http://dx.doi.org/10.1016/j.destud.2017.06.001.

PEREIRA, A. R.; HIRASHIMA, S. Q. da S.; OLIVEIRA, R. D. Utilização do espectrômetro Alta II para obtenção da absortância solar de superfícies opacas. **Revista Tecnologia e Sociedade**, [*s. l.*], v. 17, n. 46, p. 216, 2021.

PERTUZ, Alberto D.; DÍAZ-CARDONA, Sergio; GONZÁLEZ-ESTRADA, Octavio Andrés. Static and fatigue behavior of continuous fiber reinforced thermoplastic composites manufactured by fused deposition modeling technique. **International Journal of Fatigue**, [*s. l.*], v. 130, p. 105275, 2020. DOI: https://linkinghub.elsevier.com/retrieve/pii/S0142112319303792.

POPESCU, Diana *et al.* FDM process parameters influence over the mechanical properties of polymer specimens: A review. **Polymer Testing**, [*s. l.*], v. 69, n. May, p. 157–166, 2018.

SANTANA, L. *et al.* A comparative study between PETG and PLA for 3D printing through thermal, chemical, and mechanical characterization. **Revista Materia**, [*s. l.*],

v. 23, n. 4, 2018.

SCHEURER, F. Materialising complexity. **Architectural Design**, [*s. l.*], v. 80, n. 4, p. 86–93, 2010.

SPEIGHT, James G. Monomers, polymers, and plastics. *In*: HANDBOOK OF INDUSTRIAL HYDROCARBON PROCESSES. 2. ed. [*S. l.*]: Elsevier Inc., 2020. p. 597–649.

TANIKELLA, N. G.; WITTBRODT, B.; PEARCE, J. M. Tensile strength of commercial polymer materials for fused filament fabrication 3D printing. **Additive Manufacturing**, [*s. l.*], v. 15, p. 40–47, 2017. DOI: http://dx.doi.org/10.1016/j.addma.2017.03.005.

TOCHÁČEK, J.; VRÁTNÍČKOVÁ, Z. Polymer lifetime prediction: The role of temperature in UV accelerated aging of polypropylene and its copolymers. **Polymer Testing**, [*s. l.*], v. 36, p. 82–87, 2014.

TOSTO, C. *et al.* Methods for the characterization of polyetherimide-based materials processed by fused deposition modeling. **Applied Sciences**, [*s. l.*], v. 10, n. 9, 2020.

VALVEZ, S.; SILVA, A. P.; REIS, P. N. B. Optimization of Printing Parameters to Maximize the Mechanical Properties of 3D-Printed PETG-Based Parts. **Polymers**, [*s. l.*], v. 14, n. 13, 2022.

VUKASOVIC, Tomás *et al.* Characterization of the mechanical response of thermoplastic parts fabricated with 3D printing. **The International Journal of Advanced Manufacturing Technology**, [*s. l.*], v. 104, n. 9–12, p. 4207–4218, 2019. DOI: http://link.springer.com/10.1007/s00170-019-04194-z.

WANG, B. *et al.* Current progress on the 3D printing of thermosets. **Advanced Composites and Hybrid Materials**, [*s. l.*], v. 3, n. 4, p. 462–472, 2020.

WANG, Peng *et al.* Effects of FDM-3D printing parameters on mechanical properties and microstructure of CF/PEEK and GF/PEEK. **Chinese Journal of Aeronautics**, [*s. l.*], v. 34, n. 9, p. 236–246, 2021. DOI: https://doi.org/10.1016/j.cja.2020.05.040.

WARD, I. M.; SWEENEY, J. **An introduction to the mechanical properties of solid polymers**. Seconded. [*S. l.*]: John Wiley & Sons Ltd, 2004-. ISSN 0009-4978.v. 42

ZHANG, X. *et al.* Characterization of mechanical properties and fracture mode of PLA and copper/PLA composite part manufactured by fused deposition modeling. **SN Applied Sciences**, [*s. l.*], v. 1, n. 6, p. 1–12, 2019. DOI: https://doi.org/10.1007/s42452-019-0639-5.

ZIEMIAN, S.; OKWARA, M.; ZIEMIAN, C. W. Tensile and fatigue behavior of layered acrylonitrile butadiene styrene. **Rapid Prototyping Journal**, [*s. l.*], v. 21, n. 3, p. 270–278, 2015.

CHAPTER V – Research-through-Design for Manufacturing and Assembly of a Cyber-physical Climate-Active Top Lighting Cell

Abstract

Although climate-active building components trace back to the 20th century, there is still a need to assess how to design, evaluate, correct, and manufacture viable prototypes to understand if digital modeling and simulation software can adequately reproduce the dynamicity of kinematic applications. The ease of access to various computational tools for building design and assessment and desktop manufacturing techniques shifted the design workflow from a prescriptive process into a performance-informed test bed that expedites product development, cuts bottlenecks, and allows designers to work with end-use materials. Still, the interdisciplinarity and iterative nature of design-for-manufacture require management and proficiency over various processes and further complicate documentation and design correction. Thus, this study presents a comprehensive research-through-design process into the development of a proof-of-product for a cyber-physical top lighting cell driven by tilting and revolving motion. It covers material selection, component evaluations for structural integrity and light transmittance, iterative design corrections, desktop digital manufacturing, automation, and assembly. As the main result, this study documents a critical design workflow, from ideation to prototyping, behind a cyber-physical system and proposes low compute time and cost component structural integrity and optical evaluations. It also indicates best design practices for fused-deposition modeling and resolutions for digital and physical incompatibilities.

Keywords: *Digital Manufacturing; high dynamic range imaging; finite element analysis; visible light transmittance; microcontrollers.*

1. Introduction

Building enclosures are physical barriers that separate indoor spaces from the external environment's meteorological fluctuations. They intrinsically absorb or counteract multiple stimuli, acting as a passive buffer of human comfort through thermal regulation, moisture management, air infiltration and exfiltration, sound insulation, and daylight admission and blockage (Loonen, 2018; Romano *et al.*, 2018). However, passive strategies offer limited environmental control, relying on prescriptive design solutions specific to the local climate, topography, and surroundings to meet human comfort standards (Gou *et al.*, 2018), and are counterproductive to the latest concept of building envelopes: a tectonic, mutable, transient, and skin-like feature with environmental reaction (Loonen, 2018; Velikov; Thün, 2017).

The evolution of the building envelope parallels advances in computer engineering and design, mechatronics, cybernetics, and novel fabrication processes. Since the 1980s, the constant transition from paper-based to computer-integrated design has caused several changes in design thinking, allowing complex structural materialization through parametric modeling and digital manufacturing techniques (Terzidis, 2015). Computer-aided design (CAD) gradually evolved into generative tools that require a knowledge base, skill set, and conceptual principles. Unlike the early cognitive models, the design workflow became a cyclical editing process with the designer choosing among a matrix of possible designs instead of single objects (Oxman, 2017; Yang, 2020). The connection between CAD and parametric modeling introduces performative design solutions, including widespread computational techniques such as building performance simulation (BPS), automation, and digital and computer-aided manufacturing (DM and CAM). In the architecture, engineering, construction, and operation field, they enable managing the entire design process, from digital data to machines, using the Design-for-Manufacture-and-Assembly (DfMA) methodology to select, prototype, correct, and improve multiple procedural, functional, and material-related aspects (e.g., constructability, model refinement, fabrication constraints, post-production necessity, and customization and standardization rate). Hence, DfMA helps create context-specific and high-performance novel building components (Dunn, 2012; Leschok *et al.*, 2023).

This study develops a Research through Design (RtD) workflow for a climate-active top lighting cell driven by tilting and revolving motion (Lucarelli; Oliveira; Carlo,

2023). It relies on previous product ideation, building performance simulation for daylight assessment, and copolymer material evaluation and selection. The top lighting cell's objective is to supply adequate indoor work plane illuminance based on cybernetic light intensity sensors and real-time response via mechanical actuation. The RtD process encompasses product development through digital solid modeling, interactive prototyping, optical infill evaluations for light transmittance, finite element method infill assessment, digital manufacturing, cyber-physical sensing and actuating, and Alpha product assembly. In this study, section 2 presents an overview of climate-active systems, desktop manufacturing, product development, and low-cost hard robotics for cyber-physical systems within design processes. Section 3 describes the materials and methods, i.e., the Design-for-Manufacture-and-Assembly, the optical evaluations of copolymers, and the low-cost automation. Section 4 presents the results of the material analysis, the interactive digital modeling, prototyping, and editing for the proofs-of-concept and product, and Alpha product manufacture and assemblage.

2. Theoretical Framework

2.1. Computer-aided Design: Climate-Active Building Enclosures

Building enclosures inherently change, adjust, and respond to environmental stimuli by filtering, absorbing, or repelling natural elements according to their benefits or disadvantages to create a physiologically balanced space (Olgyay, 2015). According to Olgyay (2015), the human comfort zone is the successful equilibrium between energy expense and productivity.

The 20th-century architecture was a product of the Industrial Revolution and evolving construction techniques and materials. The development of heating, ventilation, and air-conditioning systems led architects to prioritize the building enclosure aesthetics, overlooking its function as a buffer of human comfort and energy conservation. Modernist minimalism freed buildings from region-based design components, sustaining a machine-like concrete, steel, and glass structure to represent industrial modernity (Frampton, 1998, 2007). Since then, the International Style has disregarded the climate, landscape, and surroundings, creating high-energy-consuming facilities.

The emergence of sustainability concerns in the late 70s and further technological advancements in energy efficiency prompted a reevaluation of building design principles, inducing the resurgence of passive strategies. However, non-flexible envelopes led to occupant modifications over the building life cycle, decreasing the anticipated indoor comfort and long-term energy savings. Although prescriptive design strategies, such as building orientation, shape, layout, openings, and material selection, supplement users' comfort conditions, active building technologies help improve environmental control by employing multifunctional, automatic, and reconfigurable components (Hosseini *et al.*, 2019). Specifically, visual comfort refers to the subjective quality of the visual environment, ensuring that users experience no discomfort or fatigue due to glare and lack of lighting uniformity. It depends on the physiology of the human eye, the amount of light and its distribution, and the spectral emission of the light source (Carlucci, 2021). Daylight improves health, awareness, and well-being, influencing the endocrine system, circadian rhythm, and other psychological aspects (Cartana, 2018; Fajkus, 2013). Among the visual comfort analyses gathered by Carlucci (2021), 50% evaluated glare, 26% concerned daylight quantity, 21% light quality, and 3% light uniformity. Lucarelli, Oliveira, and Carlo (2023) also indicate that quantitative visual metrics have appeared in 49% of all research in climate-active building enclosures since 2015. In 23% of studies, they are the only simulation objective.

Thus, shading devices are essential for visual comfort improvement, especially in climates requiring selective radiation access, affecting daylight admission and distribution, solar heat gain/loss, and the likelihood of glare. Nevertheless, daylight admission is not a strategy in which the higher the illuminance values, the better the performance (Reinhart; Mardaljevic; Rogers, 2013). Overshading excludes beneficial solar gains, and its excessive ingress causes visual discomfort and undesirable heat gains. An optimized shading device should reject unwanted beam radiation, permitting it when advantageous (Glassman; Reinhart, 2013).

The contemporary combination of active and passive systems shifted the building design process from predefined formal and physical strategies to comprehensive behavioral and performance analysis. This approach increased architectural collaboration with mechanical and electrical engineering, computing, and the physical and social sciences, addressing the environmental impact and cultivating a more

resilient and responsive architectural ethos that prioritizes sustainability without compromising design aesthetics or occupant comfort. Active building systems emerged at the end of the 20th century, enabling structures to adapt automatically to prevailing user needs and environmental conditions (Romano *et al.*, 2018). Given daily and seasonal outdoor weather variations, changes in solar positions, and dynamic sky conditions, time-changing envelope configurations are a practical approach for improving indoor environmental quality and optimizing daylight and solar radiation control (Kirimtat *et al.*, 2016).

According to Lee (2019) and Loonen (2018), computational tools help oversee the building performance design workflow, identify and incorporate human comfort strategies, and support design decisions, enabling climate-responsive building components that no longer have to compromise to one static case that performs acceptably under a wide range of conditions but is never optimal. Computational design provides a digital platform for creating various models and interactive scenarios by promoting an interconnected Plan-Do-Check-Act workflow that helps anticipate incompatibilities, enhance production, and ensure seamless translation into a physical materialization (Dunn, 2012; Linner *et al.*, 2020; Oxman, 2017). It encompasses modeling, generation, parametric design, performance simulation, algorithmic arrangements, and digital manufacturing techniques, offering more freedom in planning and testing climate-active systems.

The standard creation process within analog computation is predominantly unidirectional and disconnects the virtual environment (i.e., modeling, simulation, and representation) from physical materiality (i.e., manufacturing and assembly) (Weichel *et al.*, 2016). Since the design workflow of an active system requires functional (control systems), structural (geometry, motion, and assembly), and environmental constraints (location, orientation, boundary conditions, and weather data), the virtual/material connection supports a new depth of understanding, facilitating performance investigation (Oxman, 2006; Yang, 2020). For instance, Chapter III of this Thesis proposed a novel methodology for assessing the mechanical motion of active building components using input iterators instead of optimization algorithms. The author employed a sensibility analysis to select the most contributing motion parameters according to Moloney's (2011) classification, reducing the shape combinations and increasing the number of simulation steps, as opposed to studies that only adopted

representative scenarios (Yang, 2020). They also confirmed that assessing only a few points in time does not represent the dynamicity of daylight selection and that physical experiments are an alternate resolution for computationally expensive applications.

2.2. Computer-aided Manufacture: Product Development and Prototyping

Computational design uses algorithmic complexity theory to process input data into a matrix of formal solutions. It changed the logical design workflow by combining virtual and physical into a multi-stage strategy that prioritizes material, materialization, and fabrication tectonics within conceptual thinking to keep up with the evolution of digital manufacturing and the increase in design complexity (Oxman, 2017). With CAD and CAM, designers directly transfer information to manufacturing machines, which creates a Design-for-Manufacturing (DfM) process that alleviates geometry constraints and enables custom component production without increasing labor. For instance, DfM is a branch of Design-for-Manufacture-and-Assembly (DfMA) that focuses on designing individual components. The assembly portion of DfMA studies assemblage restrictions and the best-suited fabrication methods throughout the design phases.

In the DfM approach, “designers [can] explore the creative opportunities brought by integrating digital models and […] machines” (Raspall, 2015, p.132) and control the entire design process from concept to final product (Dunn, 2012). Its applications spread through various industries, consolidating designers as makers capable of executing, intervening, and modifying a design while working with material-related methods, shifting the creative process from form/structure/material to material/structure/form (Oxman, 2017; Paio *et al.*, 2012). It also “increases the [...] relations between structure and material within the limits of the digital manufacturing logic” (Figliola; Battisti, 2021, p.5) and allows a range of performance-based analysis and shape generation.

2.2.1. Product Development Process and Prototyping

Product design is a multidisciplinary and omnidirectional strategy that concerns idealizing, planning, defining, conceptualizing, developing, and supporting a novel product. It evaluates preliminary models using controlled and documented problem-solving and decision-making (Lutters *et al.*, 2014). The decision-making relies on abductive logic (i.e., a subjective best guess) to evolve the design based on

presuppositions, and problem-solving helps gather evidence, seek patterns, and create a performance-driven result. Although Hanington (2007) indicates three design phases in product development (ideation, exploration, and fabrication), Marquis and Deeb (2018) decompose the design workflow into six stages (discovery, planning, definition, conceptual design, development, and support). Prototyping and materialization begin in the exploratory stage, permeating the product definition, conceptual design, and development. During the exploratory stage, the product's architectural form grows from constraints with other assemblies and components. Although Figure 1 shows form, function, material, and production separately, and the design workflow representation is relatively linear, all definitions occur concurrently.

Figure 1: Product design workflow example.

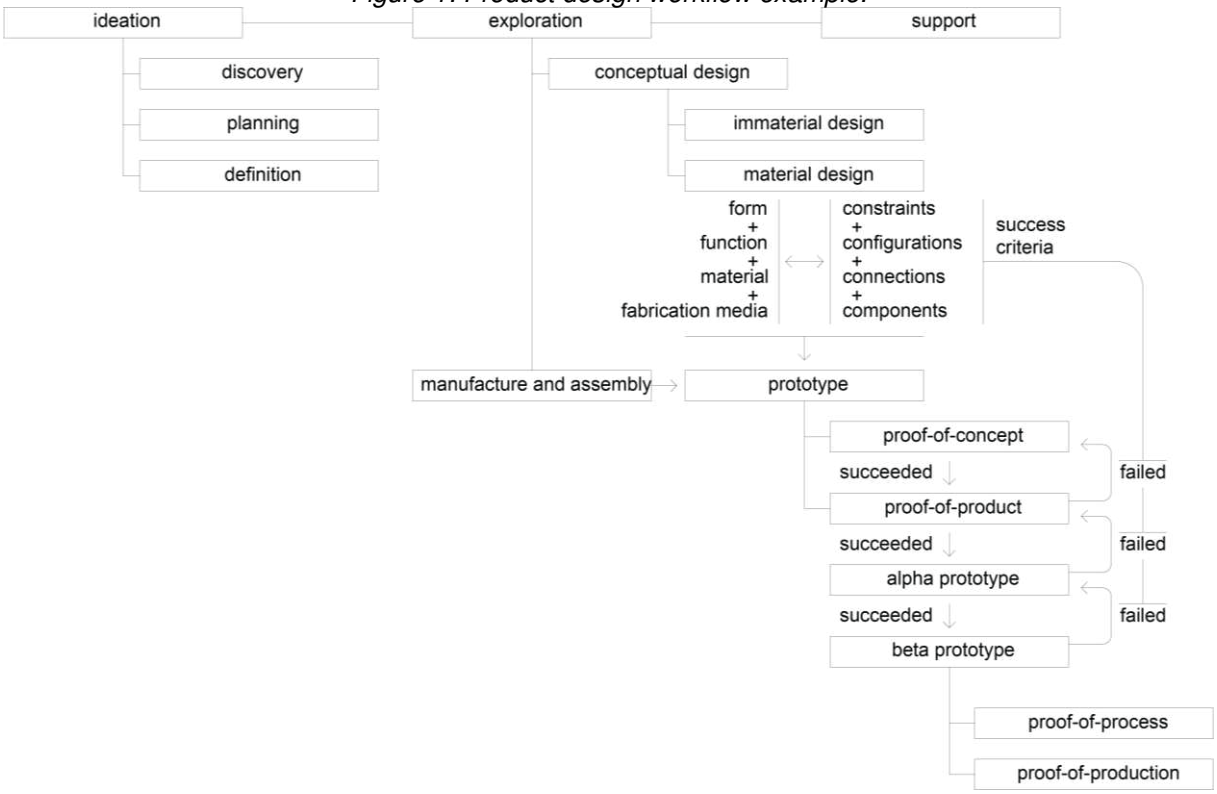

Source: The Author (2024).

Product development includes qualitative and quantitative evaluations by proofs-of-concept, product, process, or production prototypes, or Alpha, Beta, pilot, and mature products, depending on the workflow. A proof-of-concept focuses on functional aspects and engineering requirements rather than exact geometries, materials, and manufacturing processes. A proof-of-product helps refine components, assemblies, interfaces, and connections, requiring fidelity to the fabrication and materials. Alpha prototypes are the in-between both methods, even though presented after Alpha in Figure 1. For instance, CAD and CAM have greatly improved the time and cost

efficiency of building proof-of-products and subsequent categories. Proofs-of-process and production also rely on accurate form, function, material, and production. The former helps verify final geometry and manufacturing capacity, similar to Beta releases, and the latter is a preproduction run, or a pilot, manufactured just prior to the product release, i.e., a mature product.

Various investigations on DfMA focus on tinkering, rapid prototyping, designing-through-fabrication, and learning while making (de Campos *et al.*, 2019; Schön, 2017; Stappers; Giaccardi, 2017). A prototype is an approximation of a final design that represents one or more dimensions of interest (Erichsen *et al.*, 2016). Instead of validating ideas, prototypes stimulate the imagination and are a tool for building to think (Ullman, 2017). Besides assessing key functions and properties required for matured products, they fall into the learning loop category[12]. They also help communicate a concept between the originator, the development team, and the final users and define milestones along the design workflow (Schork; Kirchner, 2018).

Erichsen *et al.* (2021) separate prototyping processes according to their target audience (internal and external) and their intent (reflective and affirmative). Although their study concerns industrial DfMA experiments, their categorization elucidates which applications are the fittest for academic purposes. For instance, an internal audience represents little to no public interaction and criticism, compatible with academic research teams. Internal affirmative processes evaluate and set milestones for single parts and subsystems with high-fidelity manufacturing methods (similar to proofs-of-product), compatible with Research-through-Design procedures. In contrast, an internal reflective process is a low-fidelity and low-investment learning activity concerned with functionality and is open to criticism, change, or discard (a proof-of-concept). Thus, various academic investigations describe the dynamicity and transiency of prototyping, emphasizing the pivotal role of real-time documenting and active feedback for product development and digital fabrication (Milara *et al.*, 2019). Recording tools often include a data captor, a repository, and an interface for data retrieval. They help transfer knowledge, comply with regulatory constraints, manage risks, and ensure reproducibility and replicability (Kohtala *et al.*, 2018). As an example,

---

[12] Leifer and Steinert (2011) indicate three learning loops in product design: knowledge retention, informal team brainstorming, and tacit knowledge and skill acquirement.

Erichsen *et al.* (2021) developed a process and a research tool for compiling and analyzing data on prototyping in early-stage engineering design.

Reflective prototypes evolve from throwaway into evolutionary and incremental, i.e., they help define key components, maturing through iterative editing. Thus, the pace of prototyping and subsequent testing become critical factors. Combining digital and physical processes presents great potential for evolving and assessing product viability. Furthermore, according to Marquis and Deeb (2018, p.2), for product design, it is more “cost-effective to introduce modifications at an early stage rather than later.” Besides, the data accumulated throughout proofing checkpoints improves a product’s design and efficiency before Beta or pilot production.

2.2.2. Additive Manufacturing: Fused Deposition Modeling

Additive manufacturing (AM) comprises a series of technologies that build up objects by gradually superposing feedstock layers. Among additive processes, fused deposition modeling (FDM) is the most widespread desktop application due to its affordability, ease of use, and material availability and variety (Agirbas, 2017; Keating; Oxman, 2013). It expedites product development, offering early-stage prototyping and virtual and physical design tuning. Although FDM applications began with low-load prototypes, its technological advancements allow the printing of large-scale parts and real-time industrial applications (Leschok et al., 2023).

These processes use a thin thermoplastic filament heated above the melting point, extruded through a small nozzle, and deposited as a semi-liquid material onto the build platform, where it re-solidifies after cooling to materialize a three-dimensional object. The thinner the layers, the closer the printed object is to the digital model and the slower the operation. Feedstock thermoplastic includes general-purpose, engineering-grade, and ultra-performance materials. Apart from general-purpose filaments, these polymers and copolymers present good impact strength, can undergo high ultimate tensile and compressive stress, and resist scratching and chemicals (Jafferson; Chatterjee, 2021). Normally, prototyping processes apply general-purpose or engineering-grade polymers with low melting temperatures, such as polyethylene terephthalate glycol (PET) and acrylonitrile butadiene styrene (ABS), and copolymers such as acrylonitrile styrene acrylate (ASA) and polyethylene terephthalate glycol-modified (PETG). In FDM, filament-specific properties and printing parameters, such

as object orientation, nozzle thickness, and infill pattern and density, impact the final objects' physio-mechanical, chemical, visual, and optical properties, altering isotropy, strength, heat and moisture resistance, and surface quality (i.e., smoothness, texture, transparency, haziness, and hue) (Braconnier; Jensen; Peterson, 2020; Popescu *et al.*, 2018). For instance, inadequate print orientation and infill pattern lead to low strength and toughness in the build direction (transverse direction or Z-axis) due to poor interlayer bonding, void formation, and weak sections. Further, deficient heater block temperatures buckle the filament and clog the extruding nozzle.

Concerning light transmittance and optical properties in FDM filaments, the higher the heater block and build platform temperature, the higher the loss of gloss and surface smoothness, and the lower the color saturation (Chapter IV). The lower the print quality, the higher the visible light dispersion due to thicker layer lines. Also, polymer extrusion renders heterogeneous refractive indexes due to differences in density in amorphous and crystalline regions and solid particles of pigments or fillers. Generally, colorless polymers range from highly transparent to opaque. In transparent plastics, light scattering is minimal, and a perpendicular light incidence renders higher transmittances. Although ASTM 14782 (American Society for Testing and Materials, 2021) and ISO 13468 (International Organization for Standardization, 2019) establish polymer clarity and image-forming light transmission, FDM prints are anisotropic and scatter the light, which departs from see-through sheets, rendering the standard procedures inapplicable.

Aesthetically, the layered deposition generates a stair-stepping appearance due to polymer swelling (i.e., the bigger the nozzle diameter, the lower the printing quality, and the less precise the Z-axis height control, the thicker the layers). For pilot stages and Beta products, the prints normally require chemical or physical post-processing, such as melting, acetone smoothing, traditional machining, and sanding. Despite the post-processing, FDM is a comparably fast and clean process with no excess liquid or powder materials. Its ease and readiness to use allow for testing and improving building parts, which is crucial for climate-active systems that require multiple primary variables for materialization (Basarir; Cem Altun, 2018; Schielke, 2020).

Leschok *et al.* (2023) state that research on FDM and DfMA for architecture should further tackle printing and assembly options to assess how to split and orient prototype parts, select the best stress-strain ratio to enhance physical resilience and review the

components' optical characteristics to understand how thermoplastics age and handle weathering variations. For instance, Karagianni *et al.* (2016) designed a customizable, performance-informed shading device using small-scale FDM printers. Their study followed a linear modeling, simulation, and manufacturing process, focusing on material selection, assembly options, and constructability. Further, Grassi *et al.* (2019) developed and assessed the durability and UV stability of a high-temperature-resistant PLA mono-material shading system. The authors aged the prototypes in an age-acceleration chamber and validated the polymer optical properties utilizing a weather-exposed mockup. Their study demonstrated the efficacy of mono-material feedstock compared to composite filaments and indicated UV-resistant coating for preventing discoloration in all assessed polymers.

Regarding FDM-specific mechanical evaluations, Adams and Turner (2017) indicated that the ultimate strength, strains, and failure behavior of printed parts are functions of the infill pattern. For instance, Cho *et al.* (2019) demonstrated that a triangle pattern delivers the highest mechanical ultimate strength-to-weight ratio when compared to grid, zig-zag, rectilinear, and hexagonal patterns, and the hexagonal infill improved the mechanical resilience of mounting joints (Eryildiz, 2021). Despite FDM's anisotropy, multiple studies have already validated predictive solutions, such as the Finite Element Method, indicating high coincidence with experimental results (Galvez *et al.*, 2023).

2.3. Cyber-physical Systems (CPSs) – Mechatronics and Cybernetics

Over the last decade, the development of information and communication technologies culminated in Industry 4.0 and incited the combination of virtual and physical systems (Böke, 2020). For instance, the Internet of Things (IoT) is an open web of computing devices, actors, and mechanical machines with unique identifiers and the ability to share data over a network without human-to-human or human-to-computer interaction (Bhanu *et al.*, 2022; Böke, 2020). Until Industry 4.0, automation required extensive knowledge, which kept creative domains from experimenting with the medium (Banzi; Shiloh, 2015). The spread of the IoT, open-source culture, and affordable microcontroller boards and peripherals enabled designers and thinkerers[13]

[13] *Thinkering is a hybrid of tinkering and thinking, representing how the creative personality and creative-thinking process overlap (Michalko, 2011).*

to learn coding fundamentals, apply visual programming languages (VPLs)[14], and adopt ready-to-use sketches from public coding libraries to create advanced robotic applications. Open-source control architectures and programming languages help rethink environmentally sustainable design and energy efficiency in the built environment (Alexandru; Gheorghe, 2015; Böke, Jens; Knaack; Hemmerling, 2020). They enrich and share data among designers, assuring higher quality, reliability, greater flexibility, and lower costs in developing innovative products.

The interaction between IoT-based control and physical agents enables cyber-physical systems (CPS). After the dissemination of mechanization and information technologies, CPS is the fourth major evolution in industrial production (Wang; Törngren; Onori, 2015). For instance, cybernetics is an interdisciplinary domain concerning information and regulation in biological, mechanical, and social processing systems (Wiener, 2019). It controls the engineering aspect of mechatronics, which is the cooperation of mechanical constructions, electronics, control, and software. The transition from mechatronics into cybernetics denotes an evolution in automation strategies leading to intelligent CPSs. In CPSs, software-intensive computations manipulate and record the physical setups in a feedback loop that impacts the successive calculations (Böke, 2020; Radanliev *et al.*, 2021). Furthermore, Wang, Törngren, and Onori (2015) indicate that CPSs occur with or without internet access (i.e., decentralized, bottom-up IoT), are autonomous and cross-domain, and integrate different hierarchy levels, in contrast to mechatronic systems. They typically fall under sensor-based communication, such as wireless sensor networks and robotic systems (Bhanu *et al.*, 2022).

A microcontroller is an integrated circuit that contains a processor core, memory, and programmable input/output peripherals designed for control-oriented tasks. It manages external hardware peripherals and interacts with the environment through sensors and actuators (Garcia-ruiz; Cesar; Mancilla, 2021). Sensing devices perceive surrounding conditions, the microcontroller processes the collected data and sends impulses to actuators, and the actuators respond by moving according to pre-

---

[14] A VPL or block coding is a diagrammatic programming platform that uses boxes and arrows to facilitate the programming syntax and provide a graphical user interface. The boxes contain predefined textual programming that requires inputs from other boxes until the user reaches a working script.

programming (Moloney, 2011). Böke, Knack, and Hemmerling (2020) state that basic CPSs generally apply these electronic components due to their low-cost availability, ease of use, compatibility with prototyping processes, and open-source aspects, even if their computing power is low.

As a computer science and engineering field, robotics involves the design, mechanical construction, and operation of robots simulated via automated controls. In hard robotics, products have articulated mechanical joints and peripherals (e.g., the controller board, jumper wires, protoboard, sensors, actuators, and power source) that influence the geometry and their fabrication process (Schumacher; Vogt; Krumme, 2020). The CPS's design should encase the fragile hardware, connect the mechanical and electric parts, ensure actuation, and correctly place the sensors. DM and DfMA approaches facilitate kinematic incorporation from the initial design stages, anticipating constraints and components' placement due to high formal flexibility (Augustí-Juan, 2018; Gibson; Rosen; Stucker, 2015).

3. Methodology

The author adopted previous motion characterizations for active building applications (Lucarelli; Oliveira; Carlo, 2023), whole-building performance simulation and calibration (Lucarelli; Oliveira; Carlo, 2022), thermal and visual comfort assessment (Chapter III), physical motion constraints of tilting and revolving operations from a base case (Chapter III), and fused deposition modeling material selection based on physical and optical analysis (Chapter IV). Figure 2 shows this Chapter's workflow.

This exploratory, experimental, and constructive study employed a Research-through-Design (RtD)[15] and a Design-for-Manufacture-and-Assembly (DfMA) basis to develop a climate-active top lighting cell driven by tilting and revolving motion (Chapter III). The RtD and DfMA first stage incorporated component evaluations regarding the influence of infill patterns and density on uniaxial compressive strength and light transmittance (Section 3.1). The second phase explored the product development from a proof-of-concept to a Beta proof-of-product using iterative cycles of digital modeling

[15] *RtD is a practice-based strategy combining design stages, professional skills, and scientific inquiry to produce and disseminate contextualized, replicable, reliable, and impactful knowledge that contributes to a better understanding of future design issues (Herriott, 2019; Prochner; Godin, 2022).*

and materialization (Section 3.2). The third stage comprised the Arduino sketch programming, sensors and actuators selection and incorporation, physical motion evaluation, shape corrections, post-processing, and assembly (Section 3.3).

Figure 2: Research Workflow - main research methodologies highlighted in magenta. In cyan, each stage best covers the procedures.

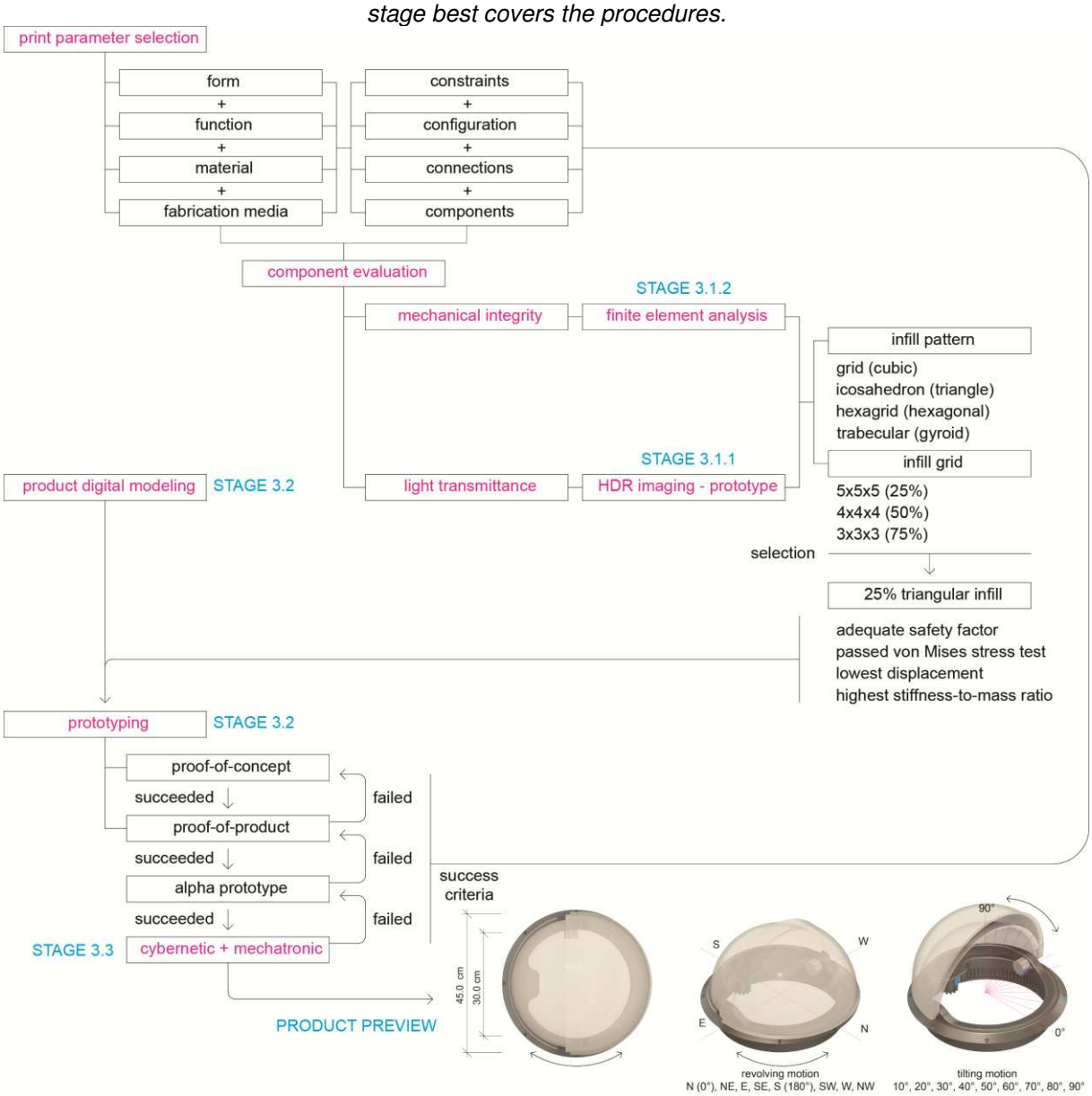

Source: The Author (2024).

3.1. Mechanical and Optical Component Properties

This study followed two methodologies for assessing the mechanical and optical properties of Fused Deposition Models (FDM). It applied a Finite Element Analysis to select the fittest infill pattern for better product structural stability and an experimental light transmittance evaluation using physical high dynamic range (HDR) luminance distribution. Both approaches are extensively employed, and therefore, it was not

within the scope of this study to compare computational simulation and physical evaluations (Galvez *et al.*, 2023; Jones; Reinhart, 2017; Weber; Reinhart; Oxman, 2020).

The author adopted PETG as feedstock for the DfMA process since previous studies indicated that this copolymer displays high ultimate tensile stress, good compressive behavior, and low discoloration and structural decline after fusion and rapid aging processes (Chapter IV). Following the same study, they also adopted PrusaSlicer as a slicing software.

3.1.1. Light Transmittance Evaluations

According to NBR 15215-4 (Associação Brasileira de Normas Técnicas, 2021), light measurements can occur on physical models in smaller scales without corrections. Therefore, for the light transmittance assessment, the author created a 30x30x20 cm box with a top opening representing a 1:10 scale model of the Hall Space presented in Chapter III (Figures 3a, b, and c). All model surfaces are blank MDF boards with a single circular roof opening, later covered with different PETG print coupons (Figure 3c). The box is inside a blacked-out room with a single light source (PAR 20, 7 w, 4000 k, 525 lm) 10 cm above the top opening, casting light on the PETG coupons. The author opted for a wider opening instead of a matrix of smaller ones as they intended to evaluate the material geometric arrangements, not the roof opening, already assessed in Lucarelli, Oliveira, and Carlo (2024).

Figure 3: *(a) Light Transmittance evaluation space; (b)* Light *transmittance coupon; (c) assembled experiment; (d) triangular, cubic, hexagon, and gyroid infill patterns.*

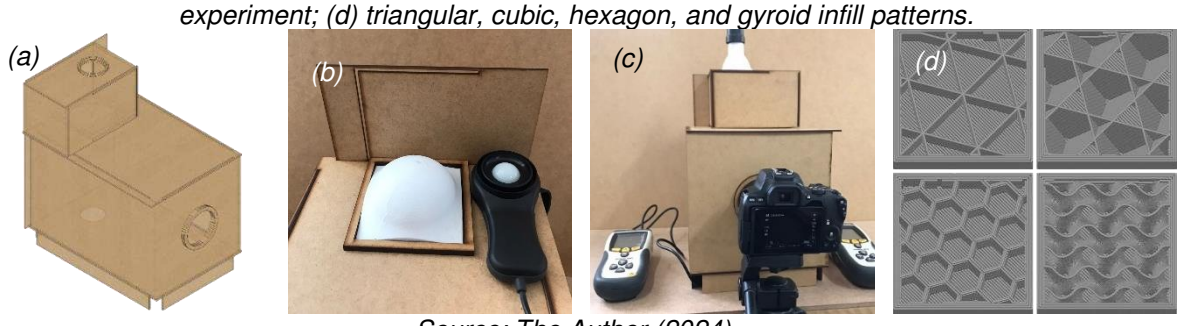

Source: The Author (2024).

The author produced 24 light test coupons[16] measuring 8.5x8.5x0.5 cm and complying with the print properties recommended in Chapter IV. Half of the coupons

[16] *The 24 coupons comprise three white and three clear coupons with 25%, 50%, and 75% cubic infill; three white and three clear coupons with 25%, 50%, and 75% gyroid infill; three*

are clear, and the other half are white. Their infill patterns are cubic, gyroid, hexagonal, and triangular (Figure 3d), as these are the most structurally sound and widespread options and present 25%, 50%, and 75% infill densities. Also, they adopted a clear PETG sheet with the same size to create a base case. The coupons had a 0.05 mm print resolution, variable infill pattern and density, and solid 0.4 mm wall widths (top, bottom, and sides). As mentioned above, the author placed each coupon below the lamp and above the top opening to assess the optical properties of each configuration.

There is a 4.5 cm circular cut on the bottom of the box, in which the author embedded a lux meter sensor (400.000 lux, ±3.0%, DT-8809A CEM) to measure the transmitted light output. A second lux meter is next to the top opening, recording the incident light input (Equation 1).

$$T = \frac{I_{tlo}}{I_{ili}} \qquad (1)$$

Where: *T: Light transmittance (%)*
I_{ili}: Incident light input Illuminance (lux)
I_{tlo}: Transmitted light output Illuminance (lux)

As the box anchored into a steady table and the experiment did not move, the incident light remained unchanged. The author collected the illuminance level inside the box for each coupon change simultaneously with the first picture taken by the camera.

For the high dynamic range imaging, a Canon Eos Rebel SL3 outfitted with an EF 8-15 mm, USM Circular Fisheye lens, hooked to a third opening on the middle of the front side of the box, large enough to fit the lens while blocking light (66 cm diameter). The 15 cm from the bottom to the lens' center is compatible with a user's eye level in a 1:10 scale. The author used exposure bracketing to capture 16 pictures for each PETG coupon replacement with exposure times ranging from 1/4000s to 8s (i.e., 8s, 4s, 2s, 1s, 1/2s, 1/4s, 1/8s, 1/15s, 1/30s, 1/60s, 1/125s, 1/250s, 1/500s, 1/1000s, 1/2000s, and 1/4000s). The aperture is at an f/4 stop, and the ISO stays at 100. They merged each bundle of 16 pictures into 24 HDR image files (one for each light transmittance coupon) using Adobe Photoshop Lightroom. They analyzed luminance

---

white and three clear coupons with 25%, 50%, and 75% hexagonal infill; and three white and three clear coupons with 25%, 50%, and 75% triangular infill.

photometric distribution using the Honeybee Radiance False Color component and Glare HDR post-processing.

3.1.2. Finite Element Analysis

The author used the top lighting cell described in Chapter III as a base for the Finite Element Models, Autodesk Fusion360 as a Finite Element software, and Autodesk Nastran as a simulation solver. The simulation requires material properties, structural loads, physical interfaces and constraints, and a simplified mesh. The material properties followed the Chapter IV findings: average Young's Moduli of 245.24 and Yield strength of 28.90 MPa. The author modeled the space used for light transmittance analysis presented in Section 3.1.1. They embedded the PETG coupons into the top opening (a representation of a roof slab) using a bonded contact with no degrees of freedom. The applied force was compressive, 2500 N, normal to the cell's geometric center, with an influence diameter of 8.5 cm. The force is sufficient to deform the coupon but is below the Ultimate Compressive and Tensile Forces of PETG prints. As the top lighting cell mainly endures compressive stress, the author did not assess tensile scenarios other than the resulting von Mises stress tension and deformation that occurred due to the compressive force.

As the slicing software imports closed objects, separates them into deposition layers, inserts infill and supports, and outputs a toolpath for the FDM printer, their properties describe the XYZ coordinates for the extrusion nozzle rather than a shape model, which is not compatible with structural analysis software. Therefore, the author reverse-engineered the .gcode files into a comparable lattice structure using Autodesk Netfabb and later imported them into Autodesk Fusion360 as simplified meshes. They also compared the sliced coupon density with the lattice model using Equation (2) to establish their compatibility. For instance, the adopted slicing software, PrusaSlicer, indicates print volume, the mass of fused material, and support percent.

$$d = \frac{F_t - (F_t F_s)}{V} \quad (2)$$

Where: *d: coupon density (g/mm^3)*
F_t: mass of fused filament (g)
F_s: percent of support filament (%)
V: Print volume (mm^3)

3.2. Design for Manufacturing and Assembly (DfMA)

Autodesk Fusion360 is one of the most established design tools for market and prototyping. Its parametric-based history line modeling approach does not depend on visual programming languages. The software is operation-based instead of sketch-based and supports advanced design options such as thickening, hollowing, and chamfering. In addition, it is interoperable with other Autodesk products employed in this study. It presents specific interfaces for product design, generative processes, animation, finite element simulation, manufacture, and mechanical drawing. In this study, the author adopted its simulation environment, as mentioned in the previous Section, and its product and generative design interfaces for product development. All simulation processes are part of the design for manufacturing and assembly (DfMA) workflow, as they help define material properties and constraints. However, the product design and prototyping cycle began with appearance models and proofs-of-concept, which is the ideation and digital modeling of the conceptual design.

Geometry, mechanical motion, and constraints are according to Chapter III and Lucarelli and Carlo's (2019) Factorial Analysis and Analysis of Variance (ANOVA) for top lighting strategies in Viçosa-Brazil. In their research, tilting responded to 67.84% model contribution with an F-value of 218.32. For revolving motion, the contribution was 4.32% (much lower than tilting but representative), and the F-value was 13.91. Therefore, the product development focused mainly on tilting motion but acknowledged revolving and applied it to the digital model and prototypes.

Following previous thermal and visual simulation results, the author divided the cell mechanical movement into sequential shading states to simplify a continuous motion, reducing the number of geometric combinations and the computational cost. Tilting states are: 0° or closed, 10°, 20°, 30°, 40°, 50°, 60°, 70°, 80° and 90°, or fully opened; and revolution stages are: 0° or north, 45°, 90°, 135°, 180° or south, 225°, 270°, and 215°. Since RtD is a cyclical trial-and-error procedure, these parameters and constraints varied according to design corrections in the subsequential design stages.

For the proofs-of-product, the author used two Prusa MINI+ and a Prusa i3 MK3 FDM printers loaded with Clear PETG filament for the shading shells (or the opening part) and White PETG for the cell structure, complying with the following fabrication parameters: 220 °C nozzle temperature, 80 °C bed temperature, 150 mm/s travel

speed, and 70 mm/s infill speed. The author opted to produce the shells using the clear filament due to its potential natural light supplementation, even in cases in which the top lighting cell remains closed due to glare, rain, or manual override. Printing resolution, infill density and geometry, print direction, and positioning, and supports' density evolved according to post-print analysis, Finite Element Evaluations, and light transmittance assessment. Since the printers' build volume is 180x180x180 mm and 250x210x210 mm, respectively, and the model needed to cover a 250 mm diameter circular roof opening, the author split the full-scale prototypes into several manageable parts, detailing the assembly sequence and connection tolerances and correcting the digital model according to physical incompatibilities. For later stages leading to Beta prototypes, the author used a Creality CR5-PRO H Industrial FDM printer with a 300x225x380 mm build volume to create full-size components, eliminating unnecessary assembly steps.

3.3. Cyber-physical System Materialization and Hard Robotics

The addition of microcontrollers, sensors, and actuators into the physical proofs-of-concept to create the cyber-physical assembly obeys the same geometric motion constraints and DfMA materialization parameters. The author used a Blackboard UNO R3 microcontroller equipped with a DHT22 air temperature and humidity sensor, a BH1750FVI-GY-30 illuminance module, an LM393 raindrop sensor, two ULN2003 drivers for two 28byj-48 5 VDC stepper motors, and a data logger shield. Based on light and rain readings, the Arduino sketch controls the two stepper motors and logs the data to an SD card. The top lighting cell should tilt according to the sequential shading states until it meets the adequate illuminance reading, reverting its motion when illuminance levels surpass the maximum threshold and closing when it rains. If it fails to reach 500 lx or all shading states provide more than 2000 lx[17], the cell should revolve 45° clockwise and repeat the tilting sequence beginning at 0° tilt angle. The first cardinal position is northeast, following Chapter III indications.

---

[17] According to NBR 8995 and EN 12464-1 (Associação Brasileira de Normas Técnicas, 2013; European Standard, 2021), 500 lx is an adequate illuminance level for office activities. Nabil and Mardaljevic (2005) indicate 2000 lx as a threshold for the likelihood of glare.

4. Results

4.1. Optical Evaluations

The experiment for obtaining light transmittance consistently indicated higher results for transparent coupons, regardless of density and infill pattern, which is theoretically and empirically coherent. Although the manufacturer specifies PETG as a high-transparency filament, this property applies to the unprocessed filament, as manufacturing at high temperatures creates opaque bodies, which becomes evident when comparing the base case (a clear PETG sheet with the same thickness) to the final product of the FDM process. Additionally, the layer deposition coupled with infill geometries increases light scattering, represented by the larger opening angle of the illumination beam. The figure in Table 1 demonstrates the luminance distribution created in Honeybee Radiance for the base case.

Table 1: Illuminance and luminance for the base case – Clear PETG Sheet.

Base Case – Clear PETG Sheet	
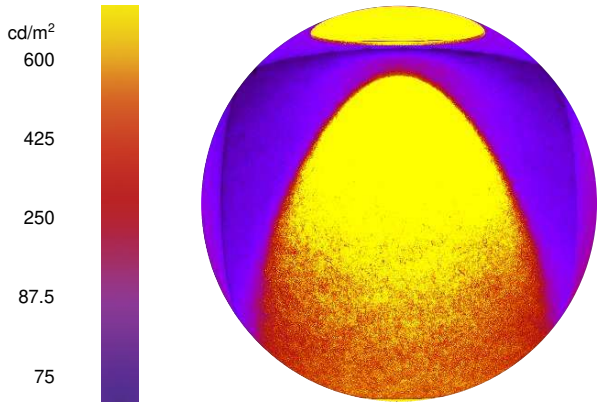	
Max. Illuminance (lx)	5590.00
Min. Illuminance (lx)	2820.00
Average (lx)	4205.00
Light Transmittance (%)	**87.51%**

Source: The Author (2024).

Compared to the images in Table 2, the light distortion is much greater in cases produced by fluid deposition. As higher transparency and lower density correspond to photometric distributions with a greater variety of false colors, the comparison between the base case and the transparent test bodies better illustrates the dispersion of lighting vectors. The author did not produce a base case with a white PETG sheet, as the lux meter positioned inside the box returned only null illuminance values. Similarly, images produced with different apertures did not capture light, which hinders HDR applications. Invariably, the images demonstrate a reduction in the density of false colors for higher infill percentages. The cubic pattern with 25% infill (Table 2) demonstrated a higher density of points near 600 cd/m^2, a value indicated by Radiance

as the highest luminance achieved by the base case. In contrast, the hexagonal infill presented lower potential for illuminating the space, followed by the gyroid pattern. It is coherent that the gyroid infill provides lower light transmission since it is not linear in the Z-axis, generating a greater number of print layers blocking the light passage. However, the hexagonal infill is linear on the Z-axis. The printer only deposits new coatings in contact with the previous layers, which would not justify a lower light transmittance. One explanation would be the greater amount of filament used for this infill, characterizing a higher density coupon, even though the infill shown by the slicing software was the same (in Section 4.2, Table 3 shows average coupon densities for the finite element structural analyses).

Table 2: HDR and illuminance of each filament color, pattern, and infill density.

		Infill Density		
		25%	**50%**	**75%**
Cubic Infill	Clear	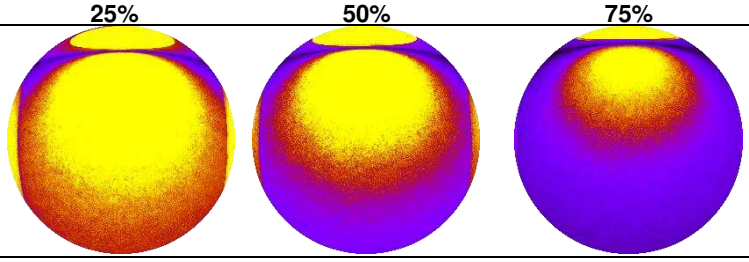		
	Max. Illuminance (lx)	1056.00	665.00	459.00
	Average (lx)	1029.00	648.50	452.00
	Min. Illuminance (lx)	1002.00	632.00	445.00
	Light Transmittance (%)	**21.42%**	**13.50%**	**9.41%**
	White	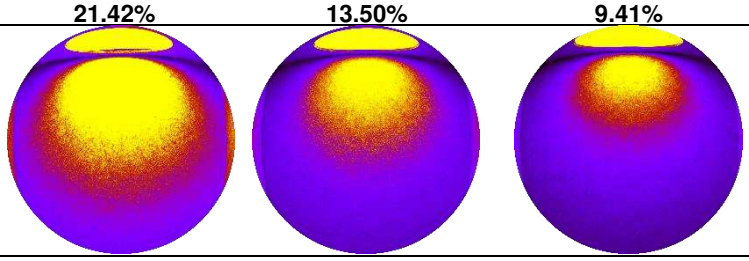		
	Max. Illuminance (lx)	375.70	248.40	154.90
	Average (lx)	374.45	247.00	154.40
	Min. Illuminance (lx)	373.20	245.60	153.90
	Light Transmittance (%)	**7.79%**	**5.14%**	**3.21%**
Triangular	Clear	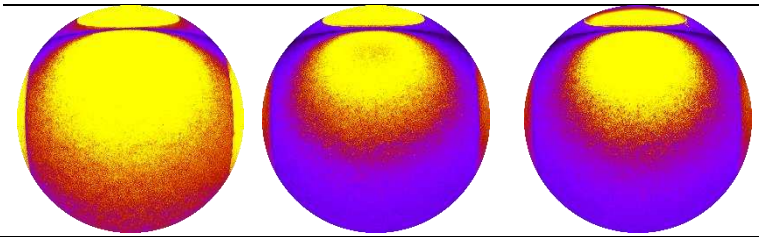		
	Max. Illuminance (lx)	900.00	801.00	721.00
	Average (lx)	882.00	771.50	682.50
	Min. Illuminance (lx)	864.00	742.00	644.00
	Light Transmittance (%)	**18.36%**	**16.06%**	**14.20%**

(Continues)

(Table 2 continues): HDR and illuminance of each filament color, pattern, and infill density.

	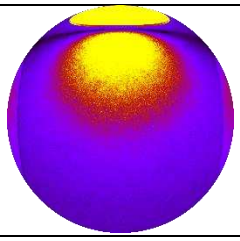	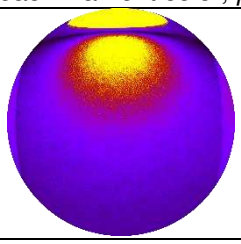	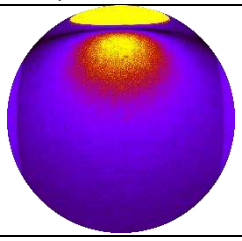	White	
Max. Illuminance (lx)	241.40	175.90	135.90		
Average (lx)	239.35	175.35	135.45		
Min. Illuminance (lx)	237.30	174.80	135.00		
Light Transmittance (%)	**4.98%**	**3.65%**	**2.82%**		

(Continues)

(Table 2 contin-

	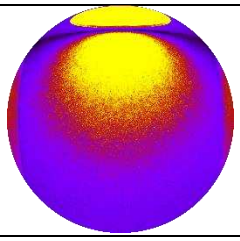	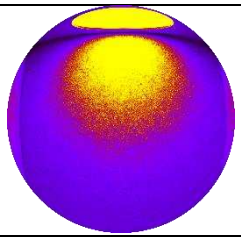	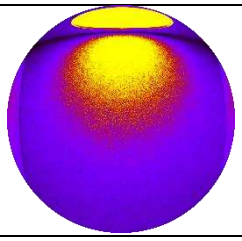	Clear	Hexagonal
Max. Illuminance (lx)	644.00	461.00	351.80		
Average (lx)	628.50	448.00	351.05		
Min. Illuminance (lx)	613.00	435.00	350.30		
Light Transmittance (%)	**13.08%**	**9.32%**	**7.31%**		
	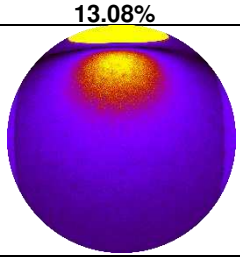	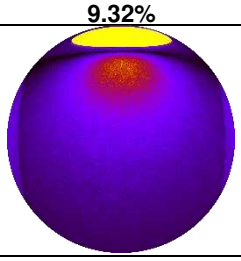	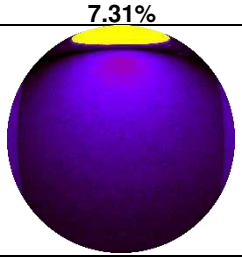	White	
Max. Illuminance (lx)	171.70	93.90	61.70		
Average (lx)	169.60	93.10	61.40		
Min. Illuminance (lx)	167.50	92.30	61.10		
Light Transmittance (%)	**3.53%**	**1.94%**	**1.28%**		
	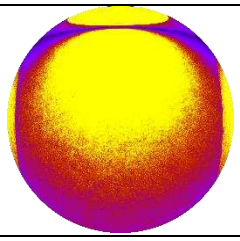	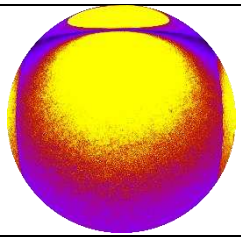	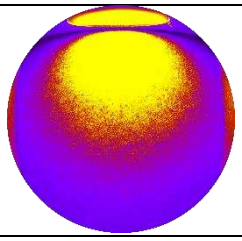	Clear	Gyroid
Max. Illuminance (lx)	788.00	577.00	455.00		
Average (lx)	775.00	559.00	445.00		
Min. Illuminance (lx)	762.00	541.00	435.00		
Light Transmittance (%)	**16.13%**	**11.63%**	**9.26%**		
	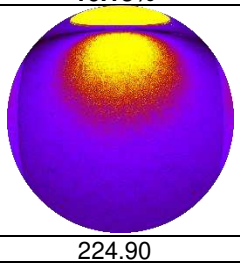	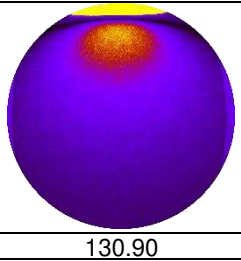	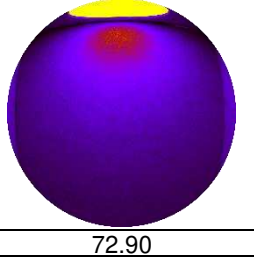	White	
Max. Illuminance (lx)	224.90	130.90	72.90		
Average (lx)	223.70	130.55	72.70		
Min. Illuminance (lx)	222.50	130.20	72.50		
Light Transmittance (%)	**4.66%**	**2.72%**	**1.51%**		

Source: The Author (2024).

The qualitative analysis of the false color map does not allow for a precise measurement of light deviation or haze, aligning with the indications of ISO 14782 (International Organization for Standardization, 2021) regarding materials with low transmittance generating results that are not highly representative of their optical characterization. Tables 1 and 2 also depict the maximum and minimum illuminance values collected by the lux meter positioned at the back of the measurement box, along with the average illuminance values and light transmittance provided by each coupon. The average illuminance near the light source was 4805 lx (with a maximum of 5800 lx and a minimum of 3810 lx), adopted as the calculation basis for all light transmittance values, as the experiment remained fastened to a table.

The light deviation analysis indicates that even for the lowest infill densities, the hexagonal and gyroid patterns achieved maximum luminous transmittances of 13.08% and 16.13%, respectively. For instance, these values are lower than that attained for the highest infill density in a triangular pattern. Overall, the clear triangular infill achieved the highest average visible light transmittance, considering the three infill percentage scenarios. Although the white filament used in the study is opaque and inhibits light passage before the FDM processing, the test coupons demonstrated light transmission capacity due to both print porosity and the low thickness of the solid layers. Therefore, even a plaque with solid infill would show low levels of light transmission until a particular thickness. Also, the printing process causes filament swelling and subsequent shrinkage, further increasing the layers' porosity. Another determining factor is the presence of burnt clumps, typical FDM printing errors, which occupy a smaller printing area due to the burning and shrinkage of the neighboring filament.

Even though luminance levels for white coupons are lower than the translucent applications, in various circumstances, the average illuminance was above 200 lx, a suitable illuminance threshold for transitional spaces. For instance, a walking activity is compatible with the work plane height at which the author positioned the lux meter sensor. These values do not characterize the entire room, as the measurement equipment is directly below the opening. However, the purpose of this work is to evaluate the percentage of PETG translucency, not its potential to achieve adequate illuminance levels.

4.2. Mechanical Evaluations

The author adopted the geometric study presented in Chapter III as the structural simulation geometry. Transposing the infill patterns to lattices and manual editing is computationally costly, as is the simulation, which requires a more refined analysis mesh to match the adopted infill size. Table 3 shows the comparison between the densities of the geometries generated by the slicer and those created and manually edited in Autodesk Netfabb.

Table 3: Infill and lattice body density.

FDM Slicer – Physical coupons				Lattice Properties – Digital FEA				Avg. Density Diff. (%)
Infill Pattern	Infill Density (%)	Used Fill. (g)	Coupon Density (g/mm³)	Lattice Pattern	XYZ Grid (mm)	Used Fill. (g)	Coupon Density (g/mm³)	
Cubic	25%	37.66	7.52E-04	Grid	5x5x5	27.88	7.53E-04	0.11%
	50%	44.57	7.88E-04		4x4x4	29.29	7.74E-04	1.81%
	75%	51.02	8.16E-04		3x3x3	32.06	8.13E-04	0.48%
Triangle	25%	38.28	7.84E-04	Icosahedron	5x5x5	44.25	7.70E-04	1.79%
	50%	45.45	8.43E-04		4x4x4	47.49	8.00E-04	0.59%
	75%	51.84	8.74E-04		3x3x3	51.51	8.41E-04	2.32%
Hexagonal	25%	41.06	7.56E-04	HexaGrid	5x5x5	30.06	7.91E-04	0.86%
	50%	50.61	7.96E-04		4x4x4	33.33	8.39E-04	0.51%
	75%	57.46	8.22E-04		3x3x3	38.26	8.59E-04	1.74%
Gyroid	25%	38.51	7.61E-04	Trabecular	5x5x5	34.34	8.60E-04	0.20%
	50%	46.11	8.13E-04		4x4x4	37.40	8.98E-04	1.75%
	75%	52.72	8.54E-04		3x3x3	40.68	9.37E-04	1.80%

Source: The Author (2024).

Among the options offered by the software, the author selected those that most closely resembled the infill patterns and modified the lattice elements to match their density and structure. After the editing process, the largest absolute discrepancy occurred between the triangular infill and the icosahedron structure. However, the difference is approximately 0.33 g when comparing a 75% triangular infill coupon and a piece with a compatible lattice. Even though all cases demonstrated low variations in volume and used filament, the higher the visual resemblance between infill and lattice, the smaller the differences. For instance, the hexagonal pattern and the hexagram lattice differed by 3.12%, considering all infill densities, while the triangular pattern reached a 4.70% dissimilarity.

Figure 4 illustrates the finite element analysis results for each infill pattern with the lowest density, which corresponds to higher light transmittances intended for the top lighting shells. Even when using a compressive force greater than the anticipated for future cell applications, the maximum deflection reached only 5 mm at the critical point in cubic, hexagonal, and gyroid structures. The most noticeable deformations occurred farther from the tilt axis and at the highest shell point, where there are no structural

constraints, unlike the lower portion of the stationary shell and the tilting juncture. The deformation is due to the compressive load pushing and spreading the shell sides in areas with minimal or no contact.

The author employed the von Mises failure criteria due to the triaxial compression scenario and the ductility of PETG. In this context, the force is deviatoric and leads to failure due to distortion rather than volume change.

Figure 4: Finite Element Analysis for 25% infill top lighting cell geometry.

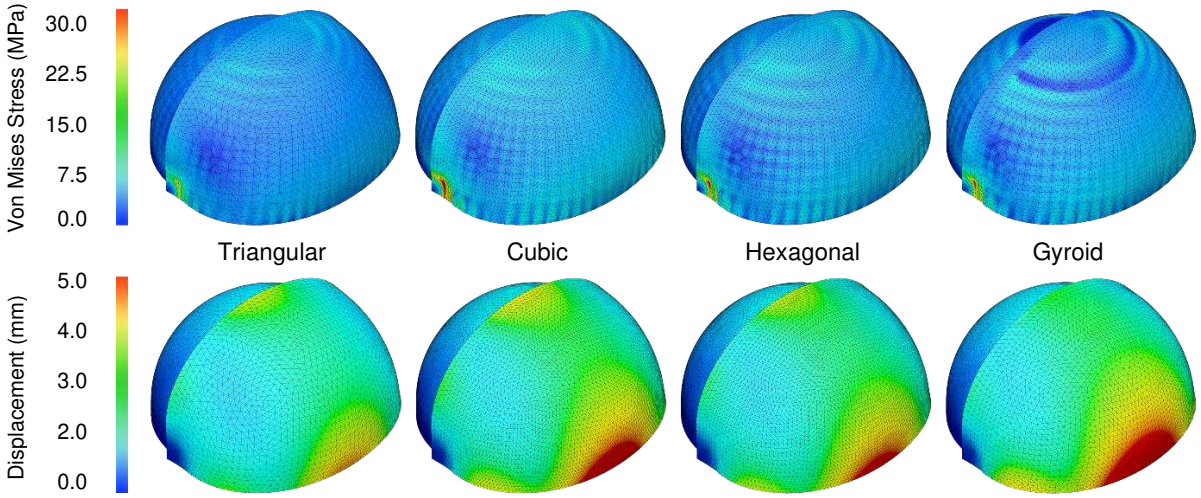

Source: The Author (2024).

A substantial portion of finite elements exhibits no tensile stress as they are only under compressive force. Given that the top lighting's base fully attaches to a rotating plaque, its deformation would result in pulling force only when the compressive force occurs at a single point rather than distributed across the surface, as in the finite element analysis. Regardless, even if the rest of the cell structure undergoes tension, the stationary ring that anchors the revolving cell into the roof slab exerts a compressive counterforce.

The same does not occur for the tiltable shell piece, which shows high-stress values at the tilt axis (i.e., the connection between the tilting motor axis, revolving base, and stationary shell). Therefore, the design exhibits the lowest anchoring surface precisely at the point where the geometry tends to open. Considering a yield strength of 28.90 MPa, the only infill pattern that did not demonstrate plastic deformation was the triangular. All other infill patterns reached the maximum distortion energy at the connection point between the cell's shells. Table 4 indicates the results for each infill density.

For all applications, the cubic and gyroid patterns did not reach the minimum safety factor of 1. The same applies to the hexagonal pattern with infill densities of 25% and 50%. Thus, except for the triangular pattern, all applications presented some instances of permanent deformation or structural failure due to breakage. Among the failing structures, the increase in infill only indicates the prevention of plastic deformation for the hexagonal pattern. Still, the applications of the triangular infill pattern consistently demonstrated higher specific stiffness, justifying its adoption in structural applications.

Table 4: Finite Element Analysis results for various infill patterns and densities.

		Triangular		Cubic		Hexagonal		Gyroid	
		Min	Max	Min	Max	Min	Max	Min	Max
25% Infill	Safety Factor (min. 1)	1.20	15.00	0.73	15.00	0.86	15.00	0.74	15.00
	von Mises Stress (MPa)	0.00	24.38	0.00	35.95	0.00	30.50	0.00	93.23
	Displacement (mm)	0.00	3.97	0.00	5.35	0.00	4.26	0.00	5.98
	Stiffness-to-mass (KN/mm)	0.60		0.58		0.55		0.57	
50% Infill	Safety Factor (min. 1)	1.35	16.92	0.83	16.93	0.99	17.19	0.82	16.81
	von Mises Stress (MPa)	0.00	21.26	0.00	31.32	0.00	26.06	0.00	81.98
	Displacement (mm)	0.00	3.46	0.00	4.66	0.00	3.64	0.00	5.26
	Stiffness-to-mass (KN/mm)	0.53		0.51		0.48		0.51	
75% Infill	Safety Factor (min. 1)	1.50	18.69	0.91	18.71	1.08	18.83	0.90	18.31
	von Mises Stress (MPa)	0.00	18.38	0.00	27.04	0.00	22.71	0.00	72.68
	Displacement (mm)	0.00	2.99	0.00	4.03	0.00	3.17	0.00	4.66
	Stiffness-to-mass (KN/mm)	0.48		0.46		0.44		0.47	

Source: The Author (2024).

4.3. Design for Manufacturing and Assembly – Alpha and Beta Prototypes

The top lighting cell has two functional and structural parts: a lighting control portion (related to its dome-like shells) and a structural anchoring (concerning the structural and mechanical parts that bind the cell to the roof slab and induce movement). Figure 5 illustrates the starting point (or the proof-of-concept) of the top lighting cell developed in Chapter III.

Based on the optical and structural properties of PETG components demonstrated in Result Section 4.1 and the material properties in Chapter IV, the author adopted transparent PETG for the lighting control shells and white for the structural anchoring and mechanical pieces. The premise is that even if the cell remains closed (due to rain, glare, or user manual override), the installation space can receive some natural light.

Thus, the shell structure used the 25% density triangular infill that achieved the highest average visible light transmittance among all studied patterns. Additionally, the infill pattern did not show structural failure, even when subjected to forces greater than those expected for a future Beta product, and its stiffness-to-mass ratio was the

highest. The author also adopted the 25% density triangular infill for the structure moving parts and 75% infill for the fastening parts. The increase in infill density for these specific cases is due to the bolted joints, which, depending on the force applied during fastening, can lead to unexpected breakage not predicted by the finite element simulation.

Figure 512: First top lighting cell configuration. Proof-of-concept to proof-of product.

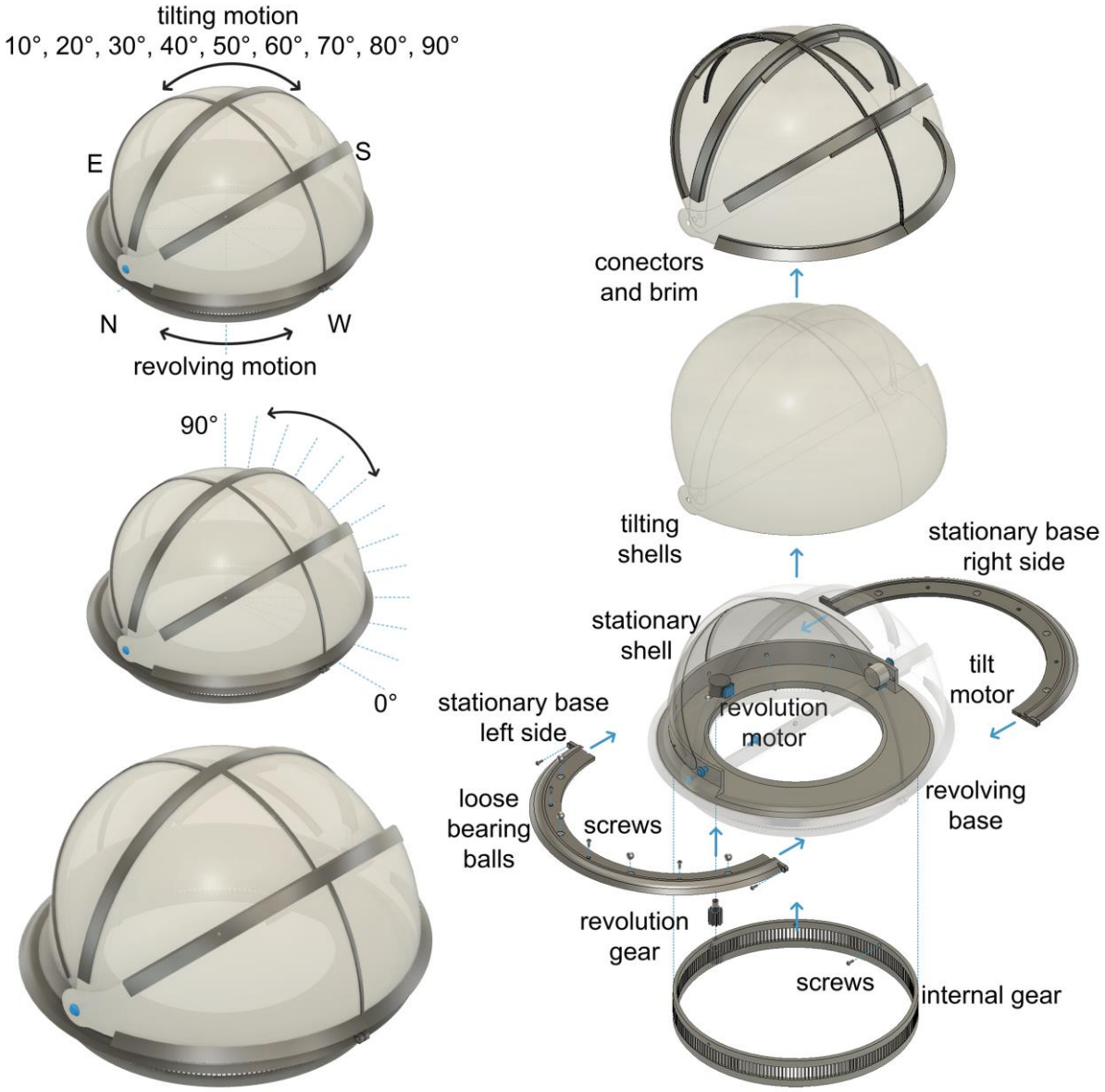

Source: The Author (2024).

For both cell portions, the author positioned the parts to achieve print layers perpendicular to the expected vertical compressive vector, unlike in the finite element analysis. The author adopted this positioning criterion since it is not possible to alter the print orientation during the fabrication process of Cartesian printers.

Figure 5 also illustrates each part, modeled and tested separately. The design is the first elaboration on the proof-of-concept shown in the methodology section (Figure 2) and the first proof-of-product guiding agent, combining all knowledge gathered during daylight simulations and material explorations produced in previous Chapters. The geometry consists of a stationary internal gear fixed to the roof opening, a smaller motor-driven gear for revolving motion, a stationary plate fastened to the roof slab holding loose ball bearings, a structural base that secures the shells, and four spherical wedges (one stationary and three movable). In the manufacturing and assembly process, the physical prototypes attach vertically to a 10 cm high cardboard tube with a 25 cm diameter, representing the slab cutout for the cell installation (Figure 6a).

Figure 6: (a) prototype for the internal gear; (b) prototype for the revolving gear.

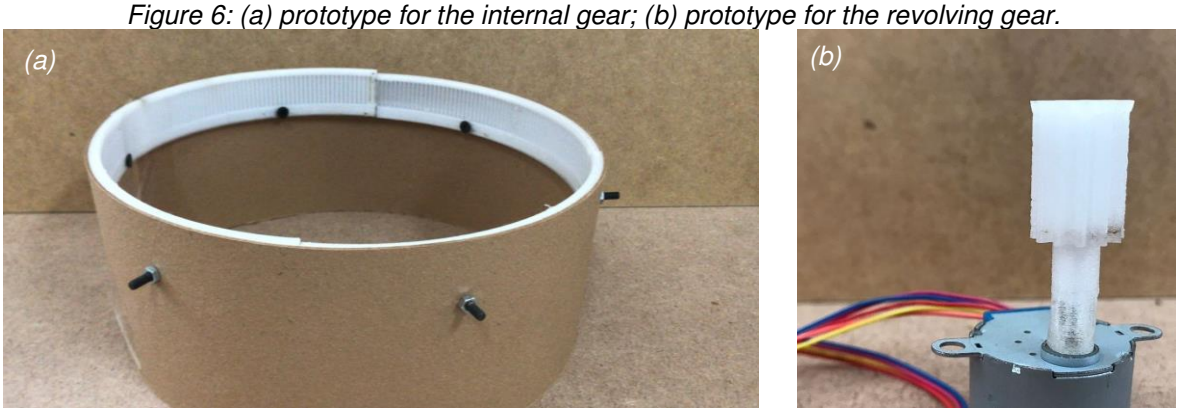

Source: The Author (2024).

The first prototypes concern the stationary and the revolution gears. The larger gear attaches to the cardboard tube's side using a bolted joint, while the smaller gear is an extension of the stepper motor's rotor shaft connected by friction fit. As the initial prints did not consider filament volumetric variations after deposition, the larger gear's tooth openings shrank. In comparison, the smaller gear's tooth thickness increased, resulting in incompatibility (Figures 6a and 6b).

Additionally, Fusion360 gear add-ons cannot generate internal gears, requiring manual calculation and a trial-and-error process. Figure 6b also shows that the first printing layer, or the wider base of the smaller gear, has a larger section than the rest of the print, indicating that the distance between the extruding nozzle and the print bed is low or the bed temperature is higher than the recommended, causing the filament to spread. The friction fit connection was not suitable due to the low tolerance adopted, and the motor shaft cracked the gear, as seen in the interface between both parts in

Figure 6b. For instance, the author adopted 0.05 mm tolerances for the first prototyping batches.

The internal gear prototype in Figure 6c indicates the need to screw the piece to the roof opening, as it is too thin to accommodate a snap fit if printed in four pieces. Chemical bonding with two-part epoxy or resin embrittles the material and creates several structurally critical points that, if broken, depend on a connection with fewer degrees of freedom. For instance, fasteners offer only one degree of freedom, in this case, pitching. If the final design comprises more than one piece, each piece requires more than one bolted connection to eliminate the pitching motion. This finding also applies to all sectioned parts that need to remain stationary.

Most misalignments are due to the number of teeth in both gears that provoke abrupt X and Y-axis changes in printing paths, causing layer shifting. All of these discoveries are correction points for the next digital model editing cycle.

The physical interaction between the revolving and bolted plates indicated that the same tolerance used for other prints was, once again, inadequate, preventing the uninterrupted cell revolution. Both structures squeezed the bearing spheres, the tight interface of PETG/PETG resulted in several sudden braking, and the print shrinkage caused continuity failures (Figure 7a and b).

Due to the weightlessness of FDM prints, the proof-of-concept adopted a Sg90 micro servomotor with a 1.6 Kg.cm torque. However, during the slicing process, PrusaSlicer indicated the need for 218.46 g of filament for the tilting shell. Considering the lever arm of the motor to be 15 cm (the distance from its shaft axis to the highest point on the shell), the maximum weight supported by the servo would be 106 g. Thus, the author adjusted the digital model to accommodate a stepper motor with a 2.2 Kg.cm torque, and product testing skipped the servomotor incorporation.

The stationary cell did not present assembly issues. However, with the motor change, the rotor shaft position shifted, and the author had to modify the side openings through which the tilt motor connects to the tilting shell. The new opening crosses the revolving plate and the stationary shell, intersecting and bolting to the tilting shell (Figure 8). As the first simulation stage in Chapter III considered three opening states following a 30° pitch, the cell's movable structure had three parts in the proof-of-

concept. With new tilting angles varying in 10° increments, the author simplified the three movable wedges into a single geometry.

Figure 7: (a) Stationary base assembly with misalignments; (b) Stationary and revolving base interface; (c) Support structures with default top layer interface; (d) organic support incompatibility; (e) stationary shell (halved wedge) with interfacing supports; (f) Alpha assembly.

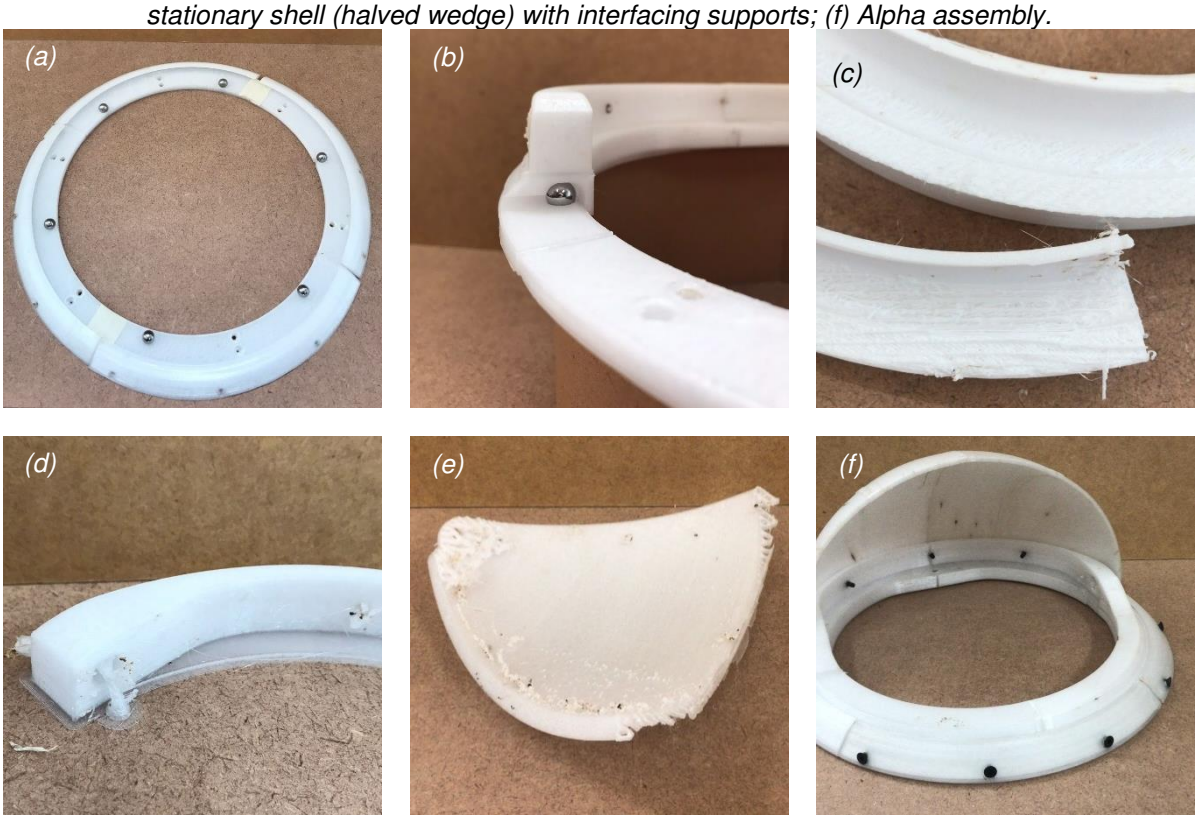

Source: The Author (2024).

They removed the shell connectors that served as bypass slicing grips to pull or push the subsequent shells but created low water tightness points. Still, since the cell diameter remained unchanged, the piece could not fit the print bed and required cutting and subsequent chemical bonding. Although the assembly process is preliminary, the author anticipated the most suitable connectors for each part. Considering that a significant part of the assembly process for the first prototyping batch concerns elements that the author will later print in one piece (past Beta prototypes), the connectors are few and relatively simple. Despite this, the screws used in the first prototyping phase do not have the appropriate length and need modifying in future phases, and it is essential to plan the sockets and bevels for nuts and screw heads. As seen in Figures 6a and 7f, the screws are not adequate for a viable product, only working for process prototypes.

Figure 8: Second top lighting cell configuration. Alpha to Beta prototyping stage.

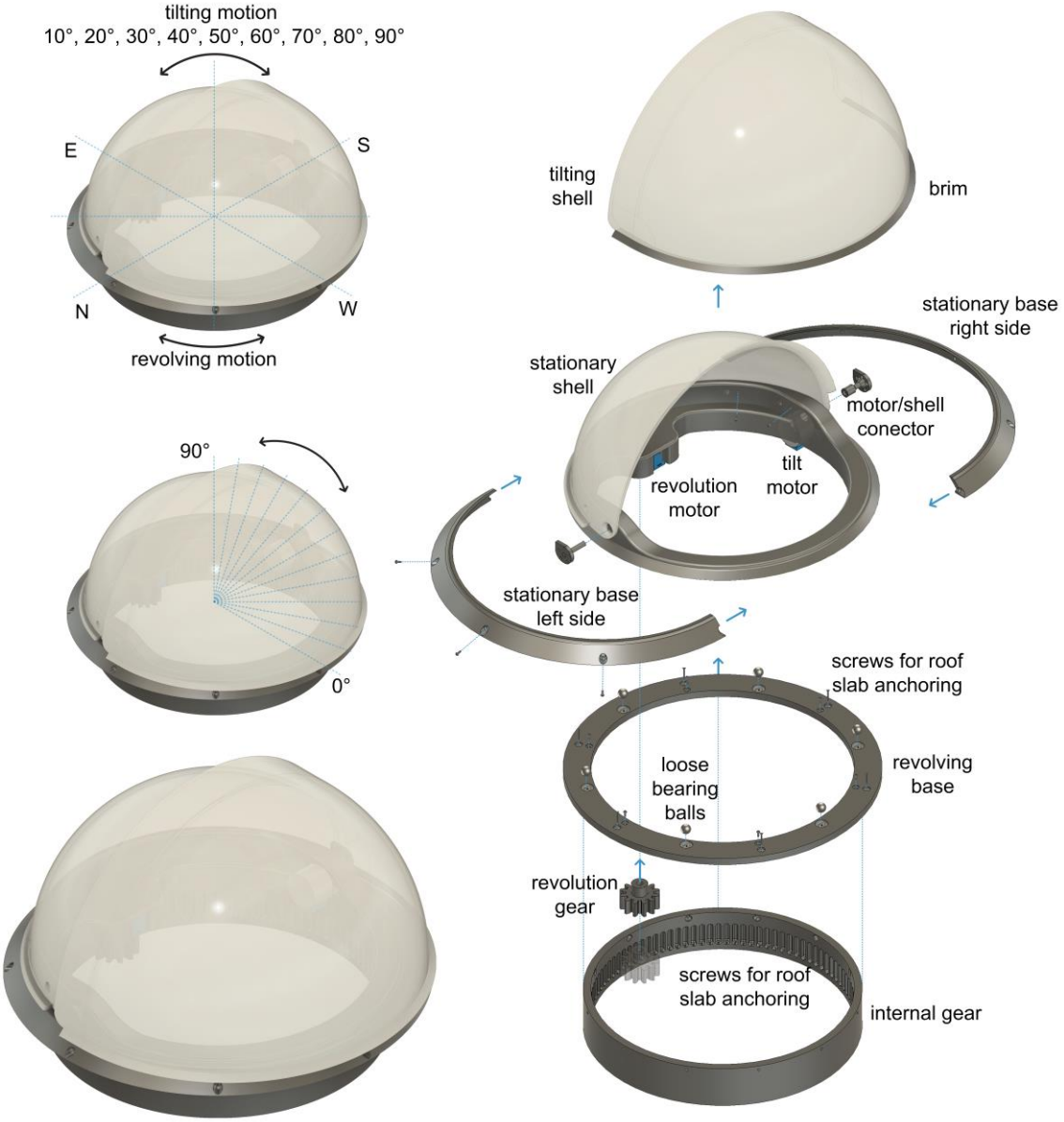

Source: The Author (2024).

Besides increasing the connection tolerances due to object swelling, the fully assembled Alpha prototype indicated the need to seal gaps between the copolymer prints and building structure and enhance the cell's water tightness. To close the gaps between the cell and the building structure, the author can use commercial silicone-based sealants and insulators. Eliminating the shell connectors reduces the likelihood of rain pervasion, but the connection between both shells still creates a gap in process prototypes. For this design, closing major slits is crucial to blocking unwanted beam radiation and protecting against the elements. Finally, the type of support structure adopted was not suitable for the prints, which, being concave, required more reinforcement with a slight intermission between the object's face and the structure.

After each print, the author updated the digital model and ensured the compatibility of all new geometries. Thus, the first model evolved into the object shown in Figure 8. In this version, the author redesigned the gears and recalculated their interface. They reduced the number of teeth to avoid printing errors due to vibration and axis deviation (common in more complex geometries with constant path changes), consequently lowering the revolution speed.

The internal gear teeth in the first design had a 1.0 mm width, revamped to five times the extrusion line width to avoid buckling and breakage (i.e., a 0.4 mm nozzle diameter renders 2.0 mm gear teeth protrusions) (Figure 9a and b).

Figure 9: (a) internal gear teeth for the Alpha proof-of-product; (b) internal gear teeth for the Beta proof-of-product; (c) revolving and internal gear assembly and motor and revolving gear friction fit; (d) new support pattern for the shell wedges; (e) stationary base assembly; (f) screw interface in Beta versus Alpha stages.

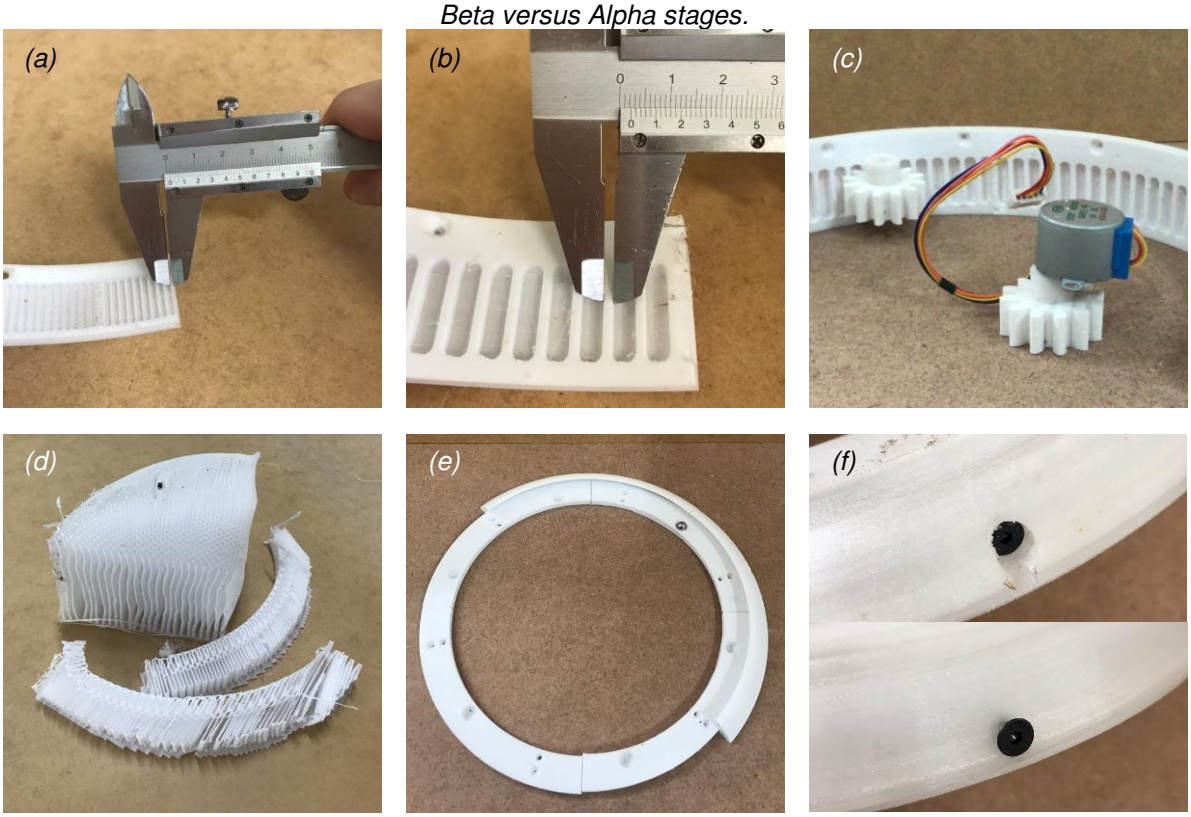

Source: The Author (2024).

They also increased the tolerance between parts to 0.4 mm, allowing friction fit connection between prints and the motor shafts (Figure 9c). The upper and lower parts of the fixed gear indents received a surface fillet to avoid supports that could hinder the contact between both PETG gears (Figure 9b). The author eliminated support structures for slopes up to 50° and catenary surfaces and changed organic supports to a rectilinear grid (Figure 9d). The stationary base that holds the ball bearings

underwent no modifications, and the interacting parts changed, considering larger printing error margins (Figure 9e).

All screw holes received a planar bevel to accommodate the screw heads (Figure 9f) and a plastic snap-fit cover to isolate the metal from the elements (Figure 10a). As these prototypes are only proofs-of-product, the author insulated the screws using industrial silicone to simulate an FDM-made screw cap. Since the caps are very small, they require a higher printing resolution and tighter nozzle holes, which would delay the DfMA workflow.

Figure 10: (a) silicon cap for screws alongside a non-beveled opening with a screw; (b) stationary base assembly; (c) stepper motor below the revolving plate, equipped with a revolving gear and connected to the stationary internal gear.

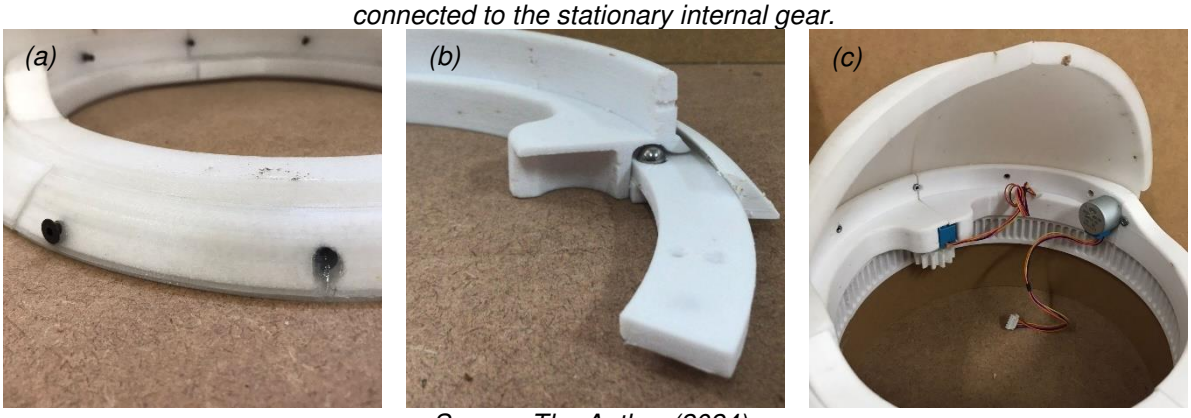

Source: The Author (2024).

Figure 10b illustrates a section of the new stationary base configuration and its interaction with the revolving plate. The larger printing tolerance for same-material interfaces generated an adequate gap, allowing the ball bearings to roll freely. The geometry that required the most corrections was the revolving plate, as it needed structural support in the groove for the ball bearings. The heterogeneous surface of the initial prototypes created motion instability, forcing the screws that hold the two stationary base structures and breaking the chemical bonding between the four separated parts. The author glued the base pieces using two-part epoxy, emulating a final manufacturing stage in which the pieces are whole. Thus, this structural problem does not occur in fully manufactured parts. Furthermore, replacing the servo with a stepper motor required reviewing how and where the actuators attach. As there is also a stepper motor for tilting the light control shell, its attachment, and positioning also required correction (Figure 10c).

The author maintained the motor shaft in the same position, avoiding major changes in the shells, as they are a result of daylight simulations and optical and

structural analysis. They produced an extender for the rotor shaft that passes through the revolving base and the fixed shell. Figures 11a through 11f show the extender and the interface between the stationary shell and the rotor axis with the connector plate for controlling the moving wedge. This extender intercepts a fixed track roller bearing that prevents the tilt axis from skewing and shields the plastic shaft extension from snagging on other plastic pieces (Figure 11a).

Figure 11: (a) fixed track roller with a tilt axis intercepting revolving base and stationary shell; (b) bolted and chemically bonded connection between tilt axis and movable shell; (c) interface between all movable assemblies with the tilting shell opened; (d) tilting axis assembly with the cell closed; (e and f) extender plate for connecting the tilting shell in opened and closed positions.

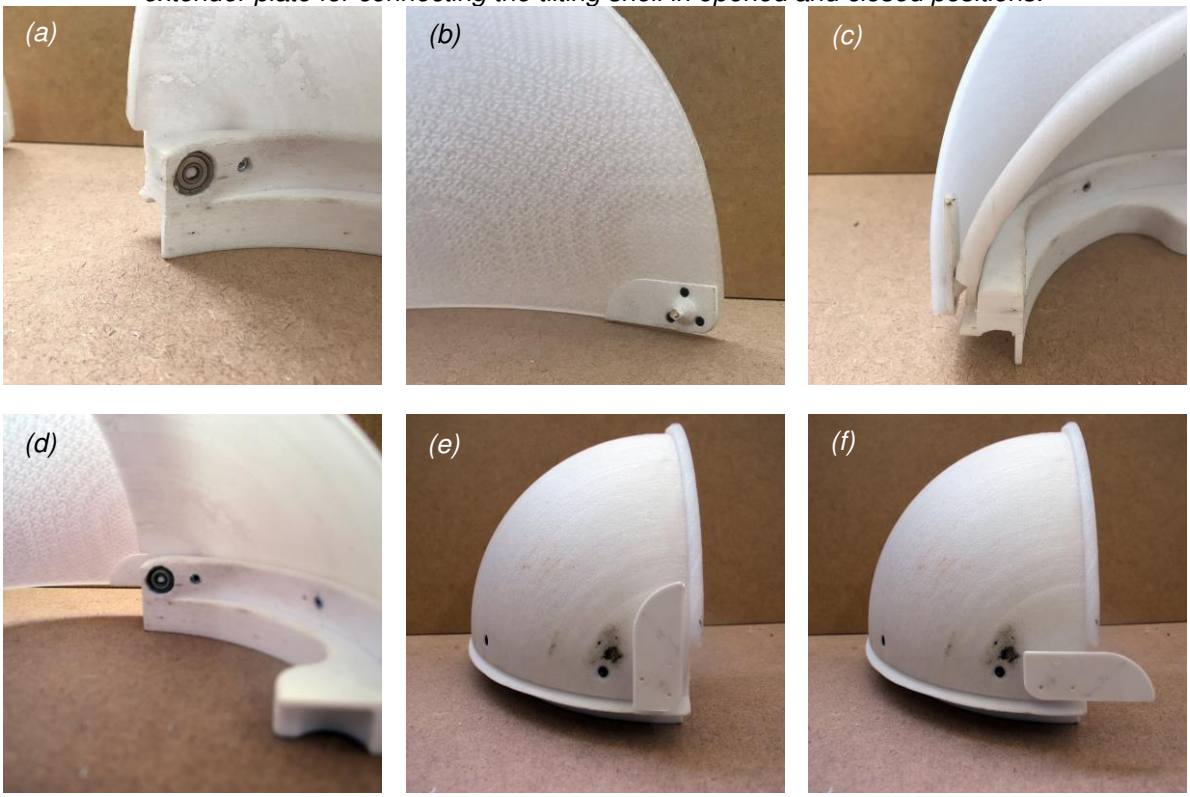

Source: The Author (2024).

The other tilt axis follows the same design, but it connects flush to the motor. The tilt plate attaches to both sides using three M2x6 bolts and a chemically bonded connection for further structural stability. As the tilt axes represent the most critical structure points according to the finite element analyses, the author further reinforced the extender with an M6x20 screw interfaced with the rotor shaft and a M6x30 screw for the standalone extender (Figure 12a and 12b). The second redesign occurred due to the extender breaking due to shear stress after the author placed an F1 Class 5 Kg weight in the top-most surface of the tilting shell (Figure 12c).

Figure 12: (a and b) new extenders with M6x30 and M6x20 bolts; © broken extenders with no bolt.

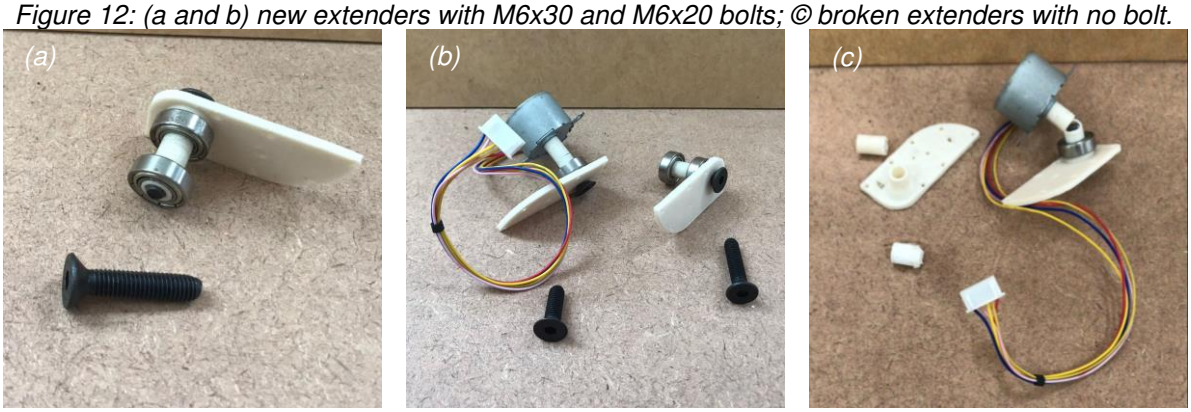

Source: The Author (2024).

They also reinforced the interface between the motor and the tilting shell by replacing the triangular infill with a 100% density rectilinear infill (PrusaSlicer only accepts 100% density infill for linear patterns) and attached the planar interface between the tilting shell and the extender using 8 M2x6 bolts (Figure 13a). For both shells, the author kept the original shape, added chamfers to protect the screws, and designed a brim protruding from the upper arch of the fixed shell to seal the junction between the two geometries (Figure 13b and 13c). The new design also features a horizontal brim extending from the lower arch of both shell pieces and encircling the base of the cell to redirect water away from the moving parts and their interface gaps.

Figure 13: (a) tilt axis connector; (b and c) interface between shells and marquee.

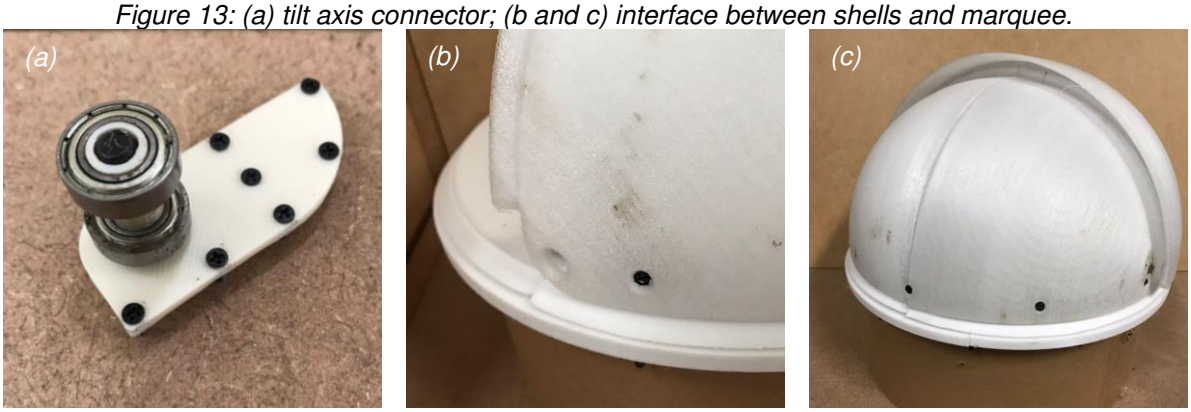

Source: The Author (2024).

Even though Figure 10c presented the first actuator insertion, the author did not design grooves for cable management since the prototyping and coding processes require constant tinkering. Wire management comes after the electronic components are irreversibly defined. Thus, the next step in the DfMA process for the cyber-physical system is coding and installing the hardware for environmental sensing and motion. The prototype only receives the minimum viable product designation when the author finalizes, automatizes, and validates the system after integrating the object with the actual building. The protoboard, where the cables connect, remains part of the system

only during the Arduino sketching phase since the iterative process of testing and correcting the code requires all components to remain interchangeable. The author tried different combinations of open-source libraries and developed the code in Appendix IV.

After programming the system, the author secured all peripherals to the cell. Still, there is no space for holding the Arduino board and the 9v battery that powers the sensors and actuators, there is no cloud connection, the illuminance sensor should be at work plane height instead of close to the cell, and the rain module should attach to the building roof slab. The Beta phase is not the last of product development. Its evolution into a minimum viable product depends on the interaction between the top lighting cell and the actual building. Thus, the author plans to assess real applications to refine the design further, define a control hub for storing all hardware components, secure all electrical wiring, and achieve a final product.

Finally, Figures 14a through 14r show the assembly process for the top lighting cell, described as follows:

a) Select the internal gear and prepare twelve M3x30 screws with twelve compatible masonry rawlplugs (Figure 14a);

b) Attach the internal gear within the roof opening using the M3x30 screws (as a Beta prototype, the author secured the bolts using hexagon nuts, later replaced with the rawlplugs) (Figure 14b);

c) Gather six M3x20 and six M3x30 screws. The former anchors the base to the roof slab, and the latter secures the gear to the stationary base (Figure 14c). Also, the base has six grooves that require a bearing sphere each.

d) The stationary base comprises two components: a horizontal anchoring element (shown in Figure 15c) and a dovetail-like structure that holds the revolving base (Figure 15d). After securing the first piece to the internal gear, the second piece encircles the assembly (Figure 15e). As the piece secures the revolving base, its top has a smaller diameter. Thus, it needs to be assembled in parts, enabling the sliding of the revolving base;

Figure 14: (a through r) assembly process for the Beta prototype.

Source: The Author (2024).

e) After assembling three securing pieces of four (Figure 15e), place a section of the revolving base above the bearing spheres and slide it into the stationary base groove (Figure 15f and 15g); repeat the process until the revolving base is complete. If produced as a whole piece, the revolving base should be positioned before the dovetail structure. Figures 15h and 15i show the full base assembly;

f) Position the stationary shell flush to the revolving base and alight the holes for the screws and nuts – seven M3x10 screws and seven M3 nuts (Figures 15j and 15k; Friction fit the bearings and nuts and bolt the shell into the base (Figures 15l through15o). Note that, below the stationary shell and aligned

with the holes for the tilting extender, there is a space for securing a ball bearing – thus, stage f is concomitant to stage h;

g) Bolt the revolving motor to the underside of the revolving base (Figure 15p) and fit the revolving gear to the rotor shaft, positioning its teeth inside the internal gear grooves (Figure 15q);

h) Combine the tilt motor with the tilt extender following Figures 15l, m, n, and r (note that the extender plate should be already attached to the tilt shell as the screwdriver cannot reach the structure after mounted): *(1) position the first ball bearing that will remain within the outer wall and below the stationary shell; (2) fit the bearing into the outer wall of the revolving plate and push the component until the extender appears flush to the inner wall; (3) insert the second bearing to secure the extender; (4) fit the tilting motor shaft to the extender; (5) bolt the motor to the inner wall of the revolving plate; (6) secure the tilt axis using the M6x20 screw;*

i) Repeat the process for the second tilt axis using an M6x30 screw instead and skipping the motor attachment; the tilting shell is resilient enough to withstand the gentle pulling force needed for inserting the second extender into its adequate position (Figure 15t and 15u);

j) Finally, connect the remaining hardware shown in Figure 15s.

5. Conclusions

The Design-for-Manufacture-And-Assembly process provided greater control over stages for the designer and reduced the time between ideation and production, especially when aided by desktop manufacturing strategies. However, its iterative and swift workflow compelled the designer to centralize the decision-making, requiring interdisciplinary knowledge due to a reduced production chain. The various stages concerning conceptualization, manufacturing, assembly, and concurrent digital and physical editing further complicated the documentation process, hindering reproducibility, which the author expected when adopting and proposing a Research-through-Design methodology. The multiple editing scales across digital and physical models also required attention, especially during fine-tuning. In these situations, the adoption of a timeline-based modeling software was appropriate, as the changes made

in previous instances caused subsequent parametric adjustment of conditional geometries. A product-oriented software also assisted in incorporating standardized mechatronics and commercially available hardware, defining standard connections, selecting degrees of freedom and spatial motion criteria, and disassembling components for digital manufacture. Regardless, this design flow presented greater complexity compared to free-form and sandbox modeling software, requiring prior systematization of key dimensions and definition of topological relationships between components. When the author over-constrained certain geometries, some edits generated incompatibilities that were easier to remodel than to rework. Although centered on product design and geared towards various manufacturing and assembly phases, the selected software still requires manufacture-specific inputs, such as tolerance indications, and a better CAD to Slicer abridgment; assembly evaluation and preparation fully depended on the designer, the editing process was lengthier than sketch-based applications, and the lack of interface for manufacture preparation culminated in more by-products.

Although this study showed only two instances of product editing, i.e., Alpha and Beta stages, each one involved several components. Overall, major design flaws were due to manufacturing processes or fabrication parameters. Despite being faster than the industrial production chain, the desktop deposition processes were unpredictable and constantly rendered components unusable due to depositing errors. For instance, the instability in XY-carriages and hotend height built inconsistent layer thicknesses, especially for those adhering to the printing bed that normally undergo further swelling; constant trembling due to high printing speed shifted the print layers, precluding friction fit connections, even though the author adopted volumetric speeds 50% below those indicated in the machines' datasets. Nozzle temperature variation introduced burnt bumps that weakened physical bonds and reduced weather tightness. All of these problems are easily solved in subsequent proofs-of-process and production when the amount of post-production and assembly is smaller, and manufacturing occurs within a controlled environment.

Invariably, the slicing software's default printing properties did not produce optimal outcomes and, therefore, designers should consider the following:

a) The author suggests suppressing connections in parts not meant for disassembling and securing the separate pieces with strong chemical bonding methods, such as two-part epoxy or UV-curable resin;

b) As for printing tolerances, despite the variability of environmental conditions and the diversity of machines employed in this study, the author indicates ±0.4% (±0.4 mm) as a best practice for plastic/plastic interfaces and ±0.2% (±0.2 mm) for plastic/machined pieces, such as nuts and motor parts;

c) The object should touch the heatbed at multiple points and comply with a maximum layer height of 75% of the nozzle diameter (i.e., for a 0.4 mm nozzle hole adopted in this study, 0.3 mm and above will not adhere to the table);

d) Base chamfers of about 0.3 mm improve first-layer accuracy and help avoid swelling and spreading; adding a brim also helps diminish squishing, but, for this research, the higher the contact between PETG and the smooth PEI sheet (the depositing surface), the higher the force needed to unbind the object;

e) Filleting corners reduces abrupt braking and, consequently, layer shifting; this indication does not apply to pieces later fabricated as a full component;

f) Features such as gear teeth should not be less than 4 times the extrusion line width to avoid buckling and breakage (i.e., a 0.4 mm nozzle diameter should contemplate a minimum feature size of 1.6 mm); also, default nozzle diameters cannot produce holes smaller than 2 mm;

g) All overhangs below 50° or twice the width of the extrusion line require a support structure; in most concave or catenary surfaces, keeping the support interface causes supports and print surfaces to merge, creating a heterogeneous finish; however, printing with no interface increases the risk of printing failure for higher layer heights.

Working directly with end-use materials, specifically with fluid deposition for desktop machines, requires evaluating the feedstock and the manufactured components as the result relies on manufacturing configurations, material quality, environmental characteristics, and equipment maintenance. Despite the various

structural evaluations of thermoplastics as raw materials, studies on prototyping and prototype integrity are still relatively rare for the construction sector, mainly due to the low adoption of thermoplastics as building components. Specific applications such as those developed in this research (maintenance of adequate structural properties in distinct anchoring situations and different degrees of freedom and visible light transmission potential) require testing methodologies to offer preambles for future applications.

For instance, this research indicated low-density triangular infill patterns for light transmission as appropriate, regardless of final geometry or anchoring surface. Although less dense infill patterns meet the integrity criteria adopted in this study, the structural analysis of components differs according to geometry, anchoring, and constraints. Thus, the author suggests the finite element methodology as satisfactory despite the complexity and remodeling required to evaluate patterns produced by slicing software. For future research, the author proposes investigating the transposition of the nozzle deposition coordinates from the slicer into CAD software, using the extrusion path as a center of mass for a sweeping operation.

Regarding the incorporation of control mechanisms, the author considered low-complexity microcontrollers appropriate despite their constant maintenance, while the peripherals remain connected with male and female jumper wires. Additionally, a Beta product cannot account for the full incorporation of mechatronic components as the cyber-physical system still needs validation before progressing to a minimum viable product that should present fewer hardware components, soldered electronics, cable management grooves, and a control hub.

Acknowledgments

This study was financed by Coordenação de Aperfeiçoamento de Pessoal de Nível Superior – Brasil (CAPES) – Finance Code 001; by Fundação de Amparo à Pesquisa de Minas Gerais (FAPEMIG) – financing notice N° 001/2021 Universal Demand - under process code APQ-00266-21; and by Conselho Nacional de Desenvolvimento Científico e Tecnológico (CNPQ) – financing notice N° 59/2022 – under process code 406426/2022-8. The author also acknowledges CenTev TecnoParq UFV (“Centro

Tecnológico de Desenvolvimento Regional de Viçosa"), MakerLab, and Agro MakerLab 4.0 for expediting the prototyping process.

REFERENCES

ABNT. ABNT NBR 15215 - Iluminação natural. [*s. l.*], 2021.

ABNT. NBR ISO/CIE 8995-1: Iluminação de ambientes de trabalho, Parte 1: Interior. [*s. l.*], p. 46, 2013. DOI: http://www.abntcatalogo.com.br/norma.aspx?ID=196479.

AGIRBAS, A. The Use of Simulation for Creating Folding Structures : A Teaching Model. *In*: 2017, Rome. **eCAADe 2017: Sharing of Computable Knowledge!** Rome: [*s. n.*], 2017. p. 325–332.

ALEXANDRU, C.; GHEORGHE, G. I. Mechatronic architectures. **AIP Conference Proceedings**, [*s. l.*], v. 1648, n. 6, p. 1–5, 2015.

AUGUSTÍ-JUAN, Isolda. **Sustainability Assessment and Development of Guidelines for Digital Fabrication in Construction**. 2018. 245 f. - Universidad Politécnica de Valencia, [*s. l.*], 2018. DOI: https://doi.org/10.3929/ethz-a-010025751.

BANZI, M.; SHILOH, M. **Make: Getting started with Arduino**. 3. ed. [*S. l.*]: Maker Media, 2015.

BASARIR, B.; CEM ALTUN, M. A redesign procedure to manufacture adaptive façades with standard products. **Journal of Facade Design and Engineering**, [*s. l.*], v. 6, n. 3, p. 077–100, 2018.

BHANU, C. *et al.* **Artificial Intelligence-based Internet of Things Systems**. [*S. l.: s. n.*], 2022.

BÖKE, J. **Thinking- Skins**. 2020. 286 f. - Delft University of Technology, [*s. l.*], 2020. DOI: https://journals.open.tudelft.nl/abe/article/view/5035.

BÖKE, Jens; KNAACK, Ulrich; HEMMERLING, Marco. Prototype of a cyber-physical façade system. **Journal of Building Engineering**, [*s. l.*], v. 31, n. November 2019, p. 101397, 2020. DOI: https://doi.org/10.1016/j.jobe.2020.101397.

BÖKE, J.; KNAACK, U.; HEMMERLING, M. Prototype of a cyber-physical façade system. **Journal of Building Engineering**, [*s. l.*], v. 31, n. March, p. 101397, 2020. DOI: https://doi.org/10.1016/j.jobe.2020.101397.

BRACONNIER, Daniel J.; JENSEN, Robert E.; PETERSON, Amy M. Processing parameter correlations in material extrusion additive manufacturing. **Additive Manufacturing**, [*s. l.*], v. 31, n. October 2019, p. 100924, 2020. DOI: https://doi.org/10.1016/j.addma.2019.100924.

CARLUCCI, F. A review of smart and responsive building technologies and their classifications. **Future Cities and Environment**, [*s. l.*], v. 7, n. 1, p. 1–12, 2021.

CARTANA, R. P. **Desempenho Térmico e Lumínico de Elementos de Controle**

Solar para Fachadas Desenvolvidos com Modelagem Paramétrica e Fabricação Digital. 2018. 348 f. - Universidade Federal de Santa Catarina, [*s. l.*], 2018.

CHO, E. E. *et al.* Investigation on Influence of Infill Pattern and Layer Thickness on Mechanical Strength of PLA Material in 3D Printing Technology. **Journal of Engineering and Science Research**, [*s. l.*], v. 3, n. 2, p. 27–37, 2019.

DE CAMPOS, Filipe Medéia *et al.* Prototyping a Facade Component. **Architecture in the Age of the 4th Industrial Revolution, eCAADe SIGraDi 2019 Vol.1**, [*s. l.*], v. 1, n. 1996, p. 179–186, 2019.

DUNN, N. **Digital Fabrication in Architecture**. London: Laurence King Publishing Ltd, 2012.

ERICHSEN, J. A. B. *et al.* Learning in Product Development: Proposed Industry Experiment Using Reflective Prototyping. **Procedia CIRP**, [*s. l.*], v. 50, n. 3, p. 454–459, 2016. DOI: http://dx.doi.org/10.1016/j.procir.2016.04.142.

ERICHSEN, J. F. *et al.* Photobooth: Gathering and analyzing data on prototyping in early-stage engineering design projects by digitally capturing physical prototypes. **Artificial Intelligence for Engineering Design, Analysis, and Manufacturing: AIEDAM**, [*s. l.*], v. 35, n. 1, p. 65–80, 2021.

ERYILDIZ, Meltem. The effects of infill patterns on the mechanical properties of 3D printed PLA parts fabricated by FDM. **Ukrainian Journal of Mechanical Engineering and Materials Science**, [*s. l.*], v. 7, n. 1–2, p. 1–8, 2021.

FAJKUS, M. Superficial Skins? Super Skins? Shading Structures and Thermal Impact Analysis. *In*: , 2013. **Energy Forum**. [*S. l.: s. n.*], 2013. p. 23–27.

FIGLIOLA, A.; BATTISTI, A. **Post-industrial Robotics: Exploring Informed Architecture**. Rome: Springer, 2021.

FRAMPTON, K. **The Evolution of 20th Century Architecture: A Synoptic Account**. Beijing: Springer-VerlagA/Vien and China Architecture & Building Press, 2007.

FRAMPTON, K. Towards a Critical Regionalism: Six points for an Architecture of Resistance. *In*: THE ANTI-AESTETIC: ESSAYS ON POSTMODERN CULTURE. [*S. l.: s. n.*], 1998. p. 16–30.

GALVEZ, Glecelyn M. *et al.* Finite Element Analysis of Different Infill Patterns for 3D Printed Tidal Turbine Blade. **Sustainability (Switzerland)**, [*s. l.*], v. 15, n. 1, 2023.

GARCIA-RUIZ, Miguel Angel; CESAR, Pedro; MANCILLA, Santana. **DIY Microcontroller Projects for Hobbyists: The ultimate project-based guide to building real-world embedded applications in C and C++ programming**. [*S. l.: s. n.*], 2021.

GIBSON, I.; ROSEN, D.; STUCKER, B. **Additive manufacturing technologies: 3D printing, rapid prototyping, and direct digital manufacturing**. 2. ed. [*S. l.*]:

Springer, 2015.

GLASSMAN, E. J.; REINHART, C. Facade optimization using parametric design and future climate scenarios. **13th BS2013**, [*s. l.*], p. 1585–1592, 2013.

GOU, S. *et al.* Passive design optimization of newly-built residential buildings in Shanghai for improving indoor thermal comfort while reducing building energy demand. **Energy & Buildings**, [*s. l.*], v. 169, p. 484–506, 2018. DOI: https://doi.org/10.1016/j.enbuild.2017.09.095.

GRASSI, Giulia; LUPICA SPAGNOLO, Sonia; PAOLETTI, Ingrid. Fabrication and durability testing of a 3D printed façade for desert climates. **Additive Manufacturing**, [*s. l.*], v. 28, n. May, p. 439–444, 2019. DOI: https://doi.org/10.1016/j.addma.2019.05.023.

HANINGTON, Bruce M. Generative Research in Design Education. *In*: , 2007, Hong Kong. **IASDR: International Association of Societies of Design Research**. Hong Kong: [*s. n.*], 2007. p. 1–15.

HERRIOTT, R. What Kind Of Research Is Research Through Design? *In*: 2019, Manchester. **IASDR: International Association of Societies of Design Research Conference**. Manchester: [*s. n.*], 2019. p. 1–11.

HOSSEINI, S. *et al.* A morphological approach for the kinetic façade design process to improve visual and thermal comfort: Review. **Building and Environment**, [*s. l.*], v. 153, p. 186–204, 2019. DOI: https://doi.org/10.1016/j.buildenv.2019.02.040.

ISO. ISO 13468 - Plastics - Determination of the Total Luminous Transmittance of Transparent Materials. [*s. l.*], 2019.

ISO. ISO 14782 - Plastics - Determination of Haze for Transparent Materials. [*s. l.*], 2021.

JAFFERSON, J. M.; CHATTERJEE, D. A review on polymeric materials in additive manufacturing. **Materials Today: Proceedings**, [*s. l.*], v. 46, p. 1349–1365, 2021.

JONES, N. L.; REINHART, C. F. Experimental validation of ray tracing as a means of image-based visual discomfort prediction. **Building and Environment**, [*s. l.*], v. 113, p. 131–150, 2017. DOI: http://dx.doi.org/10.1016/j.buildenv.2016.08.023.

KARAGIANNI, L. *et al.* Additive Manufacturing for daylight: Towards a customized shading device. **Simaud 2016: Symposium on Simulation for Architecture and Urban Design**, [*s. l.*], 2016.

KEATING, S.; OXMAN, N. Robotic Immaterial Fabrication. *In*: BRAUMANN, J.; BRELL-ÇOKCAN, S. (org.). **Robotic Fabrication in Architecture, Art, and Design**. [*S. l.*]: Springer, 2013.

KIRIMTAT, A. *et al.* Review of simulation modeling for shading devices in buildings. **Renewable and Sustainable Energy Reviews**, [*s. l.*], v. 53, p. 23–49, 2016. DOI:

http://dx.doi.org/10.1016/j.rser.2015.08.020.

KOHTALA, S. M. I. *et al.* Augmenting physical prototype activities in early-stage product development. *In*: , 2018, Linköping. **NordDesign: Design in the Era of Digitalization**. Linköping: [*s. n.*], 2018.

LEE, B. Heating, cooling, and lighting energy demand simulation analysis of kinetic shading devices with automatic dimming control for Asian Countries. **Sustainability (Switzerland)**, [*s. l.*], v. 11, n. 5, 2019.

LEIFER, L. J.; STEINERT, M. Dancing with ambiguity: Causality behavior, design thinking, and triple-loop-learning. **Information Knowledge Systems Management**, [*s. l.*], v. 10, n. 1–4, p. 151–173, 2011.

LESCHOK, M. *et al.* 3D printing facades: Design, fabrication, and assessment methods. **Automation in Construction**, [*s. l.*], v. 152, n. May, p. 104918, 2023. DOI: https://doi.org/10.1016/j.autcon.2023.104918.

LINNER, Thomas *et al.* A technology management system for the development of single-task construction robots. **Construction Innovation**, [*s. l.*], v. 20, n. 1, p. 96–111, 2020.

LOONEN, R. **Approaches for Computational Performance Optimization of Innovative Adaptive Façade Concepts**. 2018. 190 f. - Eindhoven University of Technology, [*s. l.*], 2018. DOI: www.tue.nl/taverne.

LUCARELLI, C. D. C.; CARLO, J. C. Parametric modeling simulation for an origami-shaped canopy. **Frontiers of Architectural Research**, [*s. l.*], v. 9, n. 1, p. 67–81, 2019. DOI: https://doi.org/10.1016/j.foar.2019.08.001.

LUCARELLI, C. C.; OLIVEIRA, M. M.; CARLO, J. C. Climate-active building enclosures: an integrative literature review. **PARC Pesquisa em Arquitetura e Construção**, [*s. l.*], v. 14, p. e023023, 2023.

LUCARELLI, C. C.; OLIVEIRA, M. M.; CARLO, J. C. Thermal calibration of an existing institutional building. *In*: , 2022, Porto Alegre. **XIX Encontro Nacional De Tecnologia Do Ambiente Construído**. Porto Alegre: [*s. n.*], 2022.

LUTTERS, Eric *et al.* Tools and techniques for product design. **CIRP Annals - Manufacturing Technology**, [*s. l.*], v. 63, n. 2, p. 607–630, 2014.

MARQUIS, J.; DEEB, R. S. Roadmap to a successful product development. **IEEE Engineering Management Review**, [*s. l.*], v. 46, n. 4, p. 51–58, 2018.

MICHALKO, M. **Creative Thinkering: putting your imagination to work**. [*S. l.*]: New World Library, 2011.

MILARA, Iván Sánchez *et al.* “Document-while-doing”: a documentation tool for Fab Lab environments. **Design Journal**, [*s. l.*], v. 22, n. sup1, p. 2019–2030, 2019.

MOLONEY, J. **Designing kinetics for architectural facades: state change**. [*S. l.*]: Routledge, 2011.

NABIL, A.; MARDALJEVIC, J. Useful daylight illuminance: a new paradigm for assessing daylight in buildings. **Lighting Research and Technology**, [*s. l.*], v. 37, n. 1, p. 21–59, 2005.

OLGYAY, V. **Design with climate: Bioclimatic approach to architectural regionalism**. Princeton: Princeton University Press, 2015.

OXMAN, R. Theory and design in the first digital age. **Design Studies**, [*s. l.*], v. 27, n. 3, p. 229–265, 2006.

OXMAN, R. Thinking difference: Theories and models of parametric design thinking. **Design Studies**, [*s. l.*], v. 52, p. 4–39, 2017. DOI: http://dx.doi.org/10.1016/j.destud.2017.06.001.

PAIO, A. *et al.* Prototyping Vitruvius, New Challenges: Digital Education, Research and Practice. **Nexus Network Journal**, [*s. l.*], v. 14, n. 3, p. 409–429, 2012.

POPESCU, Diana *et al.* FDM process parameters influence over the mechanical properties of polymer specimens: A review. **Polymer Testing**, [*s. l.*], v. 69, n. May, p. 157–166, 2018.

PROCHNER, Isabel; GODIN, Danny. Quality in research through design projects: Recommendations for evaluation and enhancement. **Design Studies**, [*s. l.*], v. 78, p. 101061, 2022. DOI: https://doi.org/10.1016/j.destud.2021.101061.

RADANLIEV, Petar *et al.* Artificial Intelligence and the Internet of Things in Industry 4.0. **CCF Transactions on Pervasive Computing and Interaction**, [*s. l.*], v. 3, n. 3, p. 329–338, 2021. DOI: https://doi.org/10.1007/s42486-021-00057-3.

RASPALL, Felix. A procedural framework for design to fabrication. **Automation in Construction**, [*s. l.*], v. 51, n. C, p. 132–139, 2015. DOI: http://dx.doi.org/10.1016/j.autcon.2014.12.003.

REINHART, C. F.; MARDALJEVIC, J.; ROGERS, Z. Dynamic Daylight Performance Metrics for Sustainable Building Design. **LEUKOS: The Journal of the Illuminating Engineering Society of North America**, [*s. l.*], p. 37–41, 2013.

ROMANO, R. *et al.* What is an adaptive façade? Analysis of recent terms and definitions from an international perspective. **Journal of Facade Design and Engineering**, [*s. l.*], v. 6, n. 3, p. 065–076, 2018.

SCHIELKE, T. Dynamic design with light: Media facades. *In*: SCHUMACHER, M.; VOGT, M.; KRUMME, L. A. C. (org.). **New Move: Architecture in Motion - New Dynamic Components and Elements**. [*S. l.*]: Walter de Gruyter, 2020. p. 90–93.

SCHÖN, D. A. **The reflective practitioner: How professionals think in action**. London: Routledge, 2017.

SCHORK, S.; KIRCHNER, E. Defining requirements in prototyping: The holistic prototype and process development. *In*: , 2018, Linköping. **NordDesign: Design in the Era of Digitalization**. Linköping: [*s. n.*], 2018.

SCHUMACHER, M.; VOGT, M.; KRUMME, L. A. C. **New Move: Architecture in Motion - New Dynamic Components and Elements**. [*S. l.*]: Birkhauser, 2020.

STAPPERS, P. J.; GIACCARDI, E. Research through Design. *In*: THE ENCYCLOPEDIA OF HUMAN-COMPUTER INTERACTION. [*S. l.*]: Idea Group Reference, 2017. p. 782.

TERZIDIS, K. **Permutatuion Design: Buildings, Texts, and Contexts**. [*S. l.*]: Routledge, 2015.

ULLMAN, D. G. **The Mechanical Design Process**. 6th. ed. New York: McGraw-Hill, 2017.

VELIKOV, K.; THÜN, G. Responsive Building Envelopes: Characteristics and Evolving Paradigms. *In*: TRUBIANO, F. (org.). **Design and Construction of High-Performance Homes: Building Envelopes, Renewable Energies and Integrated Practice**. [*S. l.*]: Taylor & Francis Group, 2017. p. 75–92.

WANG, L.; TÖRNGREN, M.; ONORI, M. Current status and advancement of cyber-physical systems in manufacturing. **Journal of Manufacturing Systems**, [*s. l.*], v. 37, p. 517–527, 2015.

WEBER, Ramon E.; REINHART, Christoph; OXMAN, Neri. Photon mapping of geometrically complex glass structures: Methods and experimental evaluation. **Building and Environment**, [*s. l.*], v. 180, n. April, p. 106957, 2020. DOI: https://doi.org/10.1016/j.buildenv.2020.106957.

WEICHEL, C. *et al.* ReForm: Integrating physical and digital design through bidirectional fabrication. **UIST 2015: Symposium on User Interface Software and Technology**, [*s. l.*], p. 93–102, 2016.

WIENER, N. **Cybernetics or Control and Communication in the Animal and the Machine**. 2. ed. Cambridge: The MIT Press, 2019.

YANG, C. **The Intelligent Control Strategy of Kinetic Façades for Daylight and Energy Performance**. 2020. 213 f. - University of Southern California, [*s. l.*], 2020.

CHAPTER VI – Overall Conclusions

This study developed and evaluated a design workflow for a climate-active building component based on a Research-through-Design methodology comprising ideation (discovery, planning, and definition), conceptual design (building performance simulation for environmental analysis and human comfort, material evaluation, and component assessment), and product design, manufacture, assembly, and automation (digital modeling and Alpha and Beta proofs-of-product).

The discovery and planning stages originated from a theoretical background on climate-active skins that assessed the State-of-the-Art kinematic methodologies, compiling their evaluation methods, geographical location, movement characterization, motion constraints, computational applications, simulation metrics, and optimization objectives. The literature review's main conclusions prompted new climate-active evaluations, driving the research workflow from compute-intensive applications with oversimplified simulation methodologies (that comprise most of the literature) into an evaluation and proposition of an alternative simulation process. For instance, the general conclusions for the reviewing stage are the following:

a) Research on building adaptation focuses on façades to the detriment of other envelope typologies;

b) Climate-active applications outperform optimized geometries even when the adaptation occurs every season;

c) Rigid motion patterns comprise most of the literature from 2015 onwards and present a swifter materialization workflow;

d) Illuminance-based simulations are the most common; also, frequent combinations comprise visual/thermal and thermal/energy analysis.

The main finding is that building performance simulation motors do not offer an adequate methodology for assessing the dynamicity of active typologies, and the adoption of representative dates cannot fully represent climate-dependent adaptation — further, the computational time and cost for image-based daylight simulations render whole-year analysis impractical. Even though optimization motors can automate the process, the geometric combinations for simple motion (such as heave, swaying, and surging) are not enough to avoid local optima.

Following the demand for an alternative simulation method that could better represent real-time environmental response, the author elected simple geometries (circles and wedges) and primary motion constraints (tilting and revolving) to deepen the emphasis on human visual and thermal comfort criteria within the built environment. The workflow comprised a preliminary simulation stage for representative daylight scenarios, followed by an Analysis of Variance to define the contribution of each motion pattern on daylight admission and eliminate or simplify the number of geometric combinations and, consequently, building performance simulations. For instance, the sensibility analysis revealed tilting motion as the most contributing factor, accounting for 89.50% of the model contribution. Also, time-consuming image-based glare analysis consistently remained below the perceptible discomfort band, excusing the need for compute-intensive applications and allowing the author to adopt grid-based approaches. Due to this simplification, they further increased tilting stages and fixed an orientation (Northeast, due to higher luminance availability and lesser context geometry that causes shading), rendering 40150 point-in-time simulations.

Despite the multiple apertures (10° increments from closed to 90°), the grid-based simulations demonstrated similar potential to the previously selected opening angles (30°, 60°, and 90°) — openings below 30° did not display optimal scenarios due to blocking context geometries; 60° openings adequately represent 40° and 50° scenarios; and above 70°, illuminance gains remain relatively unchanged. Therefore, the number of simulations could be as low as 16060 by adopting the previous three tilt stages. The results have also shown the limited potential of the first and last daytime hours to provide useful daylight illuminance above the selected threshold. Eliminating two hours a day can further reduce the number of simulations by 25%. Thus, the author indicates a careful assessment of weather files, especially solar radiation and sky luminance data (i.e., global horizontal, direct normal, and diffuse horizontal radiation; direct normal and diffuse horizontal illuminance; and zenith luminance), to eliminate hours with lower light availability.

Therefore, the proposed simulation workflow is as follows:

a) Selecting spatial motion;

b) Iterating motion types if needed or possible;

c) Simulating 72 representative scenarios using image-based analysis (every 15 days and three hours per day to describe various solar positions);

d) Determining which motion is the most contributing using variance-based analysis;

e) Eliminating or simplifying low-contributing input and maintaining or incrementing high-contributing parameters;

f) Evaluating if glare is below the perceptible band using image-based approaches (if yes, eliminate image-based and adopt grid-based analysis; if not, keep image-based simulations);

g) Revamping simulation time steps to all hours with daylight availability according to a careful weather file assessment;

h) Simulating all possible solutions;

i) Selecting the fittest cell position for each daylight hour.

The conceptual stage also comprises feedstock evaluations, as digitally manufactured pieces have to comply with material and materialization constraints. Since this research adopted fused-deposition desktop machines, the author selected the fittest engineering-grade thermoplastics according to the maximum nozzle and heatbed temperatures. For instance, they evaluated 120 ASA, PETG, and TRITAN™ test coupons (60 tensile experiments and 60 compressive; half white, half clear) and obtained the ultimate tensile and compressive stress, resulting strains, and Young's Moduli before and after 90 cycles of rapid weathering. They also assessed colorimetric changes using the CIE L*a*b* space and reflectance measurements. The results indicated that the increase in temperature from UVA radiation exposure augmented the materials' elasticity and elongation, leading to higher ultimate tensile stress values and lower Young's Moduli for all cases. More specifically, PETG components exhibited the highest overall ultimate tensile stresses among the unaged coupons, averaging 24.5 MPa and 28.11 MPa for white and transparent filaments, respectively. For aged compressive stress scenarios, PETG was also the most consistent material, with a reduction of only 0.97 MPa for white specimens and 1.55 MPa for transparent ones. Regarding colorimetric analysis, white PETG showed reflectance differences of about 5%, with clear coupons reaching only 1.5% after 90 aging cycles.

Therefore, the author selected PETG as the feedstock for manufacturing applications and progressed toward product digital modeling, prototyping, assembly, and automation.

The combination of various research-based computational modeling techniques, building performance evaluations, and material and materialization analysis culminated in an informed Design-for-Manufacture-and-Assembly process. The interdisciplinarity of all procedures and the broad knowledge acquired provided greater control over the product design stages, diminished the number of editing cycles, and reduced the time between ideation and proofs-of-product prototyping. Even though the workflow concentrated all decision-making on one agent, similar applications can widen the investigation scope and rely on design teams with different backgrounds (i.e., design, simulation, material evaluation, and digital manufacturing).

Although this study fully documented the Research-through-Design (RtD) workflow, the various stages concerning conceptualization, design, manufacturing, assembly, and concurrent digital and physical editing hindered clear communication, possibly failing to convey its iterative nature. Still, the author indicates the following as the main RtD findings:

a) The selection of a timeline-based modeling software helped achieve a swifter design workflow, offering straightforward editing of various geometric attributes and adjusting all constraints accordingly (or offering clash-detection notifications); however, parametric tools demand planning and more attention during the first modeling stages;

b) A product-oriented software assisted in integrating standardized hardware, helping the design comply with real-world applications;

c) Major design flaws and most time spent during the process are due to the prototyping stages that cause the digital editing process to remain still while waiting for a physical evaluation;

d) Despite various research indications, fused deposition modeling is highly unpredictable, material-intensive, and produces a substantial quantity of byproducts due to print failure or already-assessed components;

e) Working with end-use material requires evaluating the feedstock and the manufactured components, especially for plastics that undergo fused deposition that renders components anisotropic;

f) Designers should assess fused-deposition components according to their intended applications (structural and optical in this research context), as their integrity relies mainly on printing parameters instead of on the raw material characteristics;

g) Depending on their print parameters, thermoplastics are adequate for structural and mechanical applications, maintaining their physical and chemical integrity after aging; for instance, low-density triangular infill patterns presented the highest stiffness-to-mass ratio among all evaluated patterns and remained above the safety limits required for plastic components;

h) Due to the layer deposition and the thermoplastic size variation, FDM-produced pieces present visual light transmittance properties, even for opaque filaments; for instance, even white PETG with denser infill could reach 1.28% light transmittance, rendering an illuminance level of 61.40 lx;

i) The physical and digital editing cycles coupled with product-specific modeling software eased the incorporation of cybernetic and mechatronic components, even though primary evaluations cannot render a minimum viable product due to the need to maintain all connections loose.

Finally, based on all studies presented in this research, the author deems the hypothesis presented in the Thesis Overview as accepted. The exchange of static and opaque roof claddings, here represented by the building performance and simulation base cases, with a simulation-based, climate-active, and cyber-physical top lighting cell can improve daylight admission in buildings, potentializing human visual comfort. The top lighting cell incorporation also helped increase air infiltration/exfiltration and air changes per hour when needed, maintaining or boosting human thermal comfort according to the adaptive criteria.

In addition, the Research-through-Design followed by a design-for-manufacture-and-assembly workflow helped expedite various stages of the building component's design and assessment, mainly due to the physical experimentation provided by desktop digital fabrication tools, i.e., structural integrity analysis, rapid-aging of thermoplastics, chromaticity evaluations, optical degradability, and visual transmittance and reflectance measures.

The author indicates the following as future study applications:

a) The Beta phase is not the last of product development. Its evolution into a minimum viable product depends on the interaction between the top lighting cell and the actual building. The author plans to assess real applications to refine the design further, define a control hub for storing all hardware components, secure all electrical wiring, and achieve a minimum viable product. For instance, Figures 1a, b, and c show the building evaluation space in which the author should validate this study;

Figure 1: (a) Building chamber for performance monitoring under construction; (b) roof openings for the top lighting cell installation; (c) indoor space with the roof openings.

Source: The Author (2024).

b) The simulation workflow for active building components should be evaluated for other designs, motion constraints, materials, building typologies, and geographic locations; lower latitudes should work relatively similarly to this study, but the environmental response for daylight also depends on daylight availability, sky luminance, context shading geometries, and the possibility of adopting an opened lighting well (e.g., in equatorial climates, the number of hours the cell would remain closed is higher due to rain; further, the glare probability is also higher);

c) Studies should consider comparing two cyber-physical applications: one pre-programmed with the opening positions gathered via simulation and

one equipped with real-time sensing; the first application is a downgrade from a reactive to a direct system that can potentially maintain the daylight benefits achieved using more compute-intensive approaches and validate simulation motors and the simulation workflow; the downgrade only concerns the cybernetic portion of the design and offers more human interaction and control;

d) Future studies should further analyze non-visual effects of light, such as circadian entrainment and elicit alertness, and qualitative criteria regarding color (appearance and rendering), indoor-outdoor view, light distribution, and uniformity;

e) Considering the potential increase in electric energy consumption caused by actuation and real-time sensing, research should assess artificial light expenditure decrease due to daylight supplementation. Further, as the prototypes adopt Arduino microcontrollers, authors can also evaluate photovoltaic integration using micromodules;

APPENDIX I

XIX Encontro Nacional de Tecnologia do Ambiente Construído
ENTAC 2022

Ambiente Construído: Resiliente e Sustentável
Canela, Brasil, 9 a 11 novembro de 2022

Thermal calibration of an existing institutional building

Calibração térmica para uma edificação institucional existente

Caio de Carvalho Lucarelli
Universidade Federal de Viçosa | Viçosa | Brasil | lucarelli.caio@outlook.com
Matheus Menezes Oliveira
Universidade Federal de Viçosa | Viçosa | Brasil | matheus.meneses@gmail.com
Joyce Correna Carlo
Universidade Federal de Viçosa | Viçosa | Brasil | joyce.carlo@ufv.br

Abstract
Building performance simulation (BPS) exhibits an interplay of various physical parameters, only portraying limited building fundamental characteristics. Therefore, BPS calibration can increase simulation accuracy and better depict the physical space. We aimed to calibrate/validate an institutional building model in Viçosa-MG, testing parallel and serial uncertainty procedures. We conducted a manual/statistic hygrothermal calibration using surveyed indoor/outdoor air dry-bulb temperature (DBT) and relative humidity (RH). We evaluated site-specific weather files and compared simulation outputs and measured data using the Root Mean Square Error (RMSE). As a result, the validated model presented 0.56°C to 0.85°C DBT discrepancies and 3.10% to 5.90% RH differences.

Keywords: Uncertainty analysis; Whole-building performance simulation; Survey data; Model Validation.

Resumo
A simulação de desempenho permite interação entre diversos parâmetros físicos, mas representa apenas parte das características do espaço construído. Portanto, processos de calibração podem aumentar sua precisão e melhor representar particularidades do ambiente. Objetivamos calibrar/validar um modelo institucional em Viçosa-MG, testando o método de incertezas paralelo e serial. Conduzimos uma calibração higrotérmica manual/estatística aplicando medições de temperatura (TBS) e umidade (UR). Criamos arquivos climáticos locais e comparamos dados de simulação e medição usando a raiz do Erro Quadrático Médio (EQM). Assim, obtivemos um modelo validado com discrepâncias de 0.56°C à 0.85°C para TBS e 3.10% até 5.90% para UR.

Palavras-chave: Análise de incertezas; Simulação de desempenho para edificação; Medições físicas; Validação.

Como citar:
LUCARELLI, C. D. C.; OLIVEIRA, M. M.; CARLO, J. C. Thermal calibration of an existing institutional building. In: ENCONTRO NACIONAL DE TECNOLOGIA DO AMBIENTE CONSTRUÍDO, 19, 2022, Canela. **Anais**... Porto Alegre: ANTAC, 2022. p. XXX-XXX.

INTRODUCTION

The building modeling and performance simulation (BPS) comprises computer-based representations with physical principles [1]. According to Clarke and Hensen [2], BPS quantifies performance criteria suitable for building design, operation, and control, aiming to portray the dynamicity of physical processes.

However, modeling and simulating the built domain is complicated due to interacting performance expectations and unpredictability. For instance, BPS uncertainties include building geometry, material thermal properties, power consumption of electric and electronic equipment (plug loads), human-generated heat, occupancy schedules, heat gain and loss due to infiltration, and &c. [3]. Therefore, computational models should undergo verification, calibration, and validation procedures [1], as portrayed by different research pieces [4,5].

Hence our goal is to test the parallel and serial calibration procedures using a thermal and energy simulation model. This study combines indoor and outdoor hygrothermal surveys for an institutional building in Viçosa-MG, Brazil (20°45’14’’S and 42°52’54’’W). We evaluate the fittest outdoor data for assembling a simulation weather file that rightly represents surveyed indoor dry-bulb temperatures (DBT) and relative humidity (RH). We also conduct a manual/iterative hygrothermal calibration procedure using uncertainty analysis and statistical techniques for tunning multiple adjacent rooms using Ladybug Tools and sub-packages for Rhino3D+Grasshopper.

THEORETICAL FRAMEWORKS

According to Royapoor and Roskilly [6] and O’Donovan, O’Sullivan, and Murphy [7], BPS only portrays a limited part of a building’s fabric properties, occupants, and weather elements, naturally resulting in inaccuracy. Furthermore, software constraints, scarcity of surveyed input parameters, inaccuracy of weather characterization, incorrect or non-convex model geometries, and distrustful building occupancy and schedules lead to virtual model errors and simulation unpredictability.

Most researchers avoid simulation approaches due to the lack of clarity or confidence in the simulation outputs [3]. Besides, an architect, engineer, constructor, and operator (AECO) will hardly gather reliable building system characteristics.

Hence, BPS should encompass verification, calibration, and validation methods [8]. According to De Wilde [1], the AECO professional scrutinizes the conceptual building description during the verification, evaluating similarities between the actual building and the modeling geometry; the validation process delimits the model’s accuracy and ability to depict real-life spaces, and thus, is the calibration goal.

The calibration consists in revising uncertain modeling parameters to improve congruence between surveyed and simulated data. Calibration is manual/iterative (heuristic), graphical/statistic, or automated [1,7]. Normally, calibration processes adopt data-tunning using default building and operation inputs, modified according to simulation results’ precision.

As an example of a heuristic calibration, O'Donovan, Sullivan, and Murphy [7] validated a whole building energy model using indoor DBT. The authors considered shading, internal loads, and natural ventilation as uncertainties. They applied the Normalized Root Mean Square Error (NRMSE) and Normalized Mean Bias Error (NMBE), achieving 0.8°C to 1.1°C discrepancies with a maximum of 6% NMBE.

METHODOLOGY

According to the Köppen classification, Viçosa-MG is warm and temperate (Cwa) with hot and humid summers and cool to mild winters. The selected building (Fig. 01) is a part of *Universidade Federal de Viçosa Architecture Pós-Graduation Program* (Viçosa-MG 20°45'14''S and 42°52'54''W).

Figure 1: Building thermal and energy model and Ladybug Tools' Honeybee/EnergyPlus zoning.

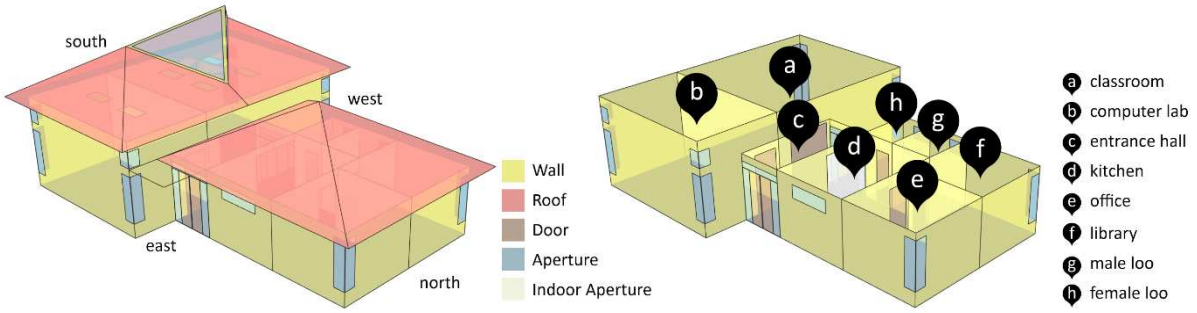

Source: The Authors.

The selected building is 110m^2, one-story, hip/Dutch-like roofed, with eight separate zones. The building is wind-exposed for North and East orientations and displays an expressive microclimate caused by a pond for South and East and a mass of vegetation and surrounding lawn for South and West. The latter represents the building's rear setback, which is also wind-protected.

We divide this study into four methodological procedures according to De Wilde's [1]:

1. Data collection: collecting building components' dimensions; gathering building fabric properties; measuring reflectance values and indoor DBT and RH; surveying occupation and ventilation schedules; estimating plug loads and lighting consumption; establishing uncertainties;
2. Weather data: surveying outdoor DBT and RH for the weather file assemblage; simulating a base case for all created weather files;
3. Simulation and calibration: choosing the fittest weather file created in step two; simulating a new base case; uncertainty analysis and parallel calibration process; serial calibration;
4. Simulation results, evaluation, and validation: comparing surveyed data and simulation results by applying statistical analysis; graphically representing data output using box-plot charts and tables; displaying validated model.

Although De Wilde [1] suggested seven steps, we amalgamate simulation and evaluation and do not adopt re-simulation as a single step since the calibration procedure (item 3) already involves re-simulating the model after each tunning.

FIRST STAGE

We conducted the architectural survey during the first phase, gathering building dimensions (i.e., floorplan, elevations, and aperture sizes). We also examined indoor/outdoor opaque and translucent materials (building fabric), adopting Weber et al.'s [10] equivalent reference models, NBR 15.220-2 and NBR 15.220-3's [11,12] materials and constructions, and NBR NM 294's [13] glass properties.

For instance, Table 1 shows the first base case construction layers, thicknesses (Thk), thermal transmittances (Ut), component thermal capacities (Ct), absorptances (α), solar transmittances (τ), solar reflectance (ρ), emissivity (ε), thermal conductivity (λ), and solar factor (FS). The materials appear from the exterior to the interior, following Ladybug Tools' Honeybee/EnergyPlus construction inputs. We employed an unedited version of TMY3 for Viçosa-MG, which offers the most reliable single-step simulation process with lower computational costs [9].

Table 1: Base case construction and material properties.

Indoor/Outdoor Walls							
9-hole brick 9x14x29 cm	Material	Thk (cm)	Ut (W/m²°C)	Ct (kJ/m²°C)	α		
	Plaster	2.50	2.39	150	0.2		
	Ceramic	1.34			-		
	Wall air gap	6.32			-		
	Ceramic	1.34			-		
	Plaster	2.50			0.2		
Roof							
Ceramic roof and concrete ceiling	Material	Thk (cm)	Ut (W/m²°C)	Ct (kJ/m²°C)	α		
	Ceramic Roof Tiles	1.00	2.05	238	0.75		
	Air gap	0.25			-		
	Concrete	10.00			-		
Floor							
Concrete Slab	Material	Thk (cm)	Ut (W/m²°C)	Ct (kJ/m²°C)	α		
	Ceramic Tiles	0.75	3.59	2.88	0.40		
	Underlayment	0.50			-		
	Concrete	5.00			-		
Windows							
Single-Pane Float Glass	Material	Thk (cm)	τ	ρ	ε	λ (W/m.K)	FS (%)
	Glass	0.3	0.88	0.07	0.84	1.00	87.00

Source: The Authors, adapted from Weber et al. [10], NBR 15.220-2 [11], NBR 15.220-3 [12], NM 294 [13].

We used an ALTA II (eleven wavelengths, from 470 to 940nm) spectrometer to measure surface reflectances, shown in Table 1 as absorptance values (α). We also collected indoor and outdoor DBT and RH from March 9th to March 31st, 2022, using hygrothermal data loggers (HOBO/ONSET U12 Temp/RH/Light accuracy: ±2°C and ±2% RH) recording every five minutes. We used six data loggers indoors (classroom, computer lab, entry hall, kitchen, office, and library) (Fig. 01) and four data loggers outdoors (one for each cardinal orientation).

We surveyed daily occupation patterns, users, electromechanical equipment, and natural conditioning tactics and modeled eight thermal zones (Fig. 01) using Ladybug Tools' Honeybee for Rhino3D+Grasshopper.

Since we monitored the building during the COVID-19 pandemic, there is no occupation on most days. Therefore, we adopted the Ladybug Tools Honeybee Small Office Building Program (Classroom, Lobby, Dining, Closed Office, and Restroom schedules) with default Honeybee office occupation and plug loads on Mondays, Wednesdays, and Fridays from 8 am to 6 pm, compatible with the surveyed occupation data. Other configurations follow Fig. 2 workflow.

Figure 2: Ladybug Tools' Honeybee workflow for occupation/activity schedule and lighting and plug power.

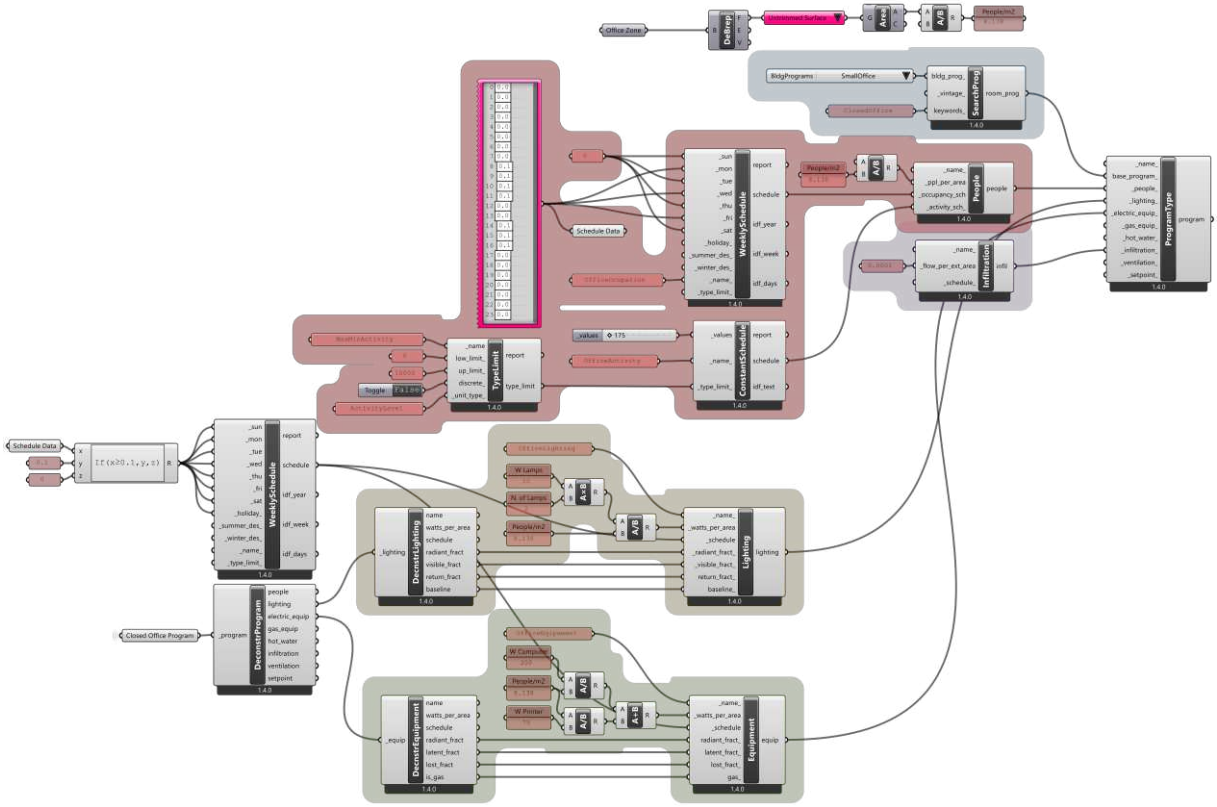

Source: The Authors. Note: Figure in High Resolution for zooming purposes.

We assume construction layers (wall and roof), ventilation (single and cross-flow stances), and soil properties as uncertain input parameters (Table 2). Therefore, we selected two wall constructions from Weber et al. [10] and one from NBR 15.220-3 [12], respecting the surveyed wall thickness and overall visible characteristics. We also selected two ceramic roof structures (i.e., concrete and PVC ceiling) since we could not distinguish all roof layers.

We also evaluated cross and single-flow ventilation. The boundary shading geometry remained as surveyed (i.e., pergola, overhangs, and surrounding vegetation). However, we changed soil aspects by applying dry dust, moist soil, and mud characteristics.

Table 2: Uncertainty Inputs for Building Constructions.

Heat Source	Uncertainty Input			
Walls	6-hole brick 9x14x24 cm			
	Material	Thk (cm)	Ut (W/m²°C)	Ct (kJ/m²°C)
	Plaster	2.50	2.39	150.00
	Ceramic	1.34		

	Air gap	6.32		
	Ceramic	1.34		
	Plaster	2.50		
	2-hole concrete block 9x19x39cm			
	Material	Thk (cm)	Ut (W/m²°C)	Ct (kJ/m²°C)
	Plaster	2.50	2.79	209.00
	Concrete	1.73		
	Air gap	5.54		
	Concrete	1.73		
	Plaster	2.50		
	Standard brick			
	Material	Thk (cm)	Ut (W/m²°C)	Ct (kJ/m²°C)
	Plaster	2.50	3.13	255.00
	Ceramic	10.00		
	Plaster	2.50		
Roof	**Ceramic roof and concrete slab**			
	Material	Thk (cm)	Ut (W/m²°C)	Ct (kJ/m²°C)
	Ceramic	1.00	2.05	238.00
	Air gap	25.00		
	Concrete	10.00		
	Ceramic roof and PVC ceiling			
	Material	Thk (cm)	Ut (W/m²°C)	Ct (kJ/m²°C)
	Ceramic	1.00	1.75	21.00
	Air gap	25.00		
	PVC ceiling	1.00		
	Underlayment	0.50		
	Concrete	5.00		

Source: The Authors, adapted from Weber et al. [10], NBR 15.220-3 [12].

SECOND STAGE

We collected outdoor DBT and RH using data loggers, protecting the equipment from beam radiation using a 90-degree, 3-way, T-shaped PVC pipe with aluminum foil.

We created five weather files, one for each outdoor-collect data corresponding to each cardinal orientation and one averaging all outdoor DBT and RH data; we edited the TMY3 weather file for Viçosa-MG using the open-source Elements Tool (Big Ladder Software).

We ran simulations for an entire year using the revised files and compared the results with the indoor surveyed data, electing the best-representing file using the Root Mean Square Error (RMSE) and the normalized RMSE (NRMSE) (Equations 1 and 2).

$$RMSE = \sqrt{\frac{\sum_{i=1}^{N}(simulated_i - surveyed_i)^2}{N}} \quad (1)$$

$$NRMSE = \frac{\sqrt{\frac{\sum_{i=1}^{N}(simulated_i - surveyed_i)^2}{N}}}{(max_{simulated} - min_{simulated})} \quad (2)$$

where: *RMSE - Root-Mean-Square Error*
$simulated_i$ - predicted/simulation values
$surveyed_i$ - surveyed data
N - total number of observations
NRMSE – Normalized RMSE
$max_{simulated}$ – maximum simulation value
$min_{simulated}$ – minimum simulation value

THIRD STAGE

After selecting the fittest weather file, we applied two distinct processes for the calibration. The first process comprises a parallel method in which we simulate specific uncertainties for a distinct input parameter (e.g., we simulate 6-hole brick and collect output data; then, we return to the base case and exchange the 6-hole brick with the 2-hole concrete block, and so forth). The second procedure comprises a serial methodology in which we combine all best-rated cases to generate an optimized, validated model.

FOURTH STAGE

We adopted EnergyPlus' Zone DBT and RH outputs and compared the simulation results with indoor surveyed data. We reassessed the methodology adopted in the previous sections, calculating the RMSE and NRMSE.

RESULTS

Table 3 shows RMSE and NRMSE for each assembled weather file simulation data. The results indicate that the TMY3 replaced with South-collected information presents the lowest overall RMSE and NRMSE for DBT and RH. For instance, we utilized NRMSE to compare DBT and RH as it displays results within the same threshold.

Table 3: DBT and RH RMSEs and NRMSEs for each thermal zone using assembled weather files.

RMSEs and NRMSEs for Indoor Air Temperature								
Weather File	**Entry Hall**	**Comp. Lab**	**Classroom**	**Kitchen**	**Library**	**Office**	**RMSE**	**NRMSE**
FileAverage	3.59	3.34	4.23	5.69	5.12	4.90	26.88	1.60
FileNorth	4.26	3.63	4.50	5.74	4.97	4.54	27.64	1.66
FileEast	3.86	3.13	4.00	5.38	4.72	4.33	25.43	1.10
FileSouth	3.03	2.10	2.89	4.55	4.19	3.90	**20.65**	**1.04**
FileWest	3.05	2.10	2.93	4.58	4.20	3.90	20.76	1.39
RMSEs and NRMSEs for Indoor Relative Humidity								
Weather File	**Entry Hall**	**Comp. Lab**	**Classroom**	**Kitchen**	**Library**	**Office**	**RMSE**	**NRMSE**
FileAverage	11.57	11.12	18.05	20.64	19.21	14.40	94.99	1.65
FileNorth	13.37	12.39	18.66	20.28	19.10	14.40	98.20	1.63
FileEast	14.46	13.20	19.75	21.68	20.54	15.52	105.15	1.74
FileSouth	12.14	8.93	13.83	17.61	16.94	13.88	**83.35**	**1.46**
FileWest	12.35	9.45	15.09	18.68	17.90	14.31	87.78	1.53

Source: The Authors.

Furthermore, FileSouth and FileWest delivered comparable results, justified by the proximity of both data loggers to a highly-vegetated, wind-protected boundary condition. We also understand that the collected data for both cardinal orientations is microclimate-affected, reproducing the same conditions in the adjacent rooms.

FileNorth and FileEast are sun and wind-exposed, have higher albedo, and are nearer impermeable surfaces, causing higher dissonances.

Following these results, we appointed FileSouth as the standard substitute for the unedited TMY3 weather file for the new base case simulations. Table 4 depicts each RMSE and NRMSE for the calibration process, displaying constructing materials,

ventilation methods, and soil characteristics as separate groups. The parallel calibration process resulted in a pre-selection of the fittest simulation inputs for the future serial calibration. We also present the improvement percentage for each uncertainty compared to the base case.

Table 4: DBT and RH RMSEs and improvement percentages compared to the base case FileSouth.

RMSEs for Indoor Air Temperature							
Input Parameter	**Entry Hall**	**Comp. Lab**	**Classroom**	**Kitchen**	**Library**	**Office**	**Improve**
Base Case - FileSouth	3.03	2.10	2.89	4.55	4.19	3.90	-
6-hole brick	0.68	0.79	0.94	2.36	0.67	0.82	69.67%
2-hole concrete block	0.63	0.78	0.89	2.29	0.60	0.89	**70.60%**
Standard brick	0.62	0.86	0.93	2.32	0.64	0.96	69.42%
Ceramic roof and concrete	1.13	1.43	1.98	3.33	1.60	1.43	**47.22%**
Ceramic roof and PVC ceiling	1.51	1.43	2.11	3.75	2.14	1.74	38.69%
Single-flow ventilation	1.03	1.78	1.82	2.71	0.87	1.07	**55.08%**
Cross-ventilation	3.03	2.10	2.89	4.55	5.13	4.01	5.11%
Dry soil	0.89	1.01	1.25	2.63	0.83	1.07	62.79%
Moist Soil	0.89	1.00	1.23	2.62	0.83	1.07	63.03%
Mud	0.88	0.98	1.21	2.61	0.82	1.07	**63.34%**
RMSEs for Relative Humidity							
Input Parameter	**Entry Hall**	**Comp. Lab**	**Classroom**	**Kitchen**	**Library**	**Office**	**Improve**
Base Case – File South	12.14	8.93	13.83	17.61	16.94	13.88	-
6-hole brick	5.53	7.27	9.45	12.85	8.78	7.87	37.91%
2-hole concrete block	5.16	6.67	9.04	12.48	8.11	7.25	**41.54%**
Standard brick	5.00	6.97	9.12	12.59	8.05	7.40	41.05%
Ceramic roof and concrete	7.36	9.17	25.33	18.07	16.07	10.13	3.34%
Ceramic roof and PVC ceiling	5.98	9.03	13.67	16.55	14.11	8.75	**18.32%**
Single-flow ventilation	5.09	9.33	12.58	13.99	9.87	6.51	**31.15%**
Cross-ventilation	12.14	8.93	13.83	17.61	16.94	13.00	1.06%
Dry sand	4.94	6.53	10.17	13.69	9.60	6.51	38.29%
Moist soil	4.93	6.48	10.08	13.65	9.52	6.51	22.60%
Mud	4.93	6.42	9.99	13.60	9.43	6.51	**63.34%**

Source: The Authors.

Even though no wall construction fully represents all surveyed DBT and RH, we understand that we can only choose one for the whole model. Therefore, comparing the improvement rate, we selected the 2-hole concrete block. For the roof construction, the concrete ceiling better represented the model for all rooms, which indicates that, even though we see PVC ceilings in the classroom and computer lab, there is a concrete layer above.

As expected, the single-flow ventilation better represented all cases for DBT. For RH, only the computer lab displayed better RMSEs for cross-ventilation due to its wind-exposed characteristic and the parallel corner windows. Even though the office and library spaces are also wind-exposed, they do not present parallel apertures.

For soil characteristics, mud-like soil showed better RMSEs due to the lawn and vegetation evapotranspiration around all zones.

After defining all suitable simulation inputs, we perform the serial calibration using the 2-hole concrete block, ceramic roof and concrete ceiling, single-flow ventilation, and mud-like soil. For instance, Table 5 demonstrates the lowest overall RMSE among all parallel calibration simulations, the final RMSE outcomes after the serial calibration, and the NRMSE for comparing temperature and humidity outputs.

Table 5: Lowest RMSE for parallel calibration and serial calibration DBT and RH RMSEs and NRMSEs.

	RMSEs and NRMSEs for Indoor Air Temperature						RMSEs and NRMSEs for Relative Humidity					
	Hall	Lab	Class	Kitchen	Library	Office	Hall	Lab	Class	Kitchen	Library	Office
Min. Parallel RMSE	0.60	0.78	0.89	2.17	0.56	0.82	4.93	6.42	9.04	12.07	8.05	6.51
RMSE Serial	0.72	0.67	0.56	0.80	0.85	0.78	5.30	5.90	3.10	5.70	5.60	5.30
NRMSE Serial	0.14	0.14	0.14	0.27	0.27	0.24	0.24	0.20	0.17	0.20	0.23	0.21

Source: The Authors.

Even though RMSEs for RH appear higher than DBT, a comparison of their normalized versions illustrates that the higher deviations occur for DBT in the kitchen, library, and office zones. Overall, we already expected the zones farther from the South to present higher divergences since their boundary conditions differ from the rear setback.

The NRMSE results conform with O'Donovan, Sullivan, and Murphy's [7] results, varying between 0.56°C and 0.85°C and are below 1°C as Rajčić, Skender, and Damjanović [14] recommended. For the RH, the model presented maximum RH divergencies of 5.90%. Rajčić, Skender, and Damjanović [14] indicated that RH between 1% and 10% vary from excellent to acceptable.

Figure 3: Surveyed data, FileSouth base case, and fully-calibrated/validated model.

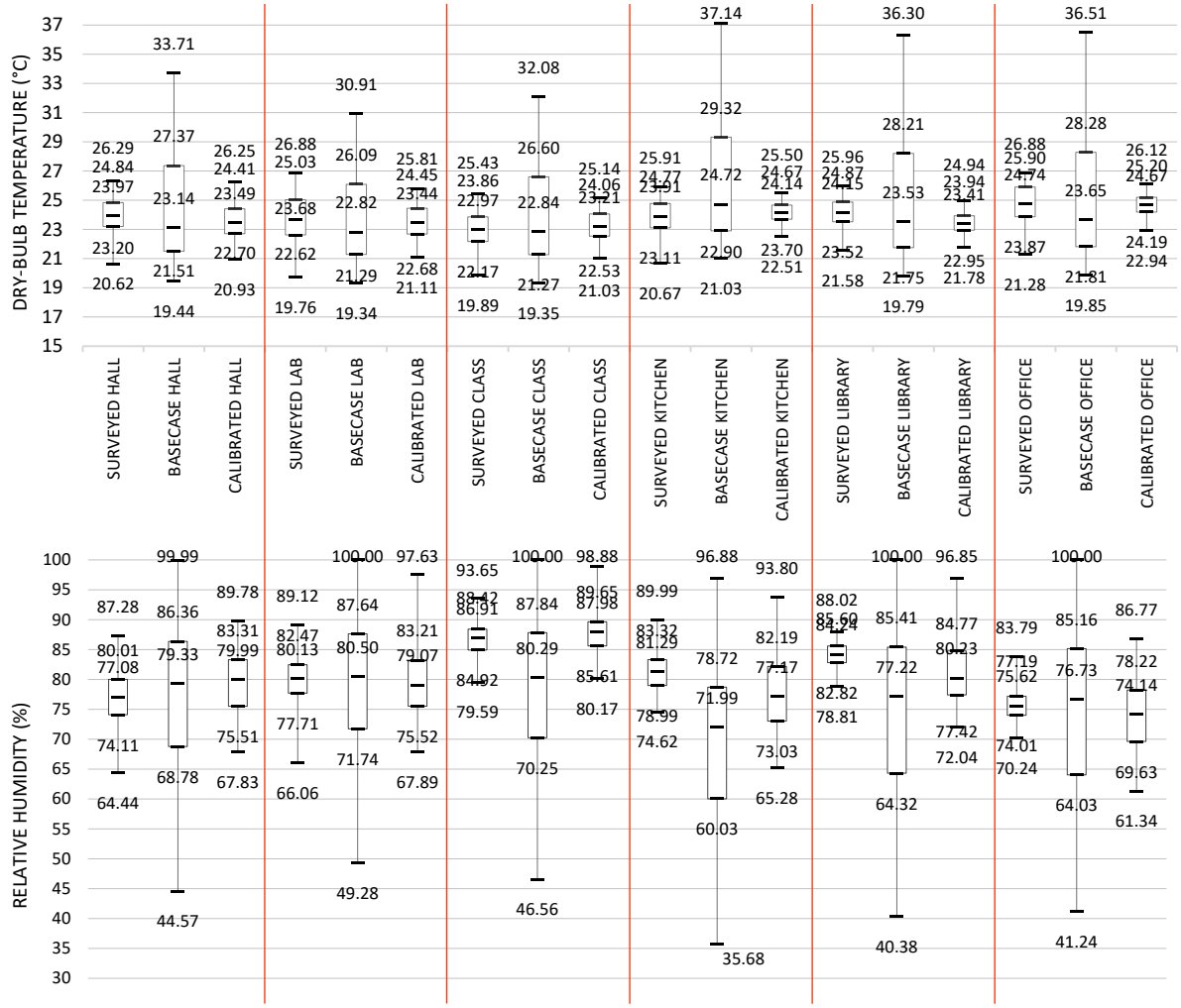

Source: The Authors.

Figure 3 illustrates the calibration/validation process by comparing DBT and RH for surveyed information, FileSouth base case, and the validated model.

CONCLUSIONS

This paper presented a straightforward verification, calibration, and validation procedure for an institutional building in Viçosa-MG applying *in-situ* DBT and RH surveys.

We assembled a fitting weather file based on statistical analysis and utilized parallel and serial uncertainty analysis. Since the building survey occurred during the COVID-19 pandemic, we had a low variability of uncertain inputs due to lacking occupation patterns and plug loads. Also, the Ladybug Tools workflow adopts a simplified version of EnergyPlus' standard simulation procedure, which seldom hinders user override possibilities. However, we found that applying both calibration techniques rendered an optimal model, consistent with the literature, with no further parametric combinations.

Overall, the assembled weather file better-represented rooms adjacent to the data logger placement but did not generate high discrepancies for the other thermal zones. For instance, DBT RMSEs presented 0.56°C to 0.85°C discrepancies, rendering a minimum of 17.58% (library) and a maximum of 31.90% (computer lab) model improvement compared to the FileSouth base case. RH RMSE results were as low as 5.90% for the worst-case scenario, with a maximum improvement of 66.06% (computer lab).

Since our simulation model presents lower divergences than other models using the same calibration/validation procedures [7,14], we consider our model validated.

ACKNOWLEDGEMENTS

This study was financed in part by the Coordenação de Aperfeiçoamento de Pessoal de Nível Superior – Brasil (CAPES) – Finance Code 001 and Fundação de Amparo à Pesquisa de Minas Gerais (FAPEMIG) – Universal Demand 001/2021 Financing Code APQ-00266-21.

REFERENCES

[1] DE WILDE, P. **Building Performance Analysis.** Oxford: John Wiley & Sons Ltd, 2018. DOI: 10.1002/9781119341901.

[2] CLARKE, J.; HENSEN, J. Integrated building performance simulation: Progress, prospects and requirements. **Building and Environment**, v. 91, p. 294–306, 2015. DOI: 10.1016/j.buildenv.2015.04.002.

[3] WESTPHAL, F. **Análise de incertezas e de sensibilidade aplicadas à simulação de desempenho energético de edificações comerciais.** 2007. Tese de Doutorado - Programa de Pós-Graduação em Engenharia Civil, Universidade Federal de Santa Catarina, Florianópolis, 2007.

[4] HUERTO-CARDENAS, H.; LEONFORTE, F.; ASTE, N.; DEL PERO, C.; EVOLA, G.; CONSTANZO, V.; LUCCHI, E. Validation of dynamic hygrothermal Simulation models for historical buildings: State of the art, research challenges and recommendations. **Building and Environment,** v. 180, p. 107081, 2021. DOI: 10.1016/j.buildenv.2020.107081.

[5] MARTÍNEZ-MARINO, S.; EGUÍA-OLLER, P.; GRANADA-ÁLVAREZ, E.; ERKOREKA-GONZÁLEZ, A. Simulation and validation of indoor temperatures and relative humidity in multi-zone

buildings under occupancy conditions using multi-objective calibration. **Building and Environment,** v. 200, 2021. DOI: 10.1016/j.buildenv.2021.107973.

[6] ROYAPOOR, M.; ROSKILLY, T. Building model calibration using energy and environmental data. **Energy and Buildings,** v. 94, p. 109–120, 2015. DOI: 10.1016/j.enbuild.2015.02.050.

[7] O' DONOVAN, A.; O' SULLIVAN, P.; MURPHY, M. Predicting air temperatures in a naturally ventilated nearly zero energy building: Calibration, validation, analysis and approaches. **Applied Energy,** v. 250, p. 991–1010, 2019. DOI: 10.1016/j.apenergy.2019.04.082.

[8] OBERKAMPF, W.; ROY, C. **Verification and Validation in Scientific Computing**. Cambridge: Cambridge University Press, 2010.

[9] GUIMARÃES, Í. B. **Análises de incertezas e sensibilidade de arquivos climáticos e seus impactos em simulações computacionais termo energéticas.** 2016. 95 f. Dissertation (MPhil) - Programa de Pós-Graduação em Arquitetura e Urbanismo, Universidade Federal de Viçosa, Viçosa, 2016.

[10] WEBER, F.; MELO, A.; MANINOSKI, D.; GUTHS, S.; LAMBERTS, R. Desenvolvimento de um modelo equivalente de avaliação de propriedades térmicas para a elaboração de uma biblioteca de componentes construtivos brasileiros para o uso no programa EnergyPlus. 2017. p. 52.

[11] ASSOCIAÇÃO BRASILEIRA DE NORMAS TÉCNICAS. **ABNT NBR 15.220-2:** Desempenho térmico de edificações Parte 2: Métodos de cálculo da transmitância térmica, da capacidade térmica, do atraso térmico e do fator solar de elementos e componentes de edificações. Rio de Janeiro, 2005.

[12] ASSOCIAÇÃO BRASILEIRA DE NORMAS TÉCNICAS. **ABNT NBR 15.220-3:** Zoneamento bioclimático brasileiro e diretrizes construtivas para habitações unifamiliares de interesse social. Rio de Janeiro, 2005.

[13] ASSOCIAÇÃO BRASILEIRA DE NORMAS TÉCNICAS NORMA MERCOSUL. **ABNT NM 294:** Vidro Float. Brasil, Argentina, Uruguai e Paraguai, 2004.

[14] RAJČIĆ, V.; SKENDER, A.; DAMJANOVIĆ, D. An innovative methodology of assessing the climate change impact on cultural heritage. **International Journal of Architectural Heritage**, v. 12, p.21-35, 2018. DOI: 10.1080/15583058.2017.1354094.

APPENDIX II

State-of-the-art research on building enclosures according to StArt Scoring criteria

Title	DOI	ISBN	Authors	Study Methodology	Location			Active Typology	Movement	Software			Simulation		StArt Score
					City	Country	Weather			Modeling	Simulation	Optimization	Objective	Metrics	
Interactive kinetic façade: Improving visual comfort based on dynamic daylight and occupant's positions by 2D and 3D shape changes	10.1016/j.buildenv.2019.106396		(Hosseini et al., 2019)	Review Simulation	Yazd	Iran	BWh	Responsive	Scaling Translating	Rhino+Grasshopper	DIVA	-	Visual	EUDI, DA, DGP, UDI	224
The Intelligent Control Strategy of Kinetic Façades for Daylight and Energy Performance	-		(Yang, 2020)	Calculation Simulation	Los Angeles	USA	Csb	Intelligent	Rotating	Rhino+Grasshopper	Ladybug Tools Honeybee	-	Thermal Visual	DGP, heat gain, UDI	212
Biomimetic Kinetic Shading Facade Inspired by Tree Morphology for Improving Occupant's Daylight Performance	10.15627/jd.2021.5		(Hosseini et al., 2021)	Review Simulation	Yazd	Iran	BWh	Biomimetic	Transforming	Rhino+Grasshopper	DIVA	-	Visual	EUDI, DA, DGP, UDI	203
Influence of two motion types on solar transmittance and daylight performance of dynamic façades	10.1016/j.solener.2020.03.017		(Shi et al., 2020)	Simulation	Singapore	Singapore	Af	Kinetic	Rotating	Rhino+Grasshopper	Ladybug Tools Honeybee	Octopus	Energy Visual	DA, Ev, Hourly energy consumption, UDI	189
Integrating interactive kinetic façade design with colored glass to improve daylight performance based on occupants' position	10.1016/j.jobe.2020.101404		(Hosseini et al., 2020)	Review Simulation	Yazd	Iran	BWh	Kinetic	Rotating Translating	Rhino+Grasshopper	DIVA	-	Visual	EUDI, DA, DGP, UDI	183
SMP Prototype Design and Fabrication for Thermo-responsive Façade Elements	10.7480/jfde.2019.1.2662		(Yoon, 2019)	Experiment Simulation	Seoul	South Korea	Dwa	Smart	Rotating	Rhino+Grasshopper	Ladybug	-	Thermal	Radiation levels	178
Optimal design of an Origami-inspired kinetic façade by balancing composite motion optimization for improving daylight performance and energy efficiency	10.1016/j.energy.2020.119557		(Le-Thanh et al., 2021)	Calculation Review Simulation	Hoh Chi Minh	Vietnam	AwAs	Intelligent	Rotating Translating	Rhino+Grasshopper	ARCHSIM DIVA	-	Visual	sDA, TEC	173
Assessment of control strategy of adaptive façades for heating, cooling, lighting energy conservation and glare prevention	10.1016/j.enbuild.2021.110739		(Lee et al., 2021)	Calculation Case Study Review	Seoul	South Korea	Dwa	Responsive	Rotating Translating	-	-	-	Energy Visual	DGP, DGI, lighting energy, SHGC	168
A morphological approach for kinetic façade design process to improve visual and thermal comfort: Review	10.1016/j.buildenv.2019.02.040		(Hosseini et al., 2019)	Review	-	-	-	Biomimetic Kinetic	-	-	-	-	-	-	165
Assessment of control strategy of adaptive façades for heating, cooling, lighting energy conservation and glare prevention	10.1016/j.enbuild.2021.110739		(Lee, 2019)	Calculation Simulation	Seoul Abu Dabi Hanoi	South Korea United Arab Emirates Vietnam	BWh Cfa Dwa	Kinetic	Rotating Translating	Sketchup3D	APACHE IES VE IT Radiance SunCast	-	Energy	cooling, heating, and lighting energy consumption, TEC	163
Shape gramma based adaptive building envelopes: Towards a novel climate responsive facade system for sustainable architectural design in Vietnam	-		(Nguyen, 2019)	Calculation Review Simulation	Hanoi Hue Saigon	Vietnam	Am AwAs Dfc	Kinetic	Transforming	Revit+ Dynamo	APACHE IES VE IT Radiance SunCast	Excel	Energy Visual	cooling, heating, and lighting energy consumption, UDI, sDA	148
Rapid Simulation of Optimally Responsive Façade during Schematic Design Phases: Use of a New Hybrid Metaheuristic Algorithm	10.3390/su11092681		(Yi et al., 2019)	Simulation	Champaign Miami Sitka	USA	Cfa Am Dfc	Kinetic	Rotating Scaling Translating	Rhino+Grasshopper	DIVA Radiance	Galapagos	Thermal Visual	ASE, DGP, sDA	141
Integrated parametric design of adaptive facades for user's visual comfort	10.1016/j.autcon.2019.102857		(Tabadkani et al., 2019)	Review Simulation	Tehran	Iran	BWk BSk	Responsive	Rotating Translating	Rhino+Grasshopper	Ladybug Tools Honeybee (DAYSIM and Radiance)	Galapagos	Visual	UDI, DGI, DGP	141
A multi-objective optimization approach for climate-adaptive building envelope design using parametric behavior maps	10.1016/j.buildenv.2020.107292		(Kim and Clayton, 2020)	Simulation	Houston	USA	Cfa	Intelligent	Rotating Translating	Rhino+Grasshopper	Ladybug Tools Honeybee (EnergyPlus and Radiance)	Octopus	Energy Visual	Cooling load, sDA	141
A user detective adaptive facade towards improving visual and thermal comfort	10.1016/j.jobe.2020.101554		(Rizi and Eltaweel, 2021)	Simulation	Tehran	Iran	BWk BSk	Responsive	Rotating	Rhino+Grasshopper	Ladybug Tools Honeybee (Radiance)	Octopus	Thermal Visual	Ev, DGP, heat gain, UDI	132
Developing an advanced daylight model for building energy tool to simulate dynamic shading device	10.1016/j.solener.2018.01.082		(Yi et al., 2019)	Experiment Simulation	Miami	USA	Cfa	Intelligent	Scaling	Rhino+Grasshopper	Arduino Ecotect Firefly DIVA (Radiance)	TAPSSA	Energy Visual Thermal	Ev, LE, sDA, solar radiation, TEC	130
Deployment and control of adaptive building facades for energy generation, thermal insulation, ventilation and daylighting: A review	10.1016/j.applthermaleng.2020.116331		(Alkhatib et al., 2021)	Review	-	-	-	Kinetic Smart Switchable	-	-	-	-	-	-	122
Self-shaping building skin: Comparative environmental performance investigation of shape-memory-alloy (SMA) response and artificial-intelligence (AI) kinetic control	10.1016/j.jobe.2020.102113		(Yi and Kim, 2021)	Calcutation Experiment	Suwon	South Korea	Dwa	Kinetic Smart	Rotating	-	Arduino Spyder (Phyton)	-	Thermal Visual	Ev, indoor temperature	120
Adaptive biomimetic facades: Enhancing energy efficiency of highly glazed buildings	10.1016/j.foar.2019.06.001		(Sheikh and Asghar, 2019)	Calculation Simulation	Lahore	Pakistan	BSh	Biomimetic Responsive	Rotating Translating	Revit+Dynamo	Ecotect Insight 360	-	Energy Thermal Visual	cooling and heating loads, Ev, irradiance levels	118
Performance Evaluation and Design of Thermo-Responsive SMP Shading Prototypes	10.3390/su12114391		(Yoon and Bae, 2020)	Experiment Simulation	Seoul	South Korea	Dwa	Smart	Rotating Translating Transforming	Rhino+Grasshopper	Ladybug Tools Honeybee (DAYSIM, EnergyPlus, Radiance, and THERM)	-	Thermal Visual	Ev, solar heat gains, UHI	118
Transformable building envelope design in architectural education	10.1016/j.promfg.2020.02.212		(Matheou et al., 2020)	Experiment Simulation	Larnaca	Cyprus	Csa	Kinetic	Rotating Translating	Rhino+Grasshopper	DIVA Energyplus	-	Visual	Ev	117
Parametric behavior maps: A method for evaluating the energy performance of climate-adaptive building envelopes	10.1016/j.enbuild.2020.110020		(Kim and Clayton, 2020)	Simulation	Houston	USA	Cfa	Responsive	Rotating Translating	Rhino+Grasshopper	Ladybug Tools Honeybee (EnergyPlus and Radiance)	Octopus	Thermal	Diffuse and beam solar radiation	115
Design approaches and typologies of adaptive facades: A review	10.1016/j.autcon.2020.103450		(Tabadkani et al., 2021)	Review	-	-	-	Biomimetic Intelligent Kinetic Responsive Smart Switchable	-	-	-	-	-	-	112

Further research pieces on building enclosures according to StArt Scoring criteria

Title	DOI	ISBN	Authors	Study Methodology	Location			Active Typology	Movement	Software			Simulation		StArt Score
					City	Country	Weather			Modeling	Simulation	Optimization	Objective	Metrics	
Prototype of a cyber-physical façade system	21995818		(Böke et al., 2020)	Experiment	-	Germany	Cfb	Responsive	R	Rhino+Grasshopper	Arduino, Firefly	-	Thermal	Indoor temperature	210
. Daylighting and visual comfort of oriental sun responsive skins: A parametric analysis	10.1007/s12273-018-0433-0		(Tabadkani et al., 2018)	Calculation Simulation	Tehran	Iran	BWk BSk	Responsive	Rotating	Rhino+Grasshopper	DIVA, LadyBug	Galapagos	Visual	DGP, Ev, DIcon, sDA, UDI, VCI	200
A performance-driven design model of territorial adaptive building skins (TABS) for daylighting performance optimization in office buildings in Egypt	-		(Elkhatieb, 2016)	Review Simulation Experiment	Cairo	Egypt	BWh	Responsive	Rotating	Rhino+Grasshopper	DIVA, LadyBug, Honeybee	-	Visual	DA, DGP, sDA, UDI	160
Self-adapting micro shading façade design using responsive polymer sheets	-		(Song et al., 2021)	Experiment Simulation	Los Angeles	California	Csb	Smart	Transforming	Rhino+Grasshopper	DIVA	-	Energy Visual	Ev	150
Parametric-based designs for kinetic facades to optimize daylight performance: Comparing rotation and translation kinetic motion for hexagonal facade patterns	10.1016/j.solener.2015.12.039		(Mahmoud and Elghazi, 2016)	Simulation	Cairo	Egypt	BWh	Kinetic	Rotating Translating	Rhino+Grasshopper	DIVA	-	Visual	Percentage of Daylit Area	137
Design method for adaptive daylight systems for buildings covered by large (span) roofs	-		(Heinzelmann, 2018)	Case Study Review Simulation	Fort Worth	USA	Cfa	Kinetic Smart	Rotating	Rhino+Grasshopper	DIVA	Galapagos	Visual	DGP, Ev	135
Using parametric BIM integration for prototyping future responsive façades	10.7480/jfde.2018.1.1865		(Mallasi, 2018)	Experiment Simulation	-	Saudi Arabia	BWh	Kinetic	Translating	Revit+Dynamo	Arduino Revit Solar Exposure Data	-	Thermal	Solar exposure	134
Use of Kinetic Facades in Enhancing Daylight Performance for Office Buildings	-		(El-Dabaa, 2016)	Case Study Simulation	Cairo	Egypt	BWk	Responsive	Rotating Translating	Rhino+Grasshopper	Ladybug Tools DIVA	TT Toolbox, Excel	Visual	Daylight Uniformity, Ev	133
Soft-Robotic-Driven Adaptive Photovoltaic Building Envelopes	-		(Svetozarevic, 2018)	Experiment Simulation Calculation	Zurich	Switzerland	Cfb	Kinetic	Rotating	Rhino+Grasshopper	Abaqus CAE DIVA	-	Airflow Energy Thermal	Electricity consumption, electricity demand, solar radiation	132
Daylight and thermal harvesting performance evaluation of a liquid filled prismatic façade using the Radiance five-phase method and EnergyPlus	10.1016/j.buildenv.2017.10.017		(Vlachokostas and Madamopoulos, 2017)	Simulation	New York	USA	Cfa	Kinetic	Rotating	SolidWorks	EnergyPlus Radiance THERM Window	-	Visual Energy Thermal	UDI, DGP	132
Photobioreactors as a dynamic shading system conceived for an outdoor workspace of the state library of Queensland in Brisbane: Study of daylighting performances	10.15627/jd.2019.14		(Lo Verso et al., 2019)	Simulation Case Study	Queenland Turin Dubai	USA Italy United Arab Emirates	Cfa Cfb BWh	Kinetic	Transforming	Rhino+Grasshopper	DIVA	-	Visual	DA, Light Transmittance, point in time Ev, UDI	132
Optimizing building net energy demand with dynamic BIPV shading	10.1016/j.apenergy.2017.05.083		(Jayathissa et al., 2017)	Calculation Simulation	Zurich	Switzerland	Cfb	Kinetic	Rotating	Rhino+Grasshopper	Ladybug Tools Honeybee (Radiance)	-	Energy	Hourly energy demand	131
Comparative Study of the Energetic Performance of Climate Adaptive Façades Compared to Static Façade Design in a Mediterranean Climate	-		(Borg et al., 2016)	Simulation	Msida	Malta	Csa	Kinetic Switchable Smart	Rotating Transforming	Rhino+Grasshopper	Ecotect IES VE Radiance	-	Thermal Visual	Cooling load, Ev	131
Climate Adaptive Building Shells for Office Buildings in Egypt: A Parametric and Algorithmic Daylight Tool	-		(Elkhatieb and Sharples, 2016)	Simulation	Cairo	Egypt	BWk	Responsive	Rotating	Rhino+Grasshopper	DIVA Evalglare Radiance	Galapagos	Visual	DGP, Ev, Illuminance contrast ratio, solar radiation	131
Dynamic Envelope and Control Shading Pattern for Office Buildings Visual Comfort in Tehran	-		(Fazeli et al., 2019)	Simulation	Tehran	Iran	BWk BSk	Kinetic	Transforming	Rhino+Grasshopper	Honeybee	-	Visual	UDI, DGP	131
External shading in buildings: comparative analysis of daylighting performance in static and kinetic operation scenarios	00038628.2016.1266991		(Grobman et al., 2017)	Simulation	Tel Aviv	Israel	Csa	Kinetic	Rotating	Rhino+Grasshopper	DAYSIM DIVA Radiance	-	Visual	UDI	130
Evaluating the daylighting performance of dynamic façades by using new annual climate-based metrics	-		(Wagdy et al., 2016)	Simulation	Boston	USA	Dfa	Kinetic	Rotating	Rhino+Grasshopper	DIVA DAYSIM Radiance	-	Visual	HsDA, HSE	126
Review on Interaction of Innovative Building Envelope Technologies and Solar Energy Gain	10.1016/j.egypro.2017.11.006		(Talaei et al., 2017)	Review	-	-	-	Biomimetic Responsive Smart	-	-	-	-	-	-	125
Optimizing the performance of variable geometry shading screens for occupant's comfort	-		(Naik et al., 2017)	Experiment Review Simulation	-	USA	Csb	Kinetic	Rotating	-	IES VE	-	Visual	DA, DGP, sDA	124
Lighting and cooling energy assessment of multi-purpose control strategies for external movable shading devices by using shaded fraction	10.1016/j.enbuild.2017.06.030		(Choi et al., 2017)	Calculation Experiment	Incheon	South Korea	Dfa	Kinetic	Rotating	-	-	-	Energy Visual	DGP, energy conservation, Ev	124
Effect of kinetic facades on energy efficiency in office buildings - hot and dry climates	-		(Bacha and Bourbia, 2016)	Simulation	Biskra	Algeria	BWh	Kinetic	Rotating Translating	Rhino+Grasshopper	Ecotect Radiance	-	Energy Thermal Visual	electric generation, Ev	121
Building applications, opportunities and challenges of active shading systems: A state-of-the-art review	10.3390/en10101672		(Al Dakheel and Aoul, 2017)	Review	-	-	-	Kinetic Switchable Smart	-	-	-	-	-	-	118
Climate-adaptive facade design with smart materials: Evaluation and strategies of thermo-responsive smart material applications for building skins in Seoul	-		(Yoon, 2018)	Review Case Study Simulation	Seoul	South Korea	Dwa	Smart	Rotating Scaling	Rhino+Grasshopper	Ladybug Tools Honeybee (Radiance)	-	Thermal	Solar radiation	117
A model for performance evaluation of climate-adaptive building envelopes using parametric models and multi-criteria optimization	-		(Kim, 2017)	Simulation	Houston	USA	Cfa	Responsive	Rotating Translating	Rhino+Grasshopper	Ladybug Tools Honeybee (EnergyPlus, DAYSIM, Radiance	Octopus	Energy Visual	Annual Solar Radiation, cooling load, sDA	116
A methodology of interactive motion facades design through parametric strategies	10.3390/app10041218		(Panya et al., 2020)	Simulation	Los Angeles	USA	Csb	Kinetic	Rotating	Rhino+Grasshopper	Ladybug Tools Honeybee (DAYSIM, DIVA)	-	Thermal Visual	Ev, PMV, sDA	114
Exploration of Adaptive Origami Shading Concepts through Integrated Dynamic Simulations	10.1061/(asce)ae.1943-5568.0000323		(Pesenti et al., 2018)	Simulation	Milan	Italy	Cfa	Smart	Translating Rotating	Rhino+Grasshopper	Ladybug Tools Honeybee	-	Energy Visual	DGP, UDI, TEC	112
A computational approach for achieving optimum daylight inside buildings through automated kinetic shading systems	10.1016/j.foar.2019.10.004		(Samadi et al., 2020)	Simulation	Tehran	Iran	BSk	Responsive	Rotating	Rhino+Grasshopper	Ladybug Tools Honeybee	Galapagos	Visual	UDI	112
The effectiveness of enviro-materially actuated kinetic facades: Evaluating the thermal performance of thermo-bimetal shading component geometries	-		(Jambo, 2017)	Case Study Review Simulation	Los Angeles Phoenix Cambridge	USA	Cfa Csa BWh	Smart	Transforming	Rhino+Grasshopper Revit+Dynamo	IES VE	-	Thermal Visual	Heating degree days, shading percentage	111
The impacts of dynamic façade shading typologies on building energy performance and occupant's multi-comfort	00038628.2017.1337558		(Elzeyadi, 2017)	Case Study Experiment Simulation	Eugene	USA	Csb	Kinetic	Rotating Translating	-	IES VE	-	Energy Visual	DGI, DGP, EUDI, sDA	110
Design optimum responsive façade based on visual comfort and energy performance	-		(Valitabar et al., 2018)	Simulation	Tehran	Iran	BSk	Kinetic	Rotating	Rhino+Grasshopper	Ladybug Tools Honeybee	-	Energy Visual	DGP, mean Ev, TEC	110
Origami Explorations a Generative Parametric Technique For kinetic cellular façade to optimize Daylight Performance	-		(ElGhazi and Mahmoud, 2016)	Simulation	Cairo	Egypt	BWk	Kinetic	Rotating Translating	Rhino+Grasshopper	DIVA	-	Visual	DA, hourly sun exposure,	108
Kinetic Shading System as a means for Optimizing Energy Load: A Parametric Approach to Optimize Daylight Performance for an Office Building in Rome	-		(Jahanara and Fioravanti, 2017)	Simulation	Rome	Italy	Csa	Biomimetic	Rotating Translating	Rhino+Grasshopper	DIVA	-	Visual	UDI	107
Parametric design and daylighting: A literature review	10.1016/j.rser.2017.02.011		(Eltaweel and Su, 2017)	Review	-	-	-	Intelligent Kinetic Responsive	-	-	-	-	-	-	105

Developing an advanced daylight model for building energy tool to simulate dynamic shading device	10.1016/j.solener.2018.01.082	(Yi et al., 2018)	Simulation	Champaign	USA	Dfa	Smart	TM	NURBS CAD Rhino+Grasshopper	EnergyPlus DIVA	-	Visual	diffuse and beam solar irradiance, Ev	104
A study of kinetic façade modelling performance using virtual reality	-	(Panya et al., 2019)	Simulation	Icheon	South Korea	Dwa	Kinetic	Rotating	Rhino+Grasshopper	Ladybug Tools	-	Visual	Annual Ev	103
Parametric analysis and systems design of dynamic photovoltaic shading modules	10.1002/ese3.115	(Hofer et al., 2016)	Calculation Experiment Simulation	Zurich	Switzerland	Cfb	Kinetic	Rotating	Rhino+Grasshopper	DIVA	-	Energy Thermal	Irradiance, insolation, PV electricity generation	103
Folding Fan Facade: Designing an actuated adaptive facade system for a fire-grain daylight control	-	(Kim, 2018)	Experiment	Cambridge	USA	Cfb	Kinetic	Translating	Rhino+Grasshopper	-	-	Visual	Ev	97
Heat-actuated Auxetic Facades	-	(Tafrihi and Abdel-rahman, 2018)	Experiment Simulation	Cairo	Egypt	BWk	Smart	TM	Rhino+Grasshopper	Honeybee	-	Visual	Ev	96
. Adaptive building facade Optimisation	-	(Chen and Huang, 2016)	Calculation Experiment Simulation	Tainan	Taiwan	Am	Kinetic	Rotating	Revit+Dynamo	Arduino EnvLoad	-	Energy	TEC	96
Adaptive Facade, the active connection between indoor and outdoor: Visual and Thermal evaluation of an adaptive facade in the urban context of Copenhagen	-	(Wang and Morata, 2019)	Review Simulation	Copenhagen	Denmark	Cfb	Kinetic	Rotating	Rhino+Grasshopper	Ladybug Tools Honeybee	Octopus	Thermal Visual	Ev, PMV, MRT, To, UDI, UTCI	95
Shape-changing Architectural Skins: A Review on Materials, Design and Fabrication Strategies and Performance Analysis	10.7480/jfde.2019.2.3877	(Vazquez et al., 2019)	Review	-	-	-	Smart	-	-	-	-	-	-	95
Applying biomimicry to design building envelopes that lower energy consumption in a hot-humid climate	10.1080/00038628.2017.1359145	(Fecheyr-Lippens and Bhiwapurkar, 2017)	Simulation	Chicago	USA	Dfa	Biomimetic Smart	TM	DesignBuilder	EnergyPlus	-	Energy	heat extraction rate, TEC	93
The development of kinetic façade units with BIM-based active control system for the adaptive building energy performance service	-	(Shen and Lu, 2016)	Experiment Simulation	Taichung	Taiwan	Cwa	Kinetic	Rotating Translating	Revit+Dynamo	Arduino	-	Visual	Ev	93
Environmental assessment of an integrated adaptive system for the improvement of indoor visual comfort of existing buildings	10.1016/j.renene.2017.07.079	(Michael et al., 2018)	Simulation	Nicosia	Cyprus	BSh	Kinetic	Rotating	Rhino+Grasshopper	Ecotect Radiance	-	Visual	DF, UDF	91
A novel framework to evaluate the performance of responsive kinetic shading devices	-	(Teksoy and Dursun, 2018)	Calculation Simulation	Izmir	Turkey	Csa	Intelligent	Rotating	Rhino+Grasshopper	Bumblebee Ladybug Tools Honeybee (EnergyPlus, DAYSIM, OpenStudio, Radiance)	CIDEA	Thermal	Ev, indoor temperature	90
Parametric modelling and simulation of an indoor temperature responsive rotational shading system design	-	(Cheng et al., 2020)	Calculation Experiment Simulation	Sheddield	UK	Cfb	Responsive	Rotating	Rhino+Grasshopper	Arduino Honeybee	-	Thermal	Indoor temperature	89
Patterns of façade system design for enhanced energy performance of multistory buildings	10.1016/j.enbuild.2016.08.051	(Hachem and Elsayed, 2016)	Simulation	Calgary	Canada	Dfc	Kinetic	Rotating Translating	Rhino+Grasshopper	EnergyPlus	-	Energy Thermal	Annual heating and cooling loads, PV generation	89
What is an adaptive façade? Analysis of recent terms and definitions from an international perspective	10.7480/jfde.2018.3.2478	(Romano et al., 2018)	Review	-	-	-	Biomimetic Intelligent Kinetic Responsive Smart Switchable	-	-	-	-	-	-	89
Adaptive building and skin: an innovative comutational workflow to design energy efficient buildings in different climate zones	10.4324/9781315081595-1	(Rossi-Schwarzenbeck and Figliola, 2019)	Simulation	Berlin	Germany	Cfb	Smart	TM	Rhino+Grasshopper	Ladybug Tools Honeybee (EnergyPlus, DAYSIM, OpenStudio, Radiance)	-	Energy Thermal	Cooling energy, UTCI, PMV	88
Current trends and future challenges in the performance assessment of adaptive façade systems	10.1016/j.enbuild.2018.09.017	(Attia et al., 2018)	Review	-	-	-	Responsive	-	-	-	-	-	-	88
Using Tensegrity and Folding to Generate Soft Responsive	-	(Abdelmohsen et al., 2016)	Experiment Simulation	Cairo	Egypt	BWh	Smart	Rotating Translating	Rhino+Grasshopper	Arduino DIVA Kangaroo Ladybug Tools	-	Thermal Visual	Ev, Solar Radiation	87
Retrofits for energy efficient office buildings: Integration of optimized photovoltaics in the form of responsive shading devices	-	(Abdullah and Alibaba, 2017)	Experiment Simulation	Erbil	Iraq	BSh	Responsive	Rotating Translating	Rhino+Grasshopper	EnergyPlus Ladybug Tools OpenStudio	-	Energy	Heating and cooling loads, TEC	85
Dynamic shading systems: A review of design parameters, platforms and evaluation strategies	10.1016/j.autcon.2019.01.014	(Al-Masrani and Al-Obaidi, 2019)	Review	-	-	-	Intelligent Kinetic Responsive	-	-	-	-	-	-	85
Daylighting Based Parametric Design Exploration of 3D Facade Patterns	-	(Narangerel et al., 2016)	Simulation	Icheon	South Korea	Dwa	Kinetic	Rotating Translating	Rhino+Grasshopper	Ladybug Tools Honeybee (Radiance)	Octopus	Visual	Ev, UDI, PV generation	85
An automated louver with innovative parametrically-angled reflective slats: Prototyping and validation via using parametric control in Grasshopper along with Arduino board	10.1016/j.enbuild.2020.110614	(Eltaweel et al., 2021)	Experiment Simulation	Nottingham	UK	Cfb	Kinetic	Rotating	Rhino+Grasshopper	Arduino Firefly Ladybug Tools Honeybee (Radiance)	-	Visual	Ev	83
A reflective adaptive solar façade for multi-building energy and comfort management	10.1016/j.enbuild.2018.07.040	(Powell et al., 2018)	Calculation Simulation	Zurich	Switzerland	Cfb	Kinetic	Rotating	Rhino+Grasshopper	EnergyPlus SolTrace Tonatiuh	-	Energy	Heating and cooling loads, TEC	83
Thermal performance optimization of parametric building envelope based on bio-mimetic inspiration	10.1016/j.asej.2020.07.007	(Abdel-rahman, 2021)	Simulation	Cairo	Egypt	BWh	Biomimetic	Rotating	Rhino+Grasshopper	EnergyPlus	Galapagos	Thermal	Cooling, heating, and lighting loads	83
Biomimetic adaptive building skins: Energy and environmental regulation in buildings	10.1016/j.enbuild.2019.109544	(Kuru et al., 2019)	Review	-	-	-	Biomimetic	-	-	-	-	-	-	82
A review of building parameters' roles in conserving energy versus maintaining comfort	10.1016/j.jobe.2020.102087	(Alsharif et al., 2021)	Review	-	-	-	Intelligent Kinetic Responsive	-	-	-	-	-	-	79
Bio-inspired Passive Kinetic Solar Shading Device for a Responsive Architectural Envelope	-	(Chayaamor-Heil and Laracuente, 2018)	Simulation	Seville	Spain	Csa	Biomimetic intelligent Smart	Translating	Rhino+Grasshopper	Ladybug Tools SMM NiTi Flexinol Mecca	-	Thermal	Solar radiation	79
Integrating illuminance and energy evaluations of cellular automata controlled dynamic shading system using new hourly-based metrics	10.1016/j.solener.2018.05.041	(Ayoub, 2018)	Simulation	Alexandria	Egypt	BWh	Intelligent	TM	Rhino+Grasshopper	DIVA	-	Energy Thermal Visual	HDI, HED, HSI, sDA, TEC	77
Shape morphing solar shadings: A review	10.1016/j.rser.2015.10.086	(Fiorito et al., 2016)	Review	-	-	-	Smart	-	-	-	-	-	-	76
Kinetic Facades the new Paradigm Shift in Architecture toward an Environmental Design Performance	10.33193/JALHSS.43.29755	(Bakr, 2019)	Review	-	-	-	Kinetic	-	-	-	-	-	-	75
Development of a self-sufficient dynamic façade within the context of climate change	10.1080/00038628.2020.1713042	(Ricci et al., 2021)	Simulation	Bologna Athens Munich Copenhagen	Italy Greece Germany Denmark	Cfa Csa Dfb Cfb	Kinetic	Rotating	Rhino+Grasshopper	Ladybug Tools Honeybee	-	Thermal Visual	Ev, MRT	72
Design optimization of solar shading systems for tropical office buildings: Challenges and future trends	10.1016/j.solener.2018.04.047	(Al-Masrani et al., 2018)	Review	-	-	-	Kinetic	-	-	-	-	-	-	72
3D-printed attachable kinetic shading device with alternate actuation: Use of shape-memory alloy (SMA) for climate-adaptive responsive architecture	10.1016/j.autcon.2020.103151	(Yi et al., 2020)	Calculation Experiment Simulation	Suwon	South Korea	Dwa	Smart	Rotating Translating	Rhino+Grasshopper	Arduino DIVA EnergyPlus	-	Visual	Ev	66
A biomimetic approach for the multi-objective optimization of kinetic facade design	-	(Jang and Kim, 2017)	Simulation	Icheon	South Korea	Dwa	Biomimetic	Rotating	Rhino+Grasshopper	Ladybug	-	Thermal	Solar radiation	65
Machine learning integration for adaptive building envelopes	-	(Smith and Lasch, 2016)	Experiment Simulation	Tucson	USA	BSh	Intelligent	TR	Rhino+Grasshopper	Ladybug Tools Honeybee (EnergyPlus)	-	Energy Thermal Visual	Ev, heating and cooling loads	64

Form follows environment: Biomimetic approaches to building envelope design for environmental adaptation	10.3390/buildings7020040	(Badarnah, 2017)	Review	-	-	-	Biomimetic	-	-	-	-	-	-	64
Building Optimization: The Adaptive Façade	10.4028/www.scientific.net/amr.1149.64	(Lanza Volpe, 2018)	Review	-	-	-	Biomimetic Kinetic Smart	-	-	-	-	-	-	63
How plants inspire façades. From plants to architecture: Biomimetic principles for the development of adaptive architectural envelopes	10.1016/j.rser.2016.09.018	(López et al., 2017)	Review	-	-	-	Biomimetic	-	-	-	-	-	-	58
A shape grammar approach to climatically adaptable façade systems with real time performance evaluation	1743-3509	(Nguyen et al., 2019)	Simulation	Derby	UK	Cfa	Kinetic	TR	Revit+Dynamo	Arduino, Firefly, Ladybird, Solar Analysis	-	Thermal Visual	Ev, net solar gains	56
An affective kinetic building façade system: mood swing	-	(Moulton et al., 2018)	Simulation	Orlando	USA	Cfa	Kinetic	Rotating	Rhino+Grasshopper	Ladybug Tools Honeybee (EnergyPlus, DAYSIM, OpenStudio, Radiance)	-	Visual	DAcon	56
Understanding kinetic architecture: typology, classification, and design strategy	10.1080/17452007.2016.1203676	(Megahed, 2017)	Review	-	-	-	Kinetic	-	-	-	-	-	-	56
Adaptive Roof Aperture for Multiple Cooling Conditions	-	(Aviv, 2018)	Simulation Experiment	Princeton	USA	Cfa	Kinetic	Rotating	Rhino+Grasshopper	Arduino Firefly	-	Airflow	Air velocity	56
Parametric analysis and systems design of dynamic photovoltaic shading modules	10.1002/ese3.115	(Hofer et al., 2016)	Experiment Simulation	Zurich	Switzerland	Cfb	Kinetic	Rotating	Rhino+Grasshopper	DIVA MATLAB	-	Energy	Global insolation, net energy demand, TEC	56
Biomimicry inspired Adaptive Building Envelope in hot climate	10.21608/erj.2020.135274	(El-Rahman et al., 2020)	Simulation	Cairo	Egypt	BWh	Biomimetic	Rotating Translating	Rhino+Grasshopper	Ladybug Tools Honeybee (EnergyPlus, OpenStudio)	-	Energy	Heating and cooling loads, To	56
O desenvolvimento de elementos de proteção de fachada responsivos – exploração e controle de um processo	10.11606/gtp.v11i2.118346	(Vaz et al., 2016)	Experiment Simulation	Recife	Brazil	Am	Kinetic	Rotating	Rhino+Grasshopper	Arduino Ecotect DIVA Geco Ghowl Gobetwino	-	Airflow	Air velocity	56

APPENDIX IV

```
#include <AccelStepper.h>
#include <Wire.h>
#include <BH1750.h>

AccelStepper motorPasso (AccelStepper::FULL4WIRE, 8, 10, 9, 11);

BH1750 lightMeter;

int position = motorPasso.currentPosition();
int minposition = 0, maxposition = -513, angle = 57;

void setup()
{
  Serial.begin(9600);
  Wire.begin();
  lightMeter.begin();
  motorPasso.setMaxSpeed(1000.0);
  motorPasso.setAcceleration(100.0);
  motorPasso.setSpeed(200);
  Serial.print("Posição: ");
  Serial.print(motorPasso.currentPosition());
  Serial.println(" passos");
  delay(2000);
}

void loop()
{
  float lux = lightMeter.readLightLevel();
  Serial.print("Luminosidade: ");
  Serial.print(lux);
  Serial.println(" lux");

  if (lux <= 500 && (position > maxposition)) {
    motorPasso.moveTo(position - angle);
    while (motorPasso.distanceToGo() != 0){
      motorPasso.run();
    }
    position = position - angle;
   Serial.print("Posição: ");
   Serial.print(motorPasso.currentPosition());
   Serial.println(" passos");
  }

  else if (lux >= 2000 && (position < minposition)) {
    motorPasso.moveTo(position + angle);
    while (motorPasso.distanceToGo() != 0){
      motorPasso.run();
    }
    position = position + angle;
```

```
    Serial.print("Posição: ");
    Serial.print(motorPasso.currentPosition());
    Serial.println(" passos");
   }
   else{}
   delay(500);
}
```